STUDY OF PONDEROMOTIVE EFFECTS IN SRF CAVITIES FOR CURRENT AND NEXT GENERATION LINEAR ACCELERATORS

By

Jacob Brown

A DISSERTATION

Submitted to
Michigan State University
in partial fulfillment of the requirements
for the degree of

Physics—Doctor of Philosophy

2026

ABSTRACT

Superconducting radiofrequency (SRF) cavities have become one of the foremost tools for creating high-power beams with any species of charged particles. A high loaded quality factor ($Q_l > 10^6$) and a high accelerating gradient allow for high-performance acceleration and efficient delivery of power to the beam. These advantages have made SRF cavities the technology of choice for existing high-beam-power accelerator facilities such as the Facility for Rare Isotope Beams (FRIB), the Spallation Neutron Source, and others. As economical and environmental considerations are becoming more critical, future machines and upgrades, such as the FRIB energy upgrade and the Proton Improvement Plan (PIP-II) at Fermi National Accelerator Laboratory are looking toward operating SRF cavities with higher Q_l ($Q_l > 10^7$) for reduced RF power costs and better beam-power delivery.

While RF power can be transferred to the beam more efficiently with a higher Q_l, there are some disadvantages. The resulting decrease in RF bandwidth results in an increase in sensitivity to disturbances, both internal and external. Acoustic vibrational noise from the cryomodule and the environment can quickly shift the cavity's resonant frequency of the cavity away from the generator frequency, leading to an increase in RF power consumption. Additionally, the ponderomotive Lorentz pressure in the cavity the cavity field can couple to the cavity's mechanical vibrational eigenmodes, leading to unstable behavior (ponderomotive instabilities).

In this work, we study the behavior of these ponderomotive instabilities in SRF cavities, with both open and closed control loops. We use measured Lorentz transfer functions of coaxial quarter-wave, half-wave, single-spoke, and 5-cell, elliptical cavities from FRIB and PIP-II and explore their differences. We use the electromechanical parameters extracted from these transfer functions to examine how the thresholds of instabilities can be affected by both linear and nonlinear control systems. We find that, at high controller gain, residual vibrational noise can be passed from the cavity phase control loop into the cavity amplitude loop, exciting electromechanical oscillations and their harmonics. We also confirm that the choice of coordinate system affects the closed loop stability, with control algorithms acting on the in-phase and quadrature components of the cavity

voltages providing higher instability thresholds than algorithms acting on the cavity amplitude and phase.

Additionally, we present the first measurements comparing ponderomotive instability thresholds at different temperatures. We find that coaxial resonators operating at 4.3 K have significantly higher instability thresholds than those operating at 2 K. We measured the quality factors of the vibrational mechanical modes at 4.3 K and found that they are lower than their measured values at 2 K. These reductions in mechanical quality factors entail higher instability thresholds. We also explore other avenues through which the oscillatory instability threshold might be increased, opening the doors for future work.

Finally, we discuss methods to further reduce RF power consumption and mitigate ponderomotive instabilities using a piezoelectric mechanical tuner. We use simulation methods to show the potential effectiveness of an active disturbance rejection control (ADRC) algorithm for tuner control loops to reduce the impact of vibrational noise on cavity performance. We benchmark the performance in simulation against the commonly used proportional-integral controller. We use simulation methods to combine ADRC with active noise cancellation to show a potential controller combination for microphonics reduction in continuous-wave machines. We demonstrate initial deployment of these algorithms for tuner control on a room temperature, helium-jacketed 5-cell elliptical, 650 MHz cavity for the PIP-II project.

Copyright by
JACOB BROWN
2026

For my Dad, Mom, Emily, and Jenn, who have supported me every step of the way.

ACKNOWLEDGEMENTS

One thing I wasn't prepared for coming into grad school was how much my life would change and how many people would come to impact my life in such a meaningful way. Along this journey, I have met so many incredible people who have helped me grow as a scientist and a person. First, I would like to express my deepest gratitude to my advisor, Ting Xu. Your insights not only helped me shape this project, but also helped me feel more confident in my work and explore more of the scientific world. I have grown significantly, technically and from a confidence standpoint, since I started, and I attribute that to your guidance. I hope we can continue to work together as I move into the next stage of my career.

I would also like to express my gratitude to Slava Yakovlev. Throughout my entire degree, you have been a staunch supporter of my work and supported my transition to Fermilab. I sincerely appreciate your optimism and passion for science, which helped me a lot this past year, which held many uncertainties. I also would like to thank my committee for their words of support, guidance, and interest in this project the last two years: Remco Zegers, Peter Ostroumov, Sergey Baryshev, and Wade Fisher.

On the FRIB side of things, there are many people I would like to thank. To Sang-hoon Kim, for the many insightful conversations over the last four years and support in forming this project. To Walter Hartung, for your help in finding the best ways to communicate my findings. To Wei Chang, for helping me set up and conduct many measurements. To Shen Zhao, for helping a physicist try to understand controls.

At Fermilab; to Sasha Sukhanov, for taking the time to help me analytically model cavities and for working with me to better our paper. To Crispin Contreras-Martinez, for the many hours of technical conversations and for being a staunch supporter of mine at Fermilab. I greatly appreciate your help and support at and outside of work even when you were dealing with so many obligations yourself. To Donato Passarelli, for being supportive of my time at Fermilab and for your career insights.

I have also made so many wonderful friends who have made life exciting and enjoyable,

especially when life seemed to be trying to beat me down. Thank you, Hannah, Aiden, Lauren and Shane for being my constant companions since we were first spending many hours surviving qualifying coursework. Thank you all so very much for all the laughs, tears, and games of pickleball that helped keep me sane. I would also like to give my gratitude to my research group: Patrick, Kaela, Ziye, Sean, and Javier, for the game nights, USPAS trips, and work conversations. I am glad I got to share the time I did with you all, and I hope the rest of your time in graduate school is as enriching as it was for me. At Fermilab, thank you to John, Cristhian, and Betiay for the lunches together.

I am also so fortunate to have so many of my early friends still present in my life who have supported me. I'd like to give my thanks to Keegan, Andrew, and Sean: for being there whenever I needed them and for being one of the best parts about coming home. The same goes for Michael, Jacob, Evan, Aidan, Alvin, Tim, and Safe for many nights of laughs and games. I am grateful for the friends I made in undergrad, who I am happy to talk to with today: Robert, Tony, Ben, Sarah, Mansoor, Ellie, and Amanda.

To Srushthi, I'd like to thank you for being a good friend and checking in with me even though we live 12 hours away from each other. Our trips together were always a highlight of the year, and I am looking forward to being able to travel more with you, because no one else opens the door for a native New Yorker. Additionally, I'd like to thank David and Arie, for showing me that maybe the West Coast is the best coast and helping to bring reading back into my life. To Kaitie, I'd like to thank you for your unwavering support and celebration of my achievements even if I didn't feel they were that special. I would also like to give my full love and thanks to Alanna; you make life so special and fun, and I am excited to explore what the future has in store for us.

Finally, I want to express my love and gratitude to my family. I would not be the man I am today, let alone in this position, without them: my dad who helped me develop my curiosities and showed the merits of working hard, my mom who encouraged me to pursue my dreams and be more than what I was, and my sisters who gave me an outlet to vent. Their sacrifices and support for me are more than I could ever ask for. To my family, I hope that I continue to make you proud,

and stay worthy of all that you have given me. I also would like to acknowledge the impact of my grandparents; I miss you both and I wish you both were here to see this.

TABLE OF CONTENTS

LIST OF TABLES x

LIST OF FIGURES xii

LIST OF ABBREVIATIONS xix

CHAPTER 1 INTRODUCTION 1
- 1.1 Forward 1
- 1.2 The Age of RF Acceleration 2
- 1.3 RF Cavities 4
- 1.4 Superconducting Linacs in the United States 16
- 1.5 Motivation of Research 22
- 1.6 Outline of Thesis 24

CHAPTER 2 CAVITY MODELING AND DYNAMICS 25
- 2.1 The Lumped Circuit Model and Beyond 25
- 2.2 Transmission Line Basics 28
- 2.3 Detuning 33
- 2.4 Ponderomotive Instabilities 46

CHAPTER 3 FEEDBACK AND CONTROLLERS FOR SRF CAVITIES 56
- 3.1 SRF Cavity Process Variables 56
- 3.2 Control Loop Configurations 64
- 3.3 Control Algorithms 70

CHAPTER 4 EFFECTS OF LINEAR AND NONLINEAR CONTROL ON PONDEROMOTIVE INSTABILITY 78
- 4.1 The Lorentz Transfer Function 78
- 4.2 Stability of the Closed Loop Cavity 82
- 4.3 Instability Measurements at Different Temperatures 101
- 4.4 Predictions for Medium Velocity, Elliptical Cavities 112

CHAPTER 5 RESONANCE CONTROL OF SRF CAVITIES 116
- 5.1 The Piezo Transfer Function 116
- 5.2 Controlling the Piezo 119
- 5.3 Simulations and Comparisons 123
- 5.4 Experimentally Testing Resonance Control Algorithms 128
- 5.5 Simulated Ponderomotive Instability with Resonance Control 139

CHAPTER 6 CONCLUSIONS 145
- 6.1 Outlook 148
- 6.2 Funding Acknowledgments 148

BIBLIOGRAPHY 150

LIST OF TABLES

Table 1.1 Comparison of relevant parameters for normal and superconducting 1.3 GHz RF pillbox cavities. In this case, we are assuming $R_{res} = 5$ nΩ and the cryogenic power is calculated assuming 30% exergetic efficiency. 14

Table 1.2 Current FRIB cavities above the double lines and the planned FRIB energy upgrade elliptical cavity below the double line specifications: geometric beta, resonant frequencies, max accelerating field, and the number of cavities within the linac. 18

Table 1.3 Table of cavities to be deployed to the PIP-II SRF linac. Features the same relevant parameters as those found in Table 1.2. 20

Table 1.4 Relevant figures of merit for different superconducting linear accelerators in the USA: the accelerated species, mode of operation, max energy, beam current, number of SRF cavities, and max bandwidth of these cavities. Max energy and beam current for heavy-ion accelerators are representative of U^{238} beams. . . 22

Table 4.1 Mechanical and electromechanical parameters for the $\beta = 0.53$ HWR obtained from Fig. 4.2. 81

Table 4.2 Amplitude and phase controller and observer bandwidths used in experimental measurements for both HWR types. Bandwidths are presumed to be for the amplitude controller unless denoted with ϕ for the phase controller. The $\beta = 0.29$ HWRs measurement are taken with $E_{acc} = 7.7$ MV/m and the $\beta = 0.53$ HWR measurements are taken with $E_{acc} = 7.4$ MV/m. 83

Table 4.3 Controller bandwidth, the oscillatory instability threshold, the peak of Eq. (3.22) at the instability threshold f_{pk}, the relevant mechanical frequency f_μ, and the harmonic of f_μ such that $f_{pk} = N f_\mu$. 91

Table 4.4 Relevant proportional and integral gains for A/ϕ, PI-controlled simulations. Included are the controller and observer bandwidths for the ADRC simulation comparison. The sampling rate is share across both simulations. 99

Table 4.5 Mechanical mode frequency, quality factors, and percent changes from the 2 K values for key modes at 2 K and 4.3 K at 22 PSIa tuner pressure. 110

Table 4.6 Simulation/analytical parameters used for instability predictions for the FRIB energy upgrade cavity. 114

Table 4.7 Simulation/analytical parameters used for instability predictions for the FRIB energy upgrade cavity. 114

Table 5.1 Mechanical parameters extracted from the piezo transfer function measurement for the room temperature HB650 cavity in Fig. 5.1. 122

Table 5.2 Mechanical parameters extracted from the piezo transfer function measurement for the room temperature HB650 cavity in Fig. 5.1. 122

Table 5.3 Controller gains and loop rates used for simulation comparison. 123

Table 5.4 Controller gains and loop rates used for simulation comparison. 123

Table 5.5 Electormechanical parameters for the HB650 cavity measured at 2 K equipped with mock tuner. Parameters are extracted from the LTF presented in Fig. 2.10. . 139

Table 5.6 Electormechanical parameters for the HB650 cavity measured at 2 K equipped with mock tuner. Parameters are extracted from the LTF presented in Fig. 2.10. . 139

LIST OF FIGURES

Figure 1.1 Acceleration scheme designed by Ising and used by Widerøe. The 's' block represents the particle source, the green dots are the particles, the accelerating gaps are denoted with 'G', and the drift tubes are the boxes with diagonal markings. Figure originally published in [13]. 3

Figure 1.2 Simplified geometry for a pillbox cavity. Beam is passed along the central axis of the cavity ($\hat{\mathbf{z}}$). 5

Figure 1.3 Field maps for TM010 electric (left) and magnetic (right) fields for a 1.3 GHz pillbox cavity (l = 115 mm, R = 88 mm) simulated using CST microwave studio [16]. The beam direction is denoted at the bottom of each field plot. Internal energy is normalized to 1 J. 8

Figure 1.4 Graph of usual frequency values v. velocity ranges for common SRF cavity geometries. On the low velocity end are coaxial resonators and elliptical for higher velocity particles. Figure was originally published in [29]. 15

Figure 1.5 Cavity forward and reflected power (top) and cavity voltage (bottom) v. time for a single RF pulse of a 650 MHz HB650 cavity. The RF pulses with a 10 Hz repetition rate, a 10 ms fill time, and a 0.55 ms flat-top time. 17

Figure 1.6 Layout of FRIB driving linac with proposed energy upgrade cryomodules. Existing coaxial cryomodules are in green with the planned FRIB energy upgrade cryodmodule placements are in blue. Figure originally published in [41]. 18

Figure 1.7 Layout of the PIP-II linac with respect to the existing accelerator facilities. Figure originally published in [44]. 19

Figure 1.8 Layout of the LCLS-II SRF addition alongside the LCLS copper linac. Figure originally published in [50]. 21

Figure 2.1 Simple RLC circuit with AC sine-wave current source with beam loading denoted by the opposite direction current source $\tilde{I}_b$. 27

Figure 2.2 CST simulation of the TM_{010} fundamental mode electric (left) and magnetic (right) fields for an FRIB energy upgrade, single-cell geometry. The internal energy in this simulation is normalized to 1 J. 27

Figure 2.3 left) Diagram of inductive coupling method for a common normal conducting cavity geometry. right) Diagram of capacitive coupling for the SRF elliptical geometry. Figure is originally from [52]. 29

Figure 2.4 Equivalent circuit model for an RF cavity equipped with a fundamental power coupler with the influence of beam loading. 30

Figure 2.5 Power requirements for the operation of two cases of E_{acc} and beam current I_b. The two cases chosen represent the operation of an FRIB energy upgrade cavity at the maximum beam current and the LB650 cavity at nominal beam current. Both curves are calculated assuming $\psi_s = 0$, i.e. the beam arrives at the crest of the RF wave, and that $Q_0 = 2 \times 10^{10}$. 34

Figure 2.6 Required power for a constant field amplitude as a function of the detuning $\Delta f = \frac{\Delta\omega}{2\pi}$ for parameters mimicking FRIB energy upgrade and LB650 operation. Vertical dashed lines represent the respective half-bandwidths in Hz. In this case, we again take $\psi_s = 0$. 36

Figure 2.7 Detuning and LHe bath pressure v. time during a microphonics survey for an HB650 cavity during microphonics survey. There is a clear correlation between the detuning offset and pressure drift. This measurement period was used to identify microphonic noise sources and attempt to characterize their strength. 40

Figure 2.8 Schematic of deformations caused by the radiation pressure of the cavity fields. Figure originally from [69]. 42

Figure 2.9 Open-loop resonance curves for a $\beta = 0.53$ HWR for two conditions. Cavity resonance curve with no LFD considered (top) and with LFD considered (bottom). For both cases, $Q_l = 1 \times 10^7$ and $E_{acc,max} = 7.4$ MV/m. The red, dashed line represents the most unstable portion of the resonance curve. The green shaded regions represent the portion of the $V/\Delta f_0$ plane where the resonance curve will be dominated by nonlinear effects. Published in [70]. . . . 44

Figure 2.10 Lorentz transfer function amplitude v. forward power modulation frequency for the HB650 cavity. Electromechanical data can be extracted for 9 modes. . . 46

Figure 2.11 Cavity field E_{acc} (top) and frequency track (bottom) v. measurement time for a case of the oscillatory instability in a self-excited SSR2 cavity. Originally published in [70]. 48

Figure 2.12 Instability threshold voltages v. static detuning offset for the HB650 cavity using mechanical parameters extracted from the Lorentz transfer function. The solid lines represent the respective instability thresholds and the shaded regions represent unstable working points. 53

Figure 3.1 Schematic of a cavity dynamic system. The generator provides a drive amplitude, phase, and frequency. The envelope equation, Lorentz force, and disturbances result in the cavity amplitude, phase, and frequency which might differ from the generator. 57

Figure 3.2 Graphical representation of the cavity voltage phasor for a $\beta = 0.53$ HWR operating at $E_{acc} = 7.4$ MV/m and a $\phi = 25^\circ$ offset. 58

Figure 3.3 Four point RF generation scheme for the generation of low-level RF carrier voltages. Produces a single period T_{rf} waveform with the amplitude and phase specified by I and Q. 60

Figure 3.4 Picture of FRIB style pneumatic tuner equipped to 322 MHz, $\beta = 0.53$ HWR assembled on the cryomodule cavity string. Labeled are the relevant tuning motion/forces. 62

Figure 3.5 Picture of a jacketed HB650 cavity equipped with a double-lever arm, piezoelectric tuner at our room temperature test bed. 63

Figure 3.6 Diagram of a cavity with closed amplitude and phase control loops. $r_{A/\phi}$ represents the setpoints of cavity amplitude and phase respectively. $G_A(s)$ and $G_\phi(s)$ are the amplitude and phase controllers respectively as well. 67

Figure 3.7 Diagram of discretized extended state observer and relevant calculation progression. 74

Figure 3.8 Arbitrary amplitude of sinusoid v. chirped sinusoid frequency for a chirp passed through an LMS filter. 77

Figure 4.1 Circuit diagram for measurement of the Lorentz transfer function. 80

Figure 4.2 Lorentz transfer function amplitude (top) and Lorentz transfer function phase (bottom) v. modulation frequency. Included are fits using Lorentzians and the parameters in Table 4.1. 81

Figure 4.3 Lorentz transfer function amplitude v. modulation frequency for two $\beta = 0.085$, 80.5 MHz QWRs. Not only does the amplitude change, the shaking of the stiffening tube of the damper causes the appearances of other peaks as seen in Cavity 1. 82

Figure 4.4 Instability threshold in terms of detuning angle v. the amplitude controller bandwidth for eight $\beta = 0.53$ HWRs within the FRIB driver linac. Included are the measurements for four $\beta = 0.29$ HWRs for comparison. 84

Figure 4.5 Plot of relevant instability driving sidebands from spectrogram data for negative detuning (top) and positive detuning (bottom). Green shaded regions represents time periods where the phase control looped is closed. Unshaded regions are phase-open regimes. 85

Figure 4.6 Circuit diagram/schematic for Simulink for the cavity and controller system. Included is (from left to right) the phase change limiter on the drive phase and the Lorentz transfer function. 87

Figure 4.7 Archival process variable samples plotted against the correlated time stamps for a positive detuning ($\psi_0 > 0$) instability event in a $\beta = 0.53$ HWR. The process variables are (from top to bottom): the envelope of E_{acc}, the cavity phase envelope ϕ_c, max forward power P_f, and cavity detuning angle ψ_0. Archival sampling is at 1 Hz or lower so finer oscillations cannot be seen. Published in [70]. 88

Figure 4.8 Instability threshold v. amplitude controller bandwidth for comparison of our measurements in linac HWRs, predictions from the Simulink model, and predictions by the analytical model. 89

Figure 4.9 Transfer function magnitude (top) and phase (bottom) v. input frequency for Eq. (3.22) in two cases: $\psi_0 = 0.1°$ and $\psi_0 = 45°$. 90

Figure 4.10 FFT amplitude of the cavity detuning (top), amplitude, and phase (both bottom) v. frequency when the instability is excited for $\omega_c = 1200$ rad/s and $\psi_0 = -23.5°$. Since modes 3 and 4 in Table 4.1 are within 1 Hz of each other, the dual excitation manifests as one peak. 92

Figure 4.11 Sideband amplitude with respect to the carrier v. measurement time for a $\psi_0 < 0$ instability measurement. Akin to Fig. 4.5, the green shaded regions represents time periods where the phase loop is closed. 92

Figure 4.12 Magnitude of Eq. (3.22) v. frequency for our four amplitude controller bandwidths ω_c at their respective analytical oscillatory instability thresholds. . . 93

Figure 4.13 Predicted oscillatory instability threshold v. amplitude controller bandwidth from the Simulink and analytical models when the strongly coupled modes are dropped to > 100 Hz leaving k_μ^L and Q_μ the same. 94

Figure 4.14 Predicted oscillatory instability threshold v. amplitude controller bandwidth for both A/ϕ and I/Q control using both the Simulink and analytical models. . . 95

Figure 4.15 Bode responses of the A/ϕ and I/Q crosstalk transfer functions for a detuning angle of $\psi_0 = 22.5°$. 97

Figure 4.16 Simulated generator Q-voltage v. generator I-voltage for A/ϕ and I/Q controlled cavities when a disturbance of $\psi_0 = 45°$ is applied. 97

Figure 4.17 Simulated generator Q-component v. I-component for ψ_0 approaching the positive side instability for $\omega_c = 4800$ rad/s, $\omega_{ob} = 19200$ rad/s on the amplitude controller. The yellow square is starting voltage when the disturbance is applied. 98

Figure 4.18 Magnitude (top) and phase (bottom) of Eq. (3.22) for cavities using ADRC and PI for A/ϕ control. The responses are simulated using the gains in Table 4.4. 100

Figure 4.19 Bode/frequency response of Eq. (3.22) with A/ϕ PI controllers using the base gains in Table 4.4 for a $\beta = 0.53$ HWR at $E_{acc} = 7.4$ MV/m and $\psi_0 = -26°$. Changed gain parameters and the corresponding curve are detailed in the plot legend. 101

Figure 4.20 Instability threshold in terms of detuning angle v. amplitude controller bandwidth for $\beta = 0.29$ HWRs at $E_{acc} = 7.7$ MV/m (top) and $\beta = 0.53$ HWRs at $E_{acc} = 7.4$ MV/m (bottom) for both 4.3 K and 2 K measurements. 102

Figure 4.21 Simulink model of ADRC+cavity system with the addition of the MTF noise source (circled in red). 103

Figure 4.22 Simulated detuning v. time when the $\beta = 0.53$ HWR is given a kick to the instability threshold with and without the MTF noise. 104

Figure 4.23 FFT amplitude of the detuning v. frequency for an instability event including noise from the microphonics transfer function. The notch in the FFT amplitude at about 300 Hz is due to the fact that the noise is sampled at that frequency. 104

Figure 4.24 Simulated detuning v. time for white noise included and without at the instability threshold. 105

Figure 4.25 FFT amplitude of the detuning v. frequency for an instability event including white noise without the MTF. We can see that modes strongly coupled to the Lorentz force are present in the spectrum (Eq. (3.22)). 106

Figure 4.26 Oscillatory instability thresholds v. percentage reduction in mechanical quality factors for $\omega_c = 4800$ rad/s, $\omega_{ob} = 19200$ rad/s, and $E_{acc} = 7.4$ MV/m. . . . 107

Figure 4.27 Photo of the experimental setup used in the accelerator tunnel to measure mechanical quality factors of $\beta = 0.53$ HWRs in their cryomodules. 108

Figure 4.28 Sideband amplitude in terms of dBc v. time for an example decay measurement. The mode excited in this decay is the 261.6 Hz resonance. 110

Figure 4.29 Mechanical quality factors v. tuner pressure for resonances we expect are combined cavity and tuner resonances (top) and for resonances that are predicted by modal simulations (bottom). 111

Figure 4.30 Instability threshold in terms of detuning angle v. amplitude controller bandwidth: measured and predicted values for 2 K and 4.3 K Q_μ values. Error bars represent the instability thresholds at the upper and lower errors for the respective Q_μ values in Table 4.5. 112

Figure 4.31 LTF amplitude v. modulation frequency for a LB650 cavity equipped with mock tuner. 113

Figure 4.32 Predicted instability thresholds v. ADRC amplitude controller bandwidth for the FRIB energy upgrade cavity operational parameters. 115

Figure 5.1 PTF amplitude v. the piezo voltage modulation frequency for a room-temperature HB650 cavity. 118

Figure 5.2 Detuning cause by piezo-voltage modulation v. modulation frequency (top), and detuning caused by a bass speaker v. modulation frequency when the piezo stacks are decoupled and the cavity is oriented vertically (bottom). 119

Figure 5.3 Diagram of an SRF with all three types of control loops: amplitude, phase, and resonance control. The amplitude and phase controllers change the drive to the cavity while the resonance controller deforms the cavity to match the drive frequency. 120

Figure 5.4 Schematic of discretized ADRC algorithm for control of the piezo transfer function in Simulink. 122

Figure 5.5 Detuning v. time for comparing the two controllers' response in response to a step/impulse disturbance. 124

Figure 5.6 Histograms for detuning counts with a PI controlled tuner (left) and an ADRC controlled tuner (right). Relevant metrics for each tuner are given in their respective titles. 125

Figure 5.7 RMS detuning over 80s v. added tone frequency. The green dashed line is the RMS detuning with no frequency control. 126

Figure 5.8 Simulated detuning v. time for tuner a tuner with and without using the LMS algorithm. 127

Figure 5.9 Histograms of detuning captured over 80 s for simulations with left) just ADRC and right) ADRC with the LMS algorithm. Included in both is the histogram of detuning with no control (i.e. raw noise). 127

Figure 5.10 Fast Fourier transform of the simulated noise spectrum with and without the LMS algorithm. ADRC is enabled in both cases. 128

Figure 5.11 Photograph of the room temperature testing bench at Fermilab (left) and the relevant circuit diagram of the bench (right). Not pictured in the photograph is the ADC and control computer. 130

Figure 5.12 Phase and piezo voltage v. time when no control is applied. Again, the cavity is tuned to the generator when V_ϕ=0.9 V. 131

Figure 5.13 Phase and piezo voltages v. time for a capture with ADRC with ω_c = 400 rad/s, ω_{ob} = 3000 rad/s, and $\hat{b} = 4.74 \times 10^6$ V/(rad/s)^2. The RMS phase voltage was $V_{\phi,RMS} = 0.900346$ V, which corresponds to $\Delta f_{RMS} = 33$ Hz for the room temperature cavity (0.06% of the cavity bandwidth). 132

Figure 5.14 Phase and piezo voltages v. time for a windowed look at the data in Fig. 5.13. . 132

Figure 5.15 RMS detuning v. respective proportional gain factors for the tuner under ADRC and PI control. Observer bandwidth and integral gain are held constant at ω_{ob} = 3000 rad/s and k_I = 2000 respectively. 133

Figure 5.16 Phase voltage v. time for different cases of proportional gain factors for the PI controlled tuner. 134

Figure 5.17 Phase voltage v. time for different cases of controller bandwidths ω_c for the ADRC controlled tuner. In the case of wc = 200 rad/s, the phase detector was turned off before the DAQ, leading to the jump. 135

Figure 5.18 Phase voltage v. time for both ADRC and PI controllers during a disturbance event (top), piezo voltage v. time for the ADRC controlled tuner (middle), and piezo voltage v. time for the PI controlled tuner (bottom). 136

Figure 5.19 Histograms of the phase voltage V_ϕ for 10 minute captures with no control, ADRC, and PI control. Both controlled datasets are the best RMS detuning cases from Fig. 5.15, with ω_c = 400 rad/s and k_P = 0.75. 137

Figure 5.20 Simulink recreation of the test bench setup. In the DESO, we use the same update equations that are present in the LabVIEW implementation. These equations are Eq. (3.34) and Eq. (3.35). 137

Figure 5.21 Simulated phase voltage v. time for the test-bench simulation with no additional noise and ω_c = 400 rad/s and ω_{ob} = 3000 rad/s. Notice the strong impulse and overshoot at the start of the simulation. 138

Figure 5.22 Instability thresholds in terms of detuning angle v. respective proportional gain factors for ADRC and PI controlled tuners. 140

Figure 5.23 Simulated detuning v. time for the Simulink model after and before the instability threshold. 141

Figure 5.24 Fourier transform amplitude of the detuning v. frequency for after and before the instability threshold. 142

LIST OF ABBREVIATIONS

MSU	Michigan State University
FRIB	Facility for Rare Isotope Beams
PIP-II	Proton Improvement Plan II
SNS	Spallation Neutron Source
CEBAF	Continuous Electron Beam Accelerator Facility
SLAC	Stanford Linear Accelerator Center
LCLS-II	Linear Coherent Light Source II
LHC	Large Hadron Collider
FCC	Future Circular Collider
ILC	International Linear Collider
SRF	Superconducting Radiofrequency
CW	Continuous Wave
QWR	Quarter-wave Resonator
HWR	Half-wave Resonator
LB650	Low-beta, 650 MHz
HB650	High-beta, 650 MHz
SSR1	Single Spoke Resonator Type 1
SSR2	Single Spoke Resonator Type 2
LLRF	Low-level Radiofrequency
PI	Proportional-integral
ADRC	Active Disturbance Rejection Control
ESO	Extended State Observer

CHAPTER 1

INTRODUCTION

1.1 Forward

For the last 100 years, advancements in nuclear and high energy physics have been driven largely by particle accelerators creating conditions not available on Earth. For nuclear physics, this includes recreating stellar environments or producing isotopes not found on Earth. These studies can be extremely diverse, requiring different species of heavy-ions with energies in the keV/nucleon-MeV/nucleon range. High energy physics of course, seeks the highest energy possible in order to recreate early universal conditions. The pursuit of these conditions requires the use of accelerators, which through a century of innovation have created a large and diverse field that is accelerator physics and engineering [1, 2, 3].

This field is a mask that covers many faces: materials science, electrical and mechanical engineering, physics, computation, and many more. It is this multi-disciplinary leaning that allows for the creation of these complex machines at large scale. Arguably, the most well known accelerator is the Large Hadron Collider (LHC), a synchrotron ring with a radius of 27 km: a machine with a size that spans across the border of two countries. This accelerator has created the highest man-made collisions of subatomic particles and probes the Standard Model with 13.7 TeV proton collisions.

As the field of accelerator science has progressed and innovated, the scope of these machines has increased. Light sources utilize high-energy electrons to produce keV, high-repetition x-rays for material, biological, and atomic dynamics studies [4]. Small-scale accelerators are also being investigated for medical treatments and infrastructure enhancements such as water purification [5, 6]. Additionally, large-scale accelerators are finding their niche in industry startups for semiconductor testing and power generation.

This thesis pertains to the stability of superconducting radiofrequency (SRF) cavities, a small part of the SRF field. The SRF field is itself an offshoot of RF acceleration. This is true for all sub-fields of science, but for this work to have meaning, we must present the context in which this

work exists. In this chapter, we present a brief history of particle accelerators and the emergence of RF acceleration. In particular, we discuss RF cavities, relevant figures of merit, and the use of superconducting materials in these cavities. These contents will allow us to lay out the path for the rest of this work.

1.2 The Age of RF Acceleration

In the classical regime, the motion of charged particles can only be altered via interactions with electric and/or magnetic fields. The force $\mathbf{F}$ exerted on a charged particle is well described by the Lorentz force law [7]:

$$\mathbf{F} = q(\mathbf{E} + \mathbf{v} \times \mu_0 \mathbf{H}), \tag{1.1}$$

where q is the particle's charge, $\mathbf{v}$ is the particle's velocity, μ_0 is vacuum permittivity, and $\mathbf{E}$ and $\mathbf{H}$ are the electric and magnetic fields, respectively. It is clear from this expression that the contribution of force from the magnetic field will always be perpendicular to the particle's motion, and thus this force contribution will not affect the kinetic energy of the particle. Conversely, the contribution of $\mathbf{F}$ from the electric field will affect the magnitude of $\mathbf{v}$ regardless of whether $\mathbf{E} \cdot \mathbf{v} = 0$ upon entering the field (that is, the electric field and velocity are perpendicular). This means that we can use a well-oriented electric field (and thus a strong potential drop along the axis of motion) to change the energy of charged particles in a way we desire.

A practical method to increase the particle's energy then is to pass particles through a static electric field generated by parallel plates with different electric potentials. In fact, this method works for smaller scale accelerators such as cathode ray tubes and up to larger machines such as the Cockcroft-Walton or Van de Graff machines [8]. Vacuum cathode ray tubes (small-scale DC scale accelerators) helped prove the existence of electrons and became an important tool in video technology in the later part of the 20th century. Cockcroft and Walton achieved the first man-made nuclear reaction with their DC accelerator by bombarding lithium with 400 keV protons to create helium. However, there are two limitations that arise from a DC machine: breakdown and size. In the presence of high DC fields, electrons can tunnel out of deformities or sharp features in the high potential regions, leading to electrical breakdown. This practically limits the voltage that can be

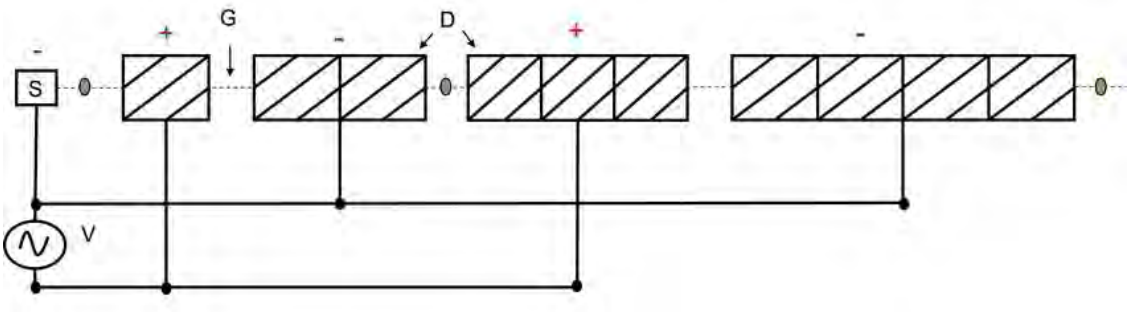


Figure 1.1 Acceleration scheme designed by Ising and used by Widerøe. The 's' block represents the particle source, the green dots are the particles, the accelerating gaps are denoted with 'G', and the drift tubes are the boxes with diagonal markings. Figure originally published in [13].

produced for a DC accelerator to a few MVs depending on the effective vacuum, accelerating gap length, and surface finish within the accelerator [9].

One solution is to then chain DC structures together. However, these structures are incredibly large: the Tandem accelerating system at Brookhaven National Lab contains two Van de Graff accelerating modules [10]. Each module is approximately 25 m long for a 15 MV potential across each structure. This corresponds to an effective gradient of 0.6 MV/m, which is inefficient from a space perspective. To reach the proton energies of the LHC, one would need to chain almost 1 million modules, resulting in a machine length of 2500 kM.

1.2.1 RF Accelerators

In 1924, Gustaf Ising proposed a method of acceleration using radiofrequency (RF) potentials to create alternating accelerating gaps between copper shielding tubes [11]. These so-called "drift tubes" would allow the particle to be shielded from the decelerating fields after one quarter RF period. A diagram of this scheme can be seen in Fig. 1.1. The drift tubes and the linear design of this accelerator would dub this style of machine as the drift tube linear accelerator (linac). The first experimental application of this design came from Rolf Widerøe in 1928 [12]. Using a 1 MHz RF source and one drift tube, he was able to accelerate potassium ions to 50 keV.

Following the advancements in high power RF technology after World War II, the idea of a high energy linac became much more attainable. Luis Alvarez would modularize and expand on Widerøe's machine, adding more drift tubes and enclosing them in a copper cavity where a standing

RF wave could form. This design incorporated a much higher operational frequency of 200 MHz for the fundamental transverse magnetic (TM) TM_{010} mode. The original Alvarez design was only able to accelerate protons to 32 MeV or about 26% percent of the speed of light at a length of 40 ft. This corresponds to an effective gradient of 2.6 MV/m, an over 400% increase in gradient from the DC tandem accelerators. While this modularization showed a great increase in gradient, there would still be room for improvement. For instance, protons need 5.7 GeV of kinetic energy to move at 99% percent of the speed of light and heavier ions even more.

This advancement came in the form of disc-loaded, traveling-wave structures. Charged particles could be injected into the crest of the traveling electric field and continuously accelerated. A transmission line is loaded with discs separated by a length determined by the RF wavelength and particle velocity. Additionally, the discs served to slow the group velocity down to below the speed of light c so the particle could maintain synchronicity with the traveling wave. It is through a combination of drift tube linacs and traveling wave systems that the Stanford Linear Accelerator Center (SLAC) was able to achieve energies up to 50 GeV [14].

The RF cavity is the most common accelerating structure for modern particle accelerators. The RF cavity is a metal structure designed to store electromagnetic field energy at a resonating frequency. An RF power source/amplifier can power and sustain the the electromagnetic field within the cavity with a fraction of the stored energy due to the high ratio of stored energy over cavity wall loss. Electric field gaps in the RF cavity can be used to accelerate charged particles.

1.3 RF Cavities

The simplest of these cavity geometries is the pillbox cavity. Ignoring any RF feed or through ports, the geometry is a cylindrical shape with radius R and length l as seen in Fig. 1.2. For any cavity, the length is determined by the chosen drive frequency f_0 (or wavelength λ) and the design velocity (dubbed the geometric beta) $\beta_g = \frac{v}{c}$, as can be seen in Eq. (1.2) [15]. The radius R is also chosen for a design frequency, as we will see shortly.

$$l = \frac{\beta_g c}{2 f_0} = \frac{\beta_g \lambda}{2}. \tag{1.2}$$

In any space, electromagnetic fields must satisfy Maxwell's equations thus the wave equations.

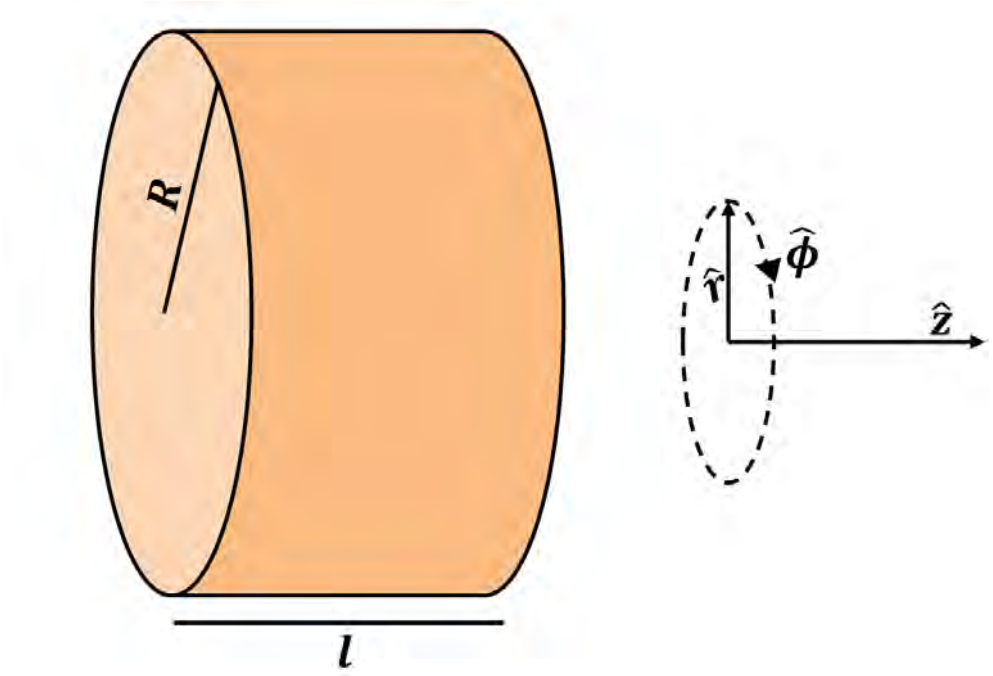


Figure 1.2 Simplified geometry for a pillbox cavity. Beam is passed along the central axis of the cavity ($\hat{\mathbf{z}}$).

In vacuum, the wave equations take the form of [7]:

$$\left(\nabla^2 + \frac{\omega^2}{c^2}\right)\mathbf{E} = 0, \tag{1.3}$$

$$\left(\nabla^2 + \frac{\omega^2}{c^2}\right)\mathbf{H} = 0, \tag{1.4}$$

where ω is the driving temporal frequency. Since there is no central or secondary conducting surface besides the cavity walls for the pillbox geometry, only the electric or magnetic field may have a z-component; the other field must have transverse components only. In our case, we are interested in increasing the energy of charged particles, meaning we must have E_z or a transverse-magentic (TM) wave.

Based on the symmetry of the geometry, we will work with cylindrical coordinates. Let us take that E_z is separable, that is E_z can be represented as a product of individual functions of the coordinate variables:

$$E_z(r, \phi, z) = F(r, \phi)Z(z), \tag{1.5}$$

for which substitution into the wave equation yields the following condition,

$$-k_{r\phi}^2 - k_z^2 + \frac{\omega^2}{c^2} = 0, \tag{1.6}$$

where $k_{r\phi}$ and k_z are constants that must sum with ω^2/c^2 to zero as we are mixing functions of different variables. Given that each term in Eq. (1.6) must be a constant, the z-component takes on a periodic form:

$$\frac{d^2Z}{dz^2} = -k_z^2 \Rightarrow Z(z) = A\sin(k_z z) + B\cos(k_z z). \tag{1.7}$$

Applying Dirichlet boundary conditions for $z = 0$, we find that $B = 0$ for the field to vanish. Applying the condition that field must also vanish at $z = l$ results in a periodic condition and the form of k_z,

$$k_z = \frac{p\pi}{l}. \;\; p \in 0, 1, 2, ... \tag{1.8}$$

With the z-component defined, we can now assume that $F(r, \phi)$ itself is separable.

$$\nabla_t(F(r,\phi)) = \nabla_t(R(r)\Phi(\phi)) = -k_{r\phi}^2, \tag{1.9}$$

where ∇_t is the transverse gradient (no z-derivative). For the Φ component, we have a simplified process: there is no internal boundary, so the electric field must be periodic in $\hat{\phi}$, that is $E_z(\phi = 0) = E_z(\phi = 2\pi)$. It is clear then that,

$$\Phi(\phi) = e^{\pm jm\phi}, \;\; m \in 0, 1, 2, ... \tag{1.10}$$

Finally, the r-dependency follows a more complex second order equation:

$$r^2\frac{d^2R}{dr^2} + r\frac{dR}{dr} + \left(k_{r\phi}^2 r^2 - m^2\right)R = 0. \tag{1.11}$$

Those familiar with cylindrical problems will recognize this as Bessel's equation of mth order, which has solutions of Bessel's functions of the first kind $J_m(r)$. Applying the condition that the field must vanish at the boundary $r = R$, we find that the value of $k_{r\phi}$ must take the value of the nth root of the mth Bessel function dubbed k_{mn}:

$$k_{r\phi} = \frac{k_{mn}}{R}. \tag{1.12}$$

The z-component of the electric field is then finally derived:

$$E_z^{mnp}(r, \phi, z) = E_{mnp} J_m(r) e^{\pm jm\phi} \sin\left(\frac{p\pi}{l} z\right), \tag{1.13}$$

where E_{mnp} is the amplitude of the mnp mode.

Now that the components are known, we can solve for the frequency of the modes:

$$\omega_{mnp} = c\sqrt{\frac{k_{nm}^2}{R^2} + \frac{p^2\pi^2}{l^2}}. \tag{1.14}$$

The simplest case is $m = p = 0$, i.e. no variation in ϕ or z. In this casec for $J_0(r)$ we take the first root as the non-trivial solution. The frequency of this so-called fundamental mode (for non-coaxial resonators) can be found using the numerical value of the J_0's roots:

$$\omega_{010} = c\sqrt{\frac{k_{01}^2}{R^2}} \approx \frac{2.405c}{R}. \tag{1.15}$$

Using Maxwell's equations, the magnetic field H_ϕ^{mnp} can be determined using Eq. (1.13). A simulation of the TM010 electric and magnetic fields for a pillbox cavity designed for $f_0 = 1.3$ GHz and $\beta_g = 1$ can be seen in Fig. 1.3.

As we can see, analytical forms for the electric and magnetic fields exist for a relatively simple geometry. Issues start to arise when this pillbox geometry is used practically. Sharp edges and corners allow for large peak fields which can cause strong electron multipacting. This leads to degradation of the cavity stored energy as these electrons traverse the cavity's axis. In general, more complex geometries must be used; geometries with fields that can no longer be analytically solved for. Finite-element method (FEM) solvers, such as CST, COMSOL, and ANSYS must be used instead to find the fields. These tools are useful also in optimizing geometries for certain figures of merit, which we will now discuss.

1.3.1 Cavity Figures of Merit

While analytical forms exist for the pillbox cavity, the formulas we describe in this section are relevant for all cavities and can be determined with FEM solvers. As mentioned earlier, cavities are storage devices for electromagnetic energy. However in storing this energy within the cavity,

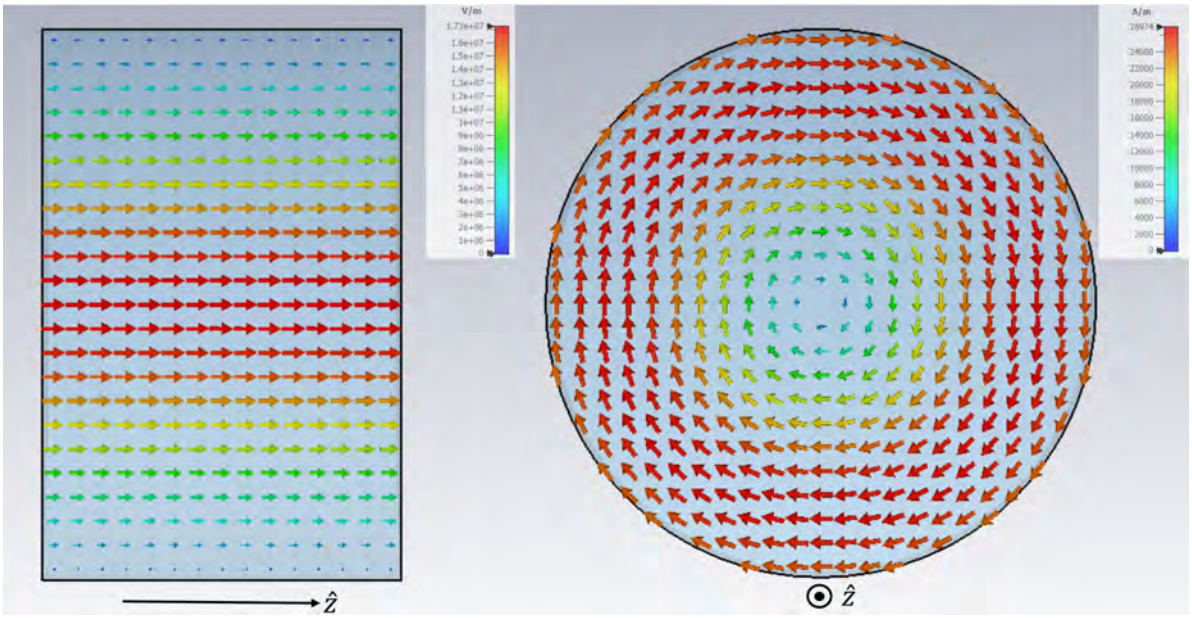


Figure 1.3 Field maps for TM010 electric (left) and magnetic (right) fields for a 1.3 GHz pillbox cavity (l = 115 mm, R = 88 mm) simulated using CST microwave studio [16]. The beam direction is denoted at the bottom of each field plot. Internal energy is normalized to 1 J.

surface currents are induced on the conducting walls which will lead to losses. A metric to gauge how well a cavity can store energy is to determine how many RF periods it would take for the energy to be dissipated. This is the purpose of one of the foremost figures of merit: the intrinsic quality factor Q_0, which can be defined in two ways.

$$Q_0 = \frac{\omega_0 U_0}{P_w} = \frac{\omega_0}{2\omega_{1/2}}, \tag{1.16}$$

where ω_0 is the resonant mode frequency, P_w is the ohmic losses in the walls, $\omega_{1/2}$ is the half-bandwidth, and U_0 is the stored energy in electric and magnetic fields. The half-bandwidth represents the frequency deviation allowable for the input power to maintain over half of the stored energy.

U_0 is dependent on the power supplied to the cavity, whereas Q_0 represents the number of RF periods that would be needed to dissipate U_0. Thus, maximizing Q_0 corresponds corresponds to a better performing resonator. For the superconducting resonator by itself, $Q_0 \sim 10^9 - 10^{10}$ (as we will see shortly). The stored energy itself is given by an integral of the field amplitude squared over

the cavity volume Ω,

$$U_0 = \frac{1}{2}\epsilon_0 \int_\Omega \mathbf{E} \cdot \mathbf{E}^* \, dV = \frac{1}{2}\mu_0 \int_\Omega \mathbf{H} \cdot \mathbf{H}^* \, dV. \tag{1.17}$$

The wall losses P_w can also be expressed as an integral of $\mathbf{H}$ over the cavity walls $\partial\Omega$,

$$P_w = \frac{1}{2}R_s \int_{\partial\Omega} \mathbf{H} \cdot \mathbf{H}^* \, dA, \tag{1.18}$$

where R_s is the average surface resistance of the cavity. This means that we can express Q_0 as a ratio of two integrals. Using Eq. (1.17) and Eq. (1.18)), we can derive a general expression for Q_0:

$$Q_0 = \frac{\int_\Omega \mathbf{H} \cdot \mathbf{H}^* \, dV}{R_s \int_{\partial\Omega} \mathbf{H} \cdot \mathbf{H}^* \, dA} = \frac{G}{R_s}, \tag{1.19}$$

where we define G as the geometry factor of the cavity. This ratio of integrals is solely dependent on the geometry of the cavity, and can be calculated with FEM solvers during the cavity design phase. During the design phase, the geometry can be optimized to maximize G (and thus the simulated Q_0). While G is dependent on the cavity geometry, R_s is dependent on the conductor material and surface conditions within the RF space. For SRF cavities, the average surface resistance is an important factor we will discuss in the comparison between SRF and normal conducting cavities.

Critical in determining the energy gain through a cavity is determining the voltage experienced by the charged particles. The static voltage through the cavity can be found via an integral; assuming that the beam travels along the central axis this voltage is,

$$V_0 = \int_{\frac{-l}{2}}^{\frac{l}{2}} E_z(r = 0, \phi, z) \, dz. \tag{1.20}$$

However, the voltage experienced by the particle is reduced as the cavity field is changing in time as the particle traverses the cavity. This accelerating voltage V_{acc} depends on the traversal time of the particle bunch (and thus the particle speed). Taking V_0 from Eq. (1.20), we can express this traversal time using the particle speed β:

$$V_{acc} = V_0 \int_{\frac{-l}{2}}^{\frac{l}{2}} \Re[e^{j(\omega_0 t + \psi_s)}] \, dz = V_0 \int_{\frac{-l}{2}}^{\frac{l}{2}} \Re\left[e^{j\left(\frac{2\pi z}{\beta\lambda} + \psi_s\right)}\right] \, dz, \tag{1.21}$$

where l is the effective length (Eq. (1.2)), ψ_s is the synchronous phase with respect to the wave crest, and β is the actual particle velocity.

Carrying out this integral and ignoring the resulting $\cos\psi$ for now, one finds the accelerating voltage V_{acc} for the pillbox cavity as,

$$V_{acc} = V_0 \frac{\sin\left(\frac{\pi l}{\beta\lambda}\right)}{\frac{\pi l}{\beta\lambda}} = V_0 \frac{\sin\left(\frac{\pi\beta_g}{2\beta}\right)}{\frac{\pi\beta_g}{2\beta}} = V_0 T(\beta), \tag{1.22}$$

where $T(\beta)$ is referred to as the transit time factor. The energy gain ΔE of a particle with charge q is therefore:

$$\Delta E = q V_{acc} \cos\psi. \tag{1.23}$$

The accelerating voltage is sometimes expressed as the accelerating gradient/electric field E_{acc}, which relates to the accelerating voltage as:

$$V_{acc} = E_{acc} l. \tag{1.24}$$

In general, the transit time factor relates to the cavity geometry and the RF frequency:

$$T(\beta) = \frac{\int_{-l/2}^{l/2} E_z(r=0,z)\cos\omega_0 t(\beta)\, dz}{\int_{-l/2}^{l/2} E_z(r=0,z)\, dz}, \tag{1.25}$$

where $t(\beta)$ is the traversal time as a function of velocity,

$$t(\beta) = \frac{2\pi c z}{v\lambda} = \frac{2\pi z}{\beta\lambda}. \tag{1.26}$$

The β that maximizes the transit time factor is referred to as the optimal beta β_{opt}. It is worth noting that it is not always true that $\beta_{opt} = \beta_g$ and it is important to differentiate between the two velocities. More complex forms of the transit time factor involving off-axis acceleration ($r \neq 0$) can be derived as well.

While Q_0 represents the energy storage capacity with respect to the losses, we can develop another figure of merit that relates the accelerating capacity of a cavity to its losses instead. In particular, we can develop an equivalent resistance across which power is dissipated, which is referred to as the shunt impedance. The shunt impedance R_{sh} can be found via [15]:

$$R_{sh} = \frac{V_{acc}^2}{2P_w}. \tag{1.27}$$

It is clear that the shunt impedance will vary with the accelerating field. In terms of cavity design, we can normalize R_{sh} by Q_0 which results in a geometry-dependent quantity. This R/Q value is again a value that is maximized during the cavity design phase. R/Q is important in determining total losses in different configurations, and we will make use of it in this chapter and the next.

It is important to note that this form varies by a convention factor of $1/2$. Thomas Wangler's book lists this relationship without it, and many electrical engineering works will include it. Either form can be used, but for consistency the same form must be used in all cases for a given work. This thesis uses the form we defined in Eq. (1.27).

1.3.2 The Normal Conducting Cavity

In the normal conducting cavity, the main limiting factor is wall losses. For normal conducting metals exposed to RF magnetic fields at their surface, the average surface resistance is given by [17]:

$$R_s = \sqrt{\frac{\omega_0 \mu_r \mu_0}{\sigma}}, \tag{1.28}$$

where μ_r is the material's relative permittivity and σ is the material conductivity. Since R_s has an inverse relationship with the conductivity, room temperature cavities are made with high-quality copper (with high conductivity $\sigma_{Cu} = 5.8 \times 10^7$ S/m). Copper also has good thermal conductivity at 300 K, allowing for good thermal management of the cavity.

1.3.3 The Superconducting Cavity

Superconductivity has had a long storied history since its first observation by Onnes in 1911 [18]. There are two main macroscopic properties of superconductivity that theoretical treatments have continuously sought to explain:

- For a given pressure, a superconducting material cooled below a critical temperature T_c will see zero DC electrical resistance.

- A superconducting material experiences diamagnetic behavior with a full expulsion of magnetic fields from the material until the reversion to the normal conducting state. This is historically referred to as the Meissner effect [19].

Notable theories of superconductivity were proposed by Fritz and Heinz London, where they showed generated surface supercurrents were responsible for the Meissner effect, allowing for the cancellation of magnetic fields within the bulk of the material [20]. However, there is still some penetration of external magnetic fields into the superconductor's surface, with the penetration depth given by:

$$\lambda = \sqrt{\frac{m_e}{\mu_0 e^2 n_s}}, \tag{1.29}$$

where m_e is the mass of the electron and n_s is the number density of supercurrent electrons. In the presence of strong H_{ext}, the supercurrents break down and the material reverts back to the normal conducting state.

The first quantum mechanical treatment of superconductivity would come in 1950 by Ginzburg and Landau [21, 22]. This phenomenological treatment was the first to explain superconductivity as superfluid electrons. In relation to this are two important variables. The first is the coherence length ξ which describes the range superfluid electrons can spread out within the wavefunction distribution ψ_0:

$$\xi = \sqrt{\frac{\hbar^2}{4m^*|\alpha(T)|}}, \tag{1.30}$$

where $\hbar$ is the reduced Planck's constant, m^* is the superfluid electron mass, and $\alpha(T)$ is a phenomenological function of temperature.

The second is a refined London penetration depth (Eq. (1.29)), which is now based on the wavefunction distribution of superfluid electrons ψ_0:

$$\lambda = \sqrt{\frac{m^*}{\mu_0 e^{*2} \psi_0^2}}. \tag{1.31}$$

This theory also establishes the two types of superconductors. Type-I superconductors behave as perfect diamagnetic materials with full expulsion of magnetic fields up until a critical external magnetic field H_c. Type-II superconductors have two critical fields H_{c1} and H_{c2}. For $H_{ext} < H_{c1}$, there is no penetration of H_{ext} into the material. For $H_{c1} < H_{ext} < H_{c2}$, there is partial penetration of flux into the superconductor up to H_{c2} where the material reverts to the normal conducting state [23].

Our modern understanding now stems from Bardeen-Cooper-Schrieffer (BCS) theory, a microscopic, quantum theory [24]. The superfluid currents in this case are not singular electrons: two electrons interacting with the crystal lattice when $T < T_c$ can experience attractive potentials between each other and form bosonic quasi-particles known as Cooper pairs. An energy gap of $E_{gap} = 2\Delta$ forms in the band structure of the material, and electrons occupying the states below this gap are capable of forming Cooper pairs. These pairs can then flow without scattering for applied DC electric fields. The coherence length ξ in this case is now the length scale at which the Cooper pairing can exist.

One of the most relevant results from BCS theory (in regard to the SRF community) is the description of surface resistance that arises in the presence of AC fields. This resistance is the result of electron inertia, with scattering occurring as the electrons switch directions with the changes in the field. This so-called BCS resistance is given by [25, 26, 27]:

$$R_{BCS}(T, f) = A \left(\frac{1}{1.5\ GHz} \right)^2 \frac{T_c}{T} \exp\left(-\frac{BT_c}{T} \right), \tag{1.32}$$

where A and B are coefficients predicted by BCS theory that are dependent on the London penetration depth λ and the superconducting energy gap Δ.

It was experimentally determined that R_{BCS} is not the only component to the surface resistance. There is a temperature-independent component relating to trapped flux and losses in normal conducting residual material on the RF surface. The total surface resistance of the SRF cavity is the sum of the BCS and residual R_{res} terms:

$$R_s(T, f) = R_{BCS}(T, f) + R_{res}. \tag{1.33}$$

Both R_{BCS} and R_{res} are sensitive to surface and heat treatments, and many studies have been undertaken by the SRF community to understand and minimize these resistances and thus maximize Q_0.

Let us now compare two cases: two normal and superconducting pillbox cavities operating at 1.3 GHz and run them at an accelerating gradient of 20 MV/m without beam. A table of relevant parameters for each case (assuming $R_{res} = 5$ nΩ for the SRF cavity) can be seen in Table 1.1. The

Table 1.1 Comparison of relevant parameters for normal and superconducting 1.3 GHz RF pillbox cavities. In this case, we are assuming R_{res} = 5 nΩ and the cryogenic power is calculated assuming 30% exergetic efficiency.

Parameter [Units]	NC-RF Value	SRF Value
G [Ω]	255	255
R/Q [Ω]	196.5	196.5
R_s [Ω]	9.3×10^{-3}	16.2×10^{-9}
Q_0 [NA]	2.7×10^4	1.6×10^{10}
P_w [W]	1×10^6	1.69
P_{cryo} [W]	NA	838

cryogenic power calculation takes a coefficient of performance cooling from 300 K to 2 K with a 30% exergetic efficiency.

It can be seen that for the same accelerating gradient, the normal conducting case deposits 1 MW of power into the walls. A continuous field is not sustainable from a required energy, thermal, and structural standpoint: the cavity will deform due to ohmic heating among other problems. For this reason, RF power must be cycled on and off during the time the beam is traversing the cavity (so-called pulsed operation).

This is the advantage SRF cavities can have: continuous-wave or constant operation at high gradients. This remains true even when we add beam-loading so long as the current remains low enough, though there are additional considerations that must be made for the calculation which we will discuss in the next chapter. Additionally, lower power requirements for pulsed operation and enabling longer duty cycles are also possible with SRF cavities. Of course this comes at the cost of cryogenic cooling, which depends heavily on Q_0. Thus the decision between the use of NC-RF and SRF cavities heavily depends on the project requirements. For this work, we will focus solely on the superconducting regime and superconducting machines.

1.3.3.1 SRF Cavity Geometries

Linear accelerators present an interesting challenge in that particles must be accelerated over a range of velocities in the same machine. One geometry of cavity is not a "one size fits all", so to say. The transit time factor $T(\beta)$ is heavily dependent on the frequency and geometry of the cavity. As such, low frequency cavities (10s of MHz) tend to have higher T for low-velocity acceleration and

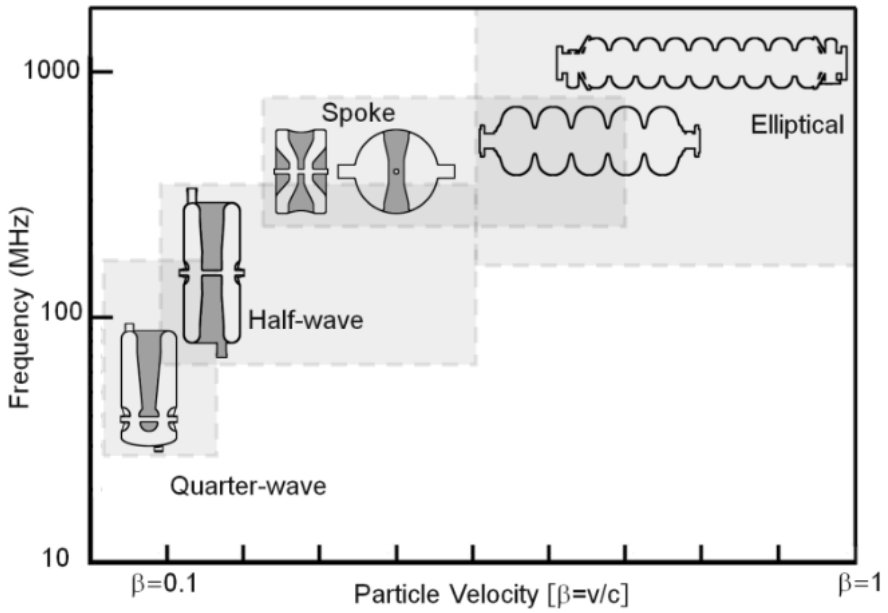


Figure 1.4 Graph of usual frequency values v. velocity ranges for common SRF cavity geometries. On the low velocity end are coaxial resonators and elliptical for higher velocity particles. Figure was originally published in [29].

vice-versa for high-frequency cavities. A graph of frequency versus particle velocity and regions of common SRF cavity geometries can be seen in Fig. 1.4.

For low-velocity acceleration, coaxial quarter-wave resonators (QWRs) and half-wave resonators (HWRs) provide a preferred option. HWRs optimized for medium velocity particles have been deployed to heavy ion linear accelerators as well. Spoke resonators are similar in geometry to HWRs and cover a similar range of velocities and frequencies. Finally, elliptical cavities are used in both medium and relativistic acceleration with the $\beta = 1$ standard being the TESLA, 1.3 GHz, nine-cell elliptical cavity [28]. Elliptical cavities are pillbox cavities that have been smoothed over to reduce electron multipacting and peak fields.

1.3.3.2 Modes of Operation

There are two common modes of operation for SRF cavities, with differences stemming from the way power is supplied to the cavity. Continuous wave operation is the simplest mode of operation: as the name suggests, power is continuously supplied to the cavity to maintain a constant cavity field. Beam can be supplied continuously or pulsed with lower repetition rates, but the cavity is

always on. With low beam current and high beam repetition rate, this mode of operation is attractive due to its simplicity. However, if the beam current is high and/or the repetition rate is low then this mode of operation can be costly in terms of power.

The second mode of operation is dubbed pulsed mode, and is common in normal conducting resonators. Power is supplied to the cavity for a brief period of time during which the beam is traversing through the cavity. The power is then turned off and the field is allowed to decay. This pulsing is then repeated at a lower rep-rate (usually at the beam repetition rate), allowing for the minimization of RF power consumption. The duty cycle of the pulse refers to the period in which RF power is supplied. For normal conducting resonators, this mode is necessary with low duty cycles due to the large power requirements and dissipation of power into the cavity walls. For SRF cavities, this mode allows for power savings for cases of large beam loading. An example of an RF pulse for the PIP-II $\beta = 0.92$, 650 MHz (HB650) cavity can be seen in Fig. 1.5.

1.4 Superconducting Linacs in the United States

This work will focus solely on current and planned linacs; in this section we will discuss existing and planned linacs using SRF technology in the United States. We will divide this section into three pieces in order to cover more accelerator use cases. This includes the discussion of heavy ion, proton, and electron use cases.

1.4.1 Heavy Ion Linacs

Heavy ion accelerators are key for low-to-medium energy nuclear physics studies. Because the accelerated species are more complex and have higher charge states than singular protons and electrons, energies are reported in electron-volts per nucleon (eV/u). Heavy-ion linacs are able to accelerate different species of ions to the relevant ranges for the desired study, which for many cases ranges from keV/u to MeV/u.

Many lower energy nuclear physics studies can be conducted with cyclotrons or even tandem Van de Graffe DC accelerators. However, SRF technology presents a useful benefit for this case. Lower beam currents mean that continuous-wave operation can be used to provide high beam energy and higher beam power on target. Because heavy ions are harder to accelerate than protons

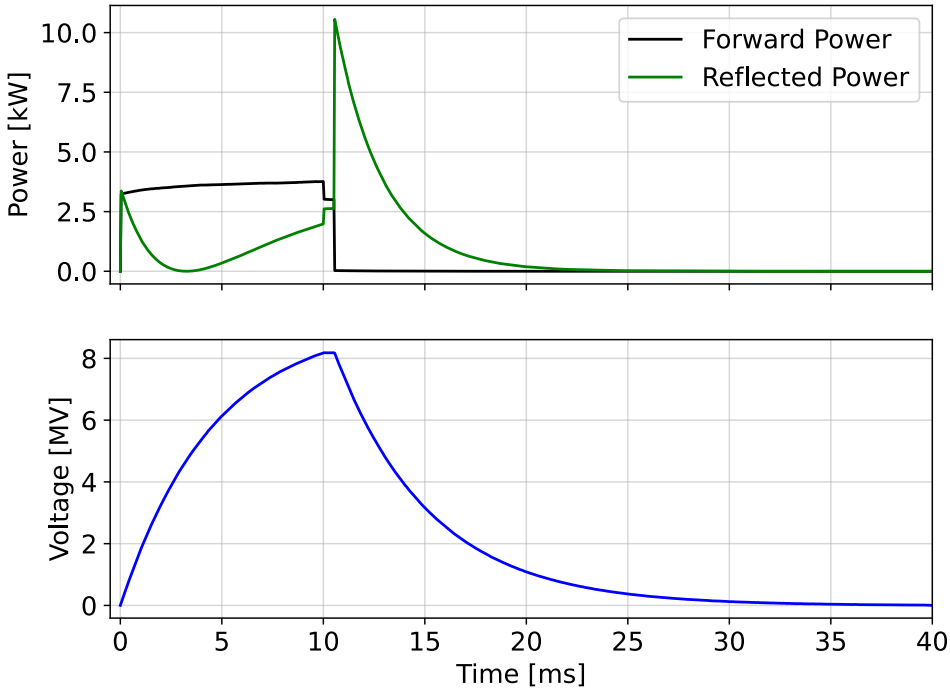


Figure 1.5 Cavity forward and reflected power (top) and cavity voltage (bottom) v. time for a single RF pulse of a 650 MHz HB650 cavity. The RF pulses with a 10 Hz repetition rate, a 10 ms fill time, and a 0.55 ms flat-top time.

and electrons, many SRF heavy ion accelerators will require cavities whose geometries cater for low to medium velocities/βs such as quarter-wave, half-wave, and spoke-style resonators[30, 31, 32, 33].

One such relevant machine is the Facility for Rare Isotope Beams at Michigan State University which began user operations in 2022 [34, 35, 36, 37]. A superconducting, 28 GHz electron-cyclotron resonance (ECR) ion source produces low-charge state ions that are passed down 3 stories to the front end and low-energy beam transport line [38]. A room temperature radiofrequency quadrupole (RFQ) is used for the initial acceleration and focusing of the beam before the superconducting sections. The driver linac has three linac segments connected by two folding segments. A diagram of the driver linac can be seen in Fig. 1.6.

The superconducting driving linac contains 324 coaxial resonators across 46 cryomodules and is capable of accelerating uranium ions to 200 MeV/u with a designed 400 kW beam power on

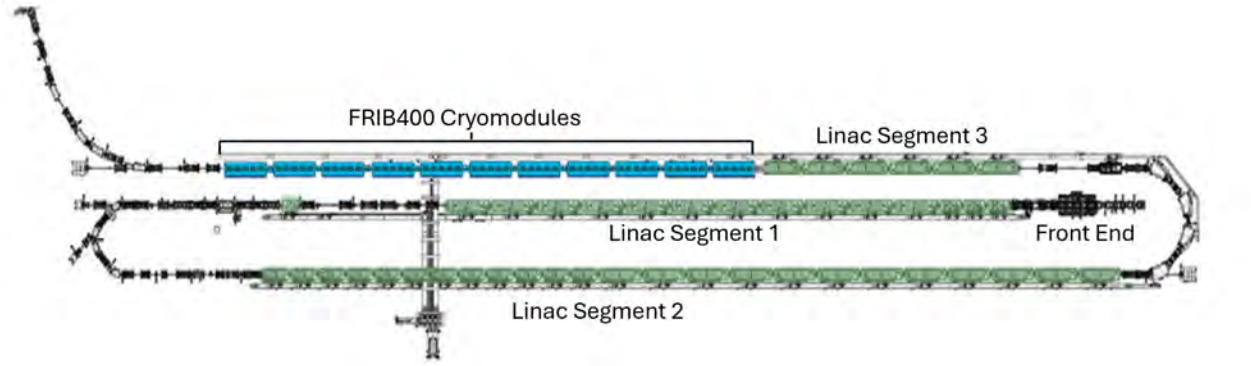


Figure 1.6 Layout of FRIB driving linac with proposed energy upgrade cryomodules. Existing coaxial cryomodules are in green with the planned FRIB energy upgrade cryodmodule placements are in blue. Figure originally published in [41].

Table 1.2 Current FRIB cavities above the double lines and the planned FRIB energy upgrade elliptical cavity below the double line specifications: geometric beta, resonant frequencies, max accelerating field, and the number of cavities within the linac.

Cavity Type	β_g	f_{res} [MHz]	Max E_{acc} [MV/m]	Num. in Linac
QWR	0.041	80.5	5.4	12
QWR	0.085	80.5	5.6	92
HWR	0.29	322	7.7	72
HWR	0.53	322	7.4	148
Elliptical	0.61	644	17.5	55

target. We present each cavity variety, their number, max E_{acc}, and geometric beta in Table 1.2. Included are the existing coaxial resonators and the planned five-cell elliptical cavity that will be used to double the linac energy [39, 40]. The location of these cryomodules with respect to the existing linac can also be seen in Fig. 1.6.

1.4.2 Proton Linacs

While still not the easiest species to accelerate, protons present some simplicity in their acceleration when compared to heavy ion species. A proton SRF linac that starts from a source must include a range of structures as the protons are accelerated from low to high velocity. The Spallation Neutron Source (SNS) which uses a 2.8 MW proton beam to produce neutrons for its users. Acceleration from the ion source to 186 MeV is handled by room temperature, copper structures. Superconducting six-cell elliptical cavities designed for $\beta_g = 0.61$ and $\beta_g = 0.81$ provide

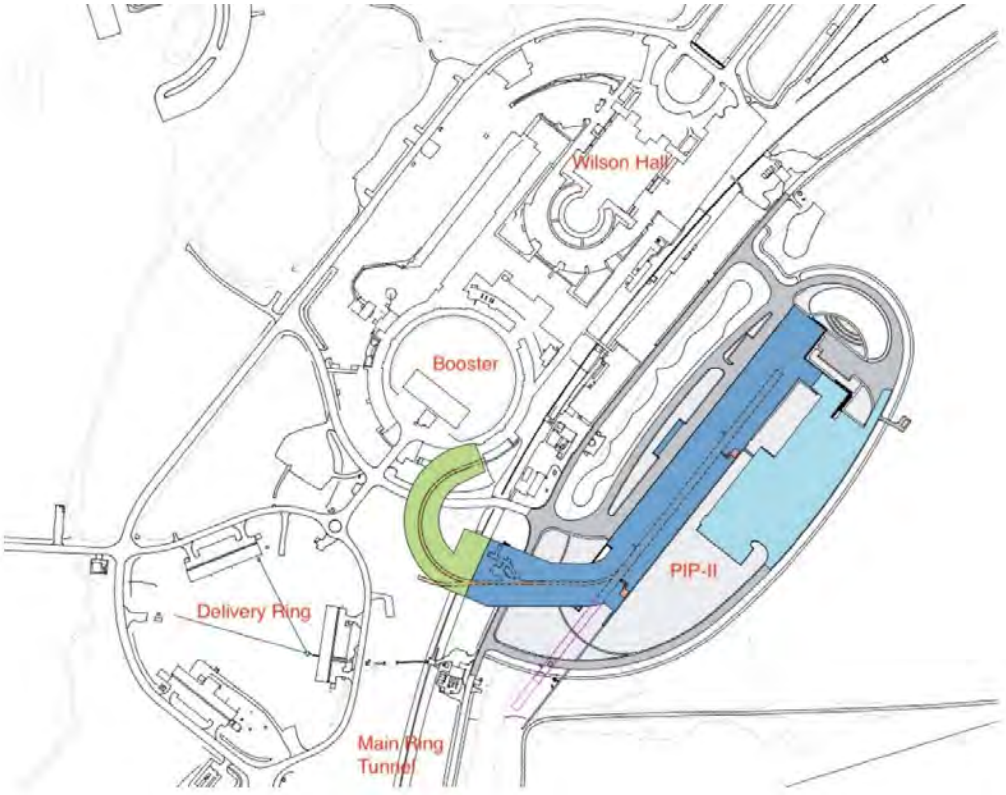


Figure 1.7 Layout of the PIP-II linac with respect to the existing accelerator facilities. Figure originally published in [44].

acceleration up to 1.3 GeV [42, 43].

The Proton Improvement Plan (PIP-II) at Fermi National Accelerator Lab is an example of a next generation linac to feature SRF cavities as the main means of acceleration. This machine will be the driving linac for the Long Baseline Neutrino Factory/Deep Underground Neutrino Experiment (LBNF-DUNE) by delivering 2 mA of 800 MeV protons to the booster ring. A diagram of the PIP-II position in regard to the existing Fermilab accelerator infrastructure can be seen in Fig. 1.7.

The driving linac has a warm front end starting with two H^- sources, low-energy beam transport lines, and a room temperature RFQ. The rest of the linac consists of SRF cavities to accelerate the beam from $\beta = 0.11$ to $\beta = 0.92$. The acceleration scheme contains one variety of HWR, two types of single spoke resonators (SSR1 and SSR2), and two varieties of five-cell elliptical cavities (LB650 and HB650). We present the same parameters as in Table 1.2 for the PIP-II resonators in Table 1.3. The careful reader might recognize that the LB650 elliptical is almost identical to the

Table 1.3 Table of cavities to be deployed to the PIP-II SRF linac. Features the same relevant parameters as those found in Table 1.2.

Cavity Type	β_g	f_{res} [MHz]	Max E_{acc} [MV/m]	Num. in Linac
HWR	0.11	162.5	9.7	8
SSR1	0.22	325	10	16
SSR2	0.47	325	11.4	35
LB650	0.61	650	16.8	36
HB650	0.92	650	18.8	24

FRIB energy upgrade cavity. As such, there is an avenue of synergy between the two machines.

1.4.3 Electron Linacs

In terms of acceleration, electrons are the easiest to accelerate to relativistic speeds and high energies. Due to their light mass, only one or two cavities are needed out of the source to reach speeds near the speed of light. This is attractive from a medium-energy nuclear physics perspective. Such is the case for the Continuous Electron Beam Accelerator Facility (CEBAF) at Thomas Jefferson National Lab. CEBAF was one of the first large scale SRF accelerators in the world, and still operates today. The electrons are recirculated through the twin linacs using two folding segments. Acceleration is carried out with 5 and 7-cell elliptical cavities operating at 1.5 GHz [45].

The reduced mass of the electron makes it easier to accelerate to higher energies, but this comes with a caveat. When traversing a curved path, energized electrons bleed off extra energy in the form of synchrotron radiation, which is described by the Larmor formula:

$$P_\gamma = \frac{q^2 c}{6\pi\epsilon_0}\frac{\beta^4\gamma^4}{\rho^2}, \tag{1.34}$$

where ρ is the bending radius, q is the charge, and γ is the Lorentz factor determined by particle speed β. This means that electrons as a species for high energy physics studies is limited to linac use or synchrotrons with large radii. This is the case for future planned SRF machines like the International Linear Collider (ILC) [46] or Future Circular Collider (FCC-ee) [47]. However, the synchrotron radiation effect can be useful for other purposes.

Accelerating electrons to high γ and using small bending radii can produce high energy x-rays. These synchrotron light sources have been in use for biological, material, and condensed matter

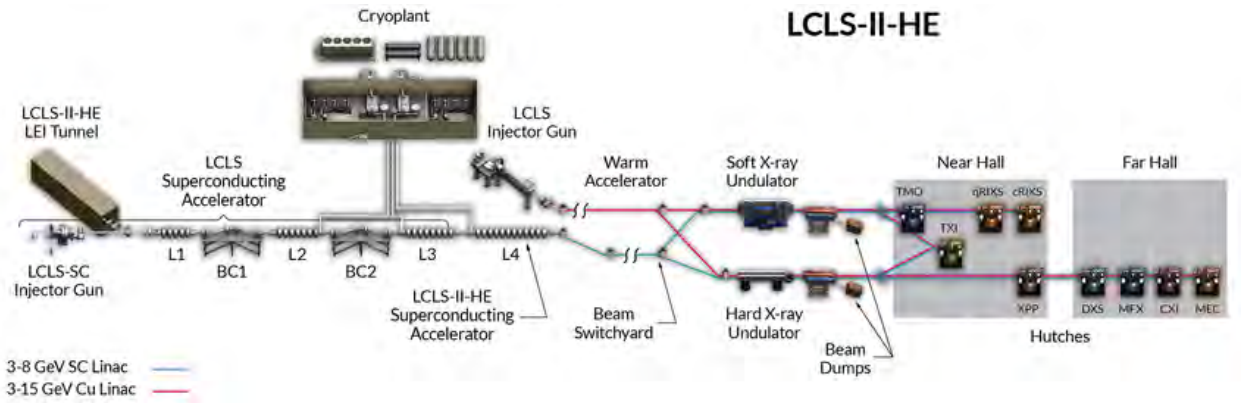


Figure 1.8 Layout of the LCLS-II SRF addition alongside the LCLS copper linac. Figure originally published in [50].

physics studies since the 1970s. The fourth generation of light sources includes the so-called x-ray free electron lasers (XFEL). Linacs are used to provide high-γ electrons and undulator/wiggler magnets are used to produce fast pulsed x-rays.

One such machine in the United States is the Linac Coherent Light Source II and its new high energy upgrade (LCLS-II-HE). This addition to the SLAC linac includes an additional 23 cryomodules of 1.3 GHz, 9-cell elliptical SRF cavities that have been designed for the ILC [48, 49]. This high energy upgrade will provide high-repetition-rate x-rays and pave the way for more precise studies of material structure and molecular dynamics.

1.4.4 Comparison

As a wrap-up, we will compare some of the most notable machines in the United States of America. We have detailed a few accelerators of different varieties in the previous sections and discussed their differences. In this section, we present a quick recap and discuss the similarities between major linacs in the US. We present a table of notable superconducting linacs in the US in Table 1.4.

There is a clear trend among CW machines: the beam current is less than 1 mA. Energy delivered to the beam means more power is required from the generator to maintain the correct field/stored energy. The larger the beam current, the larger the power requirements in order to account for energy delivery to the beam. Thus for increasingly large beam currents, CW operation

Table 1.4 Relevant figures of merit for different superconducting linear accelerators in the USA: the accelerated species, mode of operation, max energy, beam current, number of SRF cavities, and max bandwidth of these cavities. Max energy and beam current for heavy-ion accelerators are representative of U^{238} beams.

Name	Species	Operation	E_{max}	I_{beam}	# Cavs.	Δf_{max}
FRIB	Ion	CW	200 MeV/u	435 pnA	324	40 Hz
SNS	Proton	Pulsed	1.3 GeV	50 mA	81	1103 Hz
PIP-II	Proton	Pulsed	800 MeV	2 mA	135	108 Hz
CEBAF	Electron	CW	12 GeV	1-150 μA	418	220 Hz
LCLS-II	Electron	CW	8 GeV	1-300 μA	296	32.5 Hz

becomes more difficult.

For older machines such as CEBAF, legacy cryomodules contain cavities that are not equipped with mechanical frequency tuners. As such, larger bandwidths are required to ensure that deviations in resonance frequency do not lower the stored energy substantially. We will extensively discuss frequency deviations in the next chapter and deal with frequency tuning in Chapter 5. The PIP-II accelerator presents an interesting case: the mode of operation has changed a few times in the project history, starting as a pulsed machine, then changing to CW, and finally looking back towards pulsed operation. If successful, PIP-II will be one of, if not the first, large scale SRF accelerators to operate in pulsed mode with CW, narrow bandwidths.

1.5 Motivation of Research

Ecological and energy considerations have become more critical in our society. As we will come to see, there is a relationship between the bandwidth of these cavities and the power requirements for operation. SRF linacs are therefore looking towards narrower bandwidths to reduce RF power costs. With advances with digital control and machine learning, it will soon be possible to run even pulsed mode operation with a bandwidth of 10s of Hz. However, there are still some considerations that must be made.

Niobium has good mechanical and shaping properties, but has poor thermal conductivity. Cavities must therefore be shaped with a thickness of only 3-4 mm to allow for better thermal management. The result is an increased sensitivity of the resonance frequency to deformations of the cavity walls. For example, a bare prototype for the FRIB energy upgrade/LB650 cavity will

experience a 100 Hz shift from only a 435 nm squeeze of the accelerating gap. Disturbances from the environment and even the radiation pressure of the cavity field can quickly shift the frequency of the cavity and possibly lead to unstable behavior in the cavity.

These instabilities have been described theoretically since their first observation in 1967, but there has been a lack of experimental results to confirm these theoretical observations. Additionally, there has been a lack of work exploring how the thresholds of these instabilities are affected by complex feedback systems. As we move to higher fields and lower bandwidths, we must also examine more closely the systems that are used to control the cavity frequency in the face of disturbances. By keeping tight enough control on the cavity frequency, we can reduce the number of RF trips during machine operation.

In order to ensure the minimum amount of RF trips (and thus reduce the amount of accelerator downtime), detuning should be held within half of the bandwidth and have no unstable behavior within this region. For many of our narrowband cases, this means that $|f_{gen} - f_{cav}| < 20$ Hz regardless of the geometry. Pushing to higher fields in the pursuit of higher energies with narrower bandwidths reduces the margin for error in this regard.

This work seeks to close the gap in these few regards to the so-called ponderomotive instabilities and frequency control. To do so, we will:

- Extract electromechanical properties from SRF cavities during high-power testing. Analogously, we will also extract the mechanical parameters of room-temperature cavities equipped with their mechanical tuners

- Model and simulate the effect of electromechanical behavior within SRF cavities using our measured parameters and predict the instability thresholds

- Verify our predictive methods by measuring the instability thresholds in real SRF cavities in active accelerators

- Simulate the efficiency of a nonlinear control algorithm in terms of lowering frequency deviations in SRF cavities using our extracted parameters

- Demonstrate the use of this nonlinear algorithm and compare it to a traditional, linear algorithm for frequency control of a room temperature cavity

1.6 Outline of Thesis

Now that we have given the landscape in which this thesis exists, we outline the rest of this work. In the next chapter, we will discuss a more extensive treatment of the SRF cavity. This includes relevant circuit analogies and additions of the transmission line behavior of cavities. We will then discuss the mechanical nature of these cavities and discuss how this can lead to instabilities. We survey previous work done on these instabilities as well.

In Chapter 3, we will give a brief introduction to modeling dynamic systems in the Laplace domain. This will include the presence of feedback and feedforward systems. The three main process variables most relevant for SRF cavities will be introduced and there relevance to accelerator operations established. Two mechanical tuners used in current and future linacs for resonance control will be introduced. We will finish with a treatment of control algorithms that are most relevant to this work, including nonlinear feedback.

Chapter 4 will examine the behavior of instabilities present in the FRIB HWRs in the presence of nonlinear amplitude and phase control. We use simulation and analytical methods to predict the onset at which instabilities occur and compare our predictions with measurements of the instability threshold within the FRIB driving linac. We discuss how the choice of process variables can lead to different instability thresholds, and how controller driven instabilities can arise.

In Chapter 5, we will deal with resonance/frequency control after discussing amplitude and phase control in Chapter 4. We introduce the piezo transfer function and discuss measuring it. We use a measurement of the piezo transfer function for the HB650 cavity to create simulation models with which we can test different control algorithms. We present simulation comparisons of linear and nonlinear controllers for resonance control. We apply nonlinear control to a real tuner and gauge the performance in detuning reduction during room temperature testing. Finally, we discuss the behavior of the ponderomotive instabilities in the presence of resonance feedback using our simulation methods.

CHAPTER 2

CAVITY MODELING AND DYNAMICS

The cases for the use of SRF technology have been presented, and we see that these cavities have been adopted for many modern and future accelerators. With BCS theory, it is easy to see the benefits of SRF operation in terms of RF power consumption and low wall losses compared to normal conducting RF resonators. The goal of this chapter is to show a more detailed approach to modeling SRF cavities using circuitry and the considerations that must be taken to realistically operate these devices. We will cover transmission line elements and how deformations of the cavity geometry can lead to complications in cavity operation.

2.1 The Lumped Circuit Model and Beyond

In the simplest case, the SRF cavity can be modeled in the form of a lumped resistor-inductor-capacitor (RLC) circuit [15, 25]. A simplified schematic of the cavity circuit model can be seen in Fig. 2.1. For RF cavities, all three circuit quantities depend on the geometry of the cavity, though there are some similar trends that feed into their determination. We use a single-cell, elliptical geometry as an example to demonstrate these effects which we show in Fig. 2.2. For the single elliptical cell, capacitance is built up across the accelerating gap of the cell, where the electric field is strongest (denoted with the capacitor symbol). Inductance is built up in the high magnetic field regions of the periphery (denoted with the inductor symbols). These trends hold true for any cavity geometry: capacitance and inductance are built up mostly in the high field regions.

It is with these two resulting circuit quantities that the cavity resonant frequency is determined:

$$\omega_0 = \frac{1}{\sqrt{LC}}. \tag{2.1}$$

The resistance R relates to the shunt impedance of the cavity R_{sh} as $R = 2R_{sh}$ [15, 51, 25]. It is this difference in factor of two that creates the difference in notation that we mentioned in Chapter 1. The energy stored inside the cavity switches between the electric field and the magnetic field periodically. The quality factor Q_0 (as we defined in Eq. (1.16)) of the system also relates to the

circuit parameters and describes the bandwidth ($\omega_{1/2}$) of the resonator:

$$Q_0 = \frac{\omega_0}{2\omega_{1/2}} = \frac{\omega_0 \tau}{2} = \omega_0 RC = \frac{\omega_0 R}{L}, \tag{2.2}$$

where τ is the cavity decay time (or RC time constant).

The current across each of the elements in Fig. 2.1 can be found in the Fourier domain with phasor notation. Combining the elements into one lumped impedance, the current can be expressed as:

$$\tilde{I}_g = \frac{\tilde{V}}{\tilde{Z}_{tot}}, \tag{2.3}$$

where $\tilde{I}_g$ is the current from the generator, $\tilde{V}$ is the voltage across each element, and $\tilde{Z}_{tot}$ is the total impedance. In parallel form, the total impedance is:

$$\frac{1}{\tilde{Z}_{tot}} = j\omega C - \frac{j}{\omega L} + \frac{1}{R}, \tag{2.4}$$

where $j^2 = -1$. $\tilde{Z}_{tot}$ is minimized (and thus $\tilde{I}_g$ is maximized per Eq. (2.3)) when $\omega = \omega_0$. Switching back to the time domain and applying Kirchhoff's junction law, the current has the following expression:

$$I_g(t) = C\dot{V}(t) + \frac{V(t)}{R} + \frac{1}{L}\int V(t)\, dt + I_b(t), \tag{2.5}$$

where I_b is the beam current through the cavity. By taking a time derivative, we can eliminate the integral term,

$$\dot{I}_g(t) = C\ddot{V}(t) + \frac{1}{R}\dot{V}(t) + \frac{1}{L}V(t) + \dot{I}_b(t), \tag{2.6}$$

which simplifies down to a damped-driven harmonic oscillator,

$$\ddot{V}(t) + \frac{1}{RC}\dot{V}(t) + \frac{1}{LC}V(t) = \frac{1}{C}(\dot{I}_g(t) - \dot{I}_b(t)). \tag{2.7}$$

Finally, we can simplify the expression to a more common form using the RC time-constant τ and quality factor (Eq. (2.2)):

$$\ddot{V}(t) + \frac{2}{\tau}\dot{V}(t) + \omega_0^2 V(t) = \omega_0 \frac{R}{Q}(\dot{I}_g(t) - \dot{I}_b(t)), \tag{2.8}$$

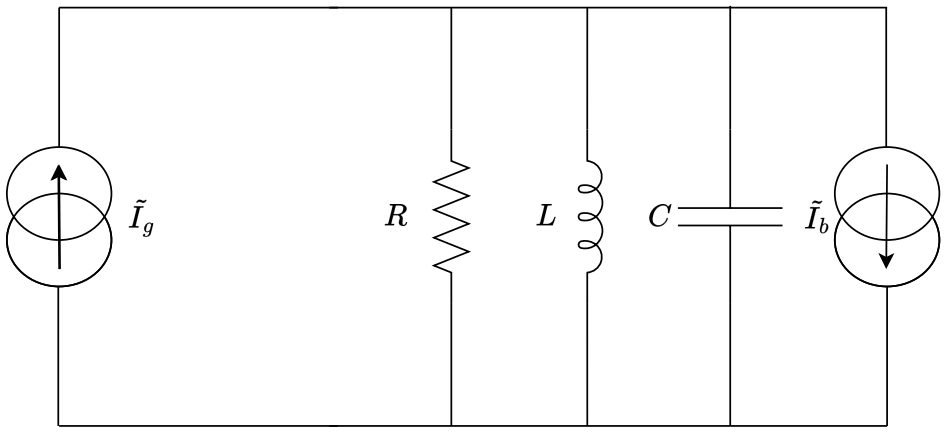


Figure 2.1 Simple RLC circuit with AC sine-wave current source with beam loading denoted by the opposite direction current source $\tilde{I}_b$.

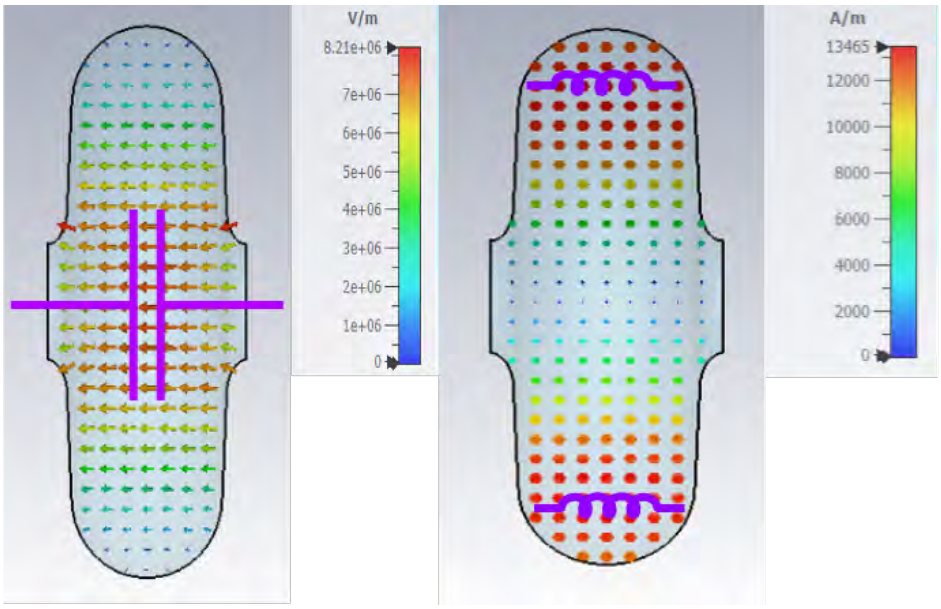


Figure 2.2 CST simulation of the TM_{010} fundamental mode electric (left) and magnetic (right) fields for an FRIB energy upgrade, single-cell geometry. The internal energy in this simulation is normalized to 1 J.

where the geometric shunt impedance R/Q arises. The dynamics of the cavity are now made more clear. The RF cavity is driven oscillator with two distinct driving terms: the generator term provides energy to the cavity, building a positive voltage across R. The beam current forms a negative voltage across R, taking energy out of the cavity. Thus to maintain cavity oscillations, the generator must continuously provide an AC drive that is stronger than the draw of the beam.

While giving a decent explanation of cavity behavior, this lumped circuit model has limitations.

The wavelength of the resonant mode is comparable to the physical size of the cavity and the components supplying power to it. In this case, the wavelike properties of electricity become more dominant. To get a more complete picture, we must move to a transmission line treatment of the cavity and power lines.

2.2 Transmission Line Basics

As we raise the frequency to the radiofrequency spectrum, the wavelengths become comparable to circuit sizes. For example, 100 MHz carriers have a wavelength of ~3 m. The wave-like properties of the fields can no longer be ignored at interfaces within the transfer line. Therefore wires with lengths >= 10% of the electrical wavelength can no longer effectively transmit the RF power, and waveguide and coaxial transmission lines must be utilized for minimal losses transmitted to the cavity. For the RF regime, capacitance and inductance are no longer lumped elements, but spread over the whole of the transmission line.

Transmission lines are described by their characteristic impedance, which is the ratio of the voltage and current sinusoids within the line. This impedance contains not only the resistive losses, but also the phase lag acquired by the voltage through the line. As such, this characteristic impedance depends on the geometry and materials of the line. In general, the ratio of the inductance and capacitance gives the characteristic line impedance for low-resistance materials [17]:

$$Z = \sqrt{\frac{l}{c_T}}, \tag{2.9}$$

where l and c_T are the inductance and capacitance per meter of the line. Vacuum has its own characteristic impedance $Z_v = 376.37\ \Omega$, which is used to scale to other transmission lines.

As the power is transmitted from one transmission line to another, RF power may be reflected back along the original line. This reflected power P_r relates to the forward power P_f as,

$$P_r = |\Gamma|^2 P_f \tag{2.10}$$

where Γ is the reflection coefficient whose square describes the amplitude of the reflected wave. Γ itself can be determined from the characteristic impedances of the two transmission lines as:

$$\Gamma = \frac{Z_2 - Z_1}{Z_2 + Z_1}, \tag{2.11}$$

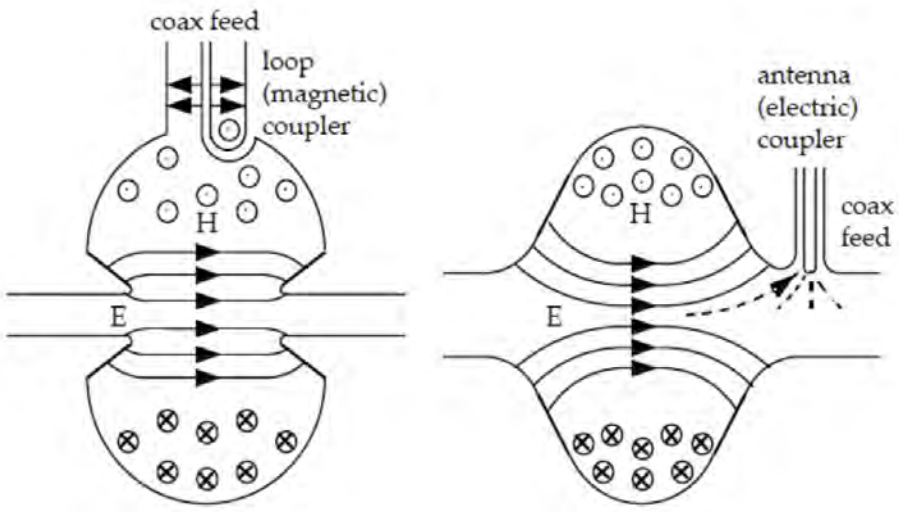


Figure 2.3 left) Diagram of inductive coupling method for a common normal conducting cavity geometry. right) Diagram of capacitive coupling for the SRF elliptical geometry. Figure is originally from [52].

where Z_2 and Z_1 are the characteristic impedances of transmission lines 2 and 1 respectively. It can be seen that when $Z_2 = Z_1$, the impedances are matched and there is no reflection of the incident/forward power between the two lines.

2.2.1 Couplers

In order to store energy, it must first be fed into the cavity. RF power must be coupled to the fundamental RF mode of the cavity from an external transmission line and generator. Specialized devices referred to as RF couplers are equipped to the cavity system to carry out this function. There are two methods to couple RF power to the cavity, inductive or capacitive coupling. Inductive coupling utilizes a waveguide with conducting loop placed into the high magnetic field region of the cavity to inductively transmit power into the cavity. Capacitive coupling follows in a similar manner, but with a different geometry. A coaxial antenna feeds and transmits RF power into the cavity near the high-electric field accelerating gap. A figure of both of these methods can be seen in Fig. 2.3.

We can modify our circuit model to account for the input coupler of the model. An example of the equivalent circuit can be seen in Fig. 2.4. In this case, the coupler also acts as a $1 : n$ transformer between the generator and the cavity. As such, the external impedance Z_e of the

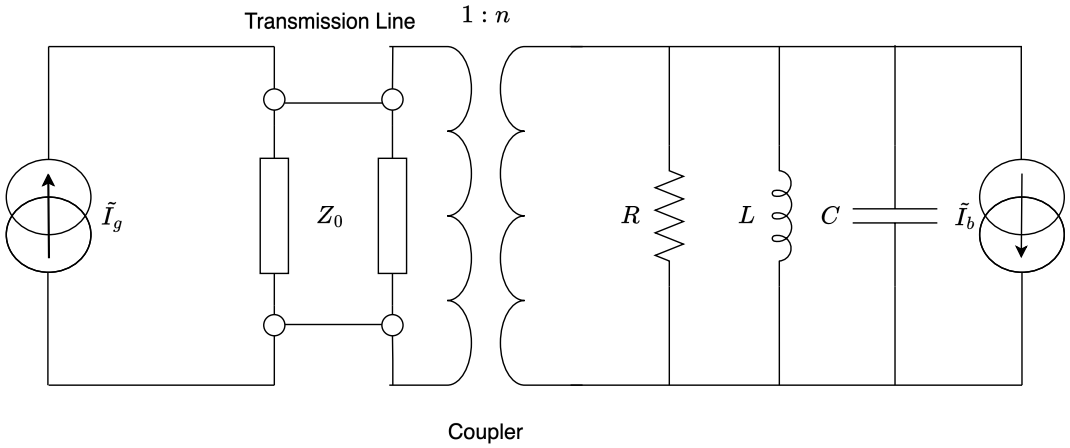


Figure 2.4 Equivalent circuit model for an RF cavity equipped with a fundamental power coupler with the influence of beam loading.

generator+transmission line+coupler from the view of the cavity is [25]:

$$Z_e = n^2 Z_0, \tag{2.12}$$

where Z_0 is the matched generator and transmission line impedance and n is the transformer turns ratio.

The coupling factor β_e is an important figure of merit in describing the behavior of the power in the cavity and coupler system:

$$\beta_e = \frac{R}{Z_e} = \frac{R_{sh}}{2Z_e}. \tag{2.13}$$

There are three regimes of β_e which represent different behaviors of the power, which we now describe.

- $\beta_e > 1$, referred to as the over-coupled regime. In this regime, most of the forward power P_f sent to the cavity is reflected on the coupler-cavity interface.
- $\beta_e = 1$, the unity regime. This is the matched impedance case, where there is no reflected power at the cavity-coupler interface.
- $\beta_e < 1$, the under-coupled regime. In this regime, most of the forward power is still reflected as in the over-coupled case.

The shunt impedance is then altered by the addition of the coupler loaded system:

$$R_l = \frac{R}{1+\beta_e} = \frac{R_{sh}}{2(1+\beta_e)}, \tag{2.14}$$

where R_l is the loaded shunt impedance.

Of course, the coupler is not a one-way window for RF power. Power can leak out of the cavity back into the coupling structure. As such, an additional quality factor can be used to describe this loss mechanism; for the forward/fundamental power coupler this quality factor is referred to as the external-Q or Q_e:

$$Q_e = \frac{\omega_0 U}{P_e}, \tag{2.15}$$

where P_e is the power that is leaking out of the cavity into the waveguide. As we remarked earlier, the beam is taking energy from the cavity and providing another loss metric and associated quality factor:

$$Q_b = \frac{\omega_0 U}{P_b}, \tag{2.16}$$

where P_b is the power extracted from the cavity by the beam. The combined cavity-coupler system with beam on can then be described with a so-called loaded quality factor Q_l:

$$\frac{1}{Q_l} = \frac{1}{Q_{ext}} + \frac{1}{Q_0} + \frac{1}{Q_b} = \frac{P_e + P_w + P_b}{\omega_0 U} = \frac{P_l}{\omega_0 U} \Rightarrow Q_l = \frac{\omega_0 U}{P_l}, \tag{2.17}$$

where P_l is the total power loss in the cavity-coupler system.

Let us consider the power losses in both the cavity and through the transmission line in the absence of beam. For applied, on-resonance voltage V, the power loss through the coupler can be described as,

$$P_e = \frac{V^2}{Z_e} = \frac{\omega_0 U}{Q_e}, \tag{2.18}$$

and losses in the walls of the cavity as,

$$P_w = \frac{V^2}{R} = \frac{\omega_0 U}{Q_0}. \tag{2.19}$$

Taking the ratio of these two expressions, we can see an important relationship form:

$$\frac{P_e}{P_w} = \frac{Q_0}{Q_e} = \frac{R}{Z_e} = \beta_e. \tag{2.20}$$

The coupling strength β_e can be determined by the ratio of Q_0 and Q_e, which is easier to experimentally determine during vertical testing and calculate with electromagnetic solvers. Additionally, a simplified condition for a matched cavity arises: $Q_e = Q_0$.

We now come to the importance of Q_l and how the coupler influences the cavity. The bandwidth (and half-bandwidth) is determined by the loaded quality factor and can be expressed in terms of Q_l and/or β_e:

$$\omega_{1/2}(\beta_e) = \frac{\omega_0}{2Q_l} = \frac{(1+\beta_e)\omega_0}{2Q_0}. \tag{2.21}$$

The coupling regimes now have different implications for the loaded bandwidth. In cases of $\beta_e \gg 1 \Rightarrow Q_0 \gg Q_e$, we have $Q_l \approx Q_e$. This is referred to as the over-coupled regime, and Q_e becomes the determining factor of the RF bandwidth. As an example, the FRIB energy upgrade cavity will operate with $Q_e = 2 \times 10^7$, which for $Q_0 \geq 2 \times 10^{10}$ will result in a 32.2 Hz bandwidth

In the matched case, $Q_e = Q_0 = Q$ and $Q_l = \frac{1}{2}Q$, the half-bandwidth is determined by,

$$\omega_{1/2}(\beta_e = 1) = \frac{\omega_0}{Q}. \tag{2.22}$$

For the strongly under-coupled regime $\beta_e \ll 1 \Rightarrow Q_e \gg Q_0$, it is now the intrinsic quality factor that becomes the determining factor for the bandwidth. In the matched and under-coupled regimes, the bandwidth becomes extremely narrow: an FRIB energy upgrade cavity operated in matched conditions would have a bandwidth of 0.06 Hz. A strongly under-coupled FRIB energy upgrade cavity would have roughly the same bandwidth, but would also experience reflection of the forward power due to the impedance mismatch.

It is important to note that for all SRF cavities, a probe coupler will also be used to couple power out of the cavity. This power will be used to sample the cavity amplitude and phase in order to perform corrections via feedback systems (Chapter 3). We refer to the forward/fundamental power-coupler with its quality factor as Q_{e1} and the so-called "pickup" coupler with its quality factor as Q_{e2}. The total loaded quality factor of the system (with beam) is then given by:

$$\frac{1}{Q_l} = \frac{1}{Q_{e1}} + \frac{1}{Q_0} + \frac{1}{Q_{e2}} + \frac{1}{Q_b}. \tag{2.23}$$

It is common to design the pickup to be coupler strongly under-coupled, such that its contribution to Q_l is negligible.

We have made it clear through Eq. (2.8) that the beam will extract energy from the cavity. In an SRF cavity, we will have $P_b \gg P_w$, and thus the largest source of losses within the cavity will be the beam itself. The generator must provide power to the cavity in order to replenish the lost energy. Q_l and the bandwidth will therefore determine the power required for operation of the RF eigenmode. On resonance, the power for an accelerating voltage of V_0 goes as

$$P_{req} = \frac{V_0^2(1+\beta)}{4\beta R_l}\left[\left(1+\frac{V_b\cos\psi_s}{V_0}\right)^2+\left(\frac{V_b\sin\psi_s}{V_0}\right)^2\right], \tag{2.24}$$

where $R_l = \frac{R}{Q}Q_l$ is the loaded shunt impedance, V_b is the voltage deposited by the beam in the cavity, and ψ_s is the synchronous accelerating phase [15]. It can be seen that beam loading changes the optimal coupling for minimized power requirements: with no beam loading, the required power is minimized with matched coupling. In the presence of beam, the required power is minimized when the coupling is matched to the beam quality factor Q_b such that most of the power is delivered to the beam.

2.3 Detuning

Aside from the effect of beam loading increasing the required power, operating at matched coupling presents another issue. For normal conducting RF cavities, $Q_0 \sim 10^4,\ 10^5$ which when combined with GHz frequencies results in incredibly large bandwidths. For SRF cavities where $Q_0 > 10^9$, a matched load can result in the opposite. As mentioned earlier, a high-Q_0 SRF cavity such as the FRIB energy upgrade cavity would experience a 0.06 Hz bandwidth in matched configuration. In perfectly isolated conditions this might be sufficient. It is with this note that we return to the extended body treatment of SRF cavities. Niobium is a poor thermal conductor, and as such SRF cavities must be machined to possess thin walls, usually on the order of 3-4 mm. This makes the cavity walls susceptible to deformations from mechanical vibrational noise.

As we discussed earlier, the resonant frequency of cavity is dependent on the geometry of the high-field regions. Deformations of these regions will cause a shift in the resonant frequency of

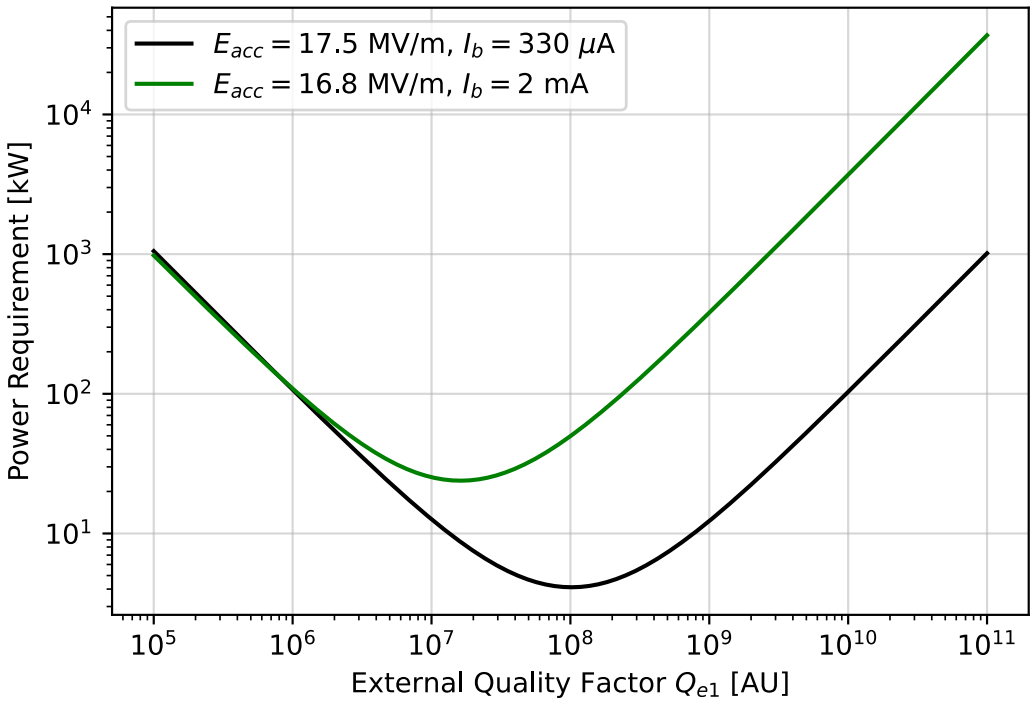


Figure 2.5 Power requirements for the operation of two cases of E_{acc} and beam current I_b. The two cases chosen represent the operation of an FRIB energy upgrade cavity at the maximum beam current and the LB650 cavity at nominal beam current. Both curves are calculated assuming $\psi_s = 0$, i.e. the beam arrives at the crest of the RF wave, and that $Q_0 = 2 \times 10^{10}$.

the cavity. For cavities that are driven with an external RF generator/clock, these deformations will cause a mismatch between the generator and the cavity frequencies ω and ω_c respectively. The magnitude of this mismatch is called detuning $\Delta\omega$, denoted in units of rad/s:

$$\Delta\omega = \omega - \omega_c. \tag{2.25}$$

The effect these low-frequency modulations can have on the signal can be well described mathematically. Let us start from Eq. (2.8) for a cavity loaded with a fundamental power coupler resulting in a loaded shunt impedance R_l. Working in the Fourier domain, the equation becomes:

$$\ddot{\tilde{V}}_c + \left(2j\omega + \frac{2}{\tau}\right)\dot{\tilde{V}}_c + \left(\omega_c^2 - \omega^2 + \frac{2j\omega}{\tau}\right)\tilde{V}_c = 2\omega_{1/2}R_l(\dot{\tilde{I}}_g + j\omega\tilde{I}_g - \dot{\tilde{I}}_b - j\omega\tilde{I}_b), \tag{2.26}$$

where $\tilde{V}_c$, $\tilde{I}_g$, and $\tilde{I}_b$ are the time-dependent cavity voltage, generator current, and beam phasor amplitudes respectively. Changes to the carrier RF are negligible and $\omega\tilde{I}_g \gg \dot{\tilde{I}}_g$. If we take

sufficiently high beam repetition rate as well, we can arrive at,

$$2j\omega\dot{\tilde{V}}_c + \left(\omega_c^2 - \omega^2 + \frac{2j\omega}{\tau}\right)\tilde{V}_c = 2j\omega_{1/2}R_l(\tilde{I}_g - \tilde{I}_b). \tag{2.27}$$

To decent approximation, we can bring detuning into the expression,

$$\omega_c^2 - \omega^2 = (\omega + \omega_c)(\omega_c - \omega) \approx -2\omega\Delta\omega. \tag{2.28}$$

With some simplifications, we can arrive at the well known envelope equation which describes the time evolution of the envelope/signal to the carrier RF:

$$\dot{\tilde{V}}_c + (\omega_{1/2} - j\Delta\omega)\tilde{V}_c = \omega_{1/2}R_l(\tilde{I}_g - \tilde{I}_b) = \omega_{1/2}(\tilde{V}_g - \tilde{V}_b), \tag{2.29}$$

where the generator voltage as seen by the cavity is $\tilde{V}_g = R_l\tilde{I}_g$ and the voltage deposited by the beam is $\tilde{V}_b = R_l\tilde{I}_b$. Taking the steady-state case of Eq. (2.29), we can arrive at the resonance curve, or the cavity amplitude as a function of detuning:

$$|\tilde{V}_c| = \frac{|\tilde{V}_g| - |\tilde{V}_b|}{\sqrt{1 + (\frac{\Delta\omega_0}{\omega_{1/2}})^2}}, \tag{2.30}$$

where $\Delta\omega_0$ is the steady-state or static detuning offset with respect to the generator.

We now see the effect that detuning can have: when the cavity is detuned from the generator, more power is required to (higher $|\tilde{V}_g|$) to keep a constant $|\tilde{V}_c|$. As can be seen from Eq. (2.30), a detuned cavity will drop the amplitude of the cavity. Thus, more power must be supplied to the cavity in order to restore the amplitude to the nominal amplitude value V_0. This detuning factor couples with the reactive portion of the beam loading as:

$$P_{req} = \frac{V_0^2(1+\beta)}{4\beta R_l}\left[\left(1 + \frac{V_b\cos\phi_s}{V_0}\right)^2 + \left(\frac{\Delta\omega}{\omega_{1/2}} + \frac{V_b\sin\phi_s}{V_0}\right)^2\right]. \tag{2.31}$$

We demonstrate the effect detuning can have on the same two previous cases (Fig. 2.5) with beam-loading in Fig. 2.6. It is with this that we show the importance of coupling considerations. Having lower Q_l (Q_{e1} in the strongly over-coupled regime) will result in a higher on-resonance power requirement, but the larger bandwidth results in less growth in required power when the cavity is detuned. This is one the main considerations that must be made when deciding coupling: what

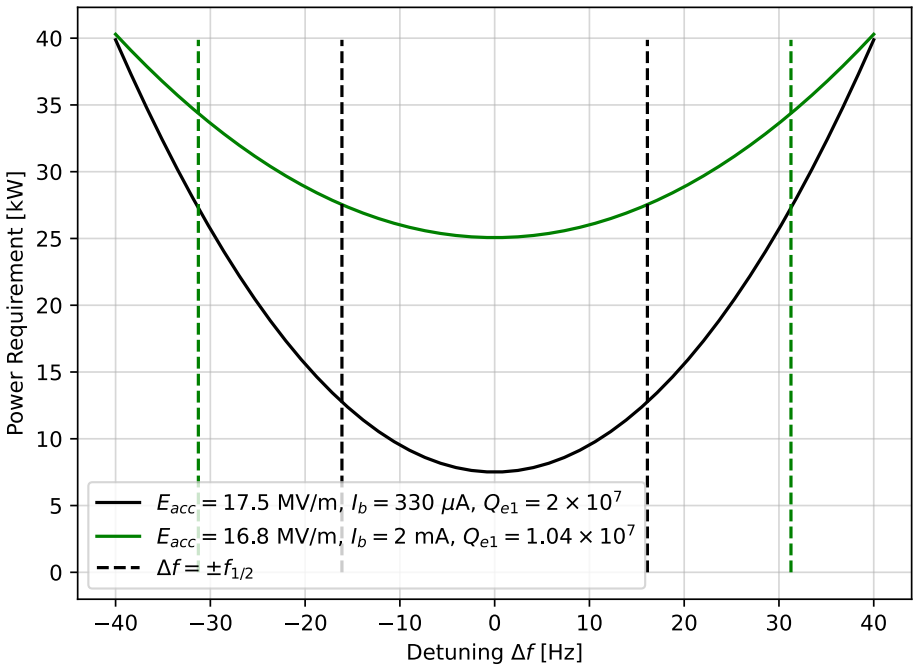


Figure 2.6 Required power for a constant field amplitude as a function of the detuning $\Delta f = \frac{\Delta\omega}{2\pi}$ for parameters mimicking FRIB energy upgrade and LB650 operation. Vertical dashed lines represent the respective half-bandwidths in Hz. In this case, we again take $\psi_s = 0$.

is the highest allowable Q_{e1} such that the on-resonance power is lower but the bandwidth is large enough to avoid large increases in power due to detuning?

In the next few sections, we will provide more details about detuning: the dynamics, the sources, and the effects it can have on the stability of the cavity. We will also supplement the material with data we have captured across a myriad of cavities. The FRIB energy upgrade and LB650 cavities were the original motivation for this body of work, and we have often compared the two in terms of their operation. Due to testing limitations, we were not able to capture much data pertaining to either cavity (what we did capture will be discussed in Chapter 4). Instead we will use data from cavities that became important to this thesis along the way: the FRIB HWRs and the PIP-II HB650 and SSR2 cavities.

2.3.1 Sources of Detuning

There are two broad types of detuning sources: deterministic and stochastic. Deterministic sources are predictable and can reliably be accounted for. The major source of deterministic

detuning is due to changes in the cavity field (Lorentz force detuning or LFD effect). There is a closed form solution for quasi-static LFD, and as we will discuss momentarily can be modeled with a series of differential equations. Another form comes from mechanical tuners that are used to counteract not only the LFD but also the stochastic effects.

Stochastic detuning sources are seemingly random: most of these sources are a result of cryomodule systems such as vacuum pumps, changes in helium level and pressure, thermo-acoustic oscillations, or even movement outside the cryomodules. There have been many studies into the sources of these so called microphonics and their suppression, especially in regard to high Q_l continuous wave machines [53, 54, 55, 56, 57, 58, 59].

While some events, like changes in liquid helium level, can be deterministic, the strength at which they impact the cavity frequency isn't always clear. Hidden/unknown cavity-to-environmental couplings are also included as sources. At 4.3 K and 1 atm, liquid helium will undergo nucleate boiling increases the noise level. Thus it is common to operate cavities at 2 K where helium is superfluid with no nucleate boiling. The sources, deterministic or not, can excite deterministic motion within the cavity. In the next section, we will derive equations of motion that govern detuning regardless of source using an elastic model. We will also discuss other deterministic effects that can be modeled.

2.3.2 Detuning Equations of Motion

We will follow along with previous derivations done by [60, 61, 62], in which we use an elastic model. Like all rigid bodies, SRF cavities have infinite mechanical vibrational resonant modes, with frequencies Ω_μ. Analogous to a taut string, each of these modes has its own characteristic shape, which we will denote with $\phi_\mu(\mathbf{r})$. Any displacement of the cavity walls $\boldsymbol{\xi}(\mathbf{r}, t)$ can be expressed as the sum of displacements of the vibrational modes:

$$\boldsymbol{\xi}(\mathbf{r}, t) = \sum_{\mu=1}^{\infty} \xi_\mu(t)\phi_\mu(\mathbf{r})\hat{\boldsymbol{\xi}}_\mu, \tag{2.32}$$

where ξ_μ is the time-dependent displacement amplitude contribution for mode μ and $\hat{\boldsymbol{\xi}}_\mu$ is the direction of motion. It is around this quantity $\xi_\mu(t)$ that we can start to construct the Lagrangian

for a single mode.

Suppose the vibrations of the cavity wall are driven with some force $\mathbf{F}$. Only the component of force inline with the the displacement $\boldsymbol{\xi}$ is relevant to the Lagrangian:

$$F_\xi = \int \mathbf{F} \cdot \boldsymbol{\xi} \, d\xi. \tag{2.33}$$

From this force, we can find the μ'th mode's contribution to F_ξ via Fourier's trick and integrating the force over the mode shape:

$$F_\mu = \int_{\partial\Omega} F_\xi \cdot \phi_\mu(\mathbf{r}) \, dA. \tag{2.34}$$

Now we can construct the Lagrangian assuming an elastic model. The potential and kinetic energies for mode μ can be respectively expressed as:

$$V_\mu = \frac{1}{2} c_\mu \xi_\mu^2, \tag{2.35}$$

$$T_\mu = \frac{c_\mu}{2\Omega_\mu^2} \dot{\xi_\mu}^2, \tag{2.36}$$

where the elastic constant c_μ relates to the mode inertial coefficient m_μ as,

$$c_\mu = \Omega_\mu^2 m_\mu. \tag{2.37}$$

The elastic losses Φ_μ can also be described with the same coordinates and constants:

$$\Phi_\mu = \frac{c_\mu}{\tau_\mu \Omega_\mu^2} \dot{\xi_\mu}^2, \tag{2.38}$$

where τ_μ is the mechanical mode decay time. With Eq. (2.35) and Eq. (2.36), we can define the Lagrangian for a single mode:

$$\mathcal{L}_\mu = T_\mu - V_\mu = \frac{c_\mu}{2\Omega_\mu^2} \dot{\xi_\mu}^2 - \frac{1}{2} c_\mu \xi_\mu^2. \tag{2.39}$$

Finally we apply the Euler-Lagrange equation,

$$\frac{d}{dt}\left(\frac{\partial \mathcal{L}_\mu}{\partial \dot{\xi_\mu}}\right) - \frac{\partial \mathcal{L}_\mu}{\partial \xi_\mu} + \frac{\partial \Phi_\mu}{\partial \dot{\xi_\mu}} = F_\mu, \tag{2.40}$$

and using the expressions in Eq. (2.39) and Eq. (2.38) and simplifying, we can get the relevant equation of motion:

$$\ddot{\xi_\mu} + \frac{2}{\tau_\mu} \dot{\xi_\mu} + \Omega_\mu^2 \xi_\mu = \frac{\Omega_\mu^2}{c_\mu^2} F_\mu. \tag{2.41}$$

We see that each mode is its own driven, damped, harmonic oscillator with driving force F_μ. We now use Slater's perturbation theorem to make the connection between ξ_μ and detuning. For small, slower perturbations from steady states, the shift in the cavity's resonance frequency relates to the shift in internal energy ΔU as:

$$\frac{\Delta\omega}{\omega_0} = \frac{\Delta U}{U_0}, \tag{2.42}$$

where U_0 is the steady state stored energy.

Eq. (2.42) can be rewritten in terms of integrals as well over the deformed volume Ω':

$$\Delta\omega = \omega_0 \frac{\int_{\Omega'} f \, dV'}{U_0} = \frac{1}{2}\omega_0 \frac{\int_{\Omega'} \epsilon_0 \mathbf{E}' \cdot (\mathbf{E}')^* + \mu_0 \mathbf{H}' \cdot (\mathbf{H}') \, dV'}{U_0}, \tag{2.43}$$

where dV' is the deviated volume due to the perturbations, $\mathbf{E}'$ and $\mathbf{H}'$ are the deviated electric and magnetic fields, and $f = F/A$ is the total force per unit area (i.e the effective pressure on the cavity's walls). We can express the volume change as $dV' = \boldsymbol{\xi} \cdot \mathbf{dA}'$, where $\mathbf{dA}'$ is the deviated surface area:

$$\Delta\omega = \omega_0 \frac{\int_{\partial\Omega'} f \cdot (\boldsymbol{\xi} \cdot \mathbf{dA}')}{U_0}. \tag{2.44}$$

If we consider the total detuning as the sum of each mode's contribution $\Delta\omega = \sum_\mu \Delta\omega_\mu$, then Eq. (2.44) can be broken into individual mode contributions as well:

$$\Delta\omega_\mu = \frac{\omega_0 F_\mu \xi_\mu}{U_0} = \omega_0 f_\mu \xi_\mu, \tag{2.45}$$

where $f_\mu = F_\mu/U_0$, or force projection normalized to the stored energy. We now see the connection between the mode displacement and the mode's detuning. Subbing Eq. (2.45) into Eq. (2.41), we get the resulting equation of motion for a mode's detuning contribution:

$$\Delta\ddot{\omega}_\mu + \frac{2}{\tau_\mu}\Delta\dot{\omega}_\mu + \Omega_\mu^2 \Delta\omega_\mu = \frac{\omega_0 U_0 f_\mu^2 \Omega_\mu^2}{c_\mu} = W_\mu, \tag{2.46}$$

where we will denote W_μ as the detuning driving force. This equation is key to the analysis and discussion for the rest of this work.

2.3.3 Microphonics

All SRF cavities will experience random vibrational noise that will occur within their cryomodule. This noise can shift the resonant frequency of the cavity and this phenomenon is referred

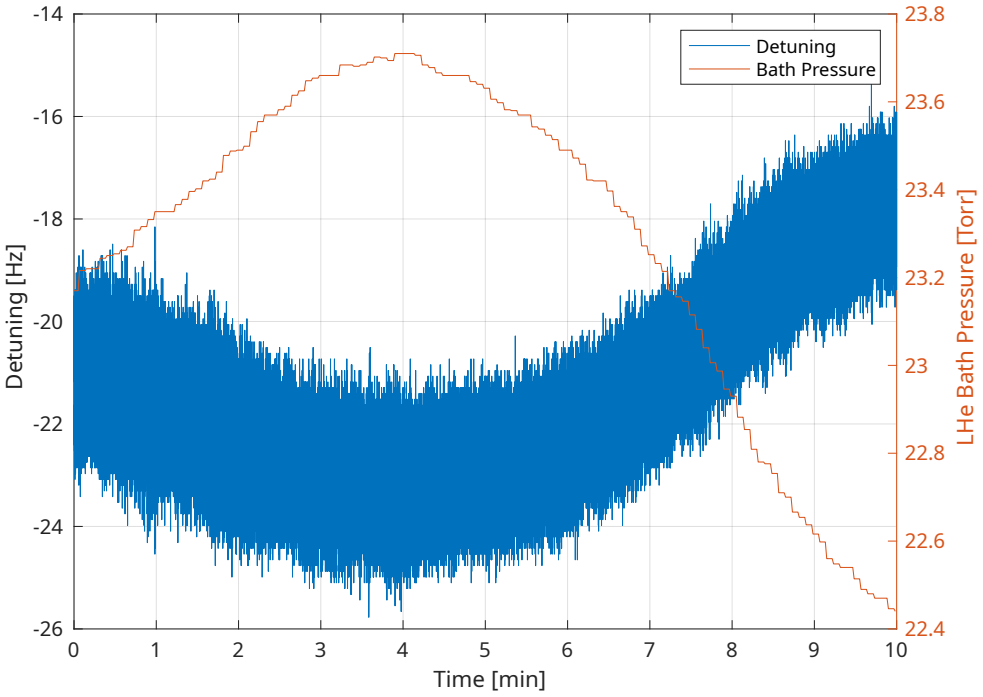


Figure 2.7 Detuning and LHe bath pressure v. time during a microphonics survey for an HB650 cavity during microphonics survey. There is a clear correlation between the detuning offset and pressure drift. This measurement period was used to identify microphonic noise sources and attempt to characterize their strength.

to as microphonics. Deviations in helium bath pressure and local temperatures can cause slow drift of the cavity resonance frequency. An example of frequency drift caused by slow changes in bath pressure can be seen in Fig. 2.7. Additional noise sources can be attributed to deviations in temperature, thermo-acoustic oscillations, and even civil construction in some cases. These events are usually stochastic, and this makes them hard to mathematically model. In these cases, the microphonics excite and couple to the mechanical modes:

$$\Delta\ddot{\omega}_\mu + \frac{2}{\tau_\mu}\Delta\dot{\omega}_\mu + \Omega_\mu^2\Delta\omega_\mu = k_\mu^M\Omega_\mu^2 N(t), \tag{2.47}$$

where $N(t)$ is the microphonics generalized force and k_μ^M is the mechanical mode's coupling strength with respect to microphonics. While microphonics is hard to model and quantify (specifically when it comes to the values for k_μ^M), Eq. (2.47) can be used to simulate cryomodule effects, with variable k_μ^M to match experimental microphonics measurements.

Microphonics is unavoidable from an operational perspective; there will always be some vibrational noise from the environment. As such, microphonics must be managed in order to avoid ballooning RF power costs. In Chapter 5, we will extensively discuss one active microphonics compensation system, the piezoelectric tuner. Now we will briefly discuss passive means of microphonics reduction. The original CEBAF cryomodule design did not include fast tuners, and as such many studies have been conducted with the goal of managing microphonics through various means. This extends to boron nanotube structures to increase stiffness, and even deploying locking/stiffening fixtures to sensitive external structures to reduce vibrations [53, 63].

Quarter-wave resonators in particular are of interest for microphonics reduction studies. The geometry of the cavity results in a strong pendulum-like mechanical mode of the inner conductor. These mechanical resonances normally have high Q_μ and can occur at relatively low frequencies. For example, the pendulum mode for the FRIB $\beta = 0.041$ QWR occurs as low as 36 Hz. A common method to dampen this mode is through frictional mechanical dampers that are inserted into the helium space of the inner conductor [64, 65, 66, 67]. Other methods have included using metal ball bearings deposited at the bottom of the inner conductor [68].

2.3.4 Lorentz Force Detuning

SRF cavities are not subject to external forces alone. A result of the stress tensor regarding electromagnetic fields is unique: the electromagnetic fields produce a radiative pressure. This pressure goes as the square of the field amplitudes, and is normal to the cavity's walls [7].

$$\mathbf{P} = \frac{1}{4}(\mu_0|\mathbf{H}|^2 - \epsilon_0|\mathbf{E}|^2) \cdot \hat{\mathbf{n}} \tag{2.48}$$

Eq. (2.48) shows the location and the behavior of the pressure. High magnetic field regions experience a ballooning pressure ($+\hat{\mathbf{n}}$), whereas high electric field regions are pulled in ($-\hat{\mathbf{n}}$). For SRF cavities, this means the frequency-determining regions will experience this pressure the strongest. A schematic of this effect can be seen in Fig. 2.8.

The ponderomotive pressure of the cavity's own fields therefore shifts the frequency of the RF cavity. The frequency shift caused by changes in the electromagnetic field is colloquially referred to as Lorentz force detuning. This effect appears naturally mathematically as well. Consider

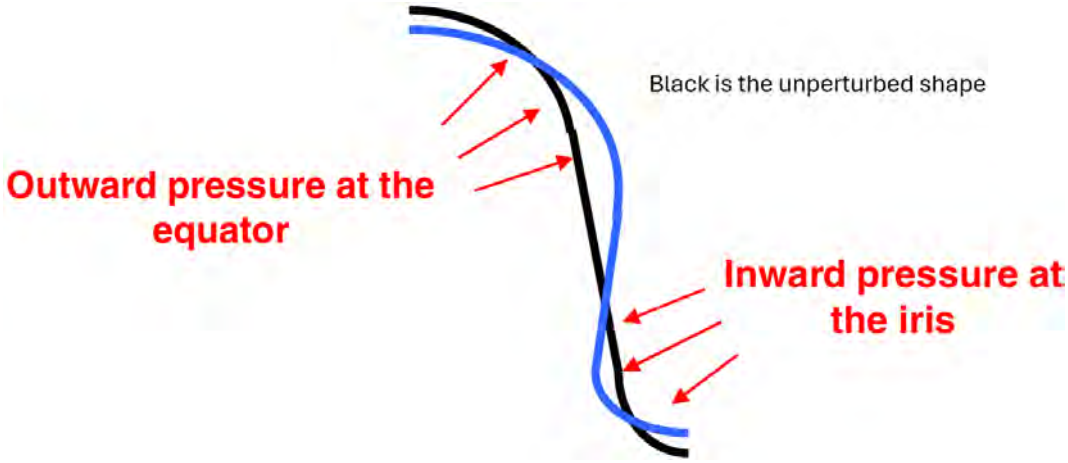


Figure 2.8 Schematic of deformations caused by the radiation pressure of the cavity fields. Figure originally from [69].

Eq. (2.46): F_μ is now the force on the walls from the radiation pressure. Additionally, we can relate the stored energy to the accelerating field. By definition, the dissipated power in the cavity walls can be expressed as:

$$P_w = \frac{\omega_0 U_0}{Q_0} = \frac{V_{acc}^2}{R} \Rightarrow \omega_0 U_0 = \frac{V_{acc}^2 Q_0}{R} = \frac{V_{acc}^2}{\frac{R}{Q}}, \tag{2.49}$$

which we can substitute into Eq. (2.46). Because work is done on the wall by the fields, the stored energy of the cavity decreases by conservation of energy. Thus we expect the resulting frequency shift to be negative by Eq. (2.42). Thus,

$$\Delta\ddot{\omega}_\mu + \frac{2}{\tau_\mu}\Delta\dot{\omega}_\mu + \Omega_\mu^2 \Delta\omega_\mu = -\frac{F_\mu^2}{c_\mu(\frac{R}{Q})}\Omega_\mu^2 V_{acc}^2 = -k_\mu^L \Omega_\mu^2 V_{acc}^2, \tag{2.50}$$

where we refer to k_μ^L as the Lorentz force detuning coefficient for mode μ. This factor is dependent on the geometry of the cavity, the overlap of the mechanical mode shape with the applied ponderomotive pressure, and the elastic properties of the mechanical mode. We see in Eq. (2.50) that the ponderomotive pressure applies a nonlinear drive to the detuning of the cavity.

2.3.4.1 Static Effects

The easiest phenomenon to see is in the static case of Eq. (2.50). As time progresses and the system settles, we arrive at the following relationship,

$$\Delta\omega_{\mu 0} = -k_\mu^L V_{acc}^2, \tag{2.51}$$

where $\Delta\omega_{\mu 0}$ is the steady state or static detuning by mode μ. The total static detuning $\Delta\omega_0$ is then:

$$\Delta\omega_0 = \sum_{\mu=1}^{\infty} \Delta\omega_{\mu 0} = -V_{acc}^2 \sum_{\mu=1}^{\infty} k_\mu^L = -k_L V_{acc}^2, \tag{2.52}$$

where k_L is referred to as the static Lorentz force detuning coefficient and is the sum of all modes' coefficients. This coefficient is easy to find experimentally; V_{acc}^2 can be increased/decreased and the resulting frequency shift can be determined, forming a linear relationship of $\Delta\omega_0$ against V_{acc}^2 from which the slope can be determined.

Let us reconsider now Eq. (2.30). We can make an adjustment to the denominator, where we let $\Delta\omega = \Delta\omega_0 - k_L|\tilde{V}_c|^2$, where $\Delta\omega_0$ is some additional static detuning offset not due to the Lorentz pressure. Using the cavity electrical decay time τ, we obtain the modified resonance curve without beam loading as:

$$|\tilde{V}_c| = \frac{|\tilde{V_g}|}{1 + (\tau\Delta\omega_0 - k_L\tau|\tilde{V}_c|^2)^2}. \tag{2.53}$$

One of the consequences of the Lorentz pressure is laid bare: the resonance curve becomes tilted. An example of this effect for the FRIB $\beta = 0.53$ half-wave resonator can be seen in Fig. 2.9. This tilting effect creates a hysteresis region, where there are multiple values of the cavity amplitude for the same detuning offset. Fig. 2.9 showcases the impact of k_L in regard to the tilt. When $k_L \approx 0$, the resonance curve appears as a linear oscillator.

When $k_L > 0$, the resonance curve tilts as we add nonlinear terms. The green shaded regions in Fig. 2.9 represent the regions in the $V/\Delta f_0$ plane where these nonlinear effects dominate over the linear terms [62]. The tilt also creates a hysteresis region, where the resonance curve has multiple V for a given Δf_0. This can open the door to instabilities, which we will discuss shortly.

2.3.4.2 Dynamic Effects

In cases of extreme disturbances, dynamic effects of the detuning equations become considerable. To examine these effects however carries some difficulty due to the nonlinear driving force. In order to carry out analysis, we must first linearize Eq. (2.50) mimicking [60, 61]; let us first consider a single mechanical mode μ. We can introduce small, time-dependent perturbations to

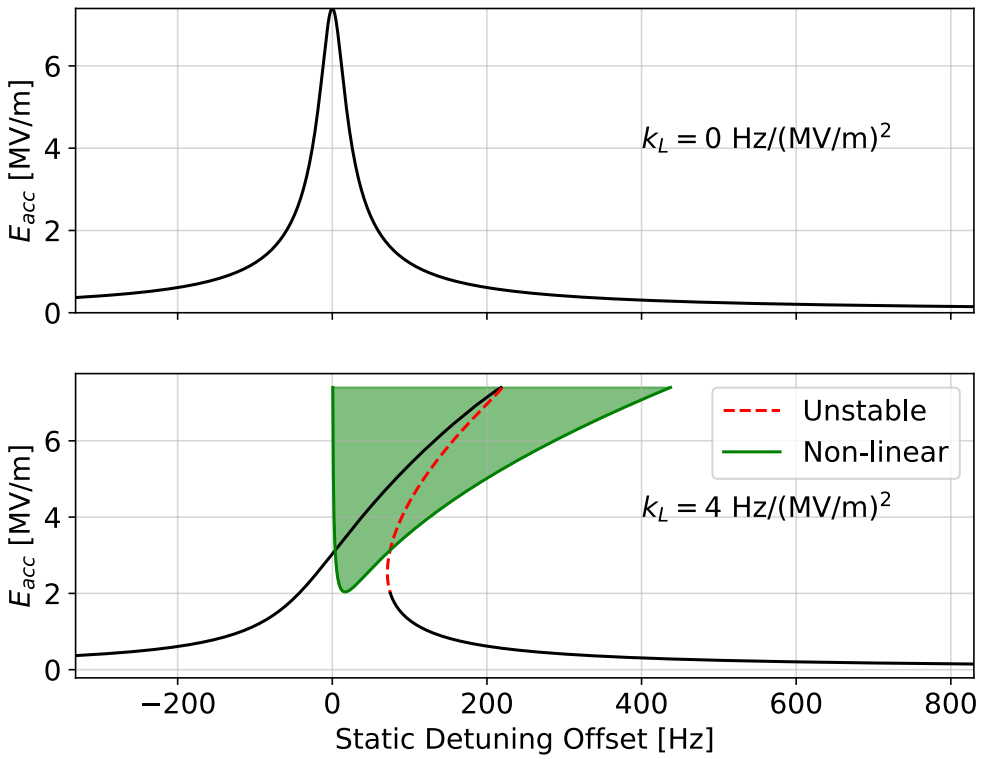


Figure 2.9 Open-loop resonance curves for a $\beta = 0.53$ HWR for two conditions. Cavity resonance curve with no LFD considered (top) and with LFD considered (bottom). For both cases, $Q_l = 1 \times 10^7$ and $E_{acc,max} = 7.4$ MV/m. The red, dashed line represents the most unstable portion of the resonance curve. The green shaded regions represent the portion of the $V/\Delta f_0$ plane where the resonance curve will be dominated by nonlinear effects. Published in [70].

the voltage and detuning around steady state values V_0 and $\Delta\omega_{\mu 0}$ respectively.

$$V_c = V_0 + \delta V(t)$$

$$\Delta\omega_\mu = \Delta\omega_{\mu 0} + \delta\omega_\mu(t)$$

Substituting the linearizing factors into Eq. (2.50) and simplifying, we arrive at the following expression:

$$\delta\ddot{\omega}_\mu + \frac{2}{\tau_\mu}\delta\dot{\omega}_\mu + \Omega_\mu^2\delta\omega_\mu = -\Omega_\mu^2\Delta\omega_{\mu 0} - k_\mu^L\Omega_\mu^2 V_0^2 - 2k_\mu^L\Omega_\mu^2 V_0\delta V. \tag{2.54}$$

We can see that in steady state conditions, the form in Eq. (2.52) is preserved. In terms of the frequency response of the system, it is convenient to use the Laplace or 's'-domain. The Laplace domain represents the time domain behavior of the system in terms of growth/damping σ and frequency response Ω with $s = \sigma + j\Omega$. Taking the Laplace transform and ignoring initial

conditions and integrator terms $(1/s)$, we arrive at:

$$\delta\omega_\mu(s)\left(s^2+\frac{2}{\tau_\mu}s+\Omega_\mu^2\right)=-2k_\mu^L\Omega_\mu^2V_0\delta V(s), \tag{2.55}$$

from which we can derive the transfer function for a single mode μ,

$$G_\mu(s)=\frac{\delta\omega_\mu(s)}{\delta V(s)}=\frac{k_\mu^L\Omega_\mu^2}{s^2+\frac{2}{\tau_\mu}s+\Omega_\mu^2}. \tag{2.56}$$

For many-mode systems, the total electromechanical gain can be characterized by the sum of each mode's transfer function,

$$G_L(s)=-2V_0\sum_{\mu=1}^{\infty}G_\mu(s). \tag{2.57}$$

This expression is known as the Lorentz transfer function (LTF), and describes the changes to the detuning of all mechanical modes per changes in the field amplitude. When $s=0$ (i.e moving to steady state), then:

$$G_L(s=0)\approx-2V_0\sum_{\mu=1}^{\infty}k_\mu^L=-2k_LV_0, \tag{2.58}$$

we approach that static gain value we expect per Eq. (2.54).

More interesting is the case when $s=j\Omega_\mu$, that is the system experiences modulations at a mechanical resonance frequency. The single mode gain for the excited mode becomes:

$$G_\mu(s=j\Omega_\mu)=-jk_\mu^LQ_\mu=k_\mu^LQ_\mu e^{\frac{-j\pi}{2}}. \tag{2.59}$$

The mode then produces an increased contribution to the detuning proportional to the mode quality factor (which can scale to 10-100s). Additionally, a 90° phase lag is acquired, which can add control difficulties for systems with feedback (see the complex component of Eq. (2.59)).

The Lorentz transfer function can be measured in strongly coupled cavities by modulating the forward power and measuring the deviations in detuning $\delta\omega$ and field δV. From these measurements, the mechanical and electromechanical properties can be calculated: Ω_μ, Q_μ, and k_μ^L. A measurement we have taken of the Lorentz transfer function amplitude for an HB650 cavity for PIP-II can be seen in Fig. 2.10.

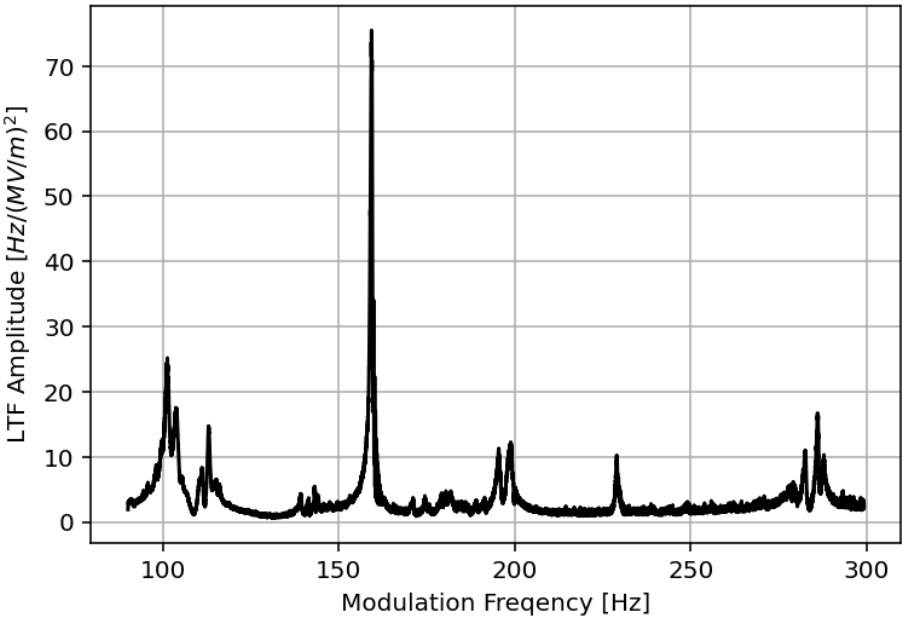


Figure 2.10 Lorentz transfer function amplitude v. forward power modulation frequency for the HB650 cavity. Electromechanical data can be extracted for 9 modes.

2.4 Ponderomotive Instabilities

In the previous section we discussed the Lorentz force detuning effect and some of the basic physical phenomena that arise in its presence. In this section we will instead focus on the possible instabilities these effects can produce. This section will deal with the open-loop cases, i.e no feedback systems present. Specific feedback systems will be described in Chapter 3 and their effects on these instabilities in Chapter 4.

2.4.1 The Monotonic Instability

The first instability to be noted is the so-called monotonic or "jump" instability. This instability pertains to the static to quasi-static regime. As the resonance curve is tilted, a hysteresis region is created; different energy levels are made ($U \propto V_c^2$) for the same value of static detuning offset. To showcase this effect, we show a detailed version of the tilted resonance curve in Fig. 2.9.

As the system comes to rest somewhere within the hysteresis region, any small, quasi-static changes will cause the field to drop to the lower energy (lower voltage state). As the field drops, mechanical modes are excited, causing additional field decreases. This instability was first documented and mathematically described by Karliner, Shapiro, Petrov, and Shekhtman for

normal conducting cavities at Novosibirsk [61, 60]. Nonlinear analysis of the Duffing equation applied to the RF equations of motion to determine the exact locations of instability, which we denote with the red dashed line in Fig. 2.9 [71, 72].

Schulze would go on to detail this in 1971 for general resonators (both NC-RF and SRF), using an elastic potential model to explain this phenomenon. In that framework, the monotonic instability can be visualized as an elastic system falling from an unstable equilibrium (local maximum) point to a stable one in the elastic potential [62]. As this instability is a result of the tilted resonance curve, any operational point outside of the hysteresis region will be free of this instability.

2.4.2 The Oscillatory Instability

We now examine the instability arising from dynamic effects. In regions free of the monotonic instability, there is another instability that can occur. This instability is characterized by a growth in mechanical oscillations (and subsequent growth in detuning) of one of the cavity or structure resonances until saturation from external non-linear forces. This instability can also occur for both generator-driven or self-excited cavities. Once the static detuning threshold is passed for a given V_{acc}, the sign in Eq. (2.57) switches from negative to positive and the detuning and voltage crows. We outline a scheme of this instability as it starts and progresses at or beyond the instability threshold.

- Some modulation of V_{acc} occurs due to either mechanical or electrical noise, producing a modulation amplitude δV_{acc}.
- The voltage modulation applies a pressure at the modulation frequency Ω_{mod}. I f $\Omega_{mod} \approx \Omega_{\mu}$, the mechanical mode can be excited.
- Cavity mechanical mode excitation results in a frequency shift $\delta\omega_{\mu}$ in accordance with the Lorentz transfer function (Eqs. 2.56, 2.57), $\delta\omega_{\mu} \propto k_{\mu}Q_{\mu}$.
- There are a few possible paths to unstable behavior from here. If the cavity is being operated in open loop and the external modulation persists, the above steps can repeat until safety interlocks engage. If there are phase feedback systems present with insufficient gain, the

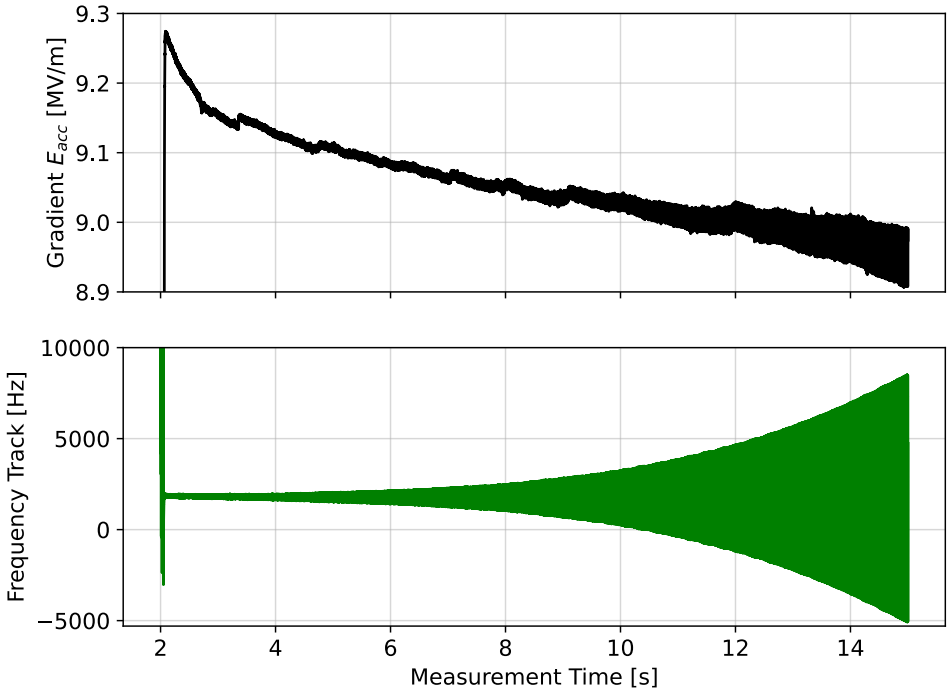


Figure 2.11 Cavity field E_{acc} (top) and frequency track (bottom) v. measurement time for a case of the oscillatory instability in a self-excited SSR2 cavity. Originally published in [70].

phase controller will send more power to the cavity to keep the phase setpoint without end. The above steps can repeat until the safety interlocks engage.

An example of the oscillatory instability that was encountered during high-power testing of a self-excited SSR2 cavity can be see in Fig. 2.11. There, we present the field and cavity frequency track with respect to the master clock in a case where the oscillatory instability was encountered. It can be seen that when the field passes the threshold (in this case E_{acc} = 9 MV/m), there is the characteristic growth in field and detuning. In this case, the detuning (deviations from the DC offset) grows to 13 kHz peak-to-peak.

2.4.3 Routh-Hurwitz Analysis

In this section we mathematically detail the criteria for ponderomotive stability for the generator-driven, open loop cavity. For simplicity, we will start with a cavity with a single mechanical resonance and then extrapolate to a many-mode system. We will make use of a linearized system,

and for that we will first need to modify the envelope equation, which we follow along from [73]. Let us start with an amplitude/phase formulation of $\tilde{V_c}$,

$$\tilde{V_c} = V_c(t)e^{j\phi(t)}, \tag{2.60}$$

from which we will apply small deviations:

$$\tilde{V_c} = (V_0 + \delta V)e^{j(\phi_0+\delta\phi)} \approx (V_0 + \delta V)(1 + j\delta\phi)e^{j\phi_0}. \tag{2.61}$$

Taking this expression and substituting it into Eq. (2.29) we can derive two equations based on the real and imaginary components:

$$\delta\dot{V} + \omega_{1/2}\delta V + V_0\Delta\omega_0\delta\phi = 0, \tag{2.62}$$

$$\dot{\delta\phi} + \omega_{1/2}\delta\phi - \frac{\Delta\omega_0}{V_0}\delta V - \delta\omega_\mu = 0, \tag{2.63}$$

where $\Delta\omega_0$ is the total static detuning offset.

If we transfer to the Laplace domain, we can deal with this problem in terms of a polynomial.

$$\delta V(s)(s + \omega_{1/2}) + V_0\Delta\omega_0\delta\phi(s) = 0, \tag{2.64}$$

$$\delta\phi(s)(s + \omega_{1/2}) - \frac{\Delta\omega_0}{V_0}\delta V(s) - \delta\omega_\mu = 0. \tag{2.65}$$

If we solve the voltage equation for $\delta\phi(s)$ and substitute into the phase equation, we can arrive at:

$$\left[(s + \omega_{1/2})^2 + \Delta\omega_0^2\right]\delta V(s) + V_0\Delta\omega_0\delta\omega_\mu(s) = 0. \tag{2.66}$$

If we examine Eq. (2.56), we can rewrite $\delta\omega_\mu(s)$ in terms of $\delta V(s)$, and thus we can simplify the expression down to the characteristic polynomial:

$$(s + \omega_{1/2})^2 + \Delta\omega_0^2 + 2V_0^2\Delta\omega_0 G_\mu(s) = 0. \tag{2.67}$$

The question of stability and defining the stable regions comes from the roots of Eq. (2.67). Cavity stability entails that all roots must have negative real components (i.e. all roots lie in the left-hand complex plane). The denominator of $G_\mu(s)$ goes as s^2 for every mechanical mode.

Therefore a single mode system will result in Eq. (2.67) being fourth order. As we have mentioned previously, the stable regions in the static case ($s = 0$) can be found through nonlinear analysis.

However, the static term in Eq. (2.67) can also yield important information. Since the coefficients of Eq. (2.67) will all be real, there is condition for guaranteed instability. If the static coefficient is less than zero, then Eq. (2.67) is guaranteed to have at least one positive, real root. The regions where this occurs are the nonlinear-dominated region described by Schulze [62]. For a single mode system, this region is described by:

$$\Delta\omega_0^2 + \omega_{1/2}^2 - 2k_\mu^L V_0^2 \Delta\omega_0 = 0. \tag{2.68}$$

There is a special case where there is only one unstable working point. When the square-root term is zero, there is a duplicate root. We can calculate what we call this critical voltage V_{crit} at which this duplicate root occurs,

$$V_{crit} = \sqrt{\frac{\omega_{1/2}}{k_\mu^L}}. \tag{2.69}$$

If $V_0 \geq V_{crit}$, there are regions where this static term can be less than zero, leading to instabilities.

For $s \neq 0$, the stability analysis becomes more complicated. We can default to the Routh-Hurwitz stability criterion to check for roots in the right-half plane. The Routh-Hurwitz stability scheme goes as follows.

- All coefficients of the characteristic polynomial **must have** the same sign as the highest order coefficient (for the single mode case, this means all coefficients must be the same sign as a_4).
- All the minor determinants of the Routh table must be greater than zero as well.

In the case of item two, the minor determinants can be determined analytically. For a fourth order polynomial of the form $a_4 s^4 + a_3 s^3 + a_2 s^2 + a_1 s + a_0$, the two relevant minor determinant conditions are:

$$a_2 a_1 - a_3 a_0 > 0 \tag{2.70}$$

$$a_3 a_2 a_1 - a_4 a_1^2 - a_3^2 a_0 > 0 \tag{2.71}$$

In the case of Eq. (2.67), we can distribute the denominator of $G_\mu(s)$ and calculate the coefficients of the polynomial.

$$a_4 = 1 \tag{2.72}$$

$$a_3 = \frac{2}{\tau_\mu} + 2\omega_{1/2} \tag{2.73}$$

$$a_2 = \Omega_\mu^2 + \omega_{1/2}^2 + \Delta\omega_0^2 + \frac{4\omega_{1/2}}{\tau_\mu} \tag{2.74}$$

$$a_1 = 2\omega_{1/2}\Omega_\mu^2 + \frac{2}{\tau_\mu}\left(\omega_{1/2}^2 + \Delta\omega_0^2\right) \tag{2.75}$$

$$a_0 = \Omega_\mu^2(\Delta\omega_0^2 + \omega_{1/2}^2 - 2\Delta\omega_0 k_\mu^L V_0^2) \tag{2.76}$$

It is clear that $a_4,\ a_3,\ a_2,\ a_1$ are all greater than zero for any detuning value, and we have covered the cases for where $a_0 < 0$. Thus we know the conditions for which item 1 is satisfied. We must look to the minor determinants to determine the stability.

This can be handled numerically for cavities with measured LTF and known mechanical parameters. In fact, this is the only reasonable path forward for real cavities which have many modes where every additional mode raises the order of the polynomial by 2. This can be handled instead by moving to a state-space representation. Alternatively, this can be done in the Laplace domain through a series of substitutions as shown by [73] (though both methods produce the same results). We can develop a scheme to numerically find the stability of many-mode systems this way, however. For a many-mode cavity with N known modes, then the state-vector can be represented by:

$$\mathbf{x} = [\delta V, \delta\phi, \delta\omega_1, \delta\dot{\omega}_1, ..., \delta\omega_N, \delta\dot{\omega}_N]^T. \tag{2.77}$$

Then the whole dynamics of the cavity's internal state can be represented by a state equation:

$$\dot{\mathbf{x}} = A\mathbf{x} + B\mathbf{u}, \tag{2.78}$$

where A and B are the state and input matrices respectively. From the amplitude, phase, and general

detuning equations, we can form the state matrix A:

$$A = \begin{bmatrix} A_{V/\phi} & S & S & \cdots & S \\ C_1 & G_1 & 0 & \cdots & 0 \\ C_2 & 0 & G_2 & \cdots & \vdots \\ \vdots & \vdots & \vdots & \ddots & \vdots \\ C_N & 0 & 0 & \cdots & G_N \end{bmatrix}, \tag{2.79}$$

where $A_{V/\phi}$ is the matrix for the amplitude phase equations:

$$A_{V/\phi} = \begin{bmatrix} -\omega_{1/2} & -\Delta\omega_o V_0 \\ \Delta\omega_0 & -\omega_{1/2} \end{bmatrix}, \tag{2.80}$$

$\tilde{S}$ is a periodic space filling matrix:

$$S = \begin{bmatrix} 0 & 0 \\ 1 & 0 \end{bmatrix}, \tag{2.81}$$

C_μ is coupling matrix which connects changes in voltages to detuning by any mode,

$$C_\mu = \begin{bmatrix} 0 & 0 \\ -2k_\mu^L \Omega_\mu^2 V_0 & 0 \end{bmatrix}, \tag{2.82}$$

and G_M is the mechanical mode parameter matrix,

$$G_M = \begin{bmatrix} 1 & 0 \\ -\Omega_\mu^2 & -\frac{2}{\tau_\mu} \end{bmatrix}. \tag{2.83}$$

As long as the LTF is defined to a specified number of modes, the coefficients of the characteristic polynomial can be found via the eigenvalues of A,

$$|A - s\mathbb{I}| = 0. \tag{2.84}$$

From this expression, the polynomial coefficients can be calculated via the Faddeev-Leverrier method numerically. The Routh table can then be formulated and the minor determinants calculated, which can implemented in different coding languages. We demonstrate this analysis for the PIP-II

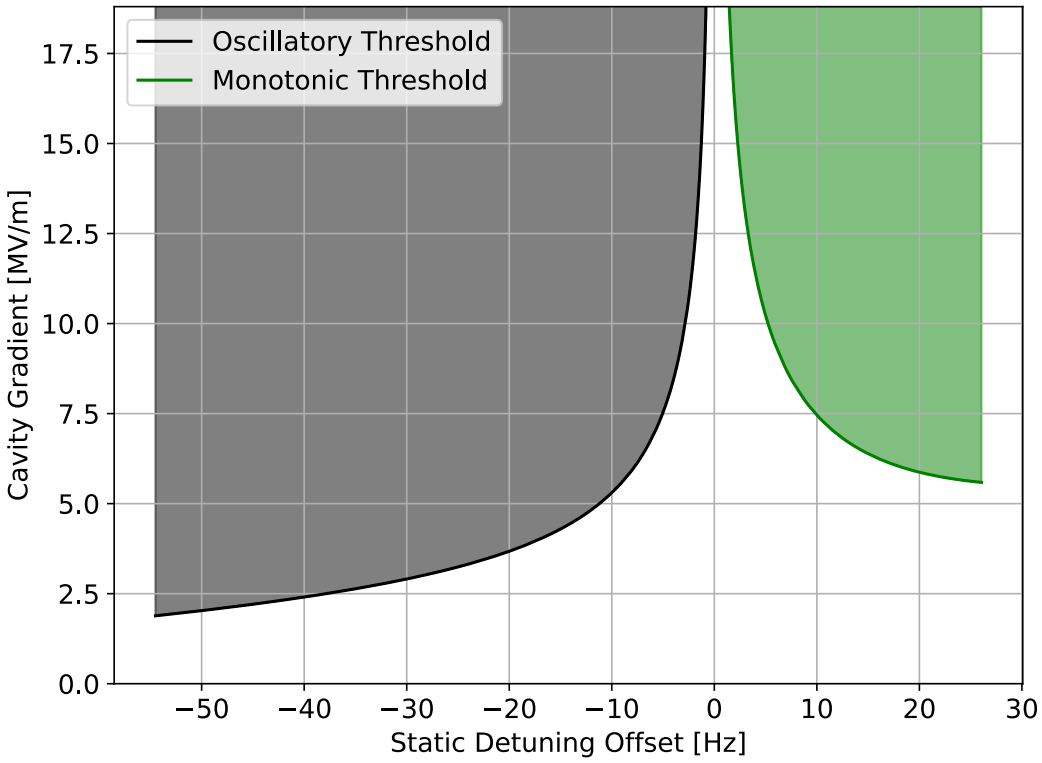


Figure 2.12 Instability threshold voltages v. static detuning offset for the HB650 cavity using mechanical parameters extracted from the Lorentz transfer function. The solid lines represent the respective instability thresholds and the shaded regions represent unstable working points.

HB650 cavity using our mechanical parameters extracted from Fig. 2.10 by presenting the regions of instability in Fig. 2.12.

As can be seen, both the oscillatory and monotonic instability thresholds can be quite close to $\Delta\omega_0 = 0$ for higher fields. Even ignoring rises in power costs, running a generator driven cavity in open loop is not feasible due to the close proximity of instability for any realistic accelerating field. Combined with the presence of microphonics, we must employ feedback mechanisms for stable operation.

2.4.4 Previous Work

Ponderomotive instabilities have been a long-standing phenomena of RF cavities systems for decades. The first cases of the monotonic instability was noted in normal conducting copper cavities at Novosibirsk. Karliner, Shapiro, Petrov, and Shekhtman were the first to mathematically derive the stability conditions under the assumption that $\Omega_\mu \tau \ll 1$[60, 61].

As we move to the superconducting regime and loaded quality factors of $10^6 - 10^7$, this condition no longer holds as τ increases significantly compared to the normal conducting cases. Schulze was the first to treat this topic in a superconducting setting, using the transfer function approach to stability (both Routh-Hurwitz and Nyquist criterion) for general $\Omega_\mu \tau$[62]:

$$\frac{2\Delta\omega_0}{\tau(\omega_{1/2}^2 + \Delta\omega_0^2)} \frac{k_\mu^L \tau_\mu \Omega_\mu^2 V_0^2}{(\omega_{1/2}^2 + \Omega_\mu^2 - \Delta\omega_0^2)^2 - \Delta\omega_0^2} < 1 \tag{2.85}$$

Additionally, he proposed the stability criterion for a superconducting resonator under proportional feedback systems for cavity amplitude, phase, and frequency. For amplitude and phase proportional control his result are as follows:

$$\frac{k_\mu^L \tau_\mu \Delta\omega_0 V_0^2 \Omega_\mu^2 \tau^3}{K_A K_\phi} \left(\frac{1}{K_A} + \frac{1}{K_\phi} \right) < 1 \tag{2.86}$$

where, $K_{A/\phi}$ are the amplitude and phase control loop gains respectively.

Delayen would carry out similar analysis for superconducting cavities operating in a self-excited loop (SEL) configuration. His analysis showed that cavities operating in an open, self-excited loop are free of any ponderomotive instability. This is due to the frequency-following nature of self-excited loop operation. Locking the phase of an SEL operated cavity will cause the appearance of ponderomotive instabilities. Delayen would provide criteria for single mechanical mode systems in open-loop, and proportional feedback systems [74, 69].

Since these primary works, there have been a few studies pertaining to this topic for different aspects. Work has been done to extrapolate Schulze's work for generator driven systems to include more advanced, linear low-level RF controllers with multiple loops (such as the commonly used proportional-integral or PI controller) as well for vector-sum control for klystron driven cavity strings with multiple cavities [75, 76, 77, 78, 79, 80, 81, 82, 83]. Yet there remain few experimental studies about the onset of ponderomotive instability to confirm these studies. More recently IMP has done a study showcasing the onset of ponderomotive instability in strongly over-coupled coaxial resonators ($Q_l \sim 10^5,\ 10^6$), showing good agreement between their analysis and experimental onset of the oscillatory instability in the presence of linear feedback [73].

In 2025, we presented initial findings on instabilities in the FRIB $\beta = 0.53$ HWRs, in which we presented preliminary results of this work [84]. FRIB utilizes nonlinear feedback systems, and in this work we noted some deviations in the behavior of our measurements when looking to theory on proportional feedback systems. This work finds its home in determining the cause of these deviations by examining the effects nonlinear feedback systems have on these instabilities. This leads to a focus on the changes in instability threshold at different controller gains rather than cavity amplitude. In particular we examine how these feedback systems change the way deviations in the cavity phase can lead to deviations in the cavity amplitude through simulated and analytical models.

Additionally, we have noted that there is a difference in the instability thresholds at different cryogenic temperatures. In particular, we note that the instability thresholds at 4.3 K are substantially higher than those measured at 2 K. This work explores different avenues through which this is possible through simulations and analysis using measured quantities. Finally, we explore how resonance control can not only help suppress ponderomotive instabilities but also prevent ballooning RF costs using nonlinear feedback controllers.

CHAPTER 3

FEEDBACK AND CONTROLLERS FOR SRF CAVITIES

Successfully accelerating charged particles depends on one thing: maintaining accelerator synchronicity. That is, particles arrive at the right accelerator elements at the right times. On the RF cavity side, this means maintaining the cavity field amplitudes and RF phase at the specified set points. As we noted in Chapter 2, SRF cavities are constantly exposed to both internal and external disturbances that affect both of those values. For practical operation of SRF cavities, cavity amplitude and phase must be controlled (either directly or indirectly) to acceptable deviations. We also noted in Chapter 2, that these disturbances will increase the power required to operate the cavity via detuning. Control over the cavity frequency is therefore important for keeping low RF power costs. In this chapter, we will discuss feedback basics, common implementations of feedback, and their effects on the presence of ponderomotive instabilities.

3.1 SRF Cavity Process Variables

In essence, the RF accelerator is one of the world's most expansive and intricate clocks. Accelerating charged particles from low energies through lattices of focusing magnets and accelerating elements requires that particle bunches arrive at the proper places at the proper times. Naively, one might guess that the pursuit of high energies would result in operating every cavity at its highest field. In reality, successful acceleration of the beam through the entire machine involves ensuring that the gain of energy through one particular cavity **does not** interfere with the acceleration at the next cavity. Additionally, particles can be delayed (or advanced) relative to the RF phase in order to maintain particle longitudinal bunching.

For this to work, the amplitude and phase of every cavity must be tightly controlled to their respective setpoints to avoid disturbing the accelerator timing scheme. Additionally, this means that cavities driven by an external generator must be supplied with a fixed frequency with respect to the accelerator master clock (self-excited cavities use the cavity frequency as reference, but the use of self-excited cavities requires additional control measures and thus we will focus on the generator-driven cavity). From a dynamic systems view, the cavity is a 3-input, 3-output process,

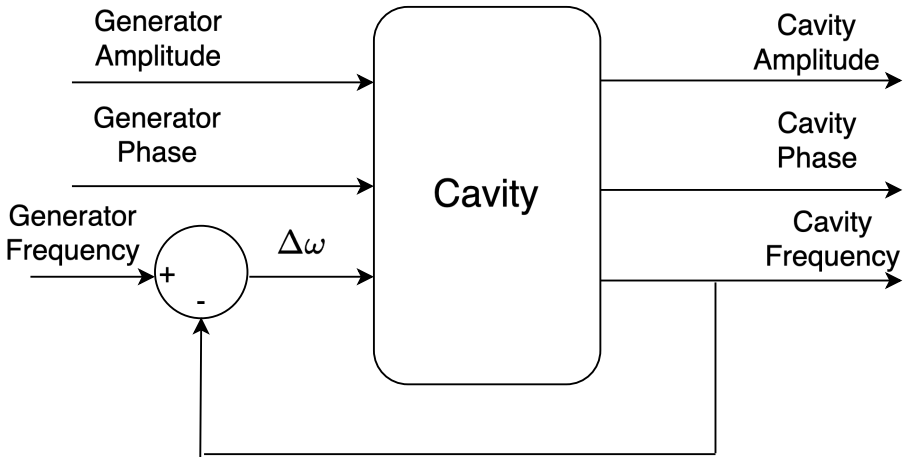


Figure 3.1 Schematic of a cavity dynamic system. The generator provides a drive amplitude, phase, and frequency. The envelope equation, Lorentz force, and disturbances result in the cavity amplitude, phase, and frequency which might differ from the generator.

with an example shown in Fig. 3.1. Cavity detuning will affect the amplitude and phase directly (recall Eq. (2.29)). With detuning being a certainty, control systems must be employed: one for each process variable.

In this section, we will briefly (and qualitatively) introduce the process variables and the digital/physical means through which the variables are controlled or produced. Looking ahead at the rest of the chapter, we will examine how control systems manifest mathematically: we will start with a general treatment that applies to each of the variables independently and then we will tie them all back together to view how some control loops interplay with each other. Finally, we will introduce relevant control algorithms for this work.

3.1.1 Amplitude and Phase

Consider the cavity voltage phasor in the complex plane, as seen in Fig. 3.2. Any phasor quantity can be described with two quantities: the amplitude or 'length' of the phasor, and the phase or angular displacement from the real axis:

$$\tilde{V}_c = Ve^{j\phi}. \tag{3.1}$$

When the cavity is tuned to the generator frequency in steady state, the generator and cavity phasors perfectly overlap. Whenever the frequency of the cavity is changed, the cavity phasor undergoes

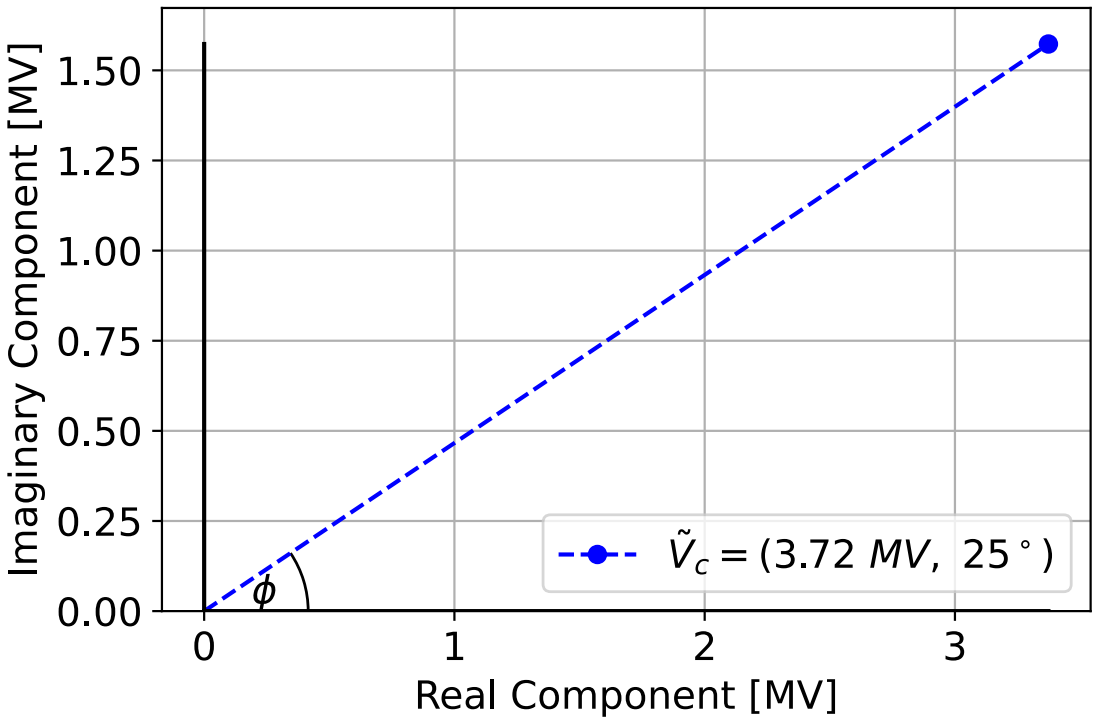


Figure 3.2 Graphical representation of the cavity voltage phasor for a $\beta = 0.53$ HWR operating at $E_{acc} = 7.4$ MV/m and a $\phi = 25°$ offset.

changes in amplitude and phase. In this situation, we need to adjust the generator phasor to bring the cavity phasor back to the desired setpoints. This requires more power to be sent from the generator to the cavity, with the power required increasing as the cavity frequency drifts further from the generator.

Corrections to the amplitude and phase are also done in polar coordinates: the length of the phasor and the angle with respect to the real axis are adjusted. This allows for some independence between the two variables in theory: adjusting the length of the phasor will not change the angle and shifting the angle will not change the length of the phasor. In practice, only the former holds. The qualitative reasoning is that a changing phase is equivalent to a changing frequency, thus leading to a changing amplitude. We will describe this effect mathematically later.

3.1.2 In-Phase and Quadrature Representation

Just as we can represent a phasor quantity with its polar coordinates (amplitude and phase), phasors can be described with Cartesian coordinates. Historically, the real component of the

phasor is referred to as the in-phase (I) component and the imaginary component as the quadrature (Q) component. These two different notations relate to each other in the usual polar-to-cartesian transforms:

$$\tilde{V} = Ve^{j\phi} = I + jQ, \tag{3.2}$$

$$I = V\cos\phi, \tag{3.3}$$

$$Q = V\sin\phi. \tag{3.4}$$

This presents another route to stabilize the amplitude and phase of the cavity: controlling the values of I/Q rather than A/ϕ. In some ways, this can be advantageous when adjustments need to be made.

Adjustments to the drive RF are handled before amplification at the low-level (hence the term low-level RF or LLRF). It is common for modern machines to handle adjustments digitally: RF from the cavity is sampled and digitized by an analog-to-digital converter (ADC). The sampled data is then digitally mixed and demodulated into the I/Q components. The controller is encoded in firmware on a field-programmable gate array (FPGA) which allows for low loop latency. If the control is configured for I/Q control, the demodulated data can then be used to adjust the drive directly. If the controller is configured for A/ϕ control, the I/Q components must be converted to polar coordinates. Arctangent is computationally expensive in firmware code, and the CORDIC algorithm is a common choice to avoid arctangent calculations. Once the A/ϕ corrections are applied, the CORDIC algorithm is used again to convert back to I/Q.

The reason to convert back to I/Q components is for low power RF generation. By using a four point, alternating sequence of I/Q voltages held over a quarter of the desired RF period, a voltage with the desired amplitude and phase can be created if the sequence is repeated [85]. We present the four-point scheme for digital RF generation in Fig. 3.3. For analog only systems, there is a practical limit on the frequencies that can be generated as the voltages need to switch 4× faster than the desired RF period. Thus high-frequency signal generation required up-conversion of the intermediate frequency. Modern DACs have fast enough clocks that even the direct generation of

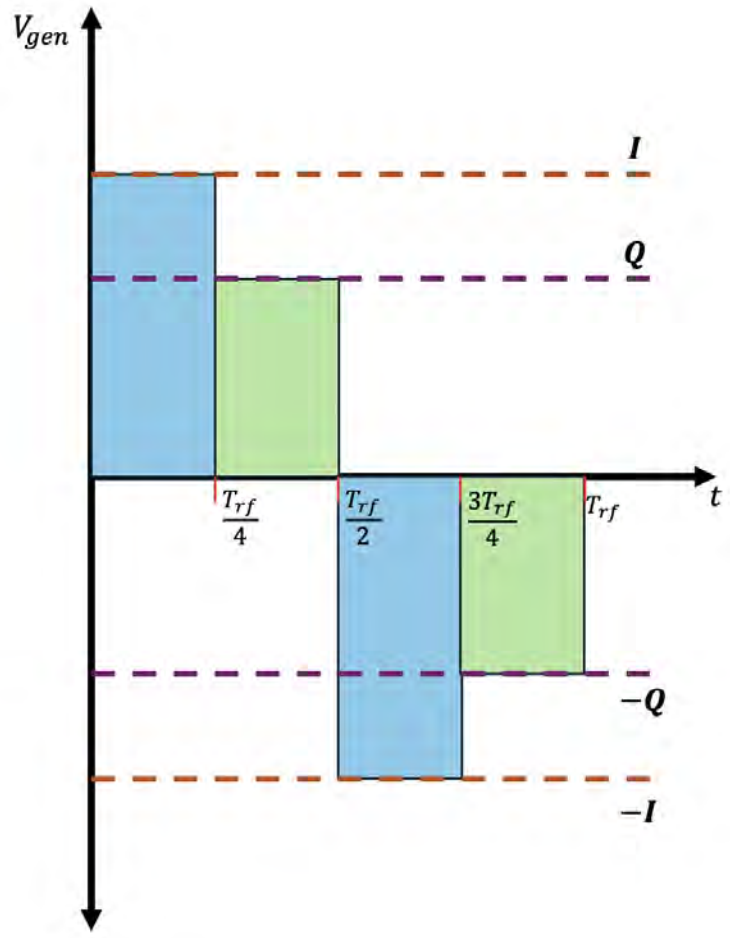


Figure 3.3 Four point RF generation scheme for the generation of low-level RF carrier voltages. Produces a single period T_{rf} waveform with the amplitude and phase specified by I and Q.

1.3 GHz signals as required for the TESLA-style cavities is possible. There has been in been an increase in available FPGAs capable controlling RF signals; providing high-speed ADCs for RF sampling, programmable logic for feedback algorithms, and high-speed DACs for generation of the corrected signals.

Thus each set of variables, A/ϕ and I/Q, presents its own unique advantages and drawbacks. In A/ϕ control, the feedback corrections must be calculated then transformed to adjustments in I/Q via the CORDIC algorithm. Amplitude and phase control allows for the more precise control of these process variables, but requires additional computational steps. By controlling I/Q the generator output can be changed directly. In this regard, I/Q feedback systems can offer lower loop latency by dropping this calculation. I/Q control is also superior for low fields, where the phase

calculation becomes more sensitive to noise for low values of I/Q.

3.1.3 Frequency

While A/ϕ and I/Q control can stabilize the cavity field and phase in the presence of detuning, the controllers themselves do not do anything to counter detuning itself. Instead, the controllers throw more power into the cavity in order to maintain synchronicity. In Chapter 2, we showed how detuning can rapidly increase the RF power draw from the generator. For an accelerator with many cavities, detuning can quickly balloon the operational costs for both pulsed and CW machines. This is one advantage of operating SRF cavities at 2 K; superfluid helium carries heat away by thermal counter-flow rather than nucleate boiling at the cavity walls, reducing the microphonic background significantly. Of course, operating at 2 K requires more wall power to maintain the environment than at 4.3 K. Thus there is a balance to be struck for power costs: providing high-Q_0 cavities with tight resonance/frequency control.

In the goal to reduce power costs and the risks of detuning-induced interlock trips, mechanical tuners are used to bring the cavity back to the generator frequency. The idea behind mechanical tuners are straightforward: the frequency determining regions of the cavity are deformed in a controlled manner in order to counteract the effects of microphonics and slow drifts due to changes in bath pressure, thermalization, etc. In this section we will discuss two different types of tuners and their operation.

For coaxial half-wave resonators (HWRs), pneumatic tuners are a popular choice. They have seen deployment in heavy-ion linacs such as FRIB, ATLAS, and RAON, and will be the tuning mechanism for the HWRs in the PIP-II linac [86, 87, 88, 89]. A picture of the FRIB-style pneumatic tuner equipped to a $\beta = 0.53$ HWR can be seen in Fig. 3.4. As their name suggests, helium gas is used to inflate/deflate a bellows system which causes deformations of the cavity from the tuner arms. A control scheme (separate from the amplitude and phase controllers) is used to control the valve for the helium flow and therefore control the deformations.

There are some caveats to this style of tuner relevant to this study. The valve opening/closing speed is set, and is relatively slow. The result is that this style of tuner cannot be used for fast

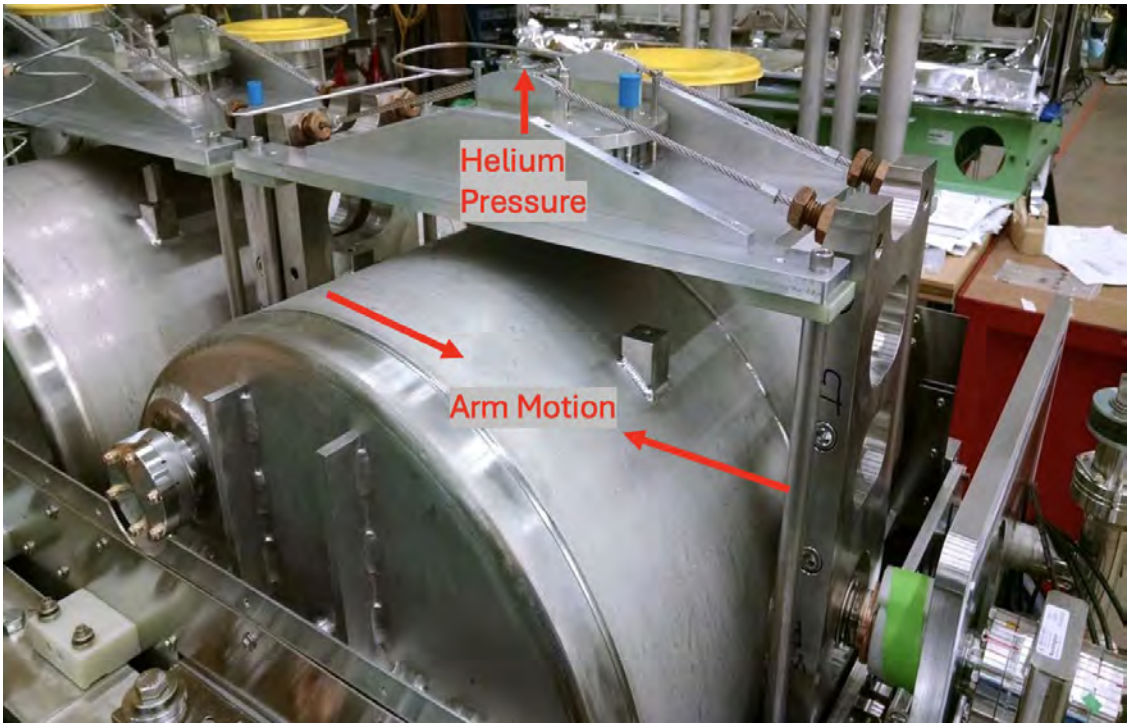


Figure 3.4 Picture of FRIB style pneumatic tuner equipped to 322 MHz, $\beta = 0.53$ HWR assembled on the cryomodule cavity string. Labeled are the relevant tuning motion/forces.

tuning of the cavity frequency. The pneumatic tuner is excellent for countering the slow drift in cavity frequency that will occur with 2 K operation, but cannot exceed 1 Hz resolution. For the pneumatic tuners at FRIB, no titanium bellows are used in the tuning region. Thus these tuners do not provide additional stiffness to the cavity and therefore do not reduce the static Lorentz force detuning effect.

Another form of mechanical tuner of interest for this study is the double lever-arm, piezoelectric tuner. This technology is mature, seeing key testing and verification for the LCLS-II high energy upgrade [90], the FRIB energy upgrade cavity [39], and PIP-II cavities (excluding the aforementioned HWRs) [91, 92, 93]. There are other forms of piezoelectric tuners such as the SACLAY [94] and blade tuners [95] as well, but these tuners are not the focus of this work.

An example of the double lever arm tuner equipped to a jacketed HB650 elliptical cavity on our resonance control test bench can be seen in Fig. 3.5. There are two main components to this tuner: a stepper motor to be used for coarse/slow tuning like the pneumatic tuner and two piezoelectric

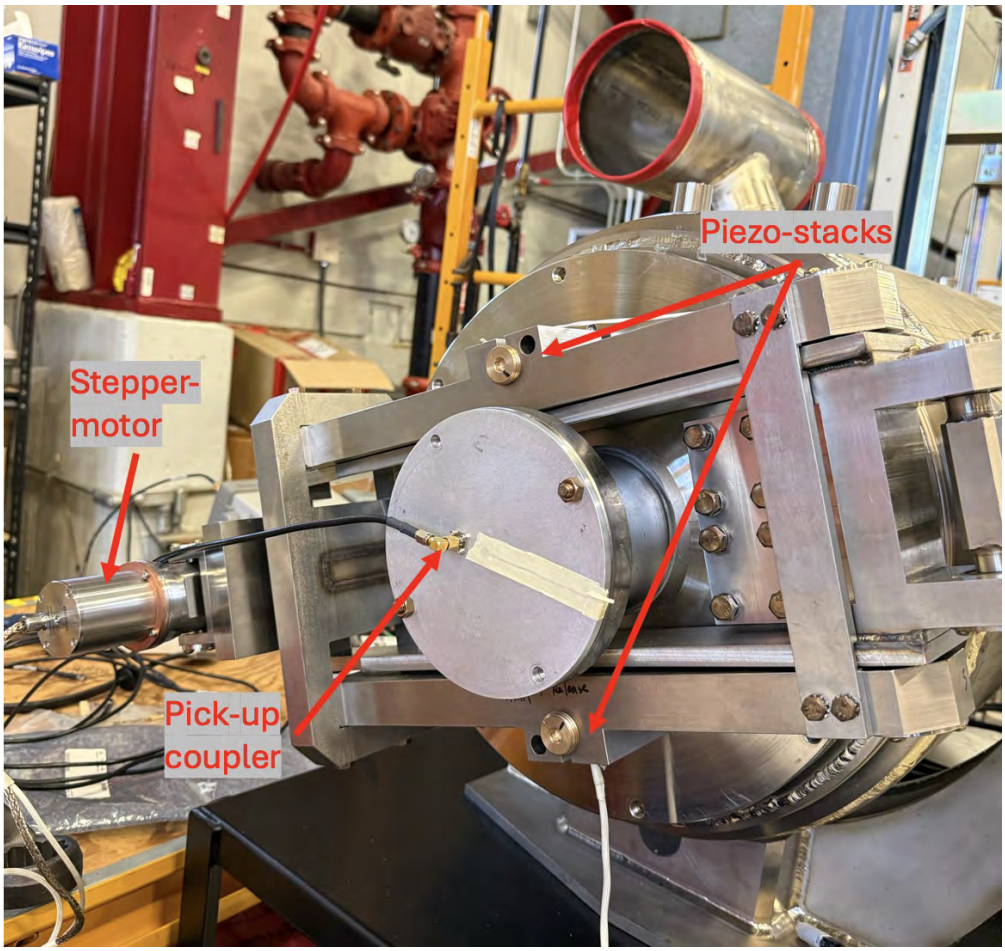


Figure 3.5 Picture of a jacketed HB650 cavity equipped with a double-lever arm, piezoelectric tuner at our room temperature test bed.

stacks with the ability to provide fast tuning to the cavity. The piezoelectric stacks are made of ferroelectric material fabricated for fast capacitance shifting [96] and thus quick deformation strokes. Additionally, the tuner structure provides additional stiffness to the cavity structure and reduces the static LFD effect. For example, the tuner will add an additional 40 kN/mm stiffness to a jacketed FRIB energy upgrade cavity or LB650 cavity which results in a $\sim$ 75% drop in simulated k_L [39].

For CW operation, the coarse/slow tuner can be be used during ramping of the field to counteract the static LFD effect. The piezo can then be used for the minimization of fast microphonic noise. The voltage applied to the piezo-stacks is regulated via a controller to keep the detuning as close to zero as possible. The piezo acts as a capacitor, and as such requires time to charge before the

deformation is delivered to the cavity. This combined with the controller loop-rate serve as limiters for the frequency range that can be controlled by the piezo-stacks.

For pulsed operation, the coarse tuner is not fast enough to deal with the repeated blows of the RF pulses. In fact, not even the piezo control loop is also not fast enough to compensate for the Lorentz force detuning before the onset of the monotonic instability. In this case, feed-forward control is used to compensate the pulse detuning [97, 98]. All PIP-II cavity types besides the HWRs and the FRIB energy upgrade elliptical cavity will utilize this style of piezoelectric tuner to provide microphonics and possibly pulse compensation in the case of PIP-II.

3.2 Control Loop Configurations

In this section, we will discuss the two main loop configurations when it comes to control: open and closed loop. For these two cases we will focus predominantly on the amplitude and phase (or analogous I/Q) control in this chapter. The effects of controllers will be critical in the next chapter, hence the focus in this one. Chapter 5 will focus predominantly on resonance/frequency control and examining its effect on the cavity.

3.2.1 The Open-loop Cavity

When the cavity is in the absence of control loops, the configuration is referred to as open-loop. That is, there are no closed control loops for any process variables. For the SRF cavity, this means power from the generator is set and does not change. An example diagram of the open-loop cavity for all three process variables we have shown in Fig. 3.1 We have discussed already some details about the open loop cavity and its stability. In this case, we can still discuss how the amplitude and phase variables can interplay with each other. Consider again the equation Eq. (2.64): by solving for the ratio of δV and $\delta\phi$, we can quantify how changes to the phase will adjust the amplitude;

$$\frac{\delta V}{\delta \phi} = \frac{-\Delta\omega_0 V_0}{s + \omega_{1/2}}. \tag{3.5}$$

There are a few details that we can pull from this expression. We can see that the channel between the two variables is low-pass filtered, with the cutoff frequency being the cavity bandwidth $\omega_{1/2}$. Additionally, when the cavity is tuned to the generator, the two variables are completely independent

of each other. They become coupled as we detune the cavity, with the coupling between amplitude and phase increasing as the detuning increases. We can derive a similar expression in terms of I and Q. We can start from the envelope equations for deviations in I and Q components (assuming the cavity starts in-phase with the generator) and separate the detuning into the static and dynamic pieces in open-loop:

$$\dot{\delta I} + \omega_{1/2}\delta I + \Delta\omega_0\delta Q = 0, \tag{3.6}$$

$$\dot{\delta Q} + \omega_{1/2}\delta Q - \Delta\omega_0\delta I - V_0\delta\omega = 0. \tag{3.7}$$

Taking the Laplace transform of Eq. (3.6) and solving for how changes in Q can change I, we find that,

$$\frac{\delta I}{\delta Q} = \frac{-\Delta\omega_0}{s + \omega_{1/2}}. \tag{3.8}$$

Because both I and Q are already voltages, the steady state voltage V_0 is not needed to translate between the two variables. In this case, we can see that Eq. (3.5) and Eq. (3.8) are identical in their functions. That is, the process variables of the open-loop cavity experience the same coupling whether the user is considering A/ϕ or I/Q process variables. This might seem self-explanatory as the difference between the two pairs of variables is just a matter of using cartesian or polar coordinates. However, differences will start to appear when we add control systems to the cavity.

3.2.2 The Closed-loop Cavity

For as long as humans have had dynamic systems, control systems have been utilized ensure that the desired output/performance is achieved. Control theory as we know it saw particular foundations established at the turn of the industrial revolution in the 18th and 19th century, with the first stability analysis carried out by Maxwell [99, 100]. The SRF cavity is no different, we must use control systems to maintain the relevant setpoints. However, we showed in the previous sections that the process variables can talk to each other, which will add additional complications.

In general, a new dynamic process is added to the overall system: the controller. It is common to work in the Laplace domain to examine the characteristic response frequencies of the system. A schematic of a cavity with closed amplitude and phase control loops can be seen in Fig. 3.6. The

difference between the cavity amplitude and phase and their respective setpoints is referred to as the error. In our cavity system, the errors can be thought of as the deviations in the amplitude and phase δV and $\delta\phi$:

$$\delta V(s) = V_g(s) - V_c(s), \tag{3.9}$$

$$\delta\phi(s) = \phi_g(s) - \phi_c(s). \tag{3.10}$$

The controller uses these errors to provide a corrected input amplitude and phase to be sent to the cavity. In the Laplace domain, this correction manifests as the product of the controller transfer function and the error:

$$V_g(s) = G_A(s)\delta V(s), \tag{3.11}$$

$$\phi_g(s) = G_\phi(s)\delta\phi(s). \tag{3.12}$$

The controllers $G_{A/\phi}$ are functions of parameters called gains, which serve to alter the response of the controllers to the desired performance. A product in the Laplace domain corresponds to convolution in the time domain. In this regard, we can shift from a static drive $\tilde{V}_{g0}$ to a dynamic one: adjustments to the amplitude and phase are made using the controller [73]:

$$\tilde{V}_g(t) = (V_{g0} - G_A * \delta V(t))e^{j(\psi_0 - G_\phi * \delta\phi(t))}, \tag{3.13}$$

where $*$ is the convolution operator, V_{g0} is the amplitude setpoint, and ψ_0 is the static detuning angle which relates to the static detuning offset as:

$$\psi_0 = \arctan\left(\frac{\Delta\omega_0}{\omega_{1/2}}\right). \tag{3.14}$$

Plugging Eq. (3.13) into the RHS of Eq. (2.29), we can start to make some observations. In steady state conditions, we can relate the cavity voltage to the drive again:

$$(\omega_{1/2} - j\Delta\omega_0)V_0 = \omega_{1/2}V_{g0}e^{j\psi_0}. \tag{3.15}$$

Returning to the dynamic front, we can express Eq. (3.1) in terms of deviations of the cavity amplitude and phase:

$$\tilde{V}_c = (V_0 + \delta V)e^{j\delta\phi} \approx (V_0 + \delta V)(1 + j\delta\phi) \approx V_0 + \delta V + jV_0\delta V. \tag{3.16}$$

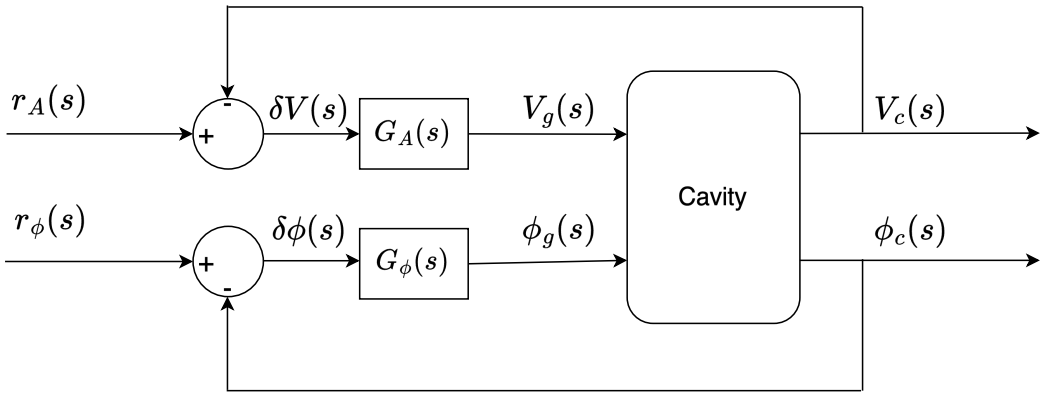


Figure 3.6 Diagram of a cavity with closed amplitude and phase control loops. $r_{A/\phi}$ represents the setpoints of cavity amplitude and phase respectively. $G_A(s)$ and $G_\phi(s)$ are the amplitude and phase controllers respectively as well.

We can also expand Eq. (3.13) using small angle expansions and Eq. (3.15):

$$\tilde{V}_g = (V_{g0} - G_A * \delta V)e^{j\psi_0}(1 - j(G_\phi * \delta\phi)) \tag{3.17}$$

$$= V_{g0}e^{j\psi_0} - e^{j\psi_0}(G_A * \delta V) - j(G_\phi * \delta\phi) \tag{3.18}$$

$$= (\omega_{1/2} - j\Delta\omega_0)V_0 - e^{j\psi_0}(G_A * \delta V) - j(\omega_{1/2} - j\Delta\omega_0)(G_\phi * \delta\phi). \tag{3.19}$$

We can plug both Eq. (3.16) and Eq. (3.19) into Eq. (2.29). Separating the resulting equation into the real and imaginary components, we obtain two equations:

$$\delta\dot{V} + \omega_{1/2}\delta V + V_0\Delta\omega_0\delta\phi = -\omega_{1/2}\cos\psi_0(G_A * \delta V) - \Delta\omega_0 V_0(G_\phi * \delta\phi), \tag{3.20}$$

$$\dot{\delta\phi} + \omega_{1/2}\delta\phi - \frac{\Delta\omega_0}{V_0}\delta V = -\omega_{1/2}\sin\psi_0(G_A * \delta V) - \omega_{1/2}(G_\phi * \delta\phi). \tag{3.21}$$

Analogous to the open-loop cavity, we can take the Laplace transform of Eq. (3.20), and solve for how deviations in phase will affect the amplitude:

$$\frac{\delta V}{\delta\phi} = \frac{-\Delta\omega_0 V_0(1 + G_\phi(s))}{s + \omega_{1/2}(1 + \cos\psi_0 \cot G_A(s))}. \tag{3.22}$$

We can make some remarks about this result. Just as in Eq. (3.5), the amplitude and phase are decoupled when the cavity is tuned to the generator. The variables again become coupled when $\Delta\omega_0 \neq 0$, except now the phase controller $G_\phi(s)$ can provide some amplification to this coupling. Conversely, the amplitude controller $G_A(s)$ can help damp this coupling, though the damping efficiency decreases as ψ_0 increases.

By taking the Laplace transforms of Eq. (3.20), Eq. (3.21), and using Eq. (2.57) we can remove δV and $\delta\phi$ and obtain a polynomial condition [73]:

$$\begin{aligned}[s + \omega_{1/2}(1 + \cos\psi_0 \cdot G_A(s))][s + \omega_{1/2}(1 + G_\phi(s))] \\ +\Delta\omega_0(1 + G_\phi(s))[\omega_{1/2}\sin\psi_0 \cdot G_A(s) + \Delta\omega_0] \\ +2V_0^2\Delta\omega_0(1 + G_\phi(s))\sum_\mu G_\mu(s) = 0.\end{aligned} \tag{3.23}$$

This is the characteristic polynomial for a cavity with amplitude and phase feedback control without any frequency/resonance control. Just as is the case with Eq. (2.67), the roots of this polynomial relate to the dynamic response of the cavity and feedback combined system. The imaginary components represent the characteristic response frequencies of the system to stimuli, and the real components of the roots correspond to the growth or damping of those frequencies. Thus to ensure that the cavity plus feedback system is stable, all of the roots should have negative real components (that is all the responses correspond to damping). Otherwise, we will experience exponential growth of the cavity field and/or phase i.e. unstable behavior. In this case, the roots of Eq. (3.23) can be found numerically with as many mechanical modes that are needed/wanted. Routh-Hurwitz can of course be used, but this can become computationally complex depending on the choice of controller.

We can derive similar equations in I/Q representation. If we assume that the cavity initially starts in-phase with the generator, then cavity and generator phasors can be represented by:

$$\tilde{V}_c = (V_0 + \delta I + j\delta Q), \tag{3.24}$$

$$\tilde{V}_g = (V_{g0} - (G_I * \delta I) - j(G_Q * \delta Q)), \tag{3.25}$$

where G_I and G_Q are the I and Q controllers respectively. Substituting these two expressions into Eq. (2.29) and again separating the real and imaginary components, we can get two differential equations:

$$\dot{\delta I} + \omega_{1/2}\delta I + \Delta\omega_0\delta Q = -\omega_{1/2}(G_I * \delta I), \tag{3.26}$$

$$\dot{\delta Q} + \omega_{1/2}\delta Q - \Delta\omega_0\delta I - V_0\delta\omega = -\omega_{1/2}(G_Q * \delta Q). \tag{3.27}$$

Analogous to Eq. (3.22), we can take the Laplace transform of Eq. (3.26) and solve for how I changes with deviations in Q:

$$\frac{\delta I}{\delta Q} = \frac{-\Delta\omega_0}{s + \omega_{1/2}(1 + G_I(s))}. \tag{3.28}$$

There are a few observations we can make by comparing Eq. (3.22) and Eq. (3.28). We can see that the Q-controller does not amplify the crosstalk between the Q and I channels the way $G_\phi(s)$ can in Eq. (3.22). It can also be seen that the I-controller's damping efficiency is not reduced as $\Delta\omega_0$ (and thus $\cos\psi_0$) increases. Thus we can see that there will be some differences in the operation of the SRF cavity depending on if A/ϕ or I/Q control is used. We will discuss this facet within the context of the ponderomotive instabilities in the next chapter.

3.2.3 The Discrete Domain

In terms of modeling dynamic systems, the Laplace domain presents a useful frame in which to work. Of course, we cannot know our process variables in continuous time: we can only measure them at sampling time periods T_s dependent on the hardware of the loop. It is therefore useful to view the progression of the system in terms of k-iterations of the sampling period T_s. This substitution allows for the relevant equations of motion to be converted to difference equations.

Alternatively, the transfer function formalism can still be used in a modified way. The Z-transform is the discrete analog to the Laplace transform [101]. In single-side cases, a discrete time-domain signal can be converted to the Z-domain via:

$$X(z) = \sum_{k=0}^{\infty} x[k] z^{-k}, \tag{3.29}$$

where z is the analogous complex variable. z can be related back to the continuous Laplace domain,

$$z = e^{sT_s}, \tag{3.30}$$

thus allowing for single-sided transformed functions into the continuous domain:

$$X^*(s) = X(z = e^{sT_s}). \tag{3.31}$$

When designing control loops, it is useful to use the discrete formalism if the sampling rate is known. This allows for the most accurate predictions that can be reasonably expected from the system.

The state-space formalism can also be discretized for more accurate performance. Consider a state-space model in the continuous time domain; for example the cavity dynamics we discussed in Chapter 2. The internal states and cavity voltage evolve in continuous time as:

$$\dot{\mathbf{x}} = A\mathbf{x} + B\mathbf{u}, \tag{3.32}$$

$$y = C\mathbf{x} + D\mathbf{u}, \tag{3.33}$$

where A, B, C and D are the state, input, output, and feed-through matrices respectively. In continuous time, we have a series of differential equations. Switching to the discrete domain however, these differential equations become the update equations for every sampling period [102]:

$$\mathbf{x}[k+1] = \Phi\mathbf{x}[k] + \mathbf{\Gamma} \cdot \mathbf{u}[k], \tag{3.34}$$

$$y[k] = \mathbf{H} \cdot \mathbf{x}[k] + \mathbf{J} \cdot \mathbf{u}[k], \tag{3.35}$$

where Φ, $\mathbf{\Gamma}$, $\mathbf{H}$, and $\mathbf{J}$ are the discretized state, input, output, and feed-through matrices respectively. The exact contents of these matrices depend on the system and the method used to discretize the system. In this work, we will use Forward Euler numerical integration to discretize systems.

3.3 Control Algorithms

So far we have talked about the process variables and practical methods of control. In terms of closed-loop design, we have left the controller as a vague transfer function $G_c(s)$. Now we will discuss the algorithms that are deployed to carry out the control as they are applied to accelerator systems. In particular, there are three algorithms important to this study.

3.3.1 Proportional-Integral-Derivative

No treatment of control systems would be complete without a discussion on the proportional-integral-derivative controller (PID). As the name suggests, there are three components to the PID controller. The error of the system, $e(t)$ is passed to the PID controller, which constructs a corrected input based on the sum of three operations [103]:

$$U(t) = [k_P + k_I \int dt + k_D \frac{d}{dt}] * e(t), \tag{3.36}$$

a proportional scale of the error (with gain k_P), the time integral of the error (with gain k_I), and the rate of change of the error (with gain k_D).

In the continuous Laplace domain, this controller has a simpler form:

$$G_c(s) = k_P + \frac{k_I}{s} + k_D s. \tag{3.37}$$

Each term has its own purpose in the controller. The proportional component is the fastest reacting term, allowing for quick corrections. If k_P is too high it can lead to overshooting of the setpoint though. The integral term is slower than the proportional term, but its integral nature allows for the correction of steady state errors over time. The derivative term can allow for the reduction of overshooting by adding some delay into the system, but there are some other complications with this term.

One might notice that the derivative term adds a non-causal element to the controller. With high-sampling frequency, a derivative controller can amplify high-frequency noise. Practically, this requires additional filtering to reduce the impact. Many prebuilt, PID simulators have built in filtering options from which the user can set the filter order N. In many accelerator control cases, such as amplitude and phase control, it is actually common to bypass this effect by neglecting the derivative term. For this treatment, we will work with the proportional-integral (PI) formalism, with a discretized form of:

$$G_c(z) = k_P + k_I \frac{T_s}{z-1}. \tag{3.38}$$

Forward-Euler integration is used in this formulation, though different integration methods can be used.

As can be seen, the PID and/or PI controller is quite simple in form and relatively easy to tune. It can also be quite effective in controlling dynamic systems. Since its conception, PID has found its home in many branches of industry and as such found its way into accelerator control. In fact its the controller of choice for amplitude, phase, and frequency control in SNS [104], LCLS-II [105], the European XFEL [106], and is the controller of choice for future machines such as PIP-II [107].

3.3.2 Active Disturbance Rejection Control

If one were to know the internal state of a system and its history, they would be able to produce an accurate prediction of the future outputs of the system. For most systems, knowing the entire internal state of the system is not feasible. For an SRF cavity, this would require knowing the cavity amplitude, phase, detuning, and their respective derivatives at a given time. Since the cavity voltage has inherent time delay, this provides an extra layer of difficulty.

In Chapter 2, we defined the state evolution of disturbances to an SRF cavity with N mechanical modes with a state-vector:

$$\mathbf{x} = [\delta V,\ \delta\phi,\ \delta\omega_1, \dot{\delta\omega}_1, ...,\ \delta\omega_N,\ \dot{\delta\omega}_N]^T \tag{3.39}$$

While measuring all of these internal states is not feasible, it is possible to estimate them. Luenberger/state observers are designed for this purpose: to estimate the internal states and their derivatives based on the input and output of the systems. However, in the context of realistic cavities, this would involve a great deal of computational power for complex systems like the SRF cavity. Additionally, there can still be external disturbances from microphonics or unknown dynamics that will affect all the state variables.

Han expanded on the concept of the state observer at the turn of the century with his "non-linear" PID controller [108]. Han postulated that if the total disturbance to the system can be estimated, then overall control of the system can be improved. Adding the total disturbance to the state vector allows an extended-state observer (ESO) to estimate it. Suppose we have a first order, dynamic system with one state variable x_1. We can construct a state-vector that includes the total disturbance d:

$$\mathbf{x} = [x_1,\ d]^T = [x_1,\ x_2]. \tag{3.40}$$

The ESO then attempts to recreate the dynamic system and estimate the state $\hat{x}_1$, the total disturbance $\hat{x}_2$, and the output $\hat{y}$, where the hats denote estimates. For a first order system modeled

by Eq. (3.32) and Eq. (3.33), the ESO tracks the dynamics of the system as,

$$\dot{\hat{\mathbf{x}}} = A\hat{\mathbf{x}} + B\mathbf{u} + \mathbf{L} \cdot (y - \hat{y}), \tag{3.41}$$

$$\hat{y} = C\hat{\mathbf{x}} + D\mathbf{u}, \tag{3.42}$$

where $\mathbf{L}$ is the observer gain vector. In the first order, continuous formalism, $\mathbf{L}$ is a function of the observer bandwidth ω_{ob}:

$$\mathbf{L} = [2\omega_{ob},\ \omega_{ob}^2]^T. \tag{3.43}$$

The observer bandwidth sets the poles or response frequency of the ESO, and represents the range the ESO can estimate over.

The estimations $\hat{\mathbf{x}}$ are then used to shape the input u to the system via a proportional-derivative (PD) scheme:

$$u = \frac{\omega_c(r - \hat{x}_1) - \hat{x}_2}{\hat{b}}, \tag{3.44}$$

where ω_c is the controller bandwidth (and proportional gain factor) and $\hat{b}$ is an estimation of the input coefficient. Like the observer bandwidth, ω_c sets the range of frequencies the controller can respond to. The $\hat{b}$ coefficient can relate to the physical system, and can be another notch to tune the controller. It is this combination of the ESO and the PD control scheme that creates active disturbance rejection control (ADRC).

Work in optimizing ADRC have been carried out by Han and Gao [109]. Vincent et al. first demonstrated ADRC use for control of the amplitude and phase in superconducting quarter-wave resonators in the ReA3 re-accelerator at FRIB (then the National Superconducting Cyclotron Laboratory) [110]. Both amplitude and phase control loops have their own ESO estimating the respective state-vectors:

$$\mathbf{x}_A = [V_c,\ d_A]^T, \tag{3.45}$$

$$\mathbf{x}_\phi = [\phi_c,\ d_\phi]^T, \tag{3.46}$$

where $d_{A/\phi}$ are the disturbances to cavity amplitude and phase respectively. With this formalism, the state-vectors are much simpler than Eq. (3.39). Instead of trying to estimate the detuning from

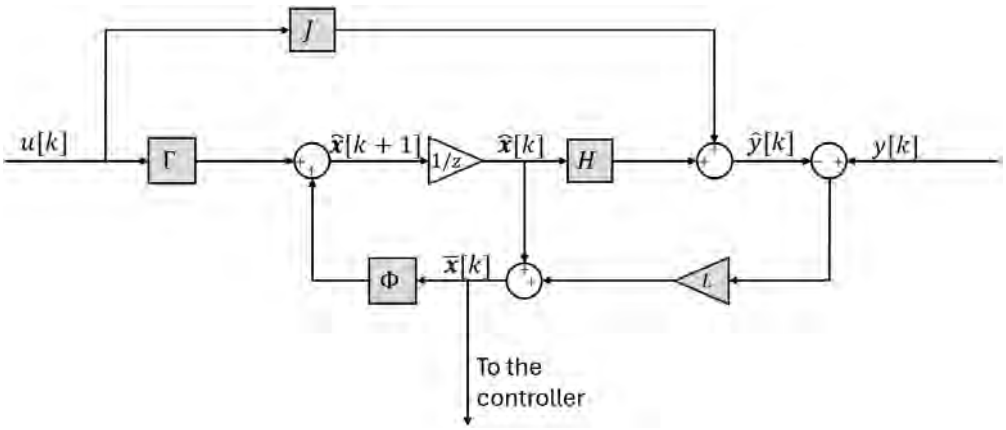


Figure 3.7 Diagram of discretized extended state observer and relevant calculation progression.

each mode, we are now trying to estimate the disturbances to the amplitude and phase from the detuning.

A discretized, fixed point ADRC algorithm has been developed for the LLRF control for the FRIB driving linac [111]. The discretized algorithm follows the formalism from Miklosovic. Radke, and Gao [102]. We will also use this form of the algorithm in this work. This implementation separates the estimates into two stages: $\bar{\mathbf{x}}$ and $\hat{\mathbf{x}}$, though they are different stages of the same estimation. We present a discretized schematic of the ESO using the terminologies of Eq. (3.34) and Eq. (3.35) in Fig. 3.7.

We denote $\bar{\mathbf{x}}$ as the corrective estimates that are used by the controller to shape the drive of the system. In general, the corrective estimates are produced via:

$$\bar{\mathbf{x}}[k] = \hat{x}[k] + \mathbf{L} \cdot (y[k] - \hat{y}[k]). \tag{3.47}$$

We can see that the state estimations are used to shape $\bar{\mathbf{x}}$, which in turn refines the state estimations to be used on the next loop cycle:

$$\hat{\mathbf{x}}[k+1] = \mathbf{\Phi}\bar{\mathbf{x}}[k] + \mathbf{\Gamma} \cdot \mathbf{u}_d, \tag{3.48}$$

where $\mathbf{u}_d = [u[k],\ y[k]]^T$. The observer gains also change as we discretize the system, with the relationship between the continuous and discrete observer bandwidths going as:

$$\beta_{ob} = e^{-\omega_{ob} T_s}. \tag{3.49}$$

First-order ADRC is the simplest approach to control the amplitude and phase of an SRF cavity since the respective dynamic equations are first order (Eq. (3.20) and Eq. (3.21)).The observer gain vector using Forward-Euler discretization for a first order ESO is then [102],

$$\mathbf{L} = \left[1 - \beta_{ob}^2,\ \frac{1}{T_s}(1 - \beta_{ob})^2\right]^T. \tag{3.50}$$

As it pertains to amplitude and phase control using ADRC, we can summarize the forms of relevant matrices that are used in the FRIB LLRF. The discretized state matrix Φ now has dependency on the sampling time:

$$\Phi = \begin{bmatrix} 1 & T_s \\ 0 & 1 \end{bmatrix}, \tag{3.51}$$

and so does the input matrix Γ,

$$\mathbf{\Gamma} = [\hat{b}T_s,\ 0]^T. \tag{3.52}$$

The FRIB amplitude and phase controllers do not use feed-through and thus $\mathbf{J} = 0$ for our case. Additionally, since we are estimating either the cavity amplitude or phase, $\hat{x}_1 = \hat{y}$. Thus, $\mathbf{H}$ is simply,

$$\mathbf{H} = [1,\ 0]. \tag{3.53}$$

ADRC can also be represented with two transfer functions by converting the continuous-time domain state-space model to the Laplace domain. The first transfer function is a pre-control-loop filter, which allows for cleaner set-point tracking. Zhao and Gao show that for first order ADRC [112], this filter can be represented as:

$$H(s) = \frac{\omega_c(s + \omega_{ob})^2}{(2\omega_c\omega_{ob} + \omega_{ob}^2)s + \omega_c\omega_{ob}^2}. \tag{3.54}$$

The controller itself can be represented by the following transfer function:

$$G_c(s) = \frac{\omega_c}{\hat{b}s}\frac{(2\omega_{ob} + \frac{\omega_{ob}^2}{\omega_c})s + 2\omega_{ob}}{s + 2\omega_{ob} + 1}. \tag{3.55}$$

Higher order formalisms of ADRC exist [113], which can be used for higher order systems. In Chapter 5, we will adapt this ADRC formalism for a second order system to control the frequency of SRF cavities.

3.3.3 Active Noise Cancellation/Least Mean Squares

The least mean squares (LMS) algorithm is an adaptive filtering element whose filtering coefficients update to remove a select frequency component from the system. It produces a plant input based off a series of weights $w(k)$:

$$U(k+1) = w(k)U(k), \tag{3.56}$$

where the weights are updated via the product of the error $e(k)$ and the adaptation rate μ,

$$w(k+1) = w(k) - 2\mu e(k). \tag{3.57}$$

As the name suggests, mu determines how many steps it will take for the algorithm to converge. Too high of an adaptation rate will result in controller instability, whereas too low of rate will result in poor control.

This algorithm has been applied to eliminate specific microphonic frequencies via the piezoelectric stacks. Most notably, this algorithm has seen success for the LCLS-II HE 1.3 GHz cavities with piezoelectric tuners and at the Cornell-Brookhaven energy recovery linac [114, 115, 116]. Two update calculations are used to calculate the canceling piezo-voltage: the I/Q components. To eliminate frequency ω_m, the following components can be added to the overall piezo output:

$$I_m(k+1) = I_m(k) - 2\mu_m \delta f \cos(\omega_m k T_s) \tag{3.58}$$

$$Q_m(k+1) = Q_m(k) - 2\mu_m \delta f \sin(\omega_m k T_s). \tag{3.59}$$

By adjusting the I/Q components of the piezo voltage, adjustments to the voltage's phase are already baked in for specific tone cancellation.

One downside of this filter is that it is very narrow-band. We show the simulated frequency response of this filter in Fig. 3.8. Only a few Hz of the chirp signal are significantly damped. Like the piezo-voltage components, the filter frequency ω_m can be finely updated with its own adaptation rate η_m. The voltage supplied to the piezo on the k'th loop is the sum of the I and Q voltages:

$$V_m(k) = I_m(k)\cos(\omega_m k T_s) + Q_m(k)\sin(\omega_m k T_s). \tag{3.60}$$

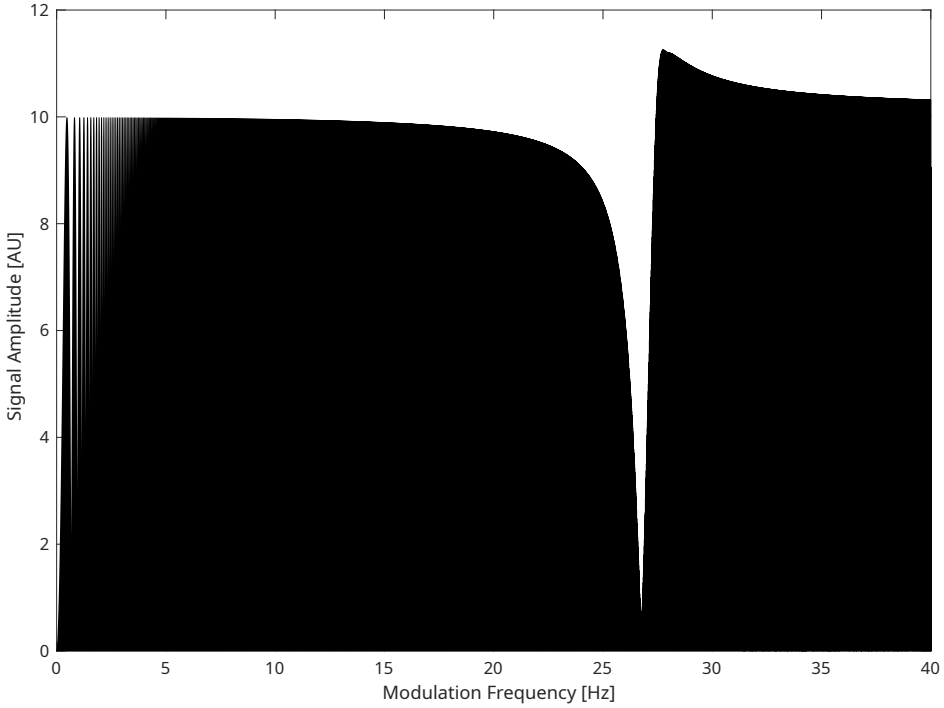


Figure 3.8 Arbitrary amplitude of sinusoid v. chirped sinusoid frequency for a chirp passed through an LMS filter.

This algorithm can be paired alongside traditional controllers for the piezo, as we will demonstrate in Chapter 5.

CHAPTER 4

EFFECTS OF LINEAR AND NONLINEAR CONTROL ON PONDEROMOTIVE INSTABILITY

4.1 The Lorentz Transfer Function

In Chapter 2, we mathematically described the cavity electromechanical behavior through the Lorentz transfer function:

$$G_L(s) = \frac{\sum \delta\omega_\mu(s)}{\delta V(s)} = 2V_{acc} \sum_\mu \frac{k_\mu^L \Omega_\mu^2}{s^2 + \frac{2}{\tau_\mu} s + \Omega_\mu^2}. \tag{4.1}$$

This transfer function is a real quantity and can be measured experimentally. Suppose the forward power to the cavity is modulated; it follows that the field in the cavity will be modulated as well. For constant modulation amplitude, this reduces the s variable to just the frequency component,

$$G_L(j\Omega) = 2V_{acc} \sum_\mu \frac{k_\mu^L \Omega_\mu^2}{\Omega_\mu^2 - \Omega^2 + \frac{2j}{\tau_\mu}\Omega}, \tag{4.2}$$

where Ω is the modulation frequency. Chirping the modulation frequency and recording the deviations in detuning and field, one can calculate the amplitude of the Lorentz transfer function quite simply:

$$|G_L(j\Omega)| = \frac{|\delta\omega(j\Omega)|}{2V_{acc}|\delta V(j\Omega)|}. \tag{4.3}$$

If the data acquisition (DAQ) setup and the modulation source share the same reference clock, then the phase response of the Lorentz transfer function is the phase difference between the detuning and voltage waveforms:

$$\angle G_L(j\Omega) = \phi_{\delta\omega} - \phi_V. \tag{4.4}$$

When the data is collected and the Lorentz transfer function amplitude is calculated, mechanical parameters can be extracted. Examining Eq. (4.2), we see that there are two extreme situations when it comes to sweeping the modulation frequency.

$$|G_L| = \begin{cases} k_\mu^L Q_\mu & \Omega = \Omega_\mu \\ \sum_\mu k_\mu^L & \Omega \ll \Omega_\mu \end{cases} \tag{4.5}$$

When a mechanical resonance is excited by the Lorentz pressure, the detuning induced is amplified by that mode's quality factor. Q_μ can be determined by fitting resonances in the LTF amplitude with a Lorentzian or through measuring the decay time. The mechanical mode coupling to the Lorentz pressure can then be found as:

$$k_\mu^L = \frac{|G_L(j\Omega_\mu)|}{Q_\mu}. \tag{4.6}$$

Additionally, when the modulation frequency is low, away from mechanical resonances, the amplitude of the Lorentz transfer function should be the sum of every mode's coupling. One might recall that this is just the static Lorentz force detuning coefficient, which is more straightforward to determine from cavity testing. Though this latter part is not necessarily important for extracting data, it is good to have as a sanity check when verifying the Lorentz transfer function measurement.

4.1.1 Experimentally obtaining the Lorentz Transfer Function

In essence, all one needs to do to obtain the Lorentz transfer function is modulate the field. As mentioned, modulating the forward power is sufficient to induce modulations in the cavity field. This modulation can be done digitally in the LLRF controller via modulating the amplitude directly or modulating the I/Q components together. However, this might not be feasible depending on the state of the controller.

In our case, it is easier to carry out the modulation with analog equipment. We detail our circuit used to measure the Lorentz transfer function in Fig. 4.1. We interrupt the forward power line from the LLRF controller to the solid-state amplifier (SSA) with a voltage-controlled attenuator (VCA). An external voltage function generator supplies a sinusoid to the VCA, creating the modulation on the forward power that is sent to the SSA and eventually the cavity.

The power transmitted out of the cavity is picked up by the LLRF controller, from which the detuning and cavity field can be collected. It is important that the amplitude and phase loops (or analogous I/Q loops) remain open so as to not alter the process variables. The LLRF controller also allows for the safety interlocks to remain active. Alternatively, one can obtain detuning and field from analog methods such as a phase-lock loop and RF crystal detector. Recently, the RF team at IMP showed success in using a grey-box model and estimation techniques to estimate relevant

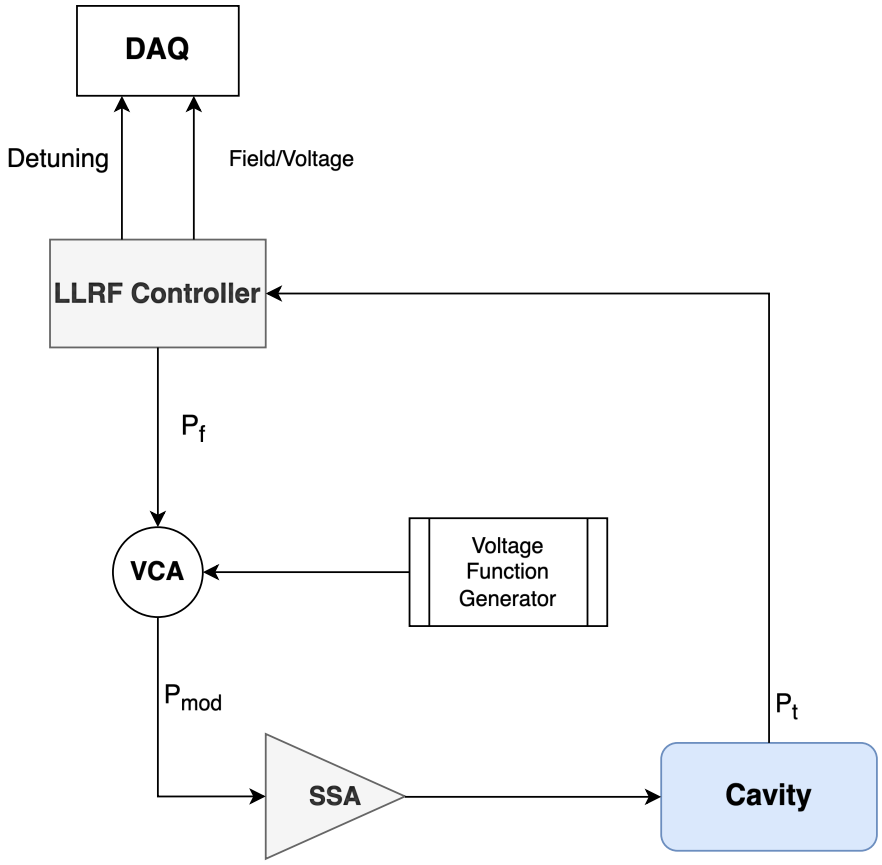


Figure 4.1 Circuit diagram for measurement of the Lorentz transfer function.

mechanical parameters of the Lorentz transfer function [117]. We note that this measurement technique will not work for all coupling strengths β_e. In the case of $\beta_e \leq 1$, the bandwidth becomes increasingly narrow and the filter-like nature of the cavity strongly attenuates signals outside the bandwidth. Sufficiently large bandwidth (low Q_L) is needed to accurately measure the mechanical resonance responses.

In the case of the FRIB $\beta = 0.53$ half-wave resonators (HWRs), the design coupling of $Q_L = 1 \times 10^7$ is sufficient in to measure the Lorentz transfer function up to 350 Hz where most of the mechanical resonances exist. We present the 200-300 Hz region of the calculated $\beta = 0.53$ Lorentz transfer function in Fig. 4.2. We will use the electromechanical data from this transfer function extensively in this chapter, with the relevant parameters presented in Table 4.1. In this case the Lorentz transfer function was determined with discrete points. If the DAQ sampling rate is sufficiently high, a continuous chirp of the modulation frequency can be used.

Table 4.1 Mechanical and electromechanical parameters for the $\beta = 0.53$ HWR obtained from Fig. 4.2.

Number	Frequency f_μ [Hz]	Q-factor Q_μ [AU]	Coupling k_μ^L [Hz/(MV/m)^2]
1	214.84	500	0.09
2	228.97	1400	0.036
3	259.3	400	0.33
4	260.12	740	0.269
5	264.38	700	0.09
6	294.39	300	0.2

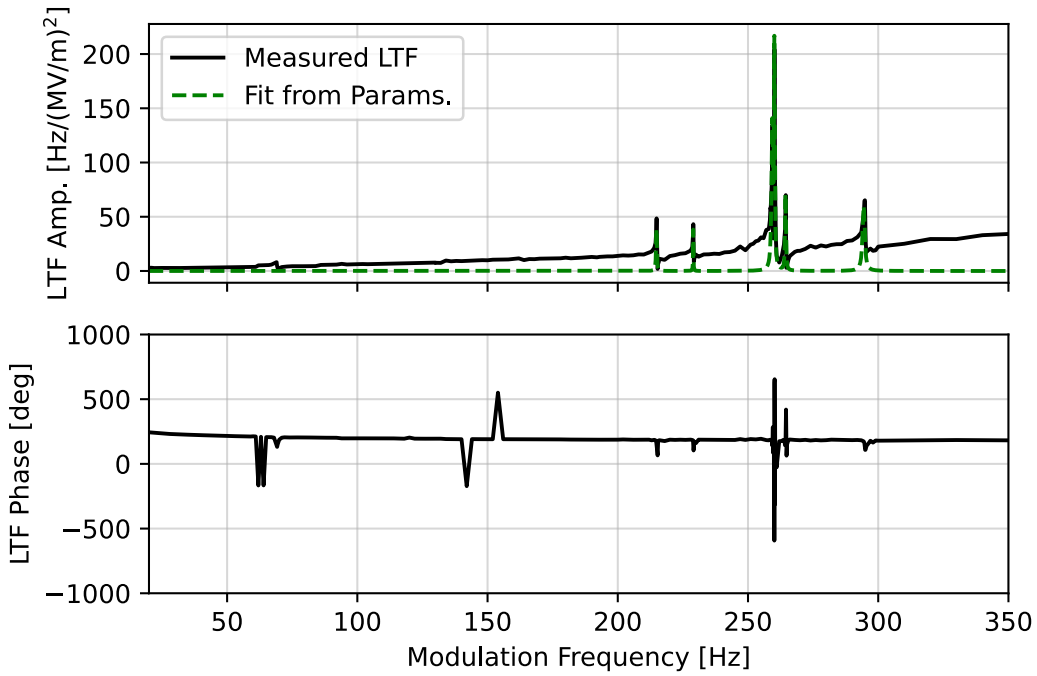


Figure 4.2 Lorentz transfer function amplitude (top) and Lorentz transfer function phase (bottom) v. modulation frequency. Included are fits using Lorentzians and the parameters in Table 4.1.

Cavities of a similar type should have close to identical LTFs when compared with each other. Some deviations can occur due to differences in cavity mounting, tuner loading, and even cryogenic conditions. For some cavity geometries, there could be other factors that can cause some stark differences. We mentioned in Chapter 2 that QWRs will usually employ some mechanical damping fixture in the inner conductor to reduce the effect of the pendulum mode. There can be significant damper-to-damper variation, and as a result can vary the LTF quite substantially as can be seen in Fig. 4.3.

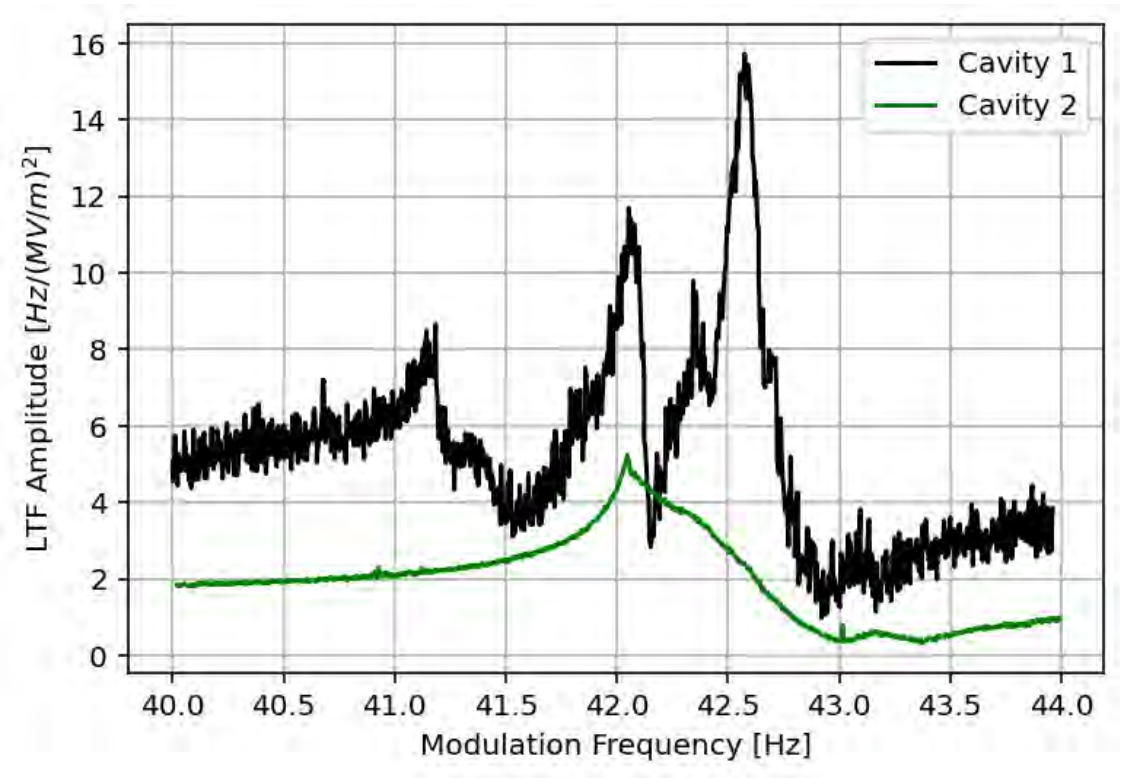


Figure 4.3 Lorentz transfer function amplitude v. modulation frequency for two $\beta = 0.085$, 80.5 MHz QWRs. Not only does the amplitude change, the shaking of the stiffening tube of the damper causes the appearances of other peaks as seen in Cavity 1.

4.2 Stability of the Closed Loop Cavity

Almost every cavity can be pushed to instability given a large enough disturbance. In this chapter, we are interested in examining the stability of cavities in the presence of and amplitude and phase (or analogous) feedback. We will focus on the $\beta = 0.53$ HWRs in this chapter for a few reasons. The pneumatic tuner utilized does not provide additional stiffness to the cavity, and thus the LFD is not reduced. Therefore this study gives us a clear look at the effects of amplitude and phase control on the instability. Second, it was noted that the $\beta = 0.53$ HWRs could experience oscillatory-like instabilities when detuning grew sufficiently large **in either direction** during FRIB production. Lastly, FRIB utilizes ADRC for amplitude and phase control and the examination of non-linear feedback systems has not yet been done. We will include analysis for a PI-controlled cavity and compare it with the ADRC-controlled cavity. An abridged version of this section was published in our paper [70], which we will present here.

Table 4.2 Amplitude and phase controller and observer bandwidths used in experimental measurements for both HWR types. Bandwidths are presumed to be for the amplitude controller unless denoted with ϕ for the phase controller. The $\beta = 0.29$ HWRs measurement are taken with $E_{acc} = 7.7$ MV/m and the $\beta = 0.53$ HWR measurements are taken with $E_{acc} = 7.4$ MV/m.

Amplitude Bandwidths	Values
ω_c [rad/s]	600, 1200, 2400, 4800
ω_{ob} [rad/s]	19200
Phase Bandwidths	Values
$\omega_{c,\phi}$ [rad/s]	600
$\omega_{ob,\phi}$ [rad/s]	9600

4.2.1 Instability Threshold Measurements

One of the main objectives of this work to understand the nature of these instabilities and the effect that ADRC has on the ponderomotive instability. Experimentally, the instability threshold can be measured using the FRIB LLRF quite simply. A forward-cavity offset is used to denote the phase difference between the cavity and generator when the cavity is tuned on resonance. By adding an adjustment to this offset, we can purposefully introduce a detuning phase/angle ψ_0 to the cavity. This phase relates to real cavity detuning as:

$$\Delta\omega_0 = \omega_{1/2} \tan(\psi_0). \tag{4.7}$$

We vary ψ_0 until the instability is excited and we see growth in the cavity amplitude and phase. Looking at the instability threshold as we vary the amplitude controller bandwidth ω_c will give us valuable information about the effect of the controller. To restrict deviations from the observer, we keep the amplitude observer bandwidth to $\omega_{ob} = 19200$ rad/s. We are particularly interested in the effects of amplitude control as it's the main prevention mechanism of ponderomotive oscillations (reducing deviations in the field). The relevant gain parameters we used in these measurements (and which will be used in the following simulations and analysis) can be found in Table 4.2.

Fig. 4.4 demonstrates two deviations in the behavior of the instability thresholds in both types of HWR [84, 70]. We see that the oscillatory instability thresholds for both types tend to decrease as the amplitude controller bandwidth increases for $\psi_0 < 0$, contrary to findings for generator-driven cavities using linear feedback systems. Additionally, both cavities possess an 'oscillatory-like' instability for $\psi_0 > 0$. Each threshold is measured twice for each cavity. Measurements for both

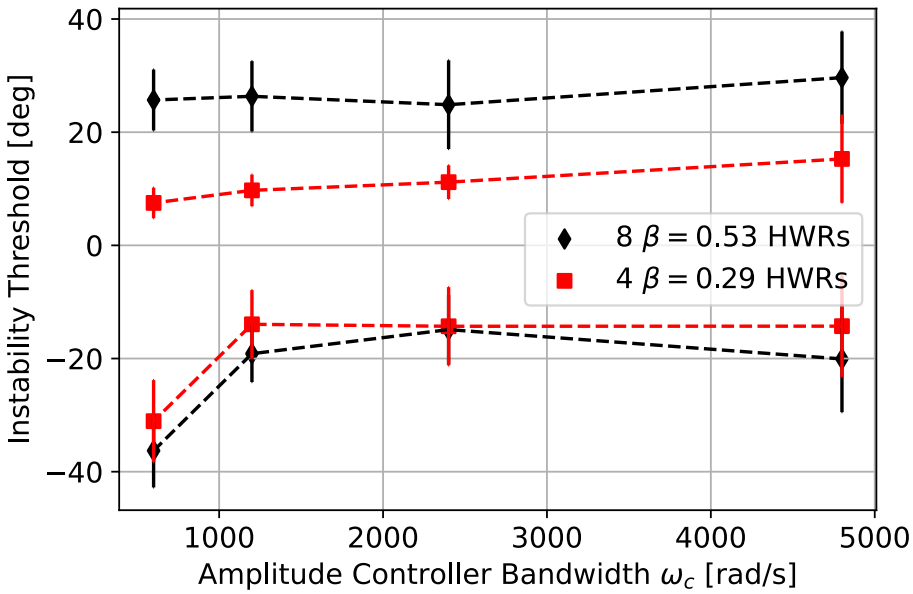


Figure 4.4 Instability threshold in terms of detuning angle v. the amplitude controller bandwidth for eight $\beta = 0.53$ HWRs within the FRIB driver linac. Included are the measurements for four $\beta = 0.29$ HWRs for comparison.

types of HWRs were taken at 2 K under usual linac operational conditions. While there is some clear cavity-to-cavity variation, we report that each cavity is consistent with itself from measurement to measurement.

Some of the $\beta = 0.53$ HWR instability threshold measurements were accompanied with spectrogram measurements of the carrier during the instability events: when the cavity was detuned positively and negatively. In both cases, sidebands denoting the growth of the instability driving frequency (or frequencies) can be seen. On a few attempts, we were able to open and then re-close the phase control loop before an instability-induced trip. It can be seen that the sidebands decay upon opening the phase control loop, confirming that this is not a strong microphonics event as microphonics would persist upon opening the phase loop. The relevant side band data can be seen in Fig. 4.5. Additionally, we see that the frequency excited for the expected oscillatory instability has the highest response in the LTF (Fig. 4.2).

For $\psi_0 < 0$, the expected regime of the oscillatory instability, we see that the sideband that is excited correlates with the strongest two modes of the LTF (see Table 4.1). On the opposite side

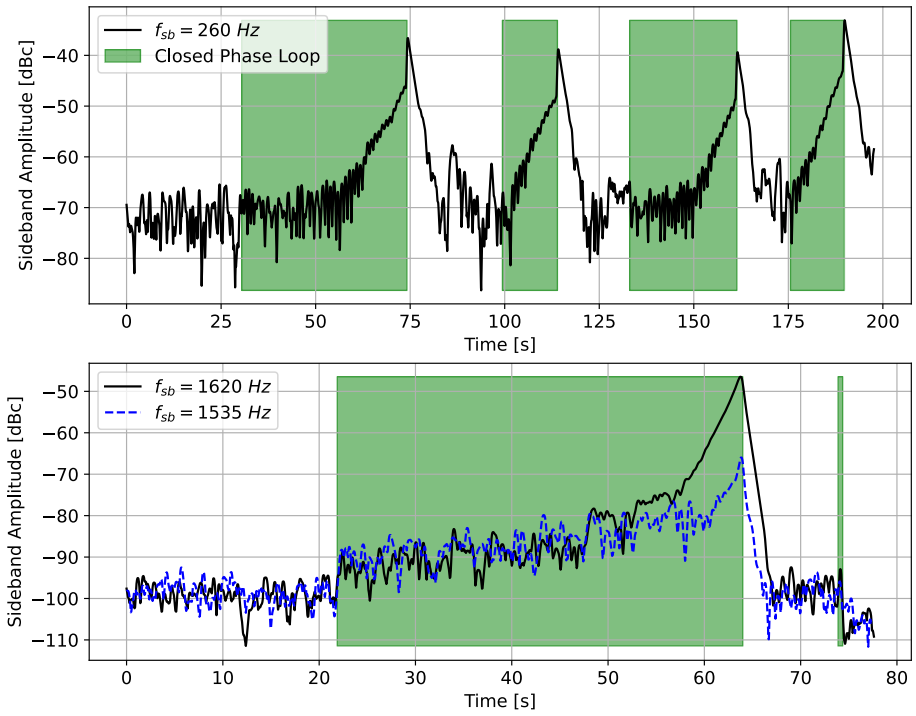


Figure 4.5 Plot of relevant instability driving sidebands from spectrogram data for negative detuning (top) and positive detuning (bottom). Green shaded regions represents time periods where the phase control looped is closed. Unshaded regions are phase-open regimes.

of the resonance curve, we see something unexpected. Two high-frequency sidebands are excited and then decay upon opening the phase loop, showing that these two components are driving this instability. Though we cannot say for sure, most of the mechanical energy in the system would exist at lower frequencies suggesting that this driver may not be mechanical.

4.2.2 Analysis and Simulation

For this section and the following three, we will work exclusively with the $\beta = 0.53$ HWR variety. At the time of writing, we do not possess a valid measurement of the Lorentz transfer function for the $\beta = 0.29$ HWR. While some important factors such as mode frequencies and some quality factors were found through other methods, there is larger uncertainty in the calculated amplitude of the LTF. As such, we will focus on the cavity with more reliable electromechanical data.

4.2.2.1 Simulink Model

Key to this section is our Simulink model/simulator. There exists already published work detailing the Simulink model [110, 84, 70], but we will summarize the details here. We show a schematic of the Simulink model in Fig. 4.6. The cavity block contains the I/Q time domain equations of the envelope:

$$\dot{I} + \omega_{1/2} I + \Delta\omega(t, d) Q = \omega_{1/2} I_g \tag{4.8}$$

$$\dot{Q} + \omega_{1/2} Q - \Delta\omega(t, d) I = \omega_{1/2} Q_g. \tag{4.9}$$

The inputs to the cavity block are the I_g, Q_g, and $\Delta\omega$ values. I_g and Q_g are determined by the feedback ADRC loops. We are using the discretized extended state observers we described in Section 3.3.2.

The detuning is calculated from the linearized Lorentz transfer function using all six modes from Table 4.1:

$$\Delta\omega(s) = 2V_{acc} \sum_{\mu}^{N} G_{\mu}(s) \delta V(s). \tag{4.10}$$

The simulation is allowed to come to steady state at the desired V_{acc}. A controllable detuning kick is then given to the cavity in the user desired direction. The deviations of the voltage then excite oscillations via the Lorentz transfer function. If the detuning kick is larger than the instability thresholds, the oscillations will then grow instead of damping out. This process mimics the experimental procedure, where a static offset is given through the forward-cavity offset.

Feedback is done via A/ϕ control, and a polar to cartesian converter block is used to translate the generator $A/\phi \rightarrow I/Q$. Similarly, a cartesian to polar converter is used to translate cavity I/Q to A/ϕ again. Its worth mentioning that these translations are not done with the CORDIC algorithm but with the regular coordinate transforms. Additionally, we have included a phase-change limiter to mimic the FRIB LLRF feature that prevents the drive phase from jumping from quadrant-to-quadrant in the complex plane. In the FRIB case, the controller drive phase $\phi_u[k]$ can not jump

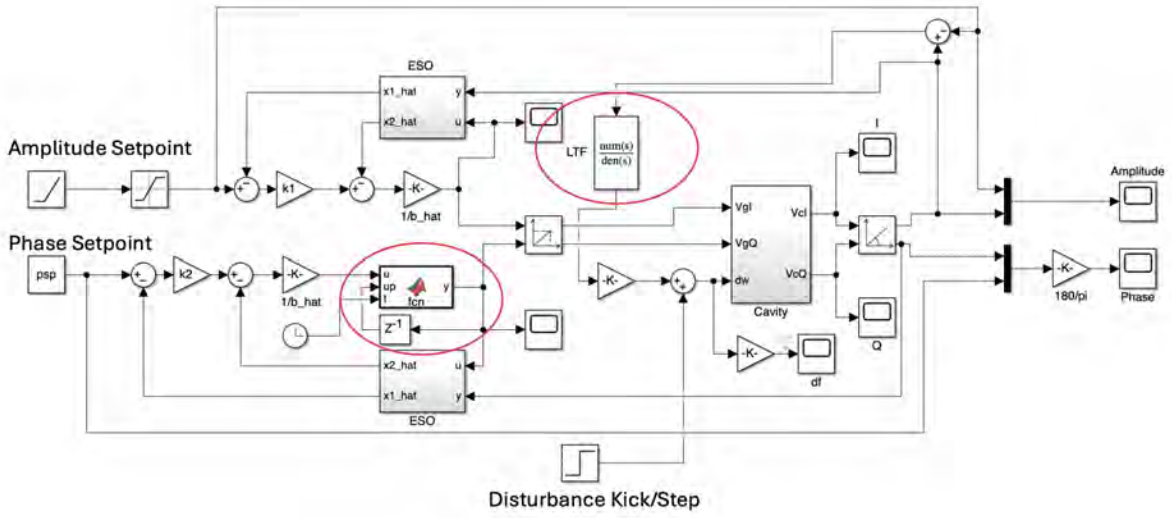


Figure 4.6 Circuit diagram/schematic for Simulink for the cavity and controller system. Included is (from left to right) the phase change limiter on the drive phase and the Lorentz transfer function.

more than 45° (or $\frac{\pi}{4}$ radians) from the previous drive phase $\phi_u[k-1]$:

$$\phi_u[k] = \begin{cases} \phi_u[k], & |\phi_u[k] - \phi[k-1]| \leq \frac{\pi}{4}, \\ \phi[k-1] + \frac{\pi}{4}, & \phi_u[k] - \phi_u[k-1] > \frac{\pi}{4}, \\ \phi[k-1] - \frac{\pi}{4}, & \phi_u[k] - \phi_u[k-1] < -\frac{\pi}{4}. \end{cases} \tag{4.11}$$

The simulations are ran with a loop rate of 200 kHz, which is about 7.5 times slower than the FRIB LLRF loop rate (1.52 MHz). However, we believe this loop rate is sufficient for our instability studies. In Fig. 4.7, we present relevant process variables during a instability event for $\psi_0 > 0$. It can be seen there and in Fig. 4.5 that the instability is built up over seconds with small changes in the phase up until the interlock trip, and thus we believe this loop rate is sufficient to catch relevant phase transients. Additionally, we have neglected to include safety interlocks in this Simulink model as Fig. 4.7 shows that the instability starts before the interlocks engage.

4.2.2.2 Analytical Model

In Chapter 3, we derived the characteristic polynomial for an SRF cavity with amplitude and phase control Eq. (3.23), where we can see the effects of the amplitude and phase controllers $G_{A/\phi}(s)$. We can add linearized transfer functions for the ADRC amplitude and phase controllers

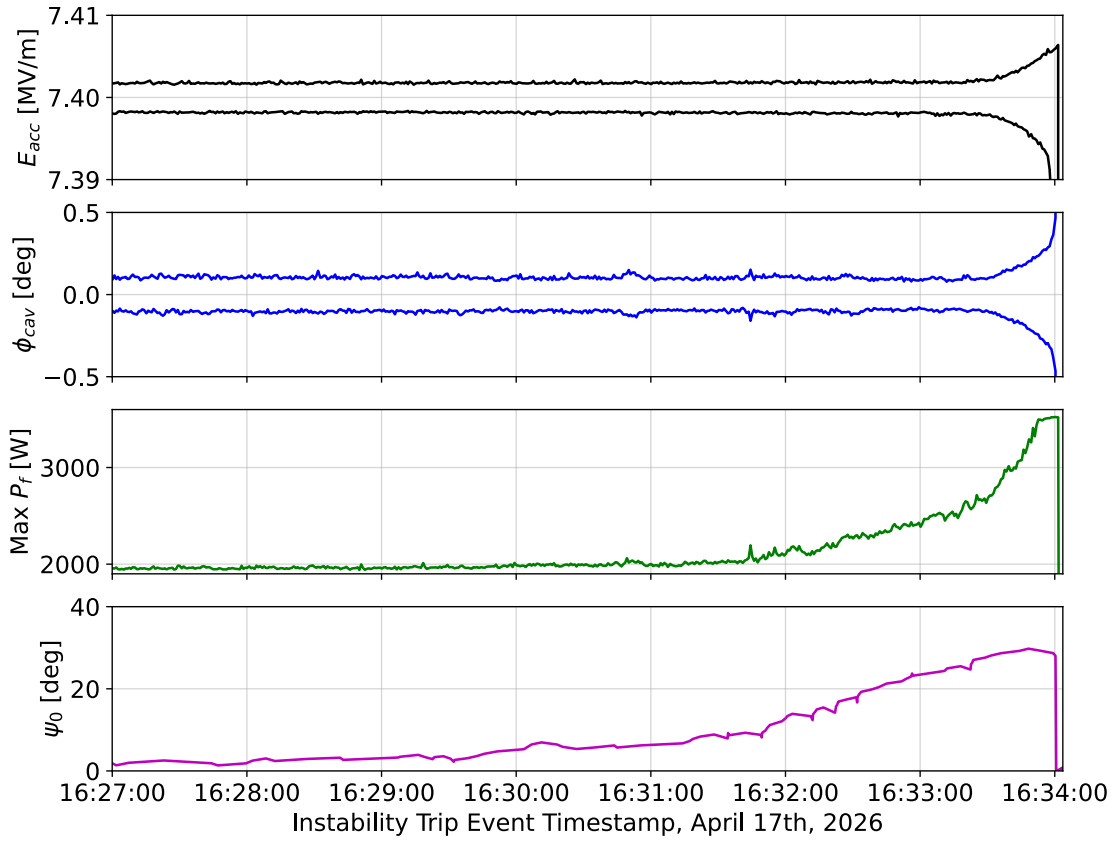


Figure 4.7 Archival process variable samples plotted against the correlated time stamps for a positive detuning ($\psi_0 > 0$) instability event in a $\beta = 0.53$ HWR. The process variables are (from top to bottom): the envelope of E_{acc}, the cavity phase envelope ϕ_c, max forward power P_f, and cavity detuning angle ψ_0. Archival sampling is at 1 Hz or lower so finer oscillations cannot be seen. Published in [70].

from Eq. (3.55). For either A/ϕ or I/Q control, the input coefficient estimate $\hat{b}$ comes from the envelope equation: $\hat{b} = \omega_{1/2}$. Both controllers will use the same transfer function form, but different gain factors. In particular, we will explore a range of amplitude controller bandwidths (for constant amplitude observer bandwidth) and fixed phase controller and observer bandwidths identical to those we explore in our measurements (Table 4.2).

It can be seen in Eq. (3.23) that the whole Lorentz transfer function can be included. MATLAB allows for us to numerically find the roots of the characteristic polynomial even when including all the mechanical modes in the $\beta = 0.53$ LTF alongside the amplitude and phase controllers. Akin to the Simulink model, we can adjust ψ_0 until Eq. (3.23) has a root with a positive real component.

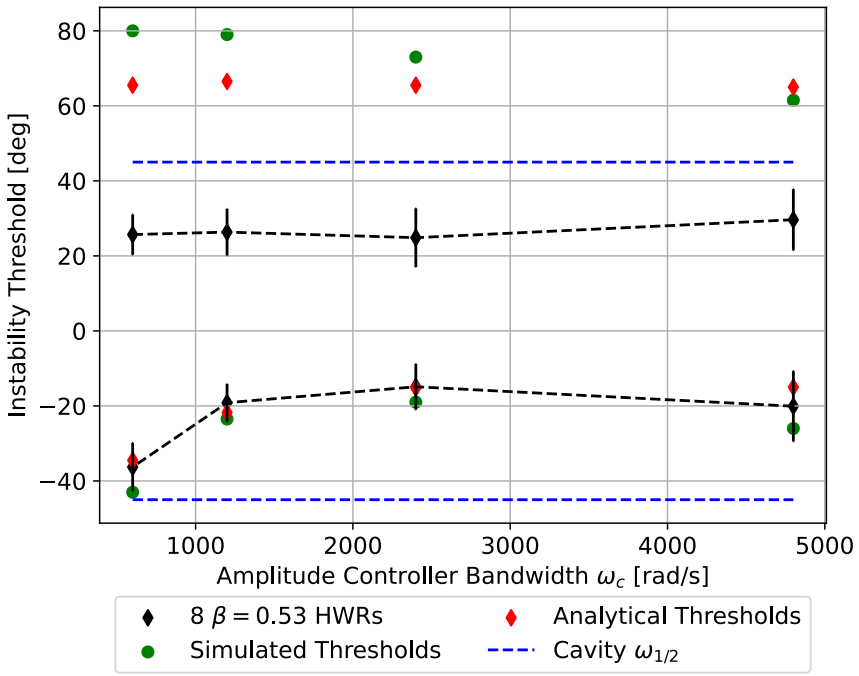


Figure 4.8 Instability threshold v. amplitude controller bandwidth for comparison of our measurements in linac HWRs, predictions from the Simulink model, and predictions by the analytical model.

This analytical model also allows for us to examine the frequency response of the entire cavity and controller system, which will be useful in our discussion.

4.2.3 Model Verification and Instability Mechanisms

We present results of the Simulink and analytical models alongside the experimental measurements in Fig. 4.8. We see that both the analytical and Simulink models provide excellent agreement with our measurements in linac cavities for $\psi_0 < 0$. Both models show that increasing the amplitude controller bandwidth will result in lower instability thresholds. For $\psi_0 > 0$, we see that the thresholds from our predictive tools are much higher than those we have measured. We will discuss this more in a moment.

Our analytical and Simulink models are able to reveal the mechanism through which the oscillatory instability thresholds are lowered with increasing ω_c. Recall earlier to Eq. (3.22), where we derived a transfer function that details how deviations in the cavity phase can lead to deviations in the cavity field. We can examine the frequency response of this transfer function

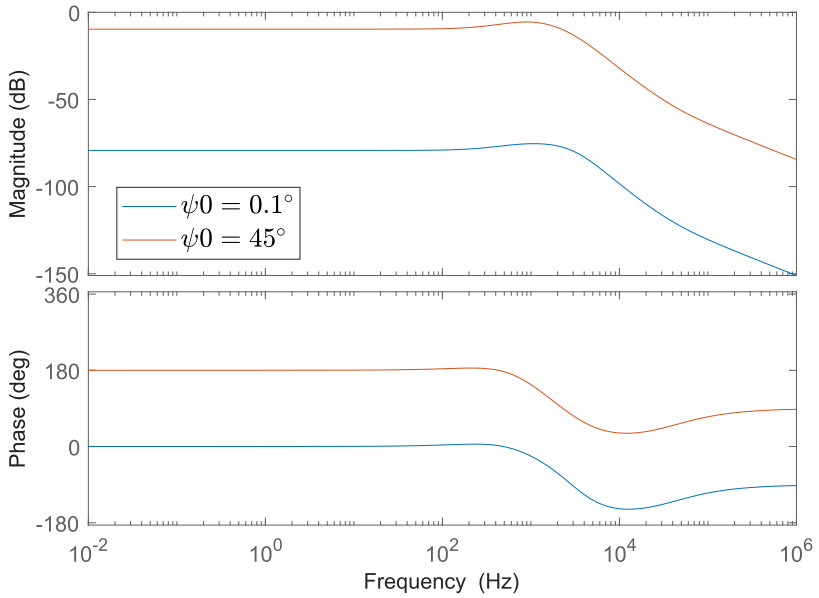


Figure 4.9 Transfer function magnitude (top) and phase (bottom) v. input frequency for Eq. (3.22) in two cases: $\psi_0 = 0.1°$ and $\psi_0 = 45°$.

with our controllers of choice with a Bode plot, which we present in Fig. 4.9. It is clear that the controllers by themselves add a peak frequency f_{pk} for which the magnitude is maximized for a given ψ_0. Varying ψ_0 will also shift the location of f_{pk} as well as the magnitude: at $\psi_0 = 0$ we have $f_{pk} = 1166$ Hz and when we shift detuning to $\psi_0 = 45°$ the peak is pushed back to $f_{pk} = 856$ Hz. We note that this behavior is symmetrical in detuning; negative or positive detuning will push f_{pk} in the same way.

We have noted in our analytical model that when the instability is encountered, the peak frequency of Eq. (3.22) approaches a harmonic of one of the mechanical modes in Table 4.1. We present a relevant table of this information in Table 4.3. It is from this information that we can identify how the oscillatory instability threshold is lowered:

- When the cavity is detuned to where the peak of Eq. (3.22) is a harmonic of a mechanical resonance, residual vibrations (in our simulated case, leftover vibrations from the step and (microphonics in the real machine) can lead to excitation of higher harmonic oscillations in the cavity field and phase passed near the peak of Eq. (3.22)

Table 4.3 Controller bandwidth, the oscillatory instability threshold, the peak of Eq. (3.22) at the instability threshold f_{pk}, the relevant mechanical frequency f_μ, and the harmonic of f_μ such that $f_{pk} = N f_\mu$.

ω_c [rad/s]	Threshold [°]	f_{pk} [Hz]	f_μ [Hz]	Harmonic f_{pk}/f_μ
4800	-15	1063.616	264.38	4
2400	-15.25	691.111	228.97	3
1200	-21.25	430.830	214.84	2
600	-34.5	251.389	259.4	1

- These excited, higher harmonics in the field lead to excitation of base mechanical modes that are strongly coupled to the Lorentz pressure
- Excitation of the strongly coupled modes through the Lorentz pressure leads to stronger oscillations of the base frequency and the harmonics, leading to a runaway effect

We can see this effect in our Simulink model by taking the fast Fourier transform of the cavity amplitude, phase, and detuning at the instability threshold. It can be seen in Fig. 4.10 that harmonics are strongly excited in the phase and amplitude, which leaks out into the detuning as well. Additionally, it can be seen that even though the other mechanical modes are excited, only modes that are strongly coupled to the Lorentz pressure are excited. Their excited harmonics lead to a feedback loop through Eq. (3.22), which leads to instability.

This is not just a manifestation of the simulation model, we can see harmonics excited upon encountering the instability in real, FRIB HWRs. If we look at the harmonics of 260 Hz in our spectrum data, we can see that the second and third harmonics are slightly excited and build up when the instability is encountered as can be seen in Fig. 4.11. Though the increase is small, there is an uptick in both sidebands before the phase loop is opened. The difficulty in seeing more of these sidebands most likely stem from the noise floor in the cryomodule.

As to the importance of the controller bandwidth in this phenomenon, we can look at the magnitude of Eq. (3.22) for different ω_c at their respective instability thresholds for the answer. We plot the magnitude of Eq. (3.22) for the four different cases in Fig. 4.12. We can see that as we increase the amplitude controller bandwidth, the peak in the magnitude becomes more defined

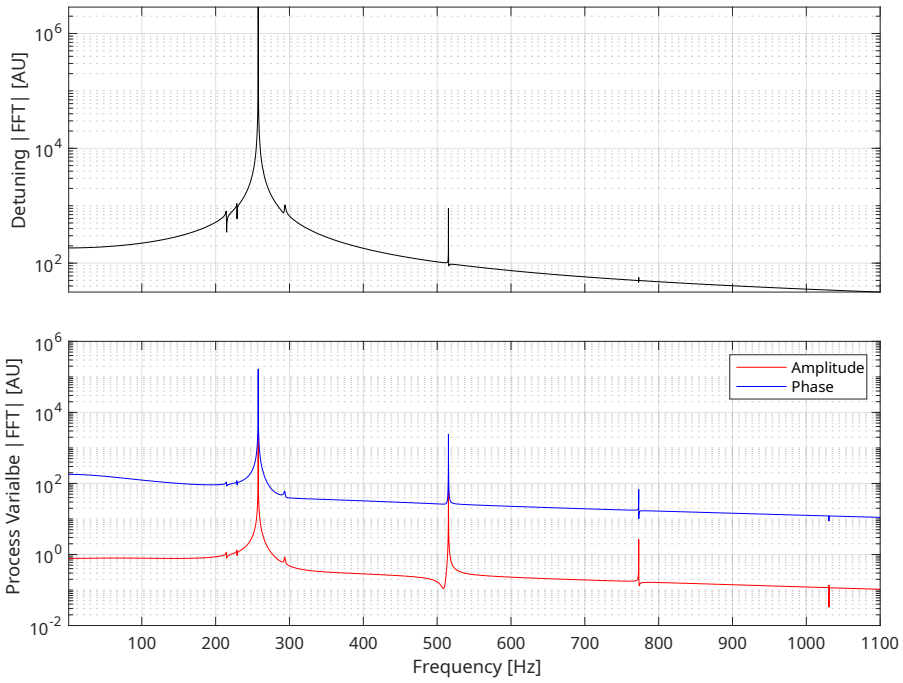


Figure 4.10 FFT amplitude of the cavity detuning (top), amplitude, and phase (both bottom) v. frequency when the instability is excited for $\omega_c = 1200$ rad/s and $\psi_0 = -23.5°$. Since modes 3 and 4 in Table 4.1 are within 1 Hz of each other, the dual excitation manifests as one peak.

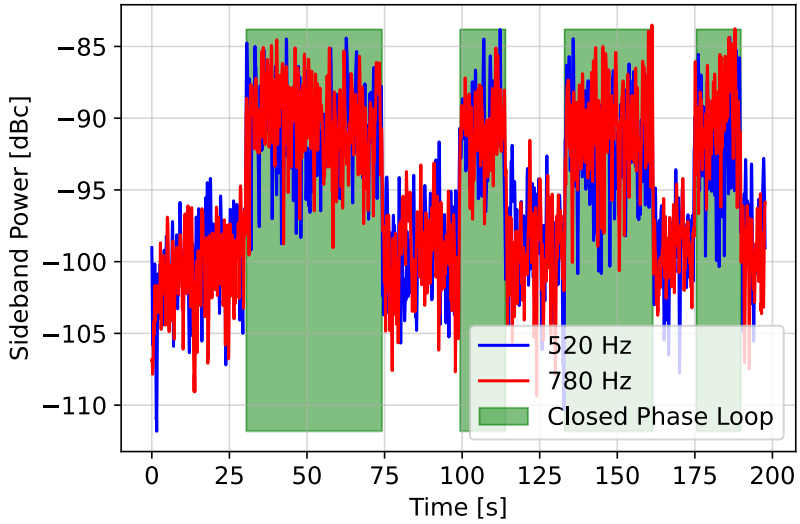


Figure 4.11 Sideband amplitude with respect to the carrier v. measurement time for a $\psi_0 < 0$ instability measurement. Akin to Fig. 4.5, the green shaded regions represents time periods where the phase loop is closed.

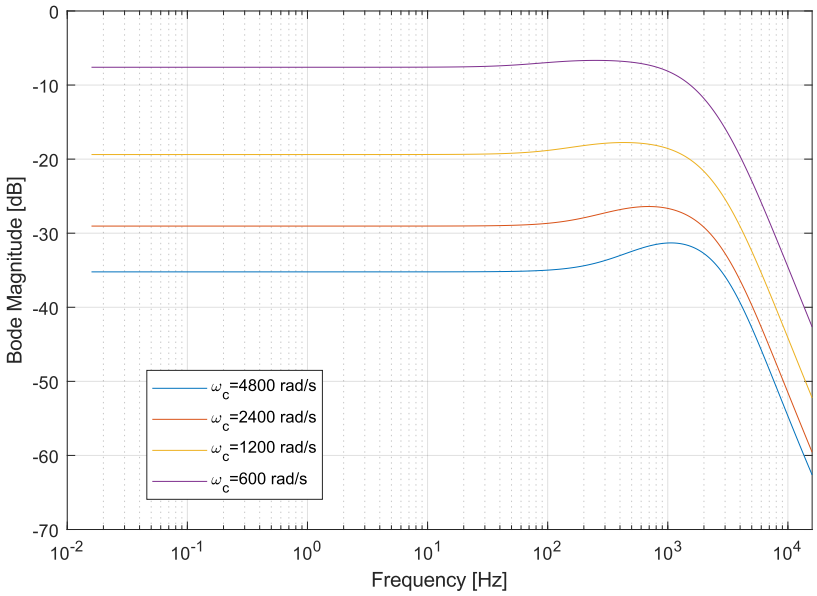


Figure 4.12 Magnitude of Eq. (3.22) v. frequency for our four amplitude controller bandwidths ω_c at their respective analytical oscillatory instability thresholds.

with respect to the lower frequency components. Thus, this peak acts more like a band-pass filter as we increase the amplitude controller and hence why the thresholds decrease as we increase ω_c.

We note that this effect of decreased oscillatory instability threshold is not a product of only using ADRC as amplitude and phase controllers. This harmonic excitation is a result of using ADRC **and** the $\beta = 0.53$ HWRs having high-frequency mechanical modes that are strongly coupled to the Lorentz pressure. If we keep the same mechanical parameters that are in Table 4.1 except that we drop modes 3 and 4 frequencies to 89.4 Hz and 90.12 Hz respectively, we can see in Fig. 4.13 that the expected trend is recovered. The frequencies 89.4 Hz and 90.12 Hz were chosen to place the modes near the edge of the strongest microphonics range (up to 100 Hz).

4.2.3.1 Positive-side Instability Discussion

In terms of the positive side instability, the list of possible sources has decreased. Both our analytical and Simulink models show > 1 kHz oscillations when the instability is excited. Fig. 4.5 shows us kHz sidebands are built up during this instability for $\psi_0 > 0$. Given what we see with how high-frequency components can be excited through Eq. (3.22), it is possible that electrical stimulus can excite this oscillatory-like behavior. Additionally, the predicted instability thresholds

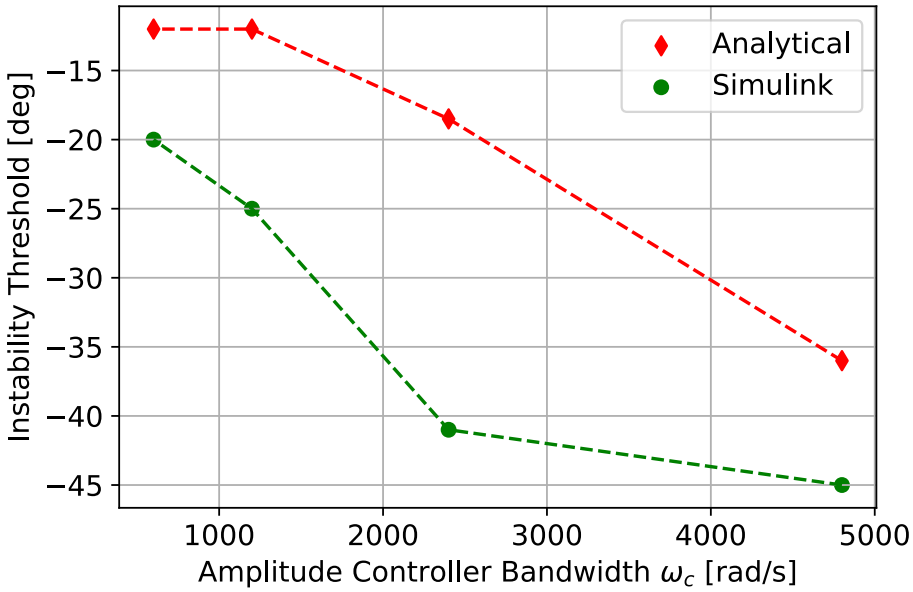


Figure 4.13 Predicted oscillatory instability threshold v. amplitude controller bandwidth from the Simulink and analytical models when the strongly coupled modes are dropped to > 100 Hz leaving k_μ^L and Q_μ the same.

for $\psi_0 > 0$ do not change when adding, removing, or changing mechanical parameters within the LTF: they only change with ω_c. All of these points lead to the conclusion that the $\psi_0 > 0$ instability is driven by the controller.

Of course, we still see large discrepancy between where our models predict these instabilities are and what the measured thresholds are for real cavities. The most notable addition to the deployed FRIB LLRF is the phase-change limiter, which we have recreated in simulation. Thus, we can rule this component out as being the source of this discrepancy between predictions and measurements. As we have mentioned earlier, instabilities are excited before the machine safety interlocks during measurements and thus do not impact the instability thresholds. The next logical step is to create a cavity emulator with the real LLRF system on an FPGA (akin to the Lawrence Berkeley National Lab 'cryomodule on a chip' [118, 119]), allowing for the most accurate simulation. From this, we would be able to identify the exact mechanism for instability within the firmware. However, this project lies outside the scope of this thesis and warrants a project in and of itself.

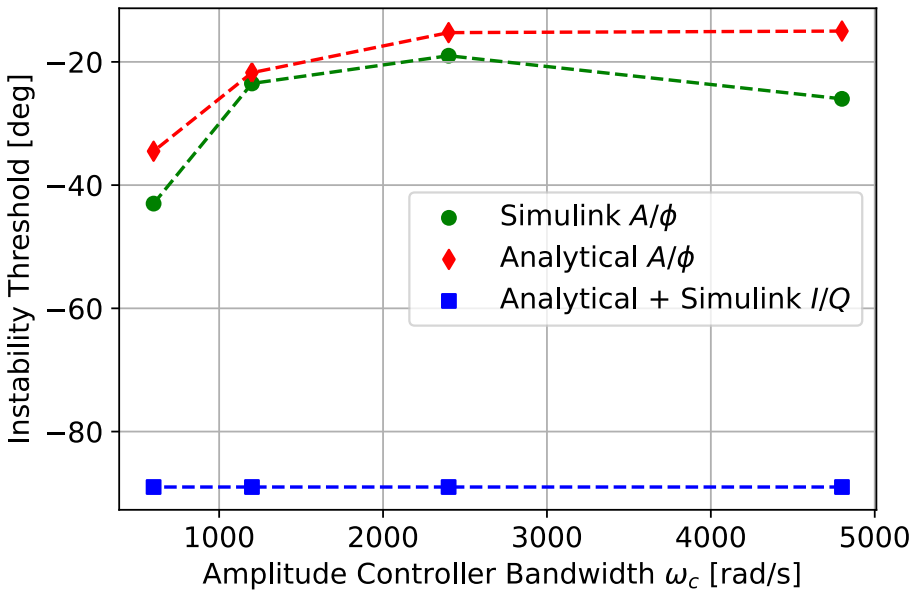


Figure 4.14 Predicted oscillatory instability threshold v. amplitude controller bandwidth for both A/ϕ and I/Q control using both the Simulink and analytical models.

4.2.4 Process Variable Comparison

In [73], the authors show analytically that I/Q control schemes are superior with regard to the oscillatory instability threshold when using PI controllers. We can confirm this is true for ADRC controllers as well. The characteristic polynomial for I/Q controlled cavities is (derivation in Appendix A):

$$\begin{aligned}[s + \omega_{1/2}(1 + G_I(s))][s + \omega_{1/2}(1 + G_Q(s))] \\ +\Delta\omega_0^2 + 2\Delta\omega_0 I_0^2 G_\mu(s) = 0\end{aligned} \tag{4.12}$$

If we reconfigure our Simulink model to I/Q control, we can compare the predicted instability thresholds between the two control schemes in Fig. 4.14 for both Simulink and analytical ADRC models. In this case, both G_I and G_Q use the same controller and observer bandwidths (as opposed to G_A and G_ϕ). In the I/Q case, we are using $\omega_{ob} = 19200$ rad/s. We see that for constant $\omega_{ob} = 19200$ rad/s, I/Q control results in no oscillatory instability up to $\psi_0 = -89°$, well beyond the thresholds of the A/ϕ system. In terms of the positive side, it remains instability-free up to $\psi_0 = 89°$ as well. So why the big difference between the two control methods?

In [73], the authors present a preliminary analytical comparison of instability thresholds under

A/ϕ and I/Q control. The authors show that under A/ϕ control, the $(1 + G_\phi(s))$ term in the A/ϕ characteristic polynomial provides the analytical difference in thresholds. Additionally, the amplitude controller terms are damped by $\cos\psi_0$ and $\sin\psi_0$. We will show how these terms can affect the system and can potentially lead to controller instability in A/ϕ controlled cavities. First, consider the crosstalk transfer functions we derived in Chapter 3 which we summarize here for convenience:

$$\frac{\delta V}{\delta \phi} = \frac{-\Delta\omega_0 V_0(1 + G_\phi(s))}{s + \omega_{1/2}(1 + \cos\psi_0 G_A(s))}, \tag{4.13}$$

and for I/Q control,

$$\frac{\delta I}{\delta Q} = \frac{-\Delta\omega_0}{s + \omega_{1/2}(1 + G_I(s))}. \tag{4.14}$$

Comparing Eq. (4.13) and Eq. (4.14), there are two striking differences: the first is that in A/ϕ control, the phase controller $(1 + G_\phi(s))$ provides additional gain for translating $\delta\phi \rightarrow \delta V$. The second is that the amplitude controller $G_A(s)$ which would damp this effect is itself damped by $\cos\psi_0$. This effect is highlighted when comparing the frequency response of the two transfer functions (Fig. 4.15). The ADRC controllers still provide a peak frequency in the response, but the magnitude is $\sim$ 20 dB less at this peak for I/Q control. Additionally, lower frequencies are extremely attenuated.

The result of these factors is that the path the generator output takes in correcting for disturbances is more sensitive to vibrations with A/ϕ control than with I/Q control. We demonstrate this effect with our two Simulink models. We apply a 45° ($\omega_{1/2}$) kick to the detuning and compare the generator outputs in Fig. 4.16. The oscillations under A/ϕ control can be seen clearly in the looping path taken, whereas the I/Q controlled system follows a more direct, linear path. This is due to attenuation of both low and high-frequency components between the two variables.

This phenomenon explains how the instability threshold can be lowered in A/ϕ control (as compared to I/Q control): in the presence of ponderomotive oscillations, the generator is not able to provide proper corrections to suppress them. This is also the mechanism through which controller instability becomes possible, which we can observe in our $\psi_0 > 0$ instabilities. As

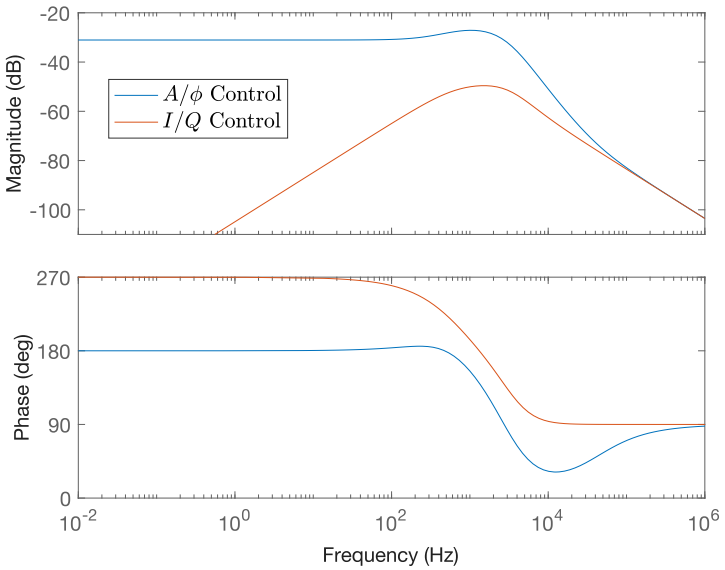


Figure 4.15 Bode responses of the A/ϕ and I/Q crosstalk transfer functions for a detuning angle of $\psi_0 = 22.5°$.

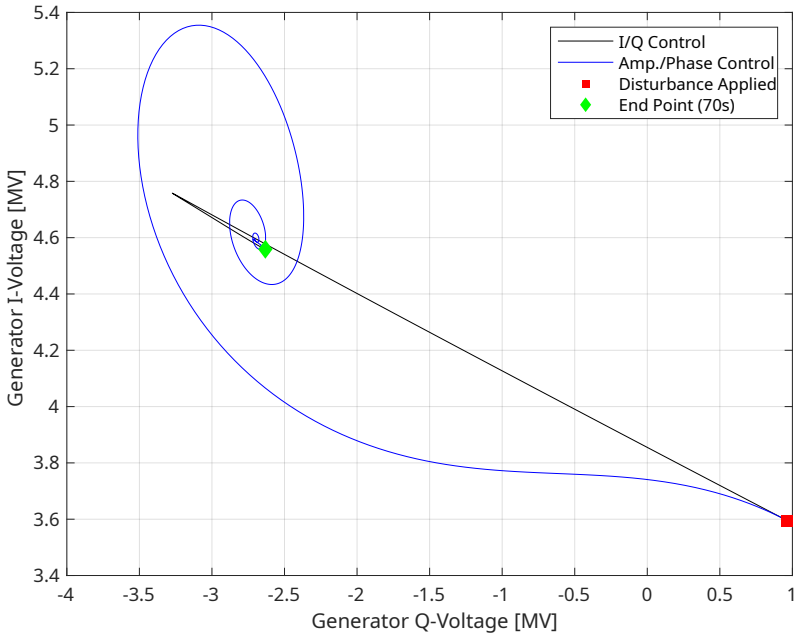


Figure 4.16 Simulated generator Q-voltage v. generator I-voltage for A/ϕ and I/Q controlled cavities when a disturbance of $\psi_0 = 45°$ is applied.

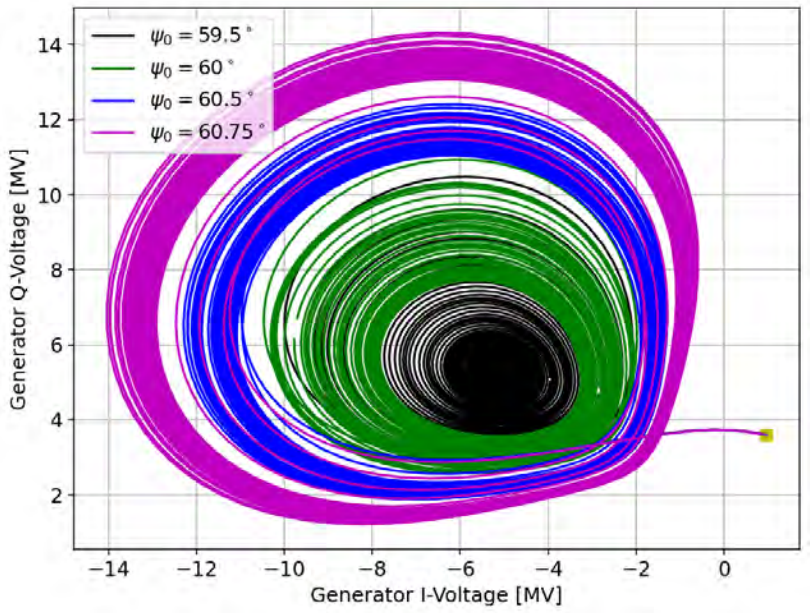


Figure 4.17 Simulated generator Q-component v. I-component for ψ_0 approaching the positive side instability for $\omega_c = 4800$ rad/s, $\omega_{ob} = 19200$ rad/s on the amplitude controller. The yellow square is starting voltage when the disturbance is applied.

detuning increases, the amplitude controller term in Eq. (4.13) is damped by $\cos\psi_0$, allowing for the cross-talk to reach a point where the generator can never converge to a stable working point.

We can see this effect in our Simulink model as we approach the positive side instability. The trajectory of the generator I/Q components for ψ_0 approaching the instability threshold at $\psi_0 = 61^\circ$ can be seen in Fig. 4.17. As the threshold is approached, we reach a detuning offset where the generator can no longer reach a steady state output and instead orbits in the complex plane with the controller response frequency (> 1 kHz). At the instability threshold, the orbits are no longer bounded, and the generator output diverges. As the crosstalk is reduced and the damping effects are removed in I/Q control, the generator is able to converge to a stable working point akin to the path in Fig. 4.17.

4.2.5 Comparing ADRC and PI Controllers

ADRC is a more recent advent of the last 30 years, and has shown promise in implementation in industry and has been successful in the implementation for amplitude and phase control at FRIB. Historically however, proportional-integral (PI) control has shown success in the control of

Table 4.4 Relevant proportional and integral gains for A/ϕ, PI-controlled simulations. Included are the controller and observer bandwidths for the ADRC simulation comparison. The sampling rate is share across both simulations.

Parameter [units]	Value
k_{PA} [AU]	132.5
k_{IA} [AU]	1000
$k_{P\phi}$ [AU]	50
$k_{I\phi}$ [AU]	500
ω_c [Hz]	4800
ω_{ob} [Hz]	19200
$\omega_{c,\phi}$ [Hz]	600
$\omega_{ob,\phi}$ [Hz]	9600
Sampling F_s [kHz]	200

amplitude and phase of SRF cavities. In this section we seek to compare the two control schemes to each other in terms of instability thresholds as well as the analysis we have presented so far.

In terms of comparing the two controllers, there isn't necessarily a direct route. The control scheme of ADRC (ignoring the ESO) is proportional-derivative, which is not used in in LLRF applications. In this section we will build off the analysis we have done in this chapter in regard to examining the responses of the system. In order to establish a baseline, we configure two Simulink models for the $\beta = 0.53$ HWR: one using PI control and the other our normal ADRC model. We adjust the gains of the PI model to match the instability threshold of the $\omega_c = 4800$ rad/s, $\omega_{ob} = 19200$ rad/s model. We present the resulting gains in Table 4.4.

Now that we have arrived at two gain sets that provide the same instability threshold ($\psi_0 = -26°$), we can examine how the response of Eq. (3.22) differs between the two controllers. We present the frequency response of the two controllers in Fig. 4.18. We can see two stark differences in the magnitude of the response between the two controllers. The PI-controlled system passes lower frequency disturbances to the phase much more easily to the cavity amplitude, while higher frequency disturbances are attenuated.

With this comparison, we can make statements about the use cases for each controller. Usage of PI controllers for A/ϕ control can be more beneficial to cavities with larger bandwidths. Not only are lower frequency disturbances easier to compensate with mechanical tuners, but the larger

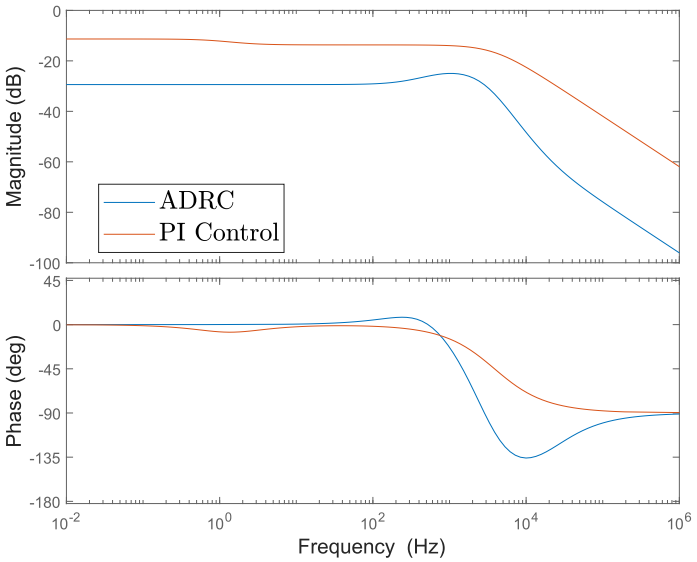


Figure 4.18 Magnitude (top) and phase (bottom) of Eq. (3.22) for cavities using ADRC and PI for A/ϕ control. The responses are simulated using the gains in Table 4.4.

bandwidths means the overall disturbance to the cavity phase from vibrations is smaller. Additionally, the attenuation of higher frequencies naturally helps prevent crosstalk between the amplitude and phase from high frequency disturbances/resonances.

ADRC can find its use-case in narrow-band cavities. We can see in Fig. 4.18 that the magnitude of the crosstalk between the phase and amplitude is on average 20 dB lower than with PI controllers, including low-frequency components. This is advantageous in narrow-band cases where a given detuning/disturbance makes a larger impact to the cavity phase. However, we have demonstrated that careful considerations must be made when the cavity possesses high-frequency mechanical resonances that are strongly coupled to the Lorentz pressure.

We know that increasing ω_c will result in a sharper peak in the frequency response, it would be interesting to see if we can see a similar effect with PI controllers. Examining Eq. (3.22), we can pick out a few trends for PI controllers; taking the proportional term as having the larger impact when compared to the integral term, we can see that increasing the amplitude proportional gain while maintaining constant phase proportional gain will result in increased attenuation of higher frequency components. Increasing the phase proportional gain while keeping constant amplitude

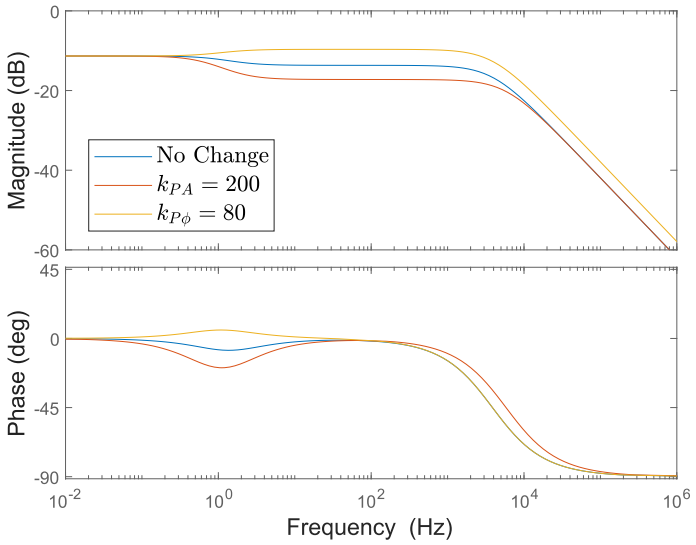


Figure 4.19 Bode/frequency response of Eq. (3.22) with A/ϕ PI controllers using the base gains in Table 4.4 for a $\beta = 0.53$ HWR at $E_{acc} = 7.4$ MV/m and $\psi_0 = -26°$. Changed gain parameters and the corresponding curve are detailed in the plot legend.

proportional gain will result in the opposite effect. We showcase these changes with respect to the PI gains in Table 4.4 and their effect on the frequency response in Fig. 4.19. From this trend, we can surmise that if we increase the phase proportional gain without adjusting the amplitude proportional gain it is possible we can encounter the same harmonic excitation that we see with ADRC.

4.3 Instability Measurements at Different Temperatures

In this section we present the first comparison of instability thresholds at different operational temperatures. During the FRIB yearly summer maintenance, there is a recommissioning period at 4.3 K for all HWRs before they are cooled to the operational temperature of 2 K. We were able to measure the instability thresholds at 4.3 K and noticed that they were higher than those at 2 K. The results of these measurements are presented in Fig. 4.20.

It is clear that in most cases, the FRIB HWRs at 4.3 K trend outside the statistical range of the thresholds at 2 K. In the case of these measurements, we stop increasing detuning around $\psi_0 = \pm 45°$ due to saturation of the forward power (for machine safety considerations). In most

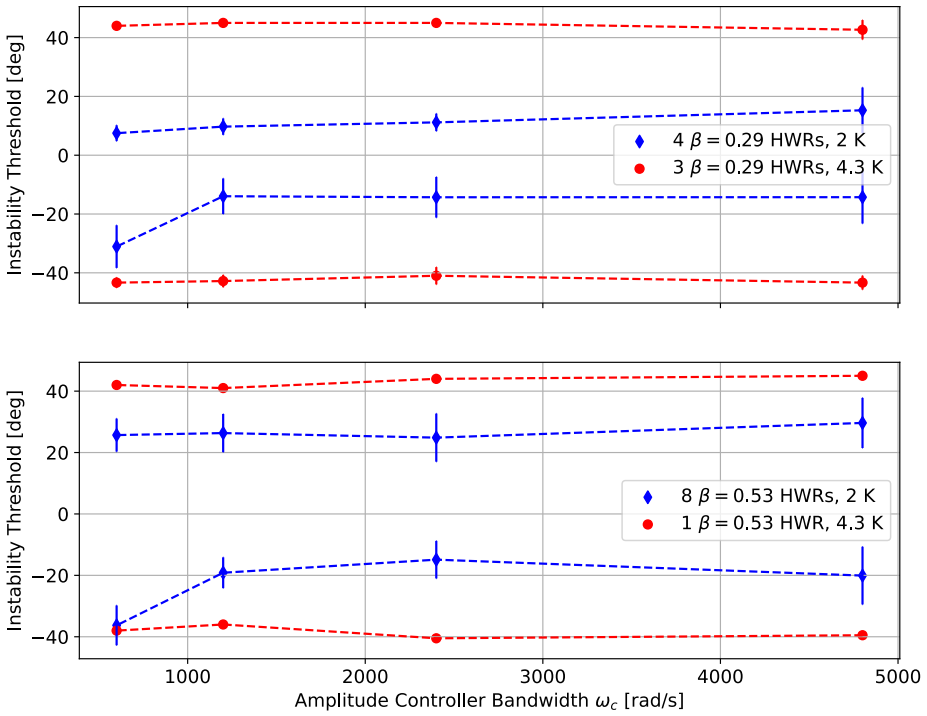


Figure 4.20 Instability threshold in terms of detuning angle v. amplitude controller bandwidth for $\beta = 0.29$ HWRs at $E_{acc} = 7.7$ MV/m (top) and $\beta = 0.53$ HWRs at $E_{acc} = 7.4$ MV/m (bottom) for both 4.3 K and 2 K measurements.

cases, the measurements were stopped just at ±45° or we encountered an instability just before this region.

4.3.1 Addition of Noise

One of the main differences between the cavity environment at 4.3 K and 2 K is the background noise. As we discussed in Chapter 2, the 4.3 K cryogenic environment is noisier than the 2 K environment. In particular, LHe is LHe-II (superfluid) at 2 K which eliminates the effect of nucleate boiling/bubbling near the cavity walls. One hypothesis we can propose that a white noise floor can influence the closed-loop system by masking disturbances from the mechanical modes.

In particular, we will make use of our A/ϕ ADRC Simulink model for the $\beta = 0.53$ HWR with some slight modifications. The modified simulation model can be seen in Fig. 4.21. We have added the microphonics transfer (MTF, Eq. (2.47)) function using the Ω_μ's and Q_μ's from the Lorentz transfer function. The real experimental microphonics couplings k_μ^M are unknown, and as such we introduced weak couplings for each mode ranging from $0.001 - 0.005$ Hz/N. The

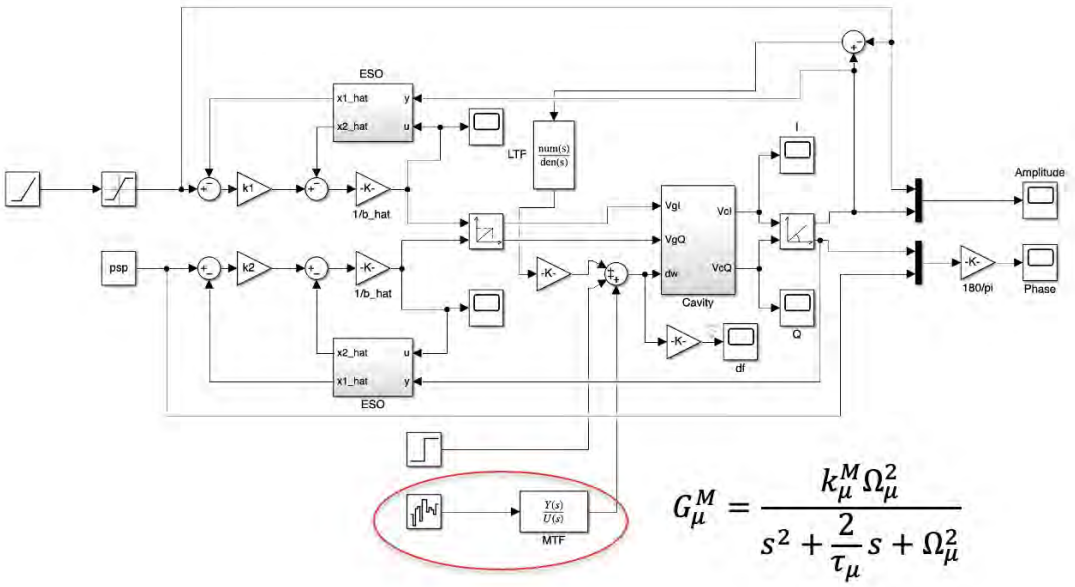


Figure 4.21 Simulink model of ADRC+cavity system with the addition of the MTF noise source (circled in red).

MTF is fed with band-limited white noise sampled at 300 Hz. The result is that the input to the MTF should mirror (to a decent approximation) the 4.3 K spectral background. We report that this does not affect the instability threshold for either side of the resonance curve. The $\psi_0 < 0$ instability sees no improvement in terms of threshold, and the rate at which the oscillations saturate is increased (Fig. 4.22). It can be seen that after the kick, there is a rapid increase in oscillations in the detuning before it settles. We see that without the noise, the instability is still excited but it takes longer to manifest. We can examine the frequency components that are excited with the MTF noise (Fig. 4.23), and we see that the detuning is dominated by the mechanical modes.

Removing the MTF and feeding the band-limited white noise directly to the cavity detuning does not provide any change either, as can be seen in Fig. 4.24. Like the case with the MTF, the system reaches saturation in the growth of oscillations faster with the noise than without. We again present the frequency components of the added noise in Fig. 4.25; we can see without the MTF, the noise is much more broadband. In terms of the positive side instability, the addition of noise also does not change the instability threshold. This makes sense on paper as we have shown that this instability is related to the A/ϕ controllers. However, it is clearly seen in Fig. 4.20 that there

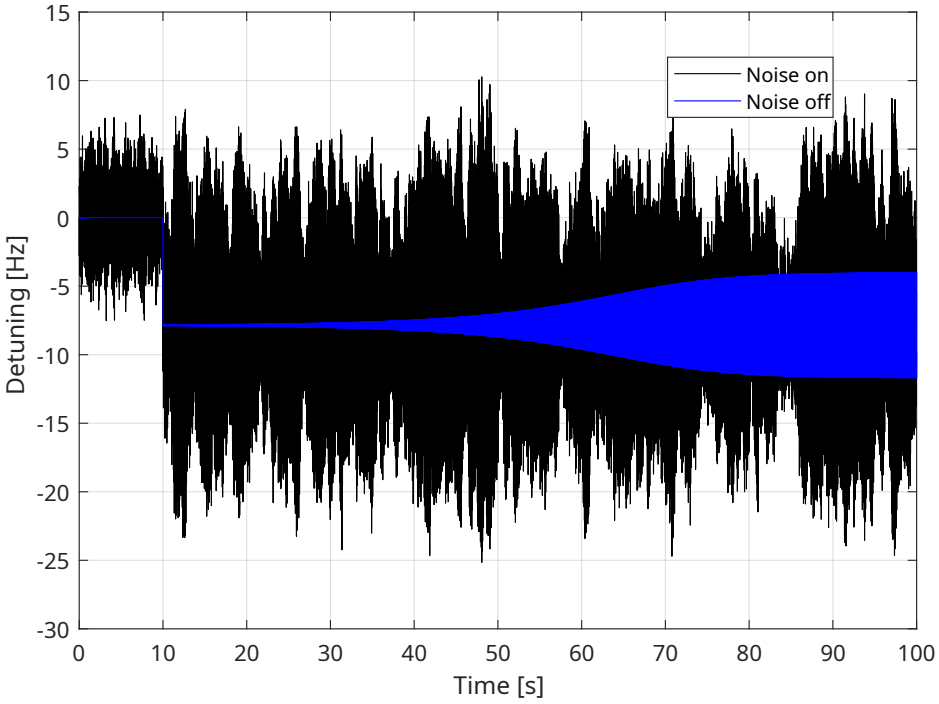


Figure 4.22 Simulated detuning v. time when the $\beta = 0.53$ HWR is given a kick to the instability threshold with and without the MTF noise.

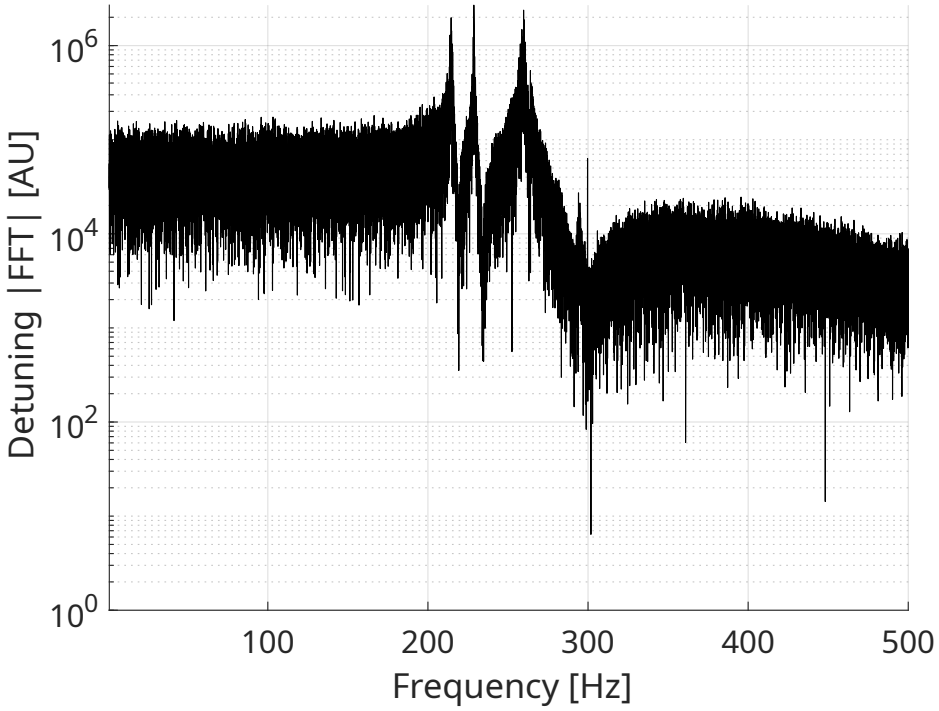


Figure 4.23 FFT amplitude of the detuning v. frequency for an instability event including noise from the microphonics transfer function. The notch in the FFT amplitude at about 300 Hz is due to the fact that the noise is sampled at that frequency.

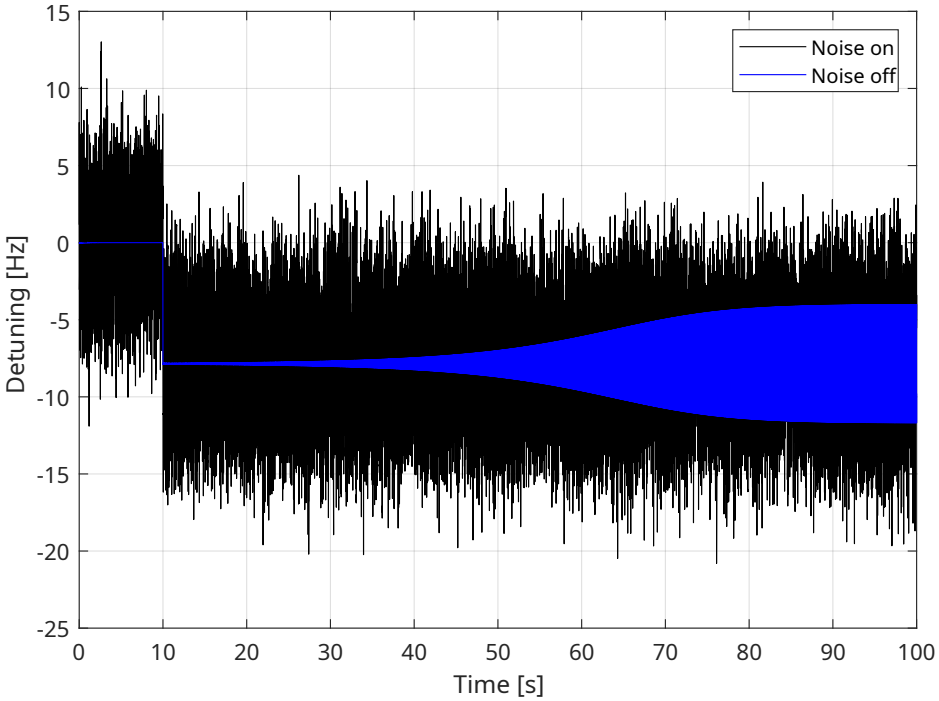


Figure 4.24 Simulated detuning v. time for white noise included and without at the instability threshold.

is a difference between the thresholds at different temperatures. That being said, our Simulink model does not match the experimentally measured instability threshold at 2 K. Additionally, we can see from Fig. 4.23 and Fig. 4.25 that our noise spectrum are quite flat except for mechanical modes. It is possible that the 4.3 K spectrum is not nearly as flat as our simulations, and has strong components that interfere with the instability. Thus, we cannot say for sure that noise doesn't affect the instability thresholds in some way. However, we can now look elsewhere to try to explain the effects we see for the oscillatory instability.

4.3.2 Bath Pressure

If we examine Eq. (3.23), we can look for terms that seem most likely to change between 4.3 K and 2 K. FRIB LLRF is handled digitally in baseband, so the responses $G_{A/\phi}(s)$ should not vary with temperature. Changes to $\omega_{1/2}$ as a result of decreased Q_0 at 4.3 K are negligible for both HWRs. With regard to the structure of $G_\mu(s)$, there are a few other options. The LFD couplings k_μ^L are dependent on the geometry and the Lorentz pressure distribution and thus should not change. Mechanical resonance frequencies Ω_μ are dependent on the stiffness of the structure, and while the

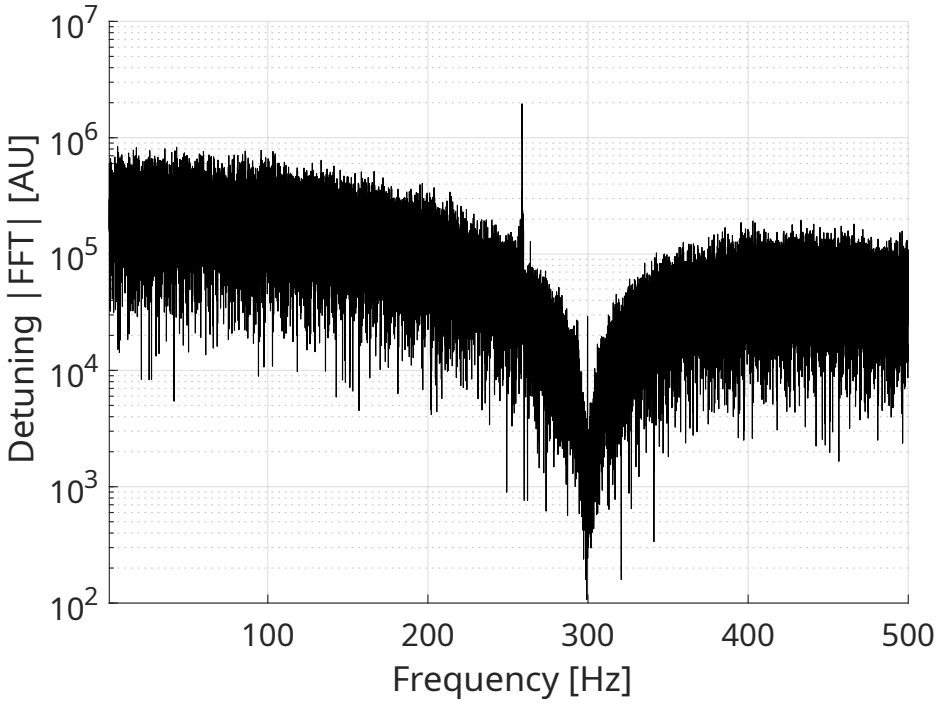


Figure 4.25 FFT amplitude of the detuning v. frequency for an instability event including white noise without the MTF. We can see that modes strongly coupled to the Lorentz force are present in the spectrum (Eq. (3.22)).

stiffness of niobium increases from room temperature to 4.3 K, the change between 4.3 K and 2 K is minimal. The final choice is that of the mode quality factor Q_μ. Increasing the structure stiffness will result in lower Q_μ, which can in turn lead to an increase in instability thresholds. While the increase in niobium stiffness from 4.3 K to 2 K is negligible, there is another variable that can be considered that might provide the difference.

At 4.3 K, the helium bath at FRIB is maintained around 880 Torr, or 1.16 atm. To maintain LHe-II, the bath must operate at conditions below the lambda point. In terms of pressure, this requires a bath pressure below 40 Torr at 2 K; a $\sim$ 95% drop in pressure. It is possible that the higher pressure of the 4.3 K bath provides additional stiffness to the cavity, thus lowering the Q of the mechanical modes. We can use our Simulink and analytical models to predict the necessary decrease in Q_μ in order to account for an increase in instability threshold up to and beyond the half-bandwidth. We optimize this decrease for ω_c = 4800 rad/s, which should correspond to an equal or larger threshold for lower ω_c. The results are graphed out in Fig. 4.26. Just as in the

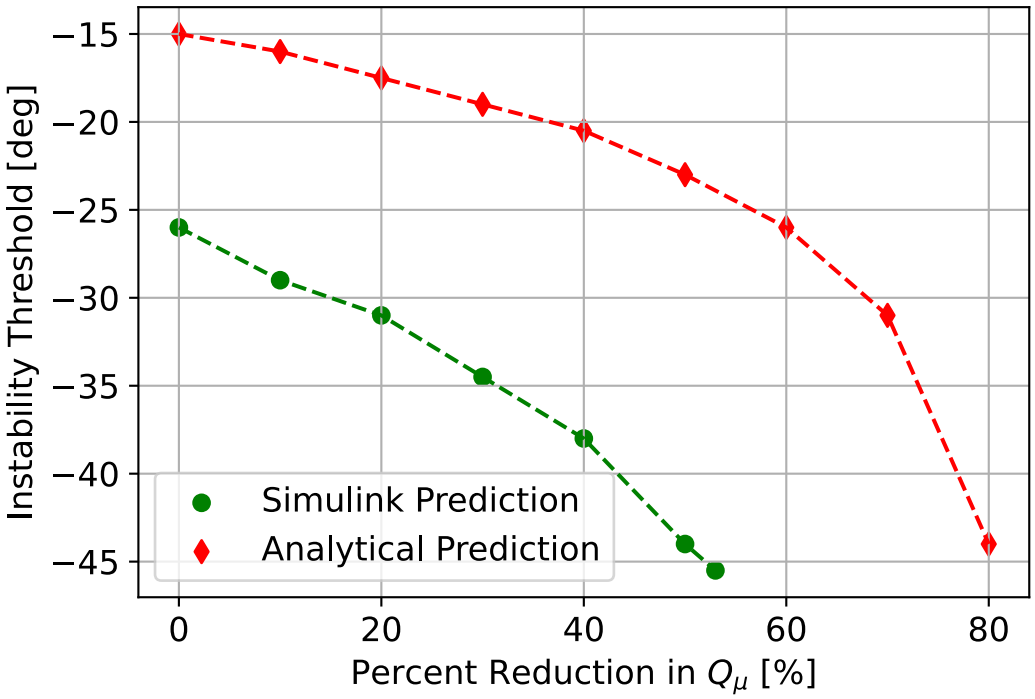


Figure 4.26 Oscillatory instability thresholds v. percentage reduction in mechanical quality factors for $\omega_c = 4800$ rad/s, $\omega_{ob} = 19200$ rad/s, and $E_{acc} = 7.4$ MV/m.

prediction of the oscillatory instability threshold, there is some spread between the prediction by the analytical model and the Simulink model. This remains true even as we reduce Q_μ. Between the two models, we can expect that a 50-80% drop in Q_μ is needed in order to push the instability thresholds to the half-bandwidth and beyond.

We report that reducing the Q_μ's does not affect the threshold on the positive side. This is expected for a controller induced instability that is independent of the electromechanical behavior in the same fashion the noise did not have an effect on the controller instability threshold.

4.3.2.1 Mechanical Quality Factor Measurements at 4.3 K

We can perform measurements to test our hypothesis in the FRIB linac during the yearly maintenance. We present a photo of the measurement setup in Fig. 4.27. The main transmission line to the fundamental power coupler is disconnected and a Type-N adapter is connected. The cavity is then driven in open-loop with an external RF generator. Impedance matching is improved at 4.3 K, so there is no need for additional amplification on the forward power. The pick-up power

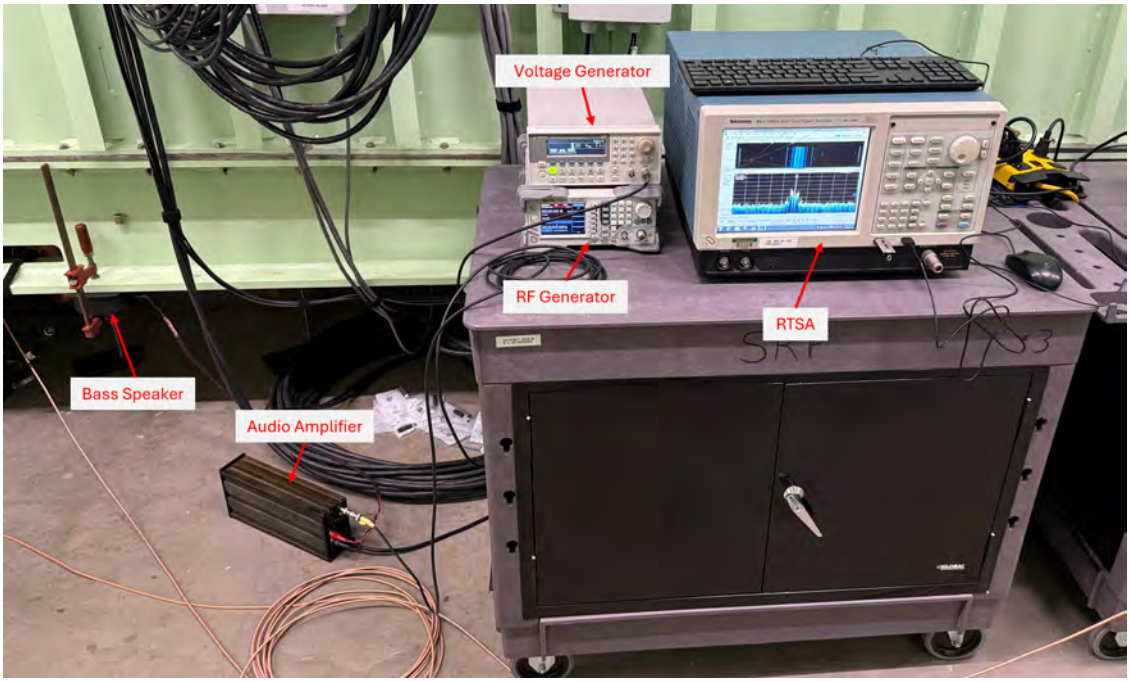


Figure 4.27 Photo of the experimental setup used in the accelerator tunnel to measure mechanical quality factors of $\beta = 0.53$ HWRs in their cryomodules.

is passed to a real time signal analyzer (RTSA) where we can examine the modulated signal from the carrier within a certain frequency span.

A bass speaker with an audio amplifier is used to shake the cryomodule; the speaker is clamped to the bottom of the cryomodule near the location of the cavity. A voltage function generator provides the sinusoid waveform to be passed to the bass speaker via the audio amplifier, allowing for variations in the frequency and amplitude specified by the voltage function generator. The exact force applied by the bass shaker is unknown, but it is not needed for this measurement; the gain of the audio amplifier is not changed between measurements and thus each cavity sees similar shaking from the speaker.

For mechanical decay measurements, one tone is excited (the mechanical resonance) and then allowed to decay. The pick-up spectra are captured and logged by the RTSA. Modulations of the cavity's amplitude and phase appear as sidebands to the carrier. The sideband amplitude with respect to the carrier ([dBc]) can be related to the phase modulation amplitude $\Delta\phi$ [120] and thus the detuning. In the first approximation of a two gap system, the detuning relates linearly to

displacement of the gaps. Thus measuring the decay of the sidebands can be related to the decay of the mechanical motion.

For these measurements, we are interested in the time it takes for the sideband to decay 6 dBc within the linear region. A linear fit can be used in this region to predict the 6 dBc decay time. An example of a decay measurement and corresponding fit is shown in Fig. 4.28. The -6 dBc decay time τ_{-6} can be converted to an exponential decay time τ_e for the mode via,

$$\tau_e = \frac{\tau_{-6}}{\frac{6}{10}\ln(10)}, \tag{4.15}$$

from which the mechanical quality factor can be found:

$$Q_\mu = \frac{\tau_{e,\mu}\Omega_\mu}{2}. \tag{4.16}$$

Using -6 dBc as a metric is not necessary, any dBc value can be used. However, using a smaller decay amount will increase the relative uncertainty, especially within the linear regression. At cryogenic temperatures, the cavity resonant frequency will drift with time, leading to changes in the sideband amplitude as the cavity shifts from the drives. For this reason, we determine the quality factor from the decay of both the positive and negative sidebands and average the two values. Two to four decays were taken for each mode across three different cavities.

We found during the measurements that the mechanical resonances are slightly shifted up from their value at 2 K, with some variations in the mechanical frequencies from cavity-to-cavity. A table of the resulting mode frequencies and quality factors at both temperatures is given in Table 4.5 for a pneumatic tuner pressure of 22 PSIa (the tuner is depressurized relative to operational pressures and is not being supplied helium gas). This tuner pressure is relevant in regard to our instability studies as this is the pressure that is set during the yearly maintenance warm-up. We see that for the four resonances we see in the Lorentz transfer function, there is a decrease in Q_μ across the board. In particular, the mode that is most strongly coupled to the Lorentz force sees a sharp decrease.

Additionally, it is also worthwhile to check the behavior of these quality factors as we vary the tuner pressure as it is possible that changing the pressure can affect the mechanical quality factors. We repeated these measurements at 30 PSIa and 40 PSIa, the results of which can be seen

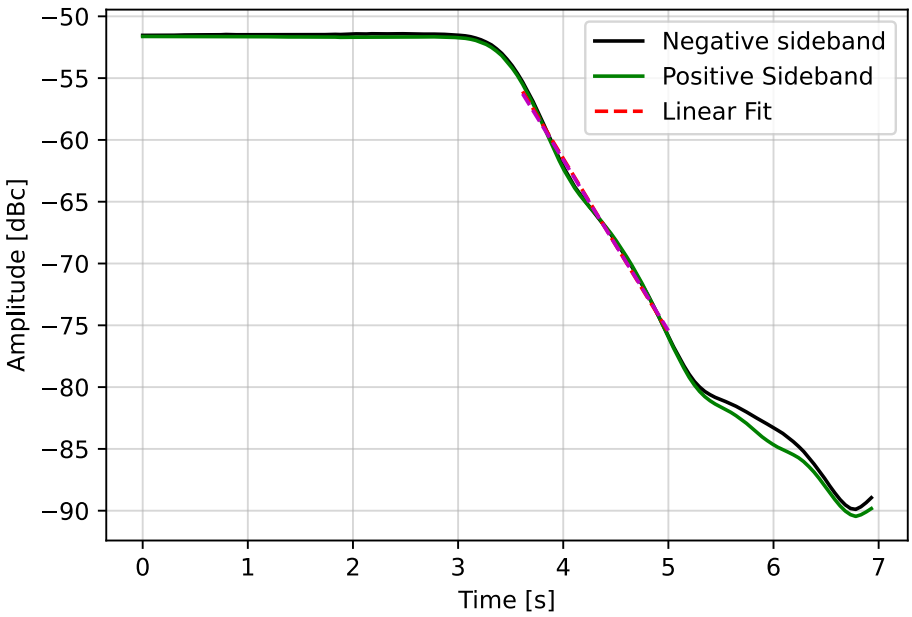


Figure 4.28 Sideband amplitude in terms of dBc v. time for an example decay measurement. The mode excited in this decay is the 261.6 Hz resonance.

Table 4.5 Mechanical mode frequency, quality factors, and percent changes from the 2 K values for key modes at 2 K and 4.3 K at 22 PSIa tuner pressure.

f_μ(2 K) [Hz]	Q_μ(2 K) [NA]	Q_μ(4.3 K) [NA]	% Change
259.3	400	290 ± 70	-27.5%
260.12	740	250 ± 30	-67.9%
264	700	400 ± 200	-33.3%
228.97	1400	900 ± 200	-35.7%

in Fig. 4.29. We note that the two resonances near 260 Hz (two modes that do not appear in modal simulations) change as we increase the tuner pressure in three cavities, whereas the 264 Hz and 228 Hz resonance frequencies stay relatively constant as we vary the tuner pressure. For this reason, we believe that the two resonances near 260 Hz are resonances of the cavity and tuner system. We plan to run modal simulations and measurements to confirm this relationship in a future work.

If we use our measured Q-factors for the appropriate modes in our Simulink and analytical models (without changing the LFD couplings), we can see what the predicted thresholds are. We plot the predicted results against the measured instability thresholds in Fig. 4.30. In this case, we are using the quality factors measured at 22 PSIa as this is the tuner pressure we measured the 4.3 K

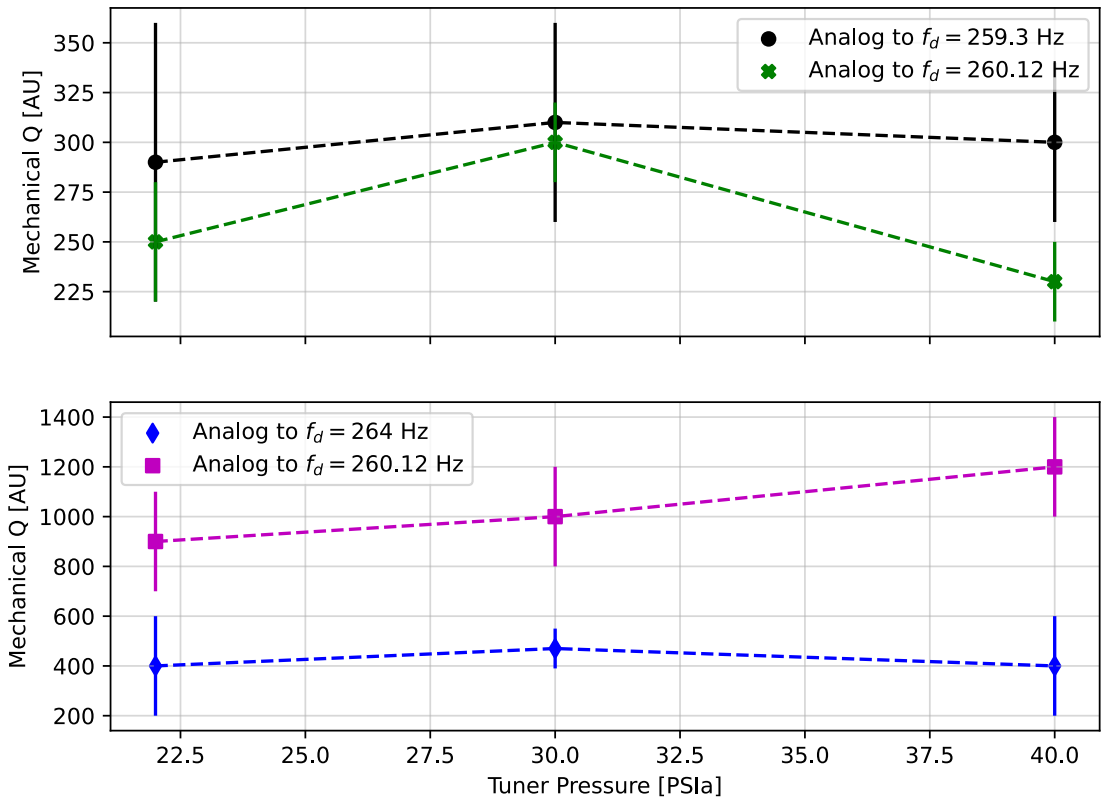


Figure 4.29 Mechanical quality factors v. tuner pressure for resonances we expect are combined cavity and tuner resonances (top) and for resonances that are predicted by modal simulations (bottom).

instability thresholds at. From Fig. 4.29, we can see that the relevant quality factors do not vary too much with pressure and therefore we do not expect much variation in the predictions with changes in tuner pressure.

It is clear from Fig. 4.30 that while a reduction in Q_μ can account for larger oscillatory instability thresholds, this reduction (as we have measured here) cannot reliably account for the measured instability thresholds we see at 4.3 K for all controller bandwidths. In our current position, there is only one parameter left to explore experimentally in terms of changes and that is the LFD couplings themselves. Our treatment here has treated k_μ^L as constant in regard to the cavity temperature. The definition of k_μ^L itself depends on the the geometry of the cavity and the overlap of the electric and magnetic fields with the mechanical mode shapes. In theory, these factors should not change much between 4.3 K and 2 K. One way to tell for sure is to measure the LTF for a cavity at 4.3 K and

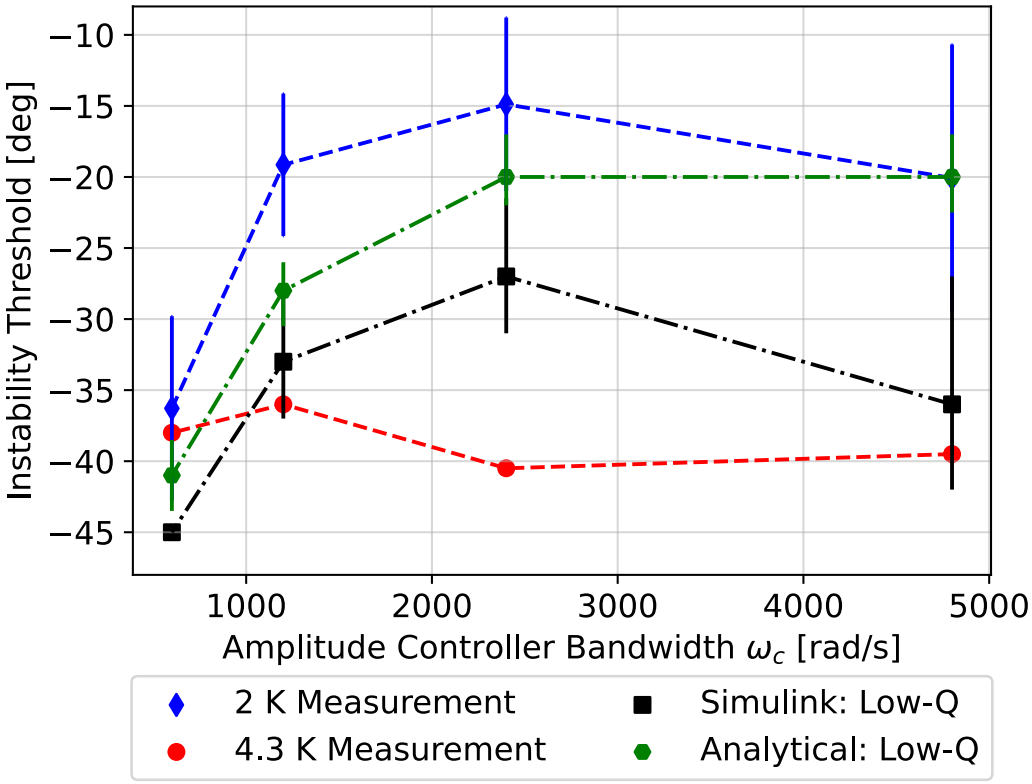


Figure 4.30 Instability threshold in terms of detuning angle v. amplitude controller bandwidth: measured and predicted values for 2 K and 4.3 K Q_μ values. Error bars represent the instability thresholds at the upper and lower errors for the respective Q_μ values in Table 4.5.

2 K to compare the couplings which we plan to conduct in the future. Due to testing availability, we were not able to accomplish this measurement in time for this work.

4.4 Predictions for Medium Velocity, Elliptical Cavities

We have shown that our predictive methods have provided accurate predictions of the onset of the oscillatory instability in narrow-band, medium-velocity coaxial resonators. Both FRIB and PIP-II utilize another cavity for medium-velocity acceleration: the $\beta_g = 0.61$, five-cell elliptical cavity. Both machines will use a nearly identical cavity; the main difference is the design resonance frequency. The FRIB energy upgrade cavity will operate at 644 MHz and the PIP-II LB650 will operate at 650 MHz.

In this section, we will present predictions of the oscillatory instability threshold for these cavities. Elliptical cavities, by their geometry, are less stiff than their coaxial counterparts. A

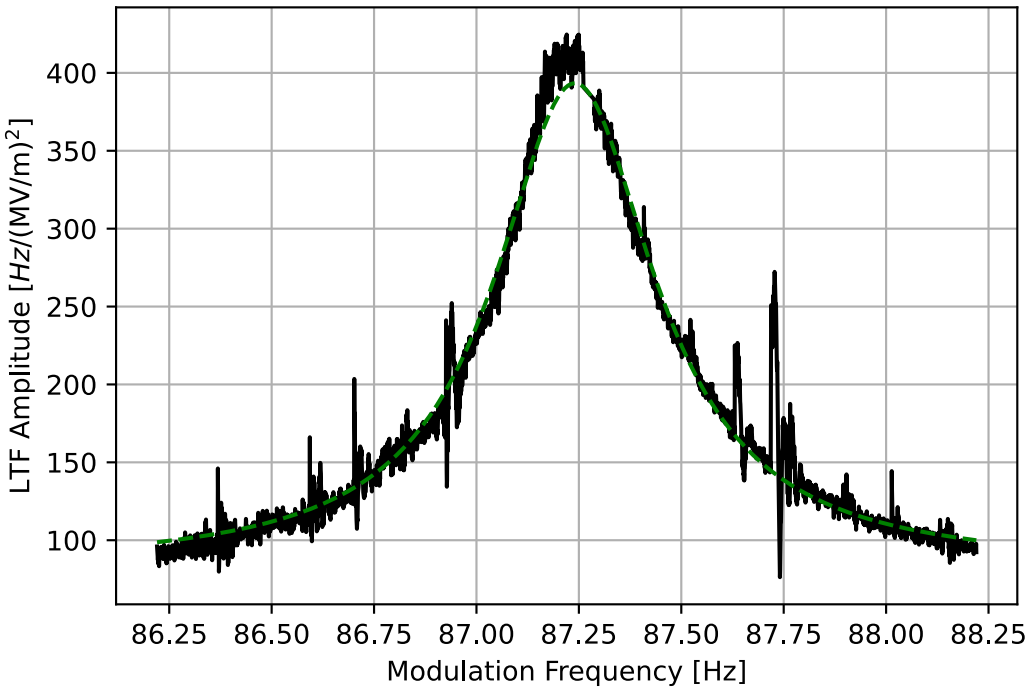


Figure 4.31 LTF amplitude v. modulation frequency for a LB650 cavity equipped with mock tuner.

result is the presence of strong, accordion-like mechanical resonances close 100 Hz for these two cavities. For both the FRIB energy upgrade and LB650 cavities, the LFD effect has been predicted to be strong, with the static Lorentz force detuning kick to be $\Delta f_{LFD} \geq 38 f_{1/2}$, or 38 times the half-bandwidth for either cavity.

To gauge the dynamic effect, we were able to capture a portion of the LTF for the LB650 cavity equipped with a mock tuner (some additional stiffness applied but not the specification tuner stiffness) at the Spoke Test Cryostat at Fermilab. We present the measurement of the LTF amplitude for the dominant mechanical mode in Fig. 4.31. The peaks and valleys in this measurements are due to strong impulse microphonics observed at the cryostat. Because the FRIB energy upgrade and LB650 cavities are nearly identical, we expect the electromechanical behavior to be very similar to each other as well.

The measurement in Fig. 4.31 gives us a baseline for this mode's coupling and Q-factor when the mock tuner is equipped. The measured static LFD coefficient for this test was 6.2 Hz/(MV/m)^2, with a measured modal coefficient 1.82 Hz/(MV/m)^2 (29% of the static coefficient). Through a

Table 4.6 Simulation/analytical parameters used for instability predictions for the FRIB energy upgrade cavity.

Quantity [units]	Value
f_0 [MHz]	644
Q_l [NA]	2×10^7
E_{acc} [MV/m]	17.5
f_μ [Hz]	87.12
Q_μ [NA]	144
k_μ^L [Hz/(MV/m)^2]	0.5343

Table 4.7 Simulation/analytical parameters used for instability predictions for the FRIB energy upgrade cavity.

series of comparisons of simulated and measured static LFD coefficients as well as assuming that the mode coefficient maintains the same percentage of the static coefficient, we can predict that with the tuner equipped the modal coefficient will have a value close to $k_\mu^L = 0.5343$ Hz/(MV/m)^2. We have measured the Q-value for the analogous mode on a room temperature cavity equipped with the real tuner to be $Q_\mu = 144$. From these two values, we can make predictive simulations/analysis for the instability thresholds in the FRIB energy upgrade cavity. We list the relevant simulation parameters for the FRIB energy upgrade cavity in Table 4.7.

We focus particularly in this section on the FRIB energy upgrade case for one particular reason: the cavity will operate at slightly higher field (17.5 MV/m v. 16.8 MV/m) for a higher Q_l (2×10^7 v. 1.01×10^7). We will therefore look at the more narrow-band case where the oscillatory instability can be more prevalent. The results of our predictive means can be seen in Fig. 4.32. As one might expect from examining Fig. 4.13, we see the expected trend in the instability threshold for the FRIB energy upgrade predictions. We see at the operational LLRF parameters for the HWRs ($\omega_c = 4800$ rad/s) the two methods produce different thresholds, with the Simulink model producing thresholds almost twice as large. As this model contains a more realistic ADRC implementation, we suggest that this threshold be the more realistic prediction.

One simple way to push the instability thresholds is to increase the controller gain beyond the HWR standard. In this case, we double the max ω_c to 9600 rad/s and see a large jump in the instability thresholds by over 15° in both prediction models. Additionally, we can increase the max

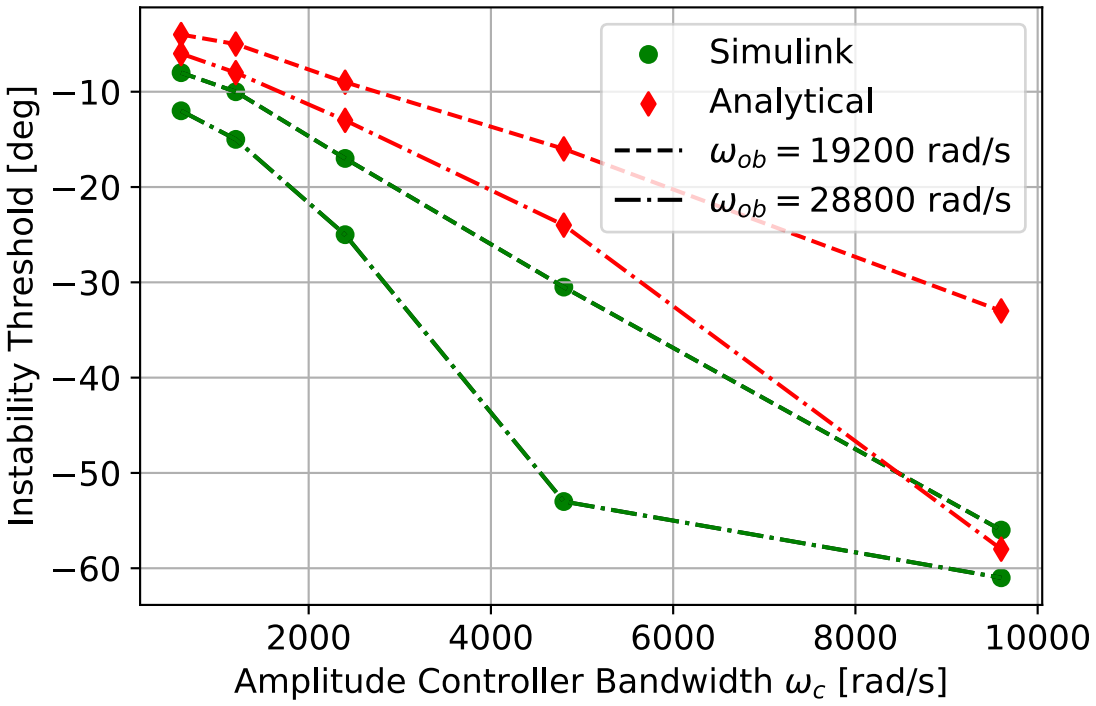


Figure 4.32 Predicted instability thresholds v. ADRC amplitude controller bandwidth for the FRIB energy upgrade cavity operational parameters.

observer bandwidth to $\omega_{ob} = 6\omega_c = 28800$ rad/s, and we see that the predicted instability threshold is pushed to $> -55°$. Thus by simply increasing our controller and observer bandwidths, the oscillatory instability can be pushed beyond the half-bandwidth. Of course, this is easier said than done and studies need to be done on whether existing LLRF/RF infrastructure can accommodate the larger controller parameters. Because the controllers themselves are unchanged, we expect the positive side instabilities to follow the same trend as the HWRs.

CHAPTER 5

RESONANCE CONTROL OF SRF CAVITIES

We have talked extensively about one of the effects of detuning in the form of the ponderomotive instabilities. In particular, we spent the last chapter discussing the effects A/ϕ and I/Q control loops can have on the instabilities. While these loops can push the instability thresholds, they do not attack the root cause: A/ϕ or I/Q controllers do not help tune the cavity back to the generator frequency, they simply provide more power to the cavity in order maintain the respective setpoints and thus accelerator synchronicity. Even without encountering the ponderomotive instabilities, detuned cavities will cost more to operate than those tuned on resonance. Additionally, too much detuning can or will lead to a trip of the machine protection interlocks through many different means, resulting in increased accelerator downtime.

The goals of resonance/frequency control are then: reduce RF power costs, prevent ponderomotive instabilities, and reduce the number of machine protection trips. In Chapter 3, we introduced the idea of frequency/resonance control and two types of tuners used to carry out frequency corrections on the cavity. In this chapter, we will focus on the piezoelectric tuner and algorithms for resonance control. This includes how to mathematically model the effects of the tuner and experimentally characterize it. We will also discuss control algorithms for the tuner and show simulated and experimental results of resonance control.

5.1 The Piezo Transfer Function

5.1.1 Mathematical Modeling

Like the Lorentz pressure, the piezo-tuner is coupled to the cavity frequency with its own characteristic driving term. For a single mechanical mode, we again have the driven oscillator equation:

$$\delta\ddot{\omega}_\mu + \frac{2}{\tau_\mu}\delta\dot{\omega}_\mu + \Omega_\mu^2\delta\omega_\mu = k_\mu^P\Omega_\mu^2 V_P(t), \tag{5.1}$$

where k_μ^P is the mode's coupling factor and $V_P(t)$ is the voltage applied to the piezo. Continuing the analogy, we can switch to the Laplace domain and define the transfer function for each mode:

$$G_\mu^P(s) = \frac{\delta\omega_\mu(s)}{V_P(s)} = \frac{k_\mu^P \Omega_\mu^2}{s^2 + \frac{2}{\tau_\mu}s + \Omega_\mu^2}. \tag{5.2}$$

In total, we define the piezo transfer function (PTF) as the sum of every mode's contribution.

$$G_P(s) = \sum_{\mu=1}^{\infty} \frac{k_\mu^P \Omega_\mu^2}{s^2 + \frac{2}{\tau_\mu}s + \Omega_\mu^2} = \sum_{\mu=1}^{\infty} G_\mu^P(s) \tag{5.3}$$

Just as in the case of the LTF, the PTF collapses to a single coefficient in steady-state conditions ($s = 0$):

$$G_P(s = 0) = \sum_{\mu=0}^{\infty} k_\mu^P = k_P, \tag{5.4}$$

where k_P is referred to as the static piezo coefficient and has units of rad/s/V.

5.1.2 Measuring the Piezo Transfer Function

Up to this point, the mathematical modeling between the LTF and the PTF has been extremely similar. Measuring the PTF and identifying relevant mechanical properties is largely the same as well. We can measure the PTF in a similar method: through modulating the piezo-stack voltage and sweeping through the modulation frequency. Recording the detuning response and piezo voltage waveforms, we can calculate the amplitude of the PTF in a manner analogous to the LTF. Unlike the LTF, the PTF can be reliably measured at both room and cryogenic temperatures. This makes testing and simulating control algorithms for piezoelectric tuners possible for a room temperature testbed. The PTF for an HB650 at our room temperature testing bench at Fermilab can be seen in Fig. 5.1.

The mode coupling strengths k_μ^P can be calculated just like the LTF couplings:

$$k_\mu^P = \frac{|G_P(j\Omega_\mu)|}{Q_\mu}. \tag{5.5}$$

Like the LTF and microphonics couplings, k_μ^P represents the overlap of the mechanical mode's shape and the deformation caused by the piezo-stacks. However, the applied static-load to the piezo-stacks will increase as we cool the cavity down to cryogenic temperatures due to contraction

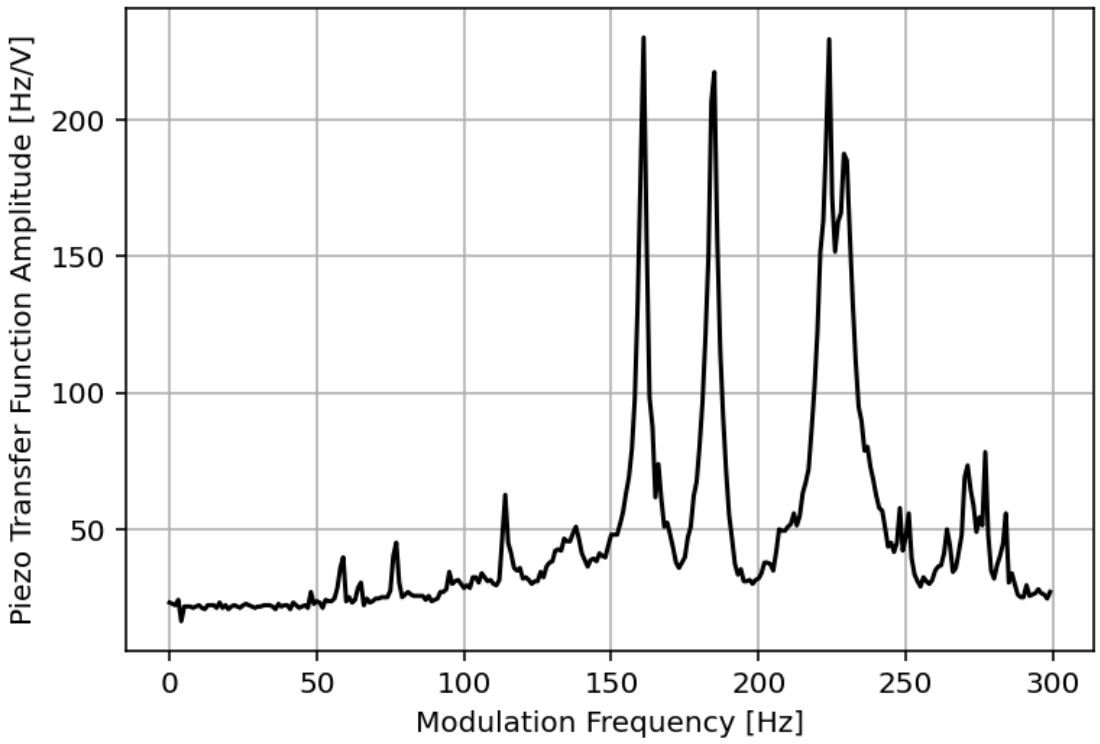


Figure 5.1 PTF amplitude v. the piezo voltage modulation frequency for a room-temperature HB650 cavity.

of the titanium and steel tuner structure. As such, the couplings will differ slightly between room and cryogenic temperatures. We have also shown that Q_μ will change at cryogenic temperatures due to differences in niobium stiffness and ambient environment differences. However, a room temperature PTF can still be used to design and simulate control algorithms which we will soon discuss.

Measuring the PTF at room temperatures can present other information as well. In one case, we were able to measure the PTF for the tuner-loaded FRIB energy upgrade cavity at room temperature. We note the detuning measurements in the top of Fig. 5.2. Note the strongly coupled resonance at 140 Hz, which could also be excited via a second harmonic with a 70 Hz drive. The strongest predicted cavity resonance is visible at 96.5 Hz, and as such this 140 Hz resonance is unexpected.

To see if this was a real cavity resonance, we decoupled the piezo-stacks from the cavity and oriented the cavity vertically to significantly reduce the effect of the tuner structure. The resulting detuning measurements can be seen in the bottom of Fig. 5.2. It is to be noted that the boundary

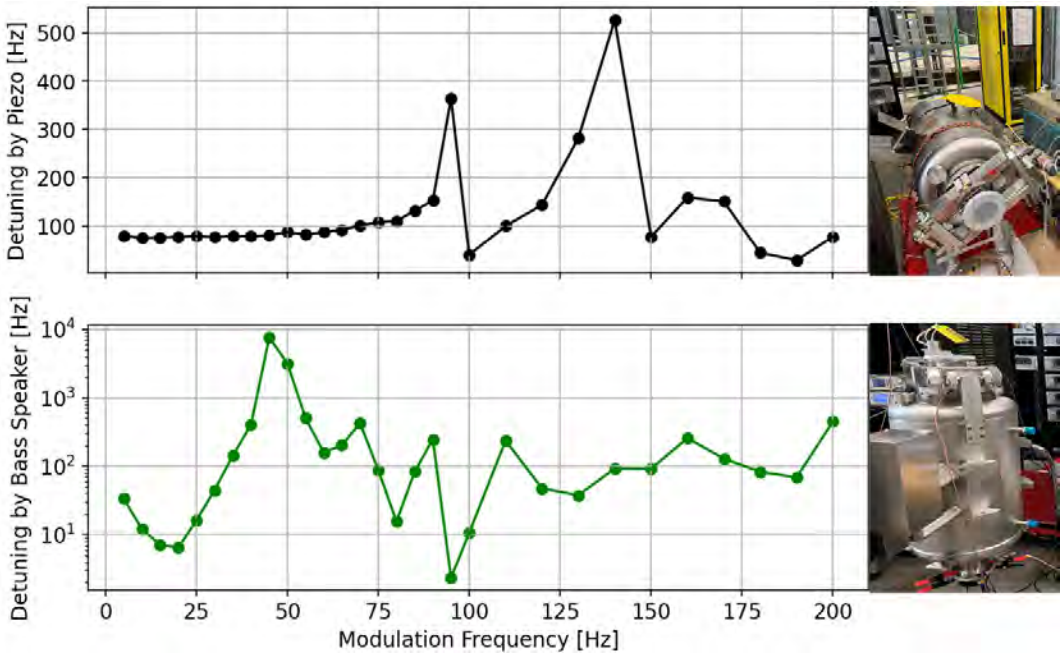


Figure 5.2 Detuning cause by piezo-voltage modulation v. modulation frequency (top), and detuning caused by a bass speaker v. modulation frequency when the piezo stacks are decoupled and the cavity is oriented vertically (bottom).

conditions change from a fixed-fixed condition to a fixed-free orientation. As such, the dominant mechanical mode falls to the half-harmonic (about 48 Hz). Driving the vibrations with a bass speaker along the beam-axis, we notice this resonance disappears. This tells us that the 140 Hz resonance is a combined cavity and tuner mode. Knowing that this mode exists at room temperature is useful as it allows us to: 1) identify it at cryogenic temperatures if a strong, unknown resonance is present during prototype testing and 2) consider it during piezo controller design.

5.2 Controlling the Piezo

In the previous chapter, we discussed at length the A/ϕ control loops and how they interplay with each other and the LTF. Controlling the tuner presents its own uniqueness when we compare it to A/ϕ control loops; in A/ϕ control, the cavity is the plant/system whose electrical behavior we are trying to control. Adding the LTF is a natural extension when designing A/ϕ control schemes as it interplays with the cavity amplitude and phase directly, but it is not controlled directly. An diagram of a cavity with amplitude, phase, and resonance control loops can be seen in Resonance control requires controlling the electrical signal applied to the piezos, and thus the plant is the PTF

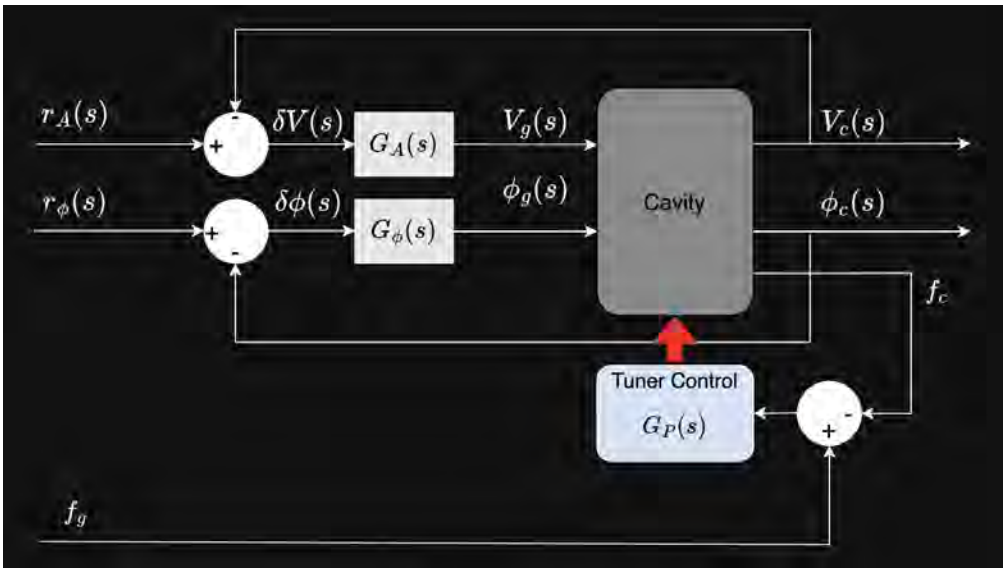


Figure 5.3 Diagram of an SRF with all three types of control loops: amplitude, phase, and resonance control. The amplitude and phase controllers change the drive to the cavity while the resonance controller deforms the cavity to match the drive frequency.

itself. In this way the problem is simplified: we are only concerned with one process variable with an independent control loop.

Even though the control loop for the piezo is different, the types controllers we can use are the same as in A/ϕ or I/Q control. PI control has already been applied to piezoelectric tuner control for low-frequency noise control [121, 77]. ADRC has been applied for resonance control for 1.3 GHz, TESLA-style cavities equipped with the SACLAY-II piezoelectric tuner [122]. Though the mechanical motion of the SACLAY-II is similar to the double, lever-arm style of LCLS-II, PIP-II, and FRIB energy upgrade cavities, the piezo couplings k_μ^P will be different.

In this section, we present a first application of ADRC to the double lever-arm style tuner to be used in PIP-II and the FRIB energy upgrade. We will showcase the algorithm employed in piezo control, and include simulations comparing the ADRC algorithm with a traditional PI controller. We then show preliminary results from our room temperature test bench using ADRC and PI algorithms.

5.2.1 Discretized ADRC for Tuner Control

We have already shown a discretized, first-order ADRC algorithm for A/ϕ control in Chapter 3. In this section, we follow along with Miklosovic, Gao, and Radke and adapt this for tuner control. The RF envelope equation that governs A/ϕ is first-order, but now each mechanical mode is a second-order oscillator. Instead of estimating each mechanical mode, we will use a second-order ADRC formulation to estimate the total detuning, derivative of the total detuning, and generalized disturbance. The update equations in Chapter 3, Section 3.3.2 still apply, but our matrices have changed to reflect the second order system. The Φ matrix is now,

$$\Phi = \begin{bmatrix} 1 & T_s & 0 \\ 0 & 1 & T_s \\ 0 & 0 & 1 \end{bmatrix}, \tag{5.6}$$

with an expanded observer gain vector,

$$\mathbf{L} = \left[1 - \beta^3,\ \frac{1}{T_s}(2 - 3\beta + \beta^2),\ \frac{1}{T_s^2}(1 - \beta)^3\right]^T. \tag{5.7}$$

Both $\mathbf{\Gamma}$ and $\mathbf{H}$ see an expansion to three elements with an extra zero at the end.

The control scheme is now adjusted for the derivative estimation. The plant input of this scheme is now given by:

$$U = \frac{\omega_c^2(R - \overline{x}_1) - 2\omega_c\overline{x}_2 - \overline{x}_3}{b_0}, \tag{5.8}$$

where $\overline{x}_1, \overline{x}_2$, and $\overline{x}_3$ are the estimations of the total detuning, its derivative, and the total disturbance respectively.

5.2.2 Tuner Control in Simulink

Simulink again shows its use as we can implement this discretized ADRC algorithm, the schematic for which we showcase in Fig. 5.4. As discussed, the plant is now the PTF. For our model, we will use the mechanical parameters for the HB650 as we measured in Fig. 5.1. We summarize the relevant parameters in Table 5.2.

One feature of the piezo-stack important to our modeling is the charging time for the piezo-stacks when a voltage is applied. In practice, this leads to an induced delay between the plant

Table 5.1 Mechanical parameters extracted from the piezo transfer function measurement for the room temperature HB650 cavity in Fig. 5.1.

Mode Number	k_μ^P [Hz/V]	Q_μ [NA]	f_μ [Hz]
1	0.2663	120	114
2	1.1803	20	136
3	1.9504	93	161
4	2.5404	73	185
5	1.3575	88	220
6	1.5715	65	226
7	0.0560	395	261
8	0.2429	145	268
9	0.1036	369	273

Table 5.2 Mechanical parameters extracted from the piezo transfer function measurement for the room temperature HB650 cavity in Fig. 5.1.

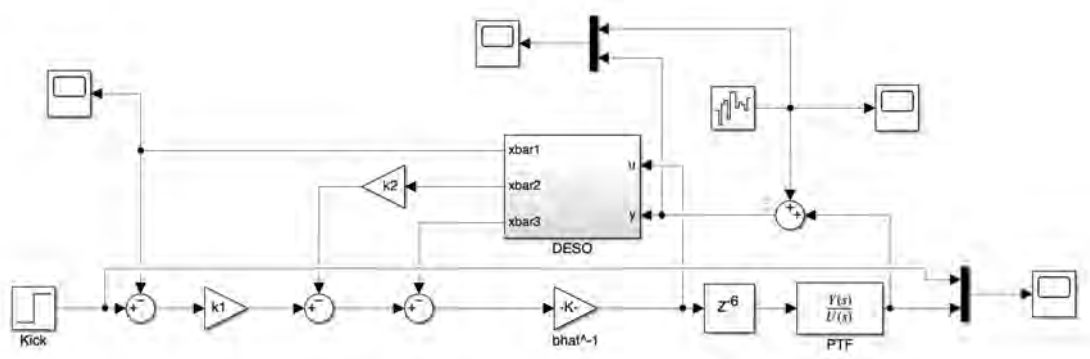


Figure 5.4 Schematic of discretized ADRC algorithm for control of the piezo transfer function in Simulink.

input and plant output. Our model in Fig. 5.4 takes this into account via the delay block (z^{-n}). We estimate the charging time of the equipped piezo-stack to be 300 μs. With a 200 kHz loop rate, this corresponds to a 6-sample delay.

Time-delay systems such as these can pose control limitations due to the mismatch between U and Y. The delays limit the estimation bandwidth of the DESO and thus control efficiency. For ADRC, [123] proposes a simple solution to help reduce the effect of the time delay: delay the input to the ESO by a time approximately close to the delay time. In this case, we put the delay block in its position to achieve this effect. For comparison, we created a second model with a discretized PI control scheme instead of the ADRC to examine the advantages and drawbacks. We present the

Table 5.3 Controller gains and loop rates used for simulation comparison.

Controller	ω_c [rad/s]	ω_{ob} [rad/s]	k_P [NA]	k_I [NA]	F_s [kHz]
ADRC	1256	6283	×	×	200
PI	×	×	0.00055	0.05	200

Table 5.4 Controller gains and loop rates used for simulation comparison.

relevant controller gains in Table 5.4.

5.3 Simulations and Comparisons

We now demonstrate a few baseline comparison simulations between ADRC and PI for tuner control. Both controllers are tuned to the max allowable proportional gain factors (ω_c and k_P in Table 5.4) before the onset of a controller induced instability. This means our simulated controllers are tuned to their fastest response times, though it is possible better long-term control is possible with alternate gain factors. One key test that can be done in comparing control algorithms is seeing both controllers' responses to sharp disturbances. In terms of tuner control, this means providing a strong detuning impulse to the output line after the PTF. We present the simulated impulse response for the two controllers in Fig. 5.5.

We see that the ADRC-controlled system settles to the setpoint 75% faster than the PI controller. For most cryomodule operation, jumps in the detuning like this are unlikely, but not impossible. For these cases, ADRC presents an advantage in recovering before a trip event. This fact will be important when we talk about ponderomotive instability with resonance control. Additionally, the fast recovery time presents a potential use case alongside a feedforward algorithm to clean up the residual detuning for low-rep-rate pulsed mode.

Another metric we can use to compare the two controllers is to simulate the detuning spread when exposed to stochastic noise. No matter the mode of operation, microphonics compensation is essential for power minimization. Testing both controllers' responses to stochastic noise is therefore a good metric to gauge energy efficiency. In our simulation, we add band-limited white noise sampled at $f_s = 30$ Hz to the output of the PTF and let the simulation run for 70 s. The cutoff of 30 Hz was chosen because we can see in microphonics measurements significant contributions from this range of components. We present the detuning after the tuner with histograms denoting

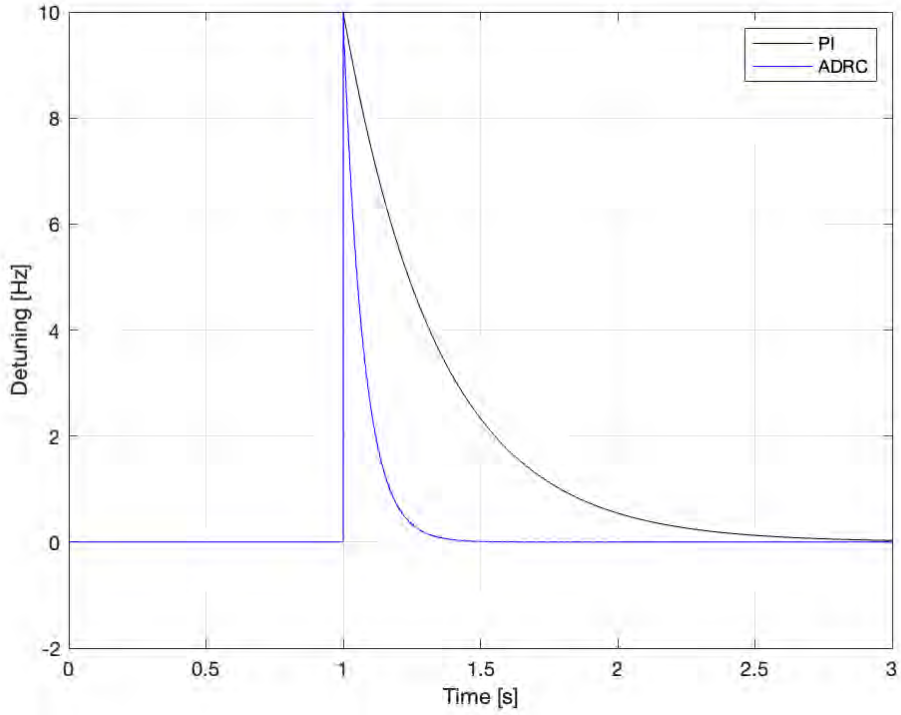


Figure 5.5 Detuning v. time for comparing the two controllers' response in response to a step/impulse disturbance.

the spread in Fig. 5.6.

We can see that with ADRC, we can save almost 1 Hz in RMS detuning over the PI-controlled tuner. This may not seem like a lot, but this effect can save a significant of power over a year of operation. Let us consider a simple example with the FRIB energy upgrade cavity operating at the specification field and coupling with a beam current of $I_b = 330\ \mu$A. Using Eq. (2.31), we can see that using ADRC can save $\sim$ 130 W of power over the PI-controlled tuner's RMS detuning. Over 5000 hours of CW operation over with the respective RMS detuning values, we can see that the ADRC-controlled cavity would use 650 kWh less power than the PI-controlled cavities. For the 55 proposed cavities for the FRIB energy upgrade, this would correspond to 35.75 MWh less RF power usage. Of course, this is a simple example based of simulated values and assumes all cavities are experiencing the same microphonics. Real operation of tuners in the proper cryogenic conditions is needed to reveal the true nature of RF power savings.

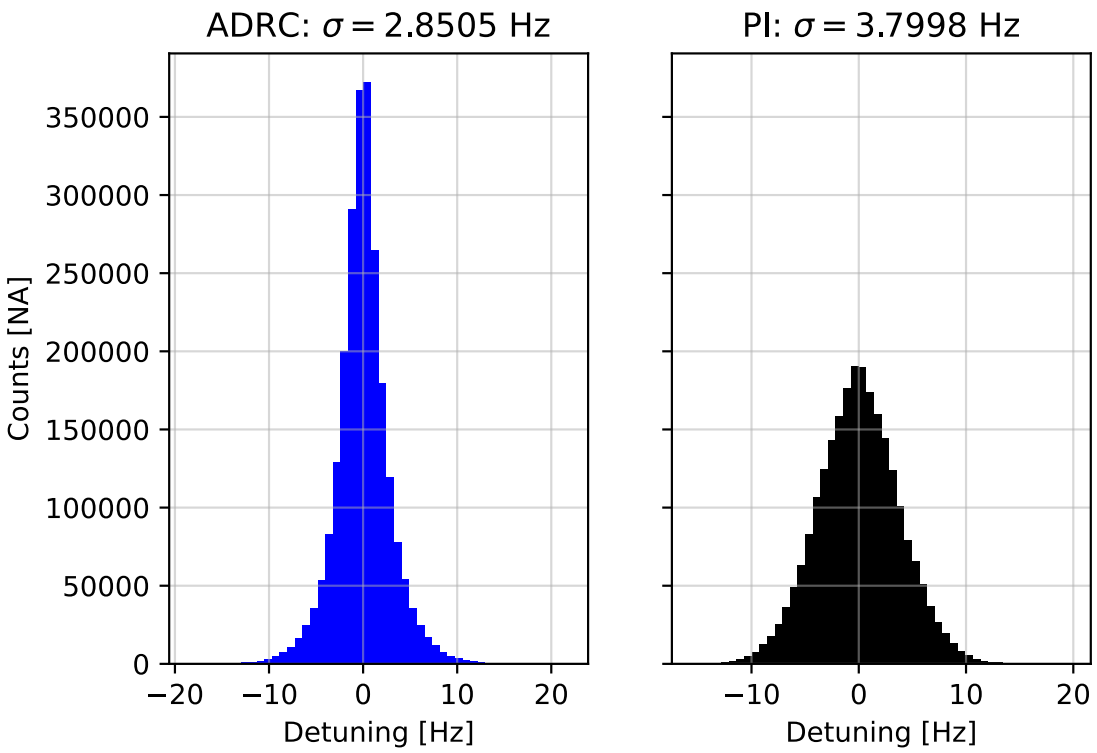


Figure 5.6 Histograms for detuning counts with a PI controlled tuner (left) and an ADRC controlled tuner (right). Relevant metrics for each tuner are given in their respective titles.

When it comes to dealing with discrete frequencies, piezo-tuners are effective in eliminating low-frequency noise. The efficiency at which these tones can be removed decreases as the tone frequency increases. To compare each controller's effectiveness at removing low-frequency tones, we add a sine wave with a 10 Hz amplitude. We vary the frequency of this noise from 0.5 Hz to 10 Hz and let the simulation run for 80 s where we calculate the RMS detuning at the end. The results can be seen in Fig. 5.7. We can again see that ADRC can give us an edge for countering low-frequency noise. Even up to 10 Hz tones, we can save almost 2 Hz of RMS detuning over the 0.5 Hz savings when compared to the PI-controlled tuner

5.3.1 Adding Noise Cancellation

In Chapter 3, we discussed the least-mean-squares (LMS) algorithm, and how it can adapt the piezo voltages to work towards cancellation of certain tones from the signal. While a finite-impulse-response filter form of the LMS algorithm exists, we will stick with time domain update

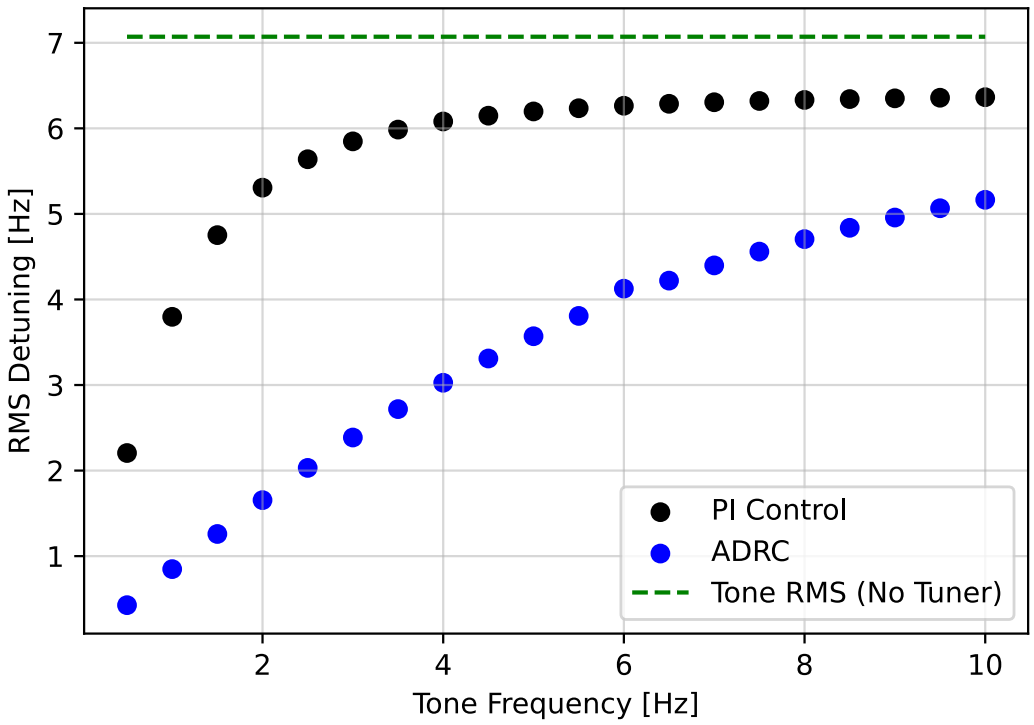


Figure 5.7 RMS detuning over 80s v. added tone frequency. The green dashed line is the RMS detuning with no frequency control.

method. In our Simulink model, we utilize the MATLAB function block using the update equations in Chapter 3. The inputs are the previously sampled piezo I_P/Q_P voltages and the simulation time. The outputs are the refined I_P/Q_P voltages, which are fed back to the input with a sample delay block. For the the first showcase, we present the effect of the LMS algorithm by itself and zero the contribution from the ADRC. We add a pure 20 Hz sinusoid with a 10 Hz amplitude to detuning. The effect of the LMS algorithm in removing the tone can be seen in Fig. 5.8.

Of course since the LMS algorithm can only target one frequency, it cannot be used in microphonics control by itself. We now pair the LMS with an ADRC controller to examine their combined effect. For this test, we use a combination of discrete frequencies we commonly see in microphonics measurements. In this spectrum there is still a 20 Hz tone, which we will let the LMS algorithm target. Without either means of control, the RMS detuning is σ_{none} = 5.75 Hz. The resulting histograms for 80 s of simulation for the two configurations are shown in Fig. 5.9.

We see that with both ADRC and the LMS algorithm, we can bring the RMS detuning down by

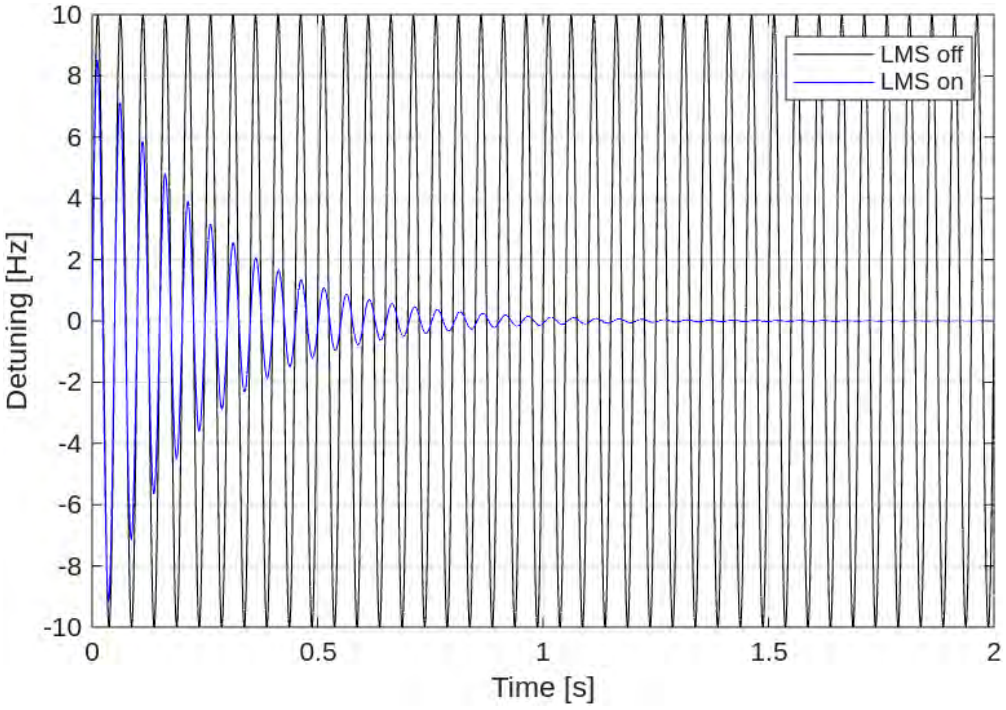


Figure 5.8 Simulated detuning v. time for tuner a tuner with and without using the LMS algorithm.

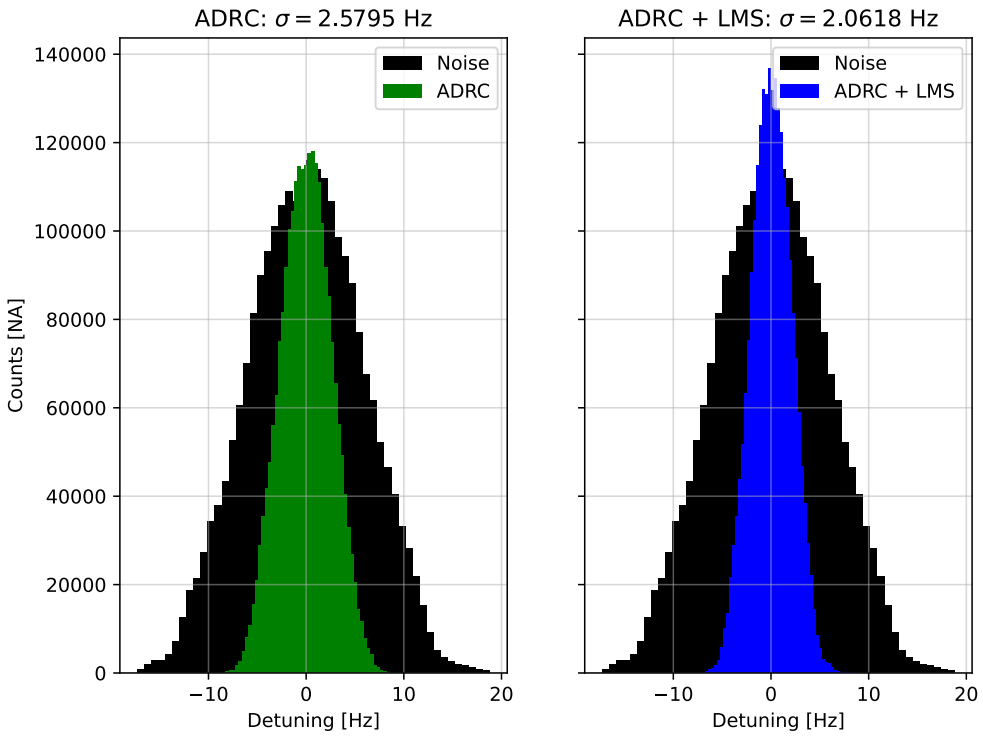


Figure 5.9 Histograms of detuning captured over 80 s for simulations with left) just ADRC and right) ADRC with the LMS algorithm. Included in both is the histogram of detuning with no control (i.e. raw noise).

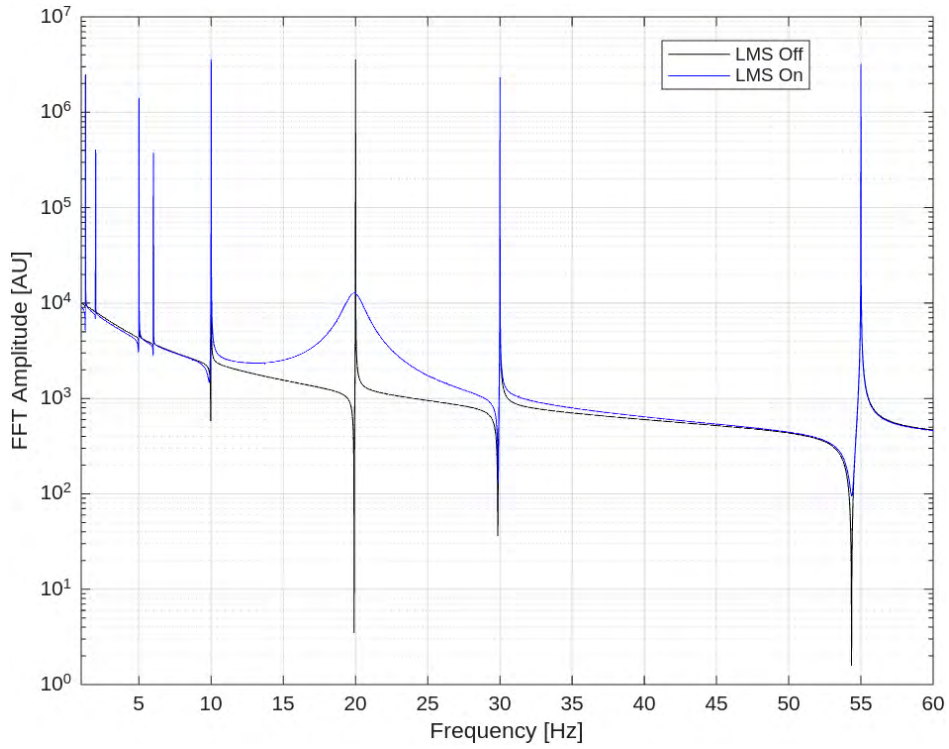


Figure 5.10 Fast Fourier transform of the simulated noise spectrum with and without the LMS algorithm. ADRC is enabled in both cases.

3.75 Hz from the no-control case. It can be seen that the 20 Hz component is the strongest out of the spectrum in Fig. 5.10. This is the advantage of using the LMS algorithm. If we can capture accurate microphonics surveys of the cryogenic environment, we can find problematic tones and deploy one or multiple LMS filters to eliminate them. Though multiple filters can be used, considerations must be made on frequency ranges to be compensated. In some cases, excessive compensation in one range will lead to worse control in another. For example in Fig. 5.10, the 20 Hz tone is significantly damped, but the lower frequency components see a slight amplification.

5.4 Experimentally Testing Resonance Control Algorithms

While testing resonance control algorithms at cryogenic temperatures would provide the most accurate representation of their performance in terms of microphonics compensation, testing costs can be cumbersome and scheduling can be difficult. It can be cost-effective and informative to test algorithms with room temperature cavities; this allows for debugging and identifying stable gain ranges before the final deployment to the cold cavity. In this section we detail the creation of such

a test bed at Fermilab and detail initial results for different resonance control algorithms deployed to a real cavity at room temperature.

5.4.1 Room Temperature Testing Bench

At the center of the testing bench is our jacketed, tuner-loaded HB650 cavity. The cavity is equipped with two probe-couplers, leading to strong under-coupling. The measured cavity forward and pick-up coupling factors were measured to be $Q_{e1} = 4.6\times10^5$ and $Q_{e2} = 2.1\times10^5$ respectively, with an intrinsic $Q_0 = 1.3\times10^4$. The resulting bandwidth ($f_{1/2} = 27.5$ kHz) is large compared to the expected detuning, meaning we can take advantage of certain equipment that cannot be used reliably at cryogenic temperatures (since $\Delta\phi \ll 1$).

A schematic of the circuit can be seen in Fig. 5.11 alongside a photo of the workbench. Our main method of tracking detuning is done with an Analog Devices AD8302 phase detector [124]. The forward and probe powers are sampled by the detector and a voltage is produced related to the phase difference $\Delta\phi$ between the forward and probe signals:

$$V_\phi = m_\phi(\Delta\phi - 90^\circ) + V_{CP}, \tag{5.9}$$

where $m_\phi = 10$ mV/1° and the center point voltage is $V_{CP} = 0.9$ V. Initially, the analog phase shifter is used to set $\Delta\phi = 0$ and then detuning can then be calculated digitally in terms of voltage deviation from V_{CP}. The phase voltage V_ϕ is sampled by an National Instruments ADC with a 20 kHz sampling rate and passed to a LabVIEW VI. It is in this VI that feedback is handled; the control algorithms (ADRC or PI) are used to calculate the necessary correctional voltage to maintain $\Delta\phi = 0$. The correctional voltage is then converted to analog via a DAC and then sent to the piezo amplifier.

It is to be noted that the test bed does not necessitate the use of a 650 MHz cavity. The phase detector, shifter, and bi-directional coupler are all capable of supporting GHz frequencies, meaning that the cavity can be swapped to any cavity for LCLS-II and PIP-II. It is also worth mentioning that this bench allows for the measurement of the room temperature piezo transfer function, allowing for relevant simulations to be made for comparison. By setting all relevant gains to zero, we can see how the cavity frequency changes in the ambient environment. For static air flow, we don't see

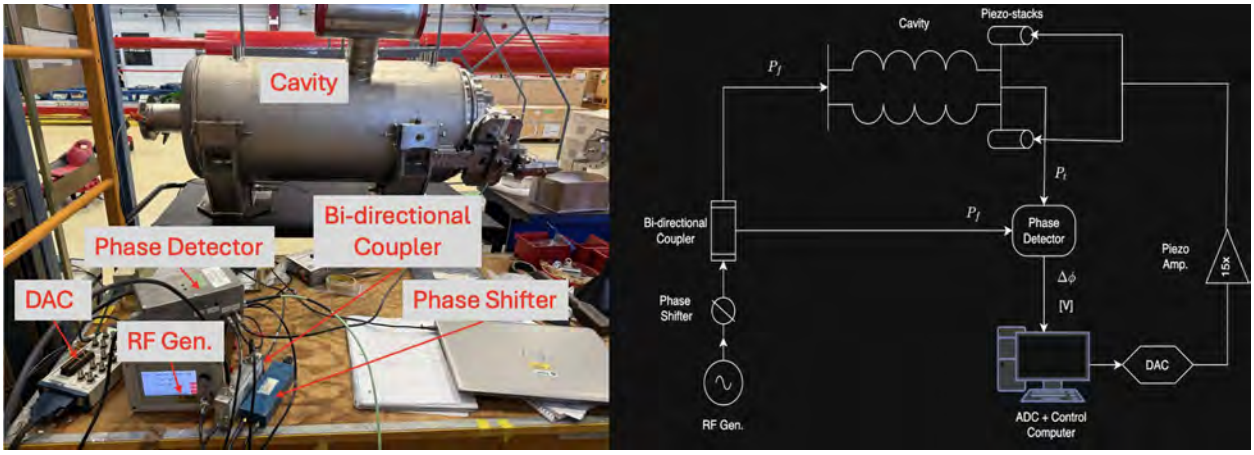


Figure 5.11 Photograph of the room temperature testing bench at Fermilab (left) and the relevant circuit diagram of the bench (right). Not pictured in the photograph is the ADC and control computer.

exceedingly strong low-frequency components (10+ Hz). However, there is an expected drift due to local temperature changes. An example of this drift can be seen in Fig. 5.12.

Further examining Fig. 5.12, one will notice that there are some sharper disturbances to the phase voltage, for which the cause is unknown. The test bench is located on the working floor of the Fermilab Industrial Center and there are many candidates: opening of garage and exit doors, lifting of heavy equipment, and/or shaking of the test bench. Additionally, swapping one phase detector with another of the same model does not remove these disturbances. Alongside the fact that the phase voltage recovers eventually, these two observations lend to the idea that the cavity is experiencing shocks from the environment. Whatever the cause, these disturbances will help us by giving the control algorithms something else to compensate for as we will discuss in the next section.

5.4.2 Baseline Algorithm Testing

Two control programs were coded in LabVIEW, one with the discretized ADRC described in Section 5.2.1 and the other with a discrete form of PI. Our sampling rate of 20 kHz is set by the LabVIEW ADC; any lower sampling from within the LabVIEW code will result in a buffer overflow. Our discretized ADRC is extremely sensitive to the sampling rate, and we can use our Simulink model to give estimates of stable gain coefficients. After manually tuning, we find that

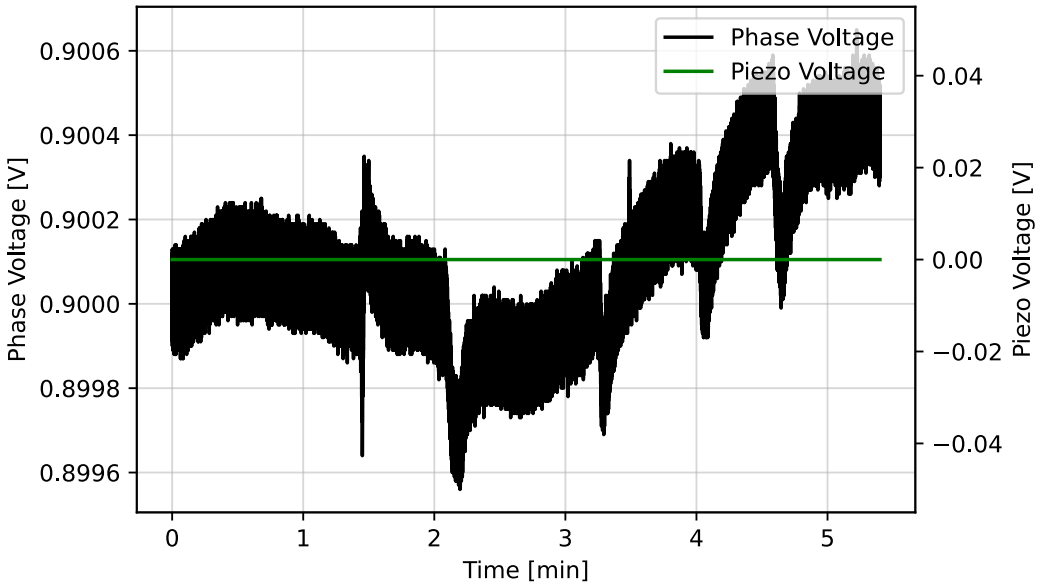


Figure 5.12 Phase and piezo voltage v. time when no control is applied. Again, the cavity is tuned to the generator when V_ϕ=0.9 V.

$\hat{b} = 4.74 \times 10^6$ V/(rad/s)^2 and $\omega_{ob} = 3000$ rad/s give the largest stable region. With this observer bandwidth, we can operate with $\omega_c \leq 600$ rad/s, with higher controller bandwidths resulting in unstable working points. Our goal is to keep the phase voltage as close to 0.9 V as possible, and thus we will include all slow drift effects in this section to view what each controller will allow.

An example of a resonance control measurement for ADRC for the best parameters can be seen in Fig. 5.13. One thing is clear from this capture, upon closing the ADRC loop, the controller first overshoots even when initially tuned to V_{CP}. This is common for any capture of ADRC regardless of ω_C. Within the first minute, the system is pushed closer to the setpoint as the ADRC corrects the estimations $\hat{\mathbf{x}}$. While the piezo voltage looks flat from 45 s onward in Fig. 5.13, this is not the case. If we window the data from 45 s to the end of the capture, we can see a more realistic representation of the ADRC behavior (as seen in Fig. 5.14. When these random disturbances occur, we can see that the piezo-stacks react in opposition to them. In fact, we can see that the piezo-stacks react with a magnitude in proportion to the disturbance. This gives an important confirmation that the piezo-stacks are acting in opposition to the disturbances and that the corrections are not random.

We can compare the performance of this algorithm's performance with that of traditional PI

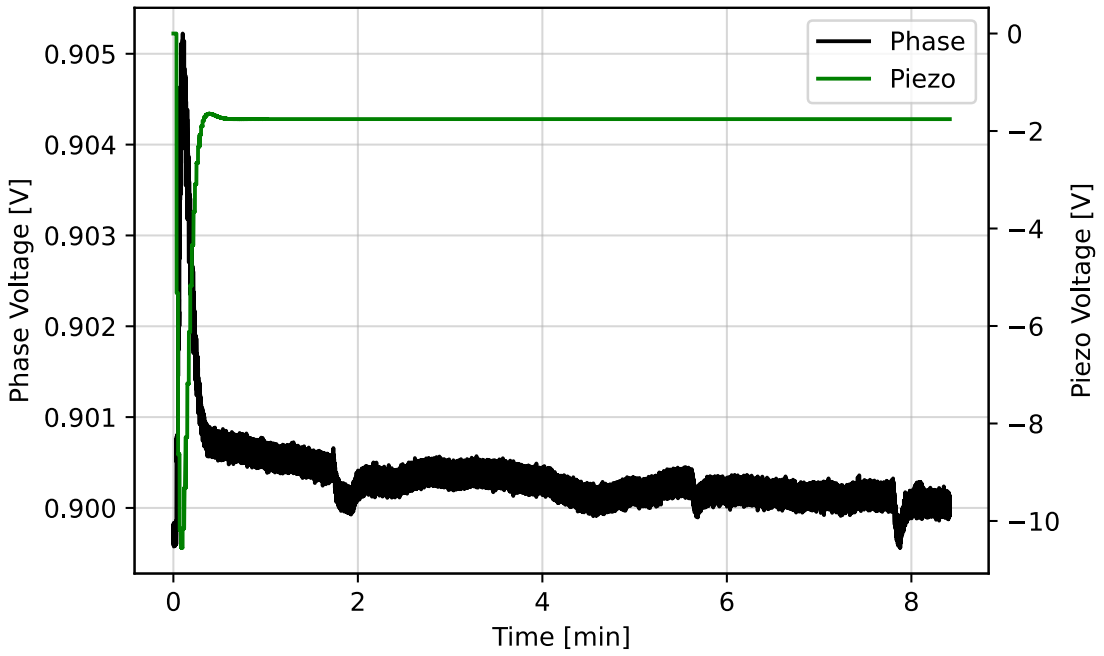


Figure 5.13 Phase and piezo voltages v. time for a capture with ADRC with $\omega_c = 400$ rad/s, $\omega_{ob} = 3000$ rad/s, and $\hat{b} = 4.74 \times 10^6$ V/(rad/s)^2. The RMS phase voltage was $V_{\phi,RMS} = 0.900346$ V, which corresponds to $\Delta f_{RMS} = 33$ Hz for the room temperature cavity (0.06% of the cavity bandwidth).

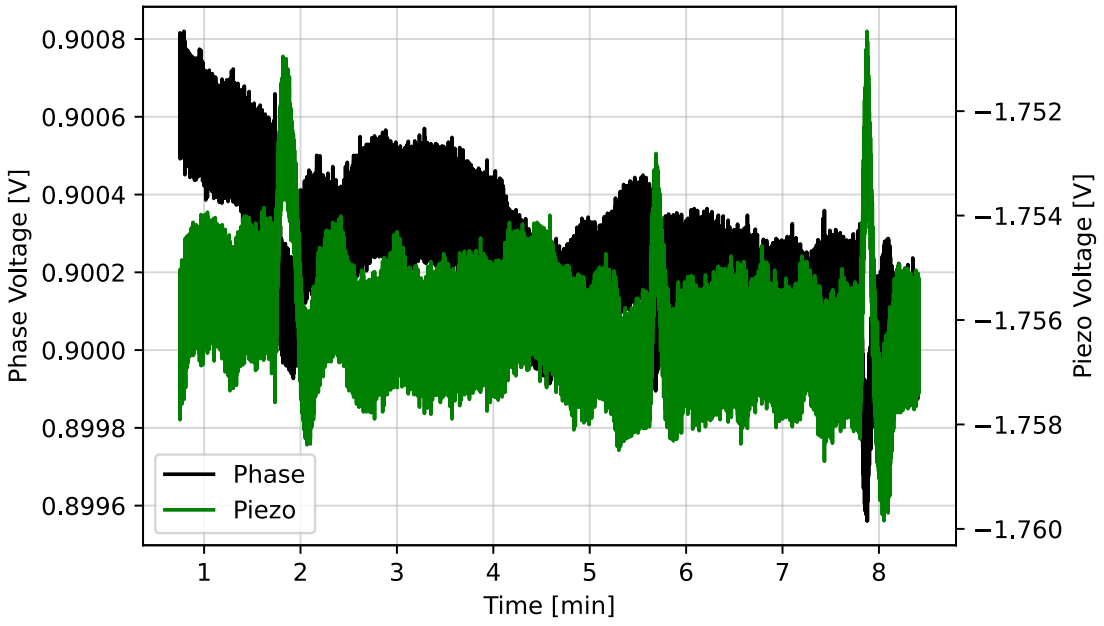


Figure 5.14 Phase and piezo voltages v. time for a windowed look at the data in Fig. 5.13.

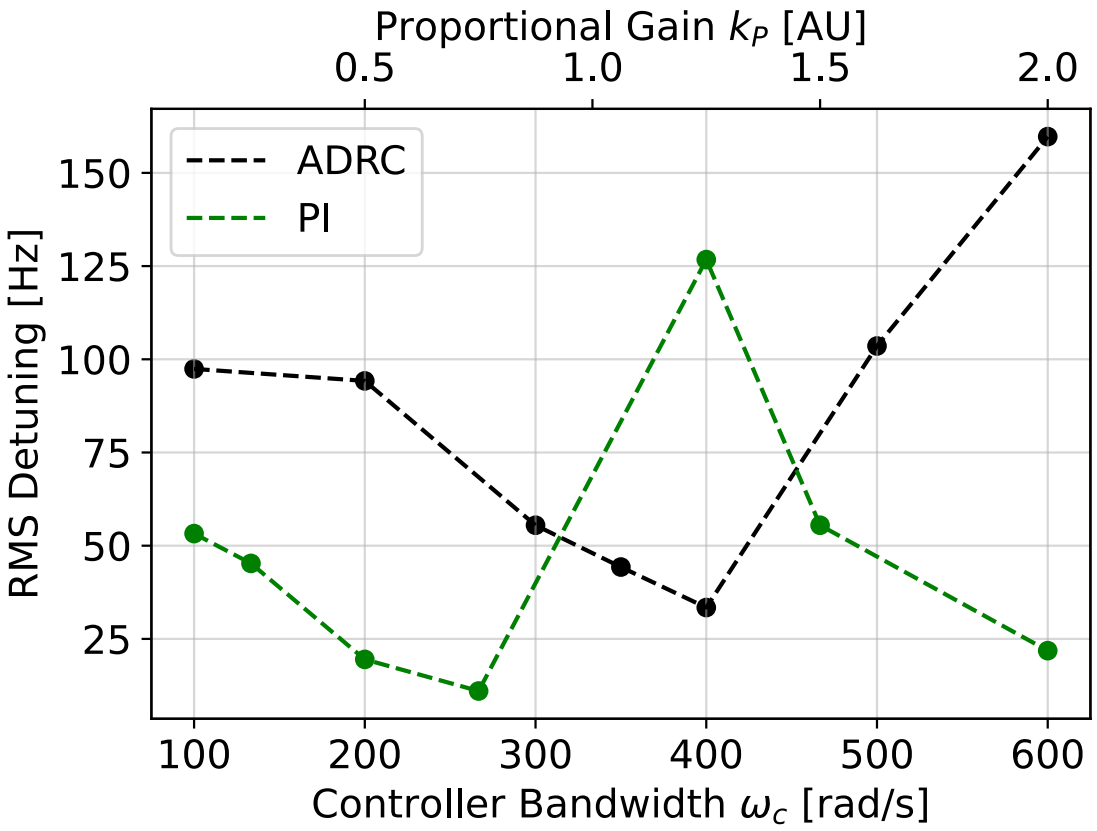


Figure 5.15 RMS detuning v. respective proportional gain factors for the tuner under ADRC and PI control. Observer bandwidth and integral gain are held constant at $\omega_{ob} = 3000$ rad/s and $k_I = 2000$ respectively.

control. Like ADRC, there is an experimental upper limit on the proportional gain k_P, where $k_P > 2$ results in unstable behavior for our cavity. We can follow along with the idea of Fig. 5.7, where we look at the RMS detuning but for different control gains up to the respective limits instead of specific tone frequencies. In Fig. 5.15, we can see some differing behavior between the two controllers: the RMS detuning for ADRC follows a more trend-like behavior with a high RMS detuning when the gain is low and then decreases as we move into the optimal tuning range of $\omega_{ob} \approx 5\omega_c$ to $10\omega_c$ and then increase again as we start to leave that working point.

For the PI controller, we see that RMS detuning varies much more wildly than with ADRC. There is a regime where the PI controller oscillates closely around zero ($k_P = 0.5 - 0.75$). Examining the phase voltage waveforms of these PI captures yields more information. We see that there is significant deviation in the phase voltage as time progresses which can signify a key detail. The fact

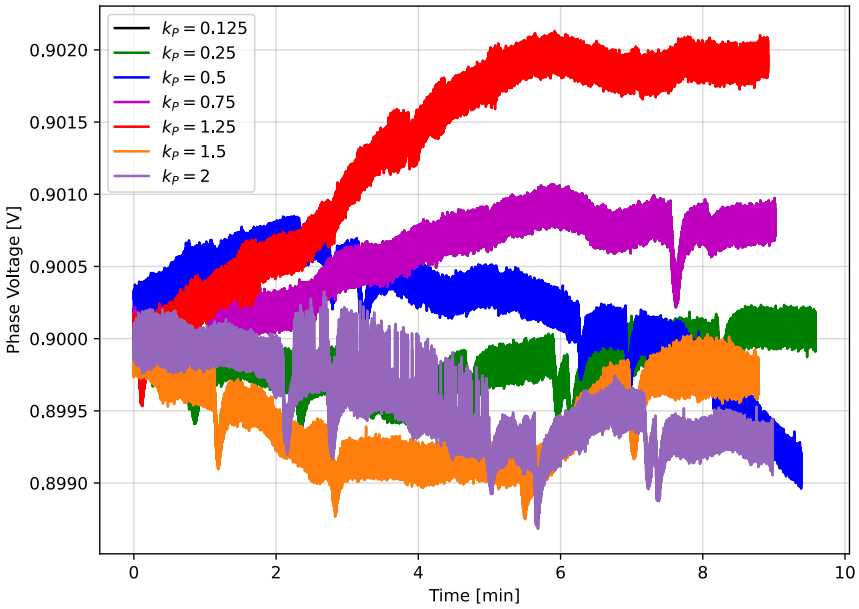


Figure 5.16 Phase voltage v. time for different cases of proportional gain factors for the PI controlled tuner.

that we see the phase voltage deviate in both directions (sometimes in the same measurement) tells us that our integral gain might not be strong enough. The integral term is used to correct steady state errors and the piezo voltage shows the algorithm trying to correct the drift, but it is clear from Fig. 5.16 that its not necessarily winning.

Conversely, the phase voltage waveforms for the ADRC measurements show more consistent behavior across the gain space, as can be seen in Fig. 5.17. The overshoot is clearly present at the start for each gain, with larger gains resulting in larger overshoots. After the initial corrections, the phase usually stays flat or works towards the setpoint slowly. A likely issue with this implementation is that the cavity bandwidth is much larger than the controller and observer bandwidths. The overall impact of a few Hz of detuning to cavity phase is incredibly small. This makes it hard for a higher-order ADRC to make estimates of the derivative and state.

Finally, we can use the random disturbances to conduct a preliminary comparison of the two controllers in regard to response. It is possible to find two cases of similar disturbances to the phase voltage for both controllers and see how the piezo voltage reacts. One such example can be seen in Fig. 5.18, where we examine the piezo response to one of these disturbances. We can see that

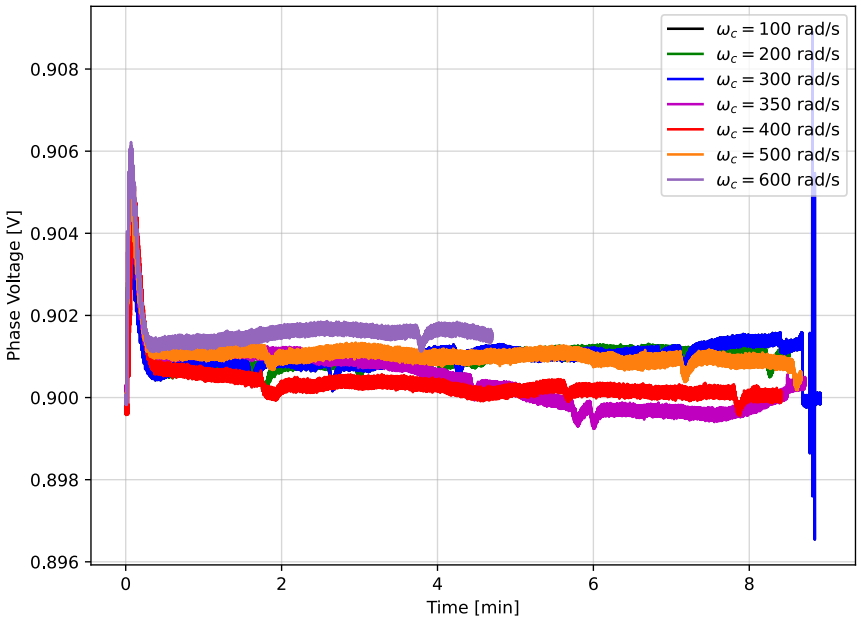


Figure 5.17 Phase voltage v. time for different cases of controller bandwidths ω_c for the ADRC controlled tuner. In the case of wc = 200 rad/s, the phase detector was turned off before the DAQ, leading to the jump.

ADRC-controlled piezo starts to react and settle a bit faster than the PI control.

That being said, neither algorithm is incredibly fast or accurate in its correction. By examining histograms of the total detuning, we can see how each algorithm performs in terms of accuracy and precision in regards to keeping the phase voltage at 0.9 V. We present the relevant histograms in Fig. 5.19. We can see that while ADRC is very precise in its control effects, its not entirely on the target. The PI controlled dataset shows a distribution a little closer to the set-point, but suffers less precision in its control. We discuss more on the limitations of each algorithm in the next section.

5.4.3 Experimental Discussion

We note that the overshoot we see in the ADRC is not an artifact of system error: we can recreate the test bench and controller in Simulink and see the response. The corresponding model can be seen in Fig. 5.20. There are some differences to the model in Fig. 5.4. One is that the DESO is converted from a vector-matrix solver to a MATLAB function that updates the state estimations with line code. This was done to match the implementation in LabVIEW. Another change is the 'digitize' function which transforms the frequency shift from the tuner back to a phase voltage

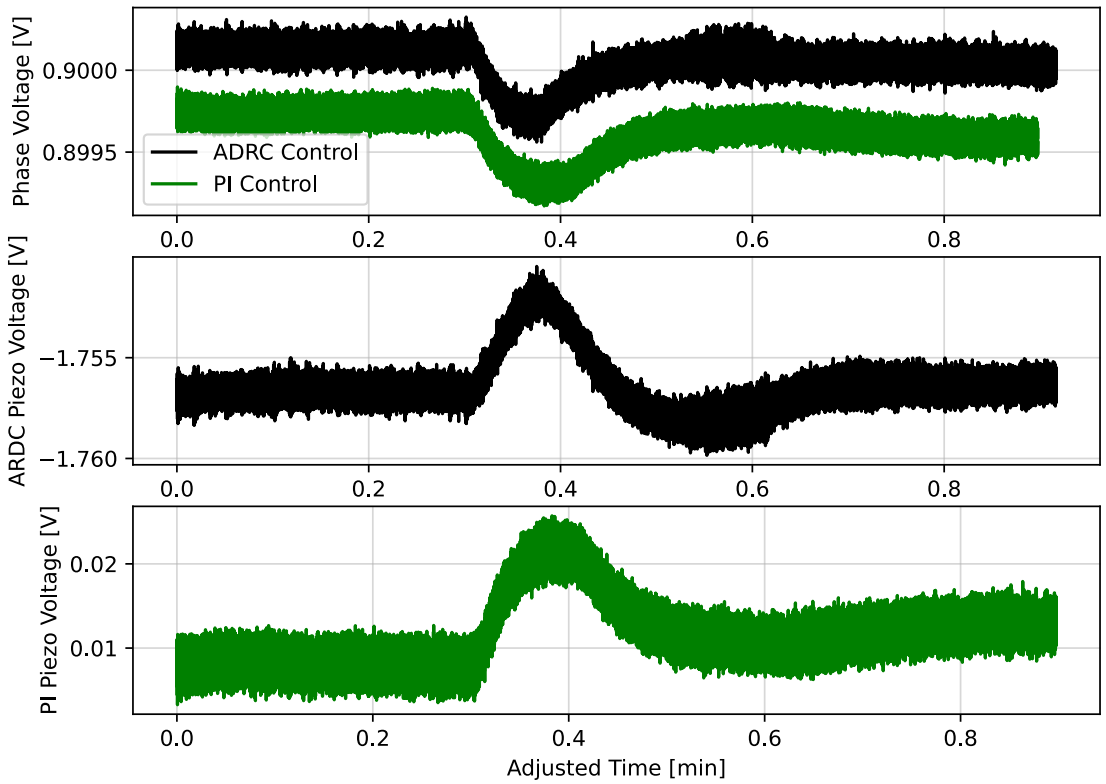


Figure 5.18 Phase voltage v. time for both ADRC and PI controllers during a disturbance event (top), piezo voltage v. time for the ADRC controlled tuner (middle), and piezo voltage v. time for the PI controlled tuner (bottom).

according to Eq. (5.9). An example output of this simulation can be seen in Fig. 5.21, where we see the same overshoot upon startup of the system.

That we see a similar effect in simulation and experiment tells us that this overshoot is related in some way to controller. The impulse-like response from the simulation at start-up might stem from the immediate shock of voltage sent to piezo-stacks, causing residual vibrations from which the cavity must recover. There are limiters that stop the amplifier voltage from reaching certain values to avoid damage to the piezo-stacks, but there are no limits on how much the voltage can change from step-to-step.

Such a limit is one area for improvement to this algorithm, though this might be beneficial on start-up. This is especially true for cold cavities where the bandwidth is much narrower and the shift of a hundred or so Hz matters much more significantly. Additionally, the steady behavior in

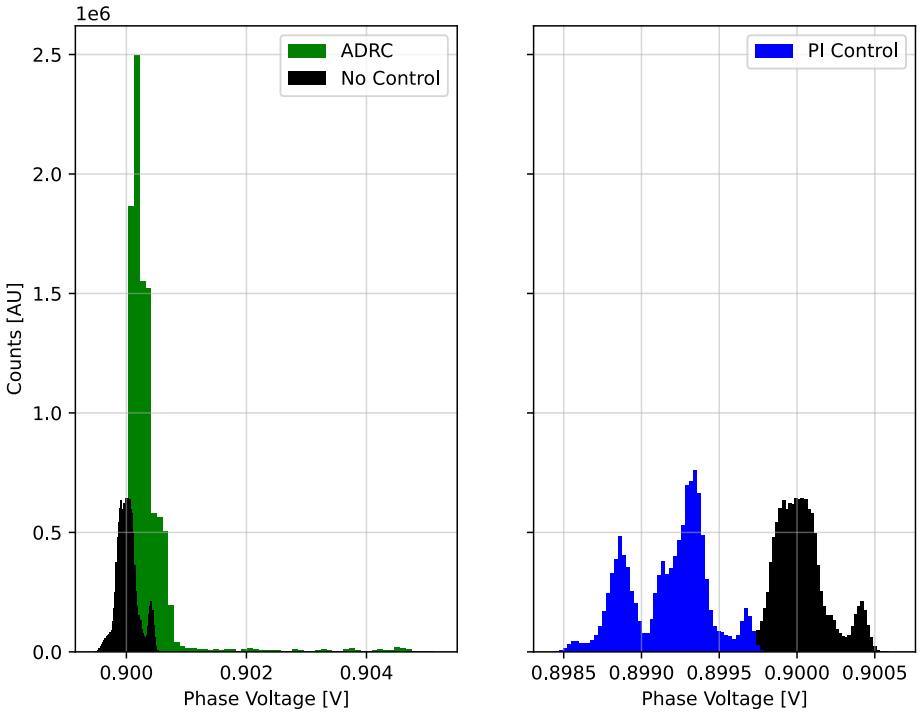


Figure 5.19 Histograms of the phase voltage V_ϕ for 10 minute captures with no control, ADRC, and PI control. Both controlled datasets are the best RMS detuning cases from Fig. 5.15, with $\omega_c = 400$ rad/s and $k_P = 0.75$.

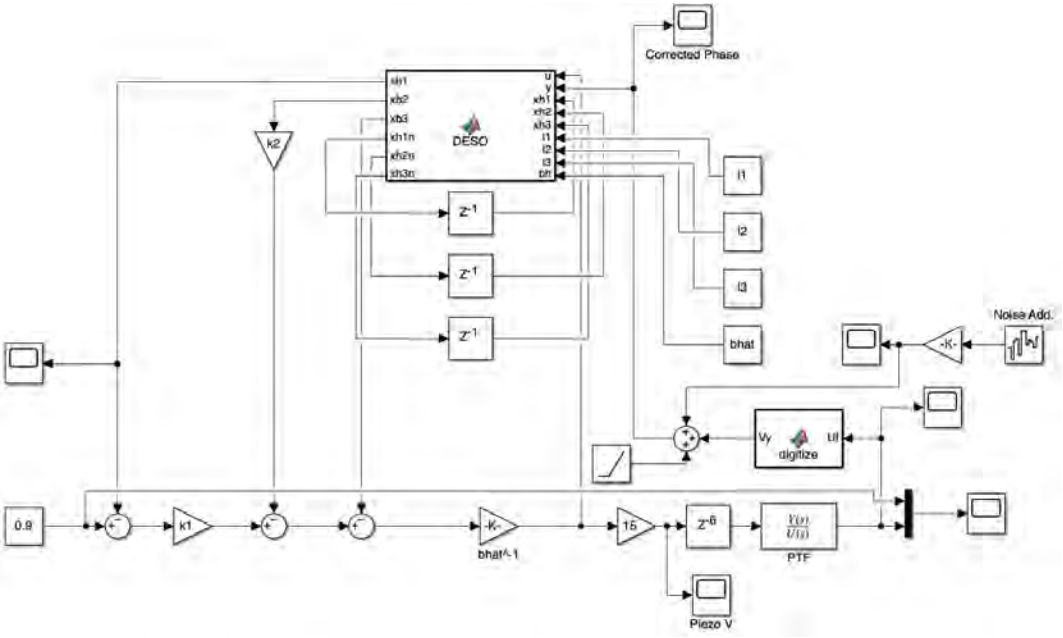


Figure 5.20 Simulink recreation of the test bench setup. In the DESO, we use the same update equations that are present in the LabVIEW implementation. These equations are Eq. (3.34) and Eq. (3.35).

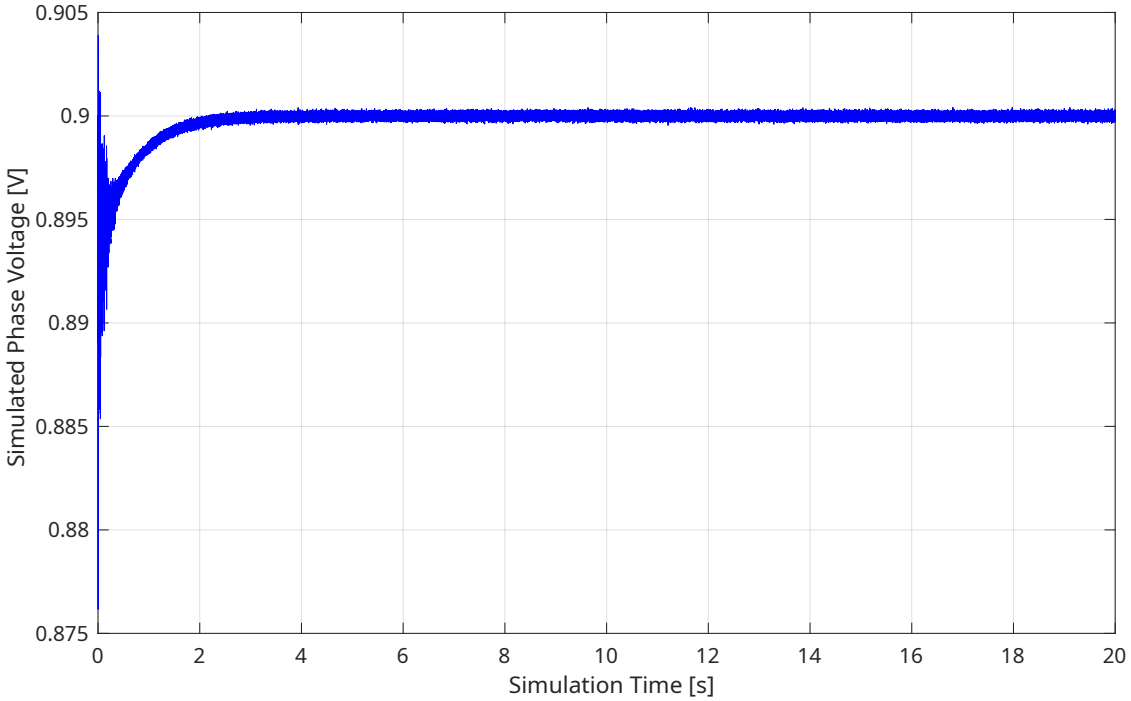


Figure 5.21 Simulated phase voltage v. time for the test-bench simulation with no additional noise and ω_c = 400 rad/s and ω_{ob} = 3000 rad/s. Notice the strong impulse and overshoot at the start of the simulation.

Fig. 5.17 past the start-up shows that if we can remove this initial jump then setpoint tracking of ADRC can be improved. Though prolonged performance of ADRC is good, if the cavity is tripped upon closing the control loop then the algorithm cannot be used. Self-excited loop can be used to start the control loop and be switched after settling, this is not necessarily the best solution.

On the PI front, our biggest limitation seems to stem from a limitation with the proportional gain factor and/or insufficient integral gain. It is clear from Fig. 5.16 that the PI-controlled system is more sensitive to background drifting effects, with the PI control not strong enough to keep the phase steady. Future work with this version of the testing bench will involve studies of integral gain and stability of the phase voltage.

In general, this bench is open to future upgrades and study. The main objective of this bench was to show feasibility and demonstrate initial algorithm performance/stability. We have shown that both algorithms can alter/control the frequency of a room temperature cavity and areas for improvement in the implementation. The next logical step is to implement these algorithms on an

Table 5.5 Electormechanical parameters for the HB650 cavity measured at 2 K equipped with mock tuner. Parameters are extracted from the LTF presented in Fig. 2.10.

Mode Number	k_μ^L $[Hz/(MV/m)^2]$	Q_μ [NA]	f_μ [Hz]
1	0.35	81	100.989
2	0.145	110	112.972
3	0.223	498	159.152
4	0.07	168	195.346
5	0.18	69	198.550
6	0.042	243	229.423
7	0.031	460	281.853
8	0.044	450	284.407
9	0.036	300	285.756

Table 5.6 Electormechanical parameters for the HB650 cavity measured at 2 K equipped with mock tuner. Parameters are extracted from the LTF presented in Fig. 2.10.

FPGA for further testing. This will also allow us to develop the LMS/NANC algorithm alongside the chosen controller with better sampling. Due to testing window limitations, we were unable to test these algorithms on cold cavities. This is another crucial step we must take in the future to ensure the success of our algorithms.

5.5 Simulated Ponderomotive Instability with Resonance Control

With accurate measurements of PTF and LTF, one can construct a combined model that contains both of these effects. A/ϕ control can also be included: in this case however we are interested in seeing how the peizoelectric tuner can fight ponderomotive instabilities. With open A/ϕ control loops, we again have a risk in encountering the monotonic instability on the positive side of the curve. In this section, we will compare ADRC and PI-controlled tuners.

Just like in Chapter 4, we will add detuning offsets to the cavity with sharp kicks; for slow drifts it is expected that the tuner will effectively prevent ponderomotive instabilities. In this examination, we will use a model of the HB650, 650 MHz, five-cell elliptical cavity. We briefly presented the graph of the LTF for the HB650 in Chapter 2, and we summarize the relevant modal parameters in Table 5.6. We will use the specification coupling and field $Q_L = 9.6 \times 10^6$ and $E_{acc} = 18.8$ MV/m.

Just as in Chapter 4, we are interested in the behaviors of the instability thresholds as functions of controller gains for each respective algorithm. We will start and work around gains similar to those

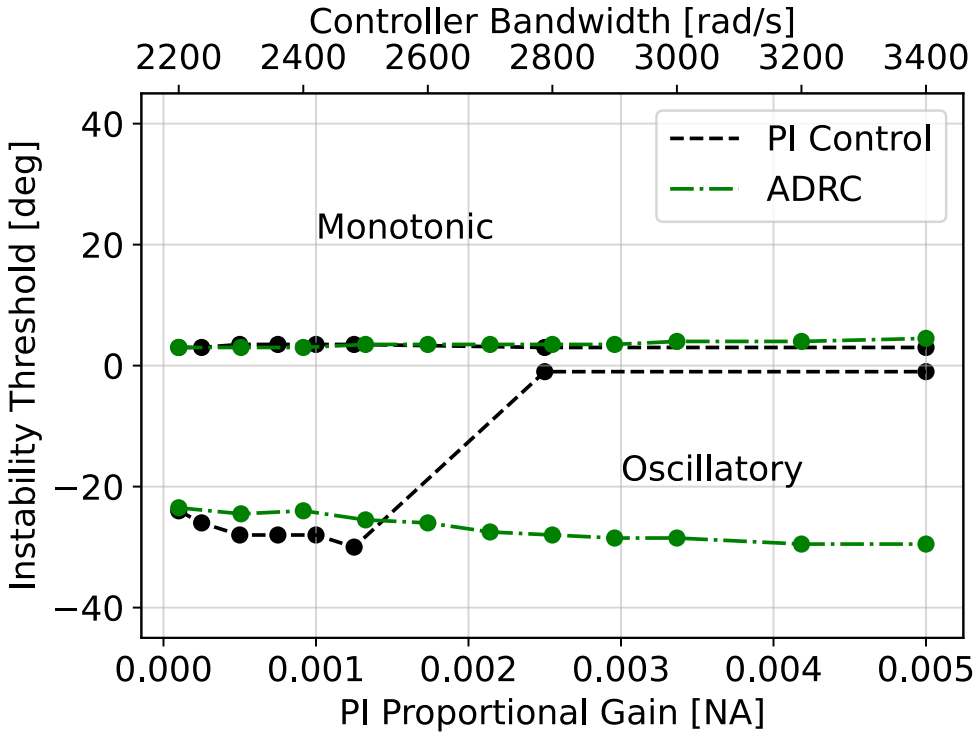


Figure 5.22 Instability thresholds in terms of detuning angle v. respective proportional gain factors for ADRC and PI controlled tuners.

in *Table* 5.4. The integral gain remains constant at $k_I = 0.05$. For the ADRC, we scale $\omega_{ob} = 5\omega_c$ in order to make sure the tuned gain range is maintained. We present the results of our survey in Fig. 5.22. There are some interesting remarks to be made from the findings in Fig. 5.22. First pertains to the monotonic instability: the thresholds are insensitive to both proportional gain and controller type. In terms of threshold, our open-loop Routh-Hurwitz solver predicts the monotonic instability at 1.449 Hz. On average, the Simulink model predicts the instability at 2.04 Hz. Thus, the tuner control does not push the threshold much.

This falls in line with what one might expect for the monotonic instability. The progress of the monotonic instability is very fast: it is unlikely that with the capacitive nature of the piezo-stacks that the tuner can counter the detuning before the drop in field. This is why feed-forward is so essential for pulsed operation, otherwise the piezo-tuner cannot react fast enough before the field drop. In terms of the oscillatory instability, we must first discuss the nature of the instability with tuner control. It is hard to determine at what threshold ponderomotive oscillations appear. Due to

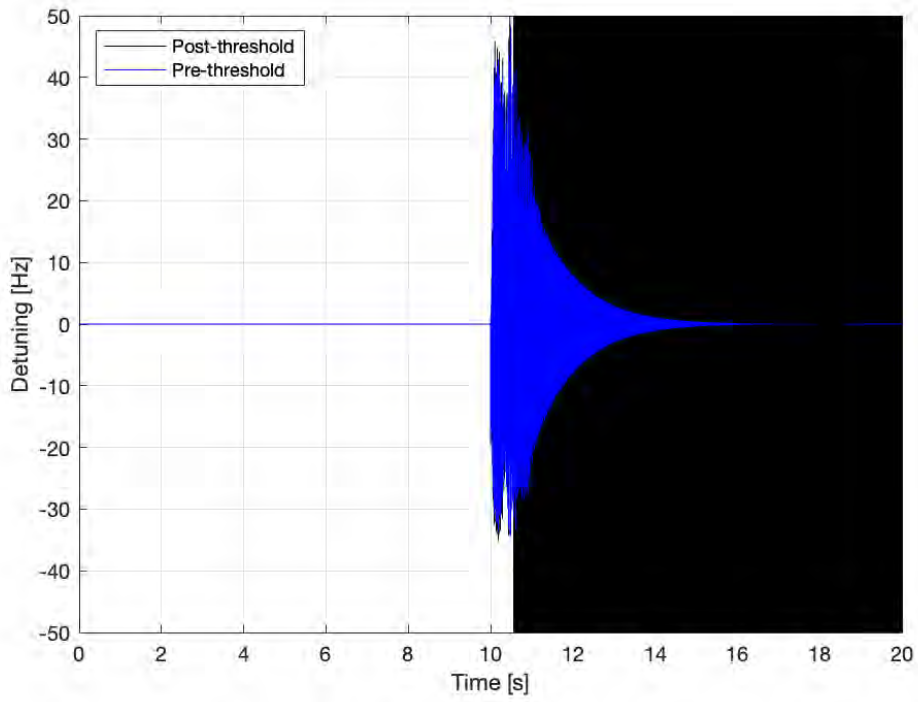


Figure 5.23 Simulated detuning v. time for the Simulink model after and before the instability threshold.

the more independent nature of the tuner control loop, it is likely that the exact thresholds don't change much. As we increase the detuning kick, more oscillations will be excited at first then damped as the tuner pushes the cavity below the threshold and towards the generator frequency. Eventually, the tuner loses and a combined instability is excited which is the threshold we present in Fig. 5.22. We present the time domain waveforms of this instability in Fig. 5.23.

We note that this instability is a combined result of ponderomotive oscillations and the tuner control. The driving oscillations before the thresholds are from the 159 Hz mode. At and after the threshold, the main driver is the 101 Hz mode. The spectral differences can be seen in Fig. 5.24. We note that changing the absolute and relative tolerances of the solver does not change the instability threshold or simulated detuning values, suggesting that this is not a numerical instability.

5.5.1 Discussion

One of the main sources of error that is hard to quantify stems from the different environments in which the transfer function data was collected. The LTF must be collected during high-power

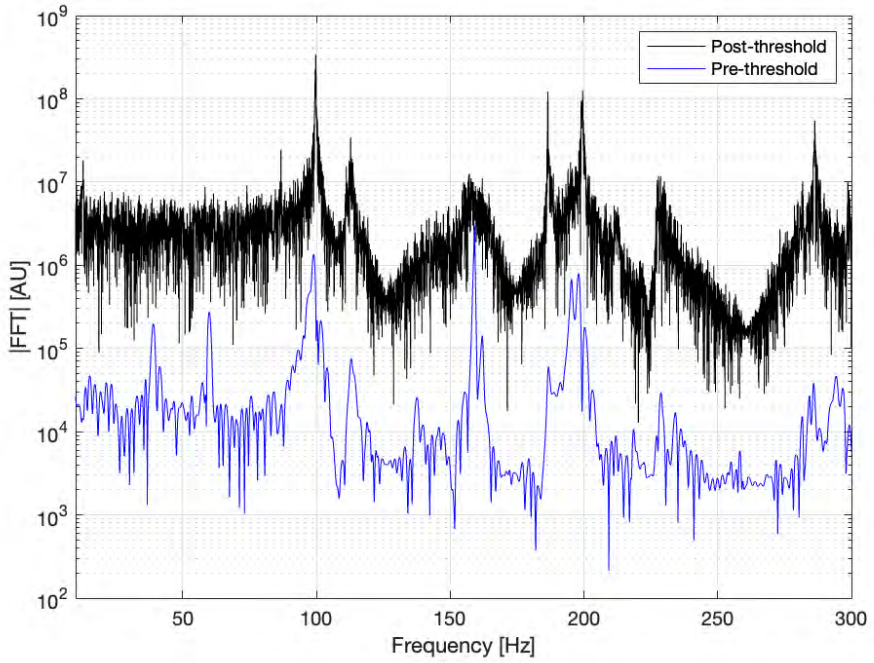


Figure 5.24 Fourier transform amplitude of the detuning v. frequency for after and before the instability threshold.

testing at cryogenic temperatures. As mentioned before, niobium stiffness increases when cooled to LHe temperatures. Additionally, the HB650 from which we measured the LTF was equipped with a mock tuner and not the real piezoelectric tuner. The result is that the couplings k_μ^L and quality factors Q_μ in this cavity are higher than what they would be for a cavity equipped with the tuner. So in one aspect, these predicted thresholds are an under-estimation for a real tuner-controlled HB650 cavity.

On the contrary, the HB650 without any tuner still has a relatively lower Lorentz force detuning effect when compared to other PIP-II and FRIB cavities. Thus the instability thresholds in Fig. 5.22 should be considered an overestimation of the tuner's effect when applied to **other cavities**, even if the tuner couplings are similar. This again shows the importance of measuring these transfer functions whenever possible when stability is considered.This means both f_μ and Q_μ are different between the two transfer functions are different. It is clear that the LTF values are the more accurate in recreating effects at the operational environment. However it is not easy to match modes between

the two temperatures. Sometimes it is clear as for the $\sim$ 160 Hz modes in Table 5.2 and Table 5.6. In order to avoid mismatching modes, we kept each transfer function separate, which will inevitably lead to differences from reality.

5.5.2 Analytical Modeling Difficulties

Trying to analytically model the instability thresholds for a cavity with only frequency control via a piezoelectric tuner poses some difficulties. Consider the detuning equation of motion for mode μ in the presence of the electromechanical and tuner feedback:

$$\Delta\ddot{\omega}_\mu + \frac{2}{\tau_\mu}\Delta\dot{\omega}_\mu + \Omega_\mu^2\Delta\omega_\mu = -k_\mu^L\Omega_\mu^2 V_c^2(t) + k_\mu^P\Omega_\mu^2 V_P(t). \tag{5.10}$$

Following from a tuner control loop like in Fig. 5.4, we can express the piezo voltage as the time convolution of the total detuning and the piezo controller $G_c^P(t)$:

$$V_P(t) = -(G_c^P(t) * \Delta\omega(t)). \tag{5.11}$$

Herein lies the difficulty: it is not easy to decompose the equation of motion into similar variables because the piezo voltage will change based on the **total** detuning $\Delta\omega$, not just one mode's component. It is possible for a one-mode system to simplify the system. Let us follow the normal linearization procedure for the Lorentz force with deviations of the detuning from steady state. For a single mode system and neglecting static terms:

$$\begin{aligned}\delta\ddot{\omega}_\mu + \frac{2}{\tau_\mu}\delta\dot{\omega}_\mu + \Omega_\mu^2\delta\omega_\mu &= -2V_0k_\mu^L\Omega_\mu^2\delta V + k_\mu^P\Omega_\mu^2\delta V_P \\ &= -2V_0k_\mu^L\Omega_\mu^2\delta V - k_\mu^P\Omega_\mu^2(G_c^P * \delta\omega_\mu)\end{aligned}$$

Taking the Laplace transform, we can work to simplify the equation.

$$\delta\omega_\mu(s)[s^2 + \frac{2}{\tau_\mu}s + \Omega_\mu^2] = -2V_0k_\mu^L\Omega_\mu^2\delta V(s) + k_\mu^P\Omega_\mu^2 G_c^P(s)\delta\omega_\mu(s) \tag{5.12}$$

$$\delta\omega_\mu(s) = -2V_0G_\mu^L(s)\delta V(s) - G_\mu^P(s)G_c^P(s)\delta\omega_\mu(s) \tag{5.13}$$

$$\delta\omega_\mu(s) = \frac{-2V_0G_\mu^L(s)}{1 + G_\mu^P(s)G_c^P(s)}\delta V(s) \tag{5.14}$$

Consider the characteristic polynomial we derived for the open-loop cavity in Chapter 2:

$$(s + \omega_{1/2})^2 + \Delta\omega_0^2 + V_0\Delta\omega_0\delta\omega(s) = 0. \tag{5.15}$$

Substituting the Eq. (5.14) into the characteristic polynomial, we can arrive at the total characteristic polynomial for a single mechanical mode cavity with tuner control:

$$(s + \omega_{1/2})^2 + \Delta\omega_0^2 - \frac{2V_0^2\Delta\omega_0 G_\mu^L(s)}{1 + G_\mu^P(s)G_c^P(s)} = 0. \tag{5.16}$$

Again the prediction power of this expression is limited, as only a single mode can be used. For instability studies with no tuner, a single mode might be sufficient if the instability driving mode is the considered resonance. However, our Simulink model shows two different modes at play and thus is not necessarily applicable in this case (Fig. 5.24. This difficulty to model single mode systems alongside the lost information from using only one mode [70], suggests that using numerical methods with all possible modes provides the best predicting power.

CHAPTER 6

CONCLUSIONS

The successful delivery of beam to the target and subsequent experimental facilities requires stable accelerating gradients and cavity phases. For machines with low beam-loading, CW operation of cavities with high Q_l ($\geq 10^6$) becomes feasible. While these higher Q_l's allow for lower on-resonance power requirements, the narrow bandwidth($\sim$ 10s Hz) means any disturbances to the cavity can rapidly increase the RF power requirements. Additionally, the ponderomotive radiation pressure of the electromagnetic fields opens the door for instabilities in generator-driven cavities if there is a large frequency mismatch between the two. Strong microphonics or instabilities can lead to dangerous levels of power draw and a trip in the RF safety interlocks and thus machine downtime.

In Chapter 2, we extensively the covered modeling of SRF cavities: we presented a detailed resonant circuit model describing the cavity alongside the generator and input coupler. We extended the cavity to a transmission line treatment and showed how the circuit parameters R, L, and C manifest in the real cavity: determination of the frequency ω_0 and coupling strength β_e. We used an elastic model to derive the equations of motion for mechanical vibrational modes in terms of their detuning contribution $\delta\omega_\mu$. We derived the state matrix A for the combined electromechanical system and demonstrated the regions of stability for an HB650 cavity using the Routh-Hurwitz stability criterion. We saw that even for a cavity with relatively weak Lorentz force detuning, the regions of stability are narrow for the operational E_{acc} and Q_l. We must employ feedback algorithms to counter these effects.

We discussed the three main process variables of the SRF cavity. We demonstrated that the cavity voltage phasor can be represented in both polar and Cartesian coordinates. We derived relevant transfer functions that describe the crosstalk between the amplitude and phase channels (or analogous I and Q voltages) in both open and closed-loop configurations; the choice of process variables does not matter for the open-loop cavity, but cavities with I/Q control experience less variable cross talk than in A/ϕ control. In this chapter, we also discussed relevant control algorithms,

such as a form of discretized active disturbance rejection control. This implementation can be used for A/ϕ, I/Q, and resonance control.

Chapter 4 used the combined elements of Chapters 2 and 3, where we examined the behavior of the ponderomotive instability thresholds using ADRC. We used a discrete, numerical simulation and analytical model to predict instability thresholds using electromechanical data for the FRIB $\beta = 0.53$ HWR. Our predictive methods show great agreement with measured oscillatory instability thresholds from HWRs within the FRIB driver linac. For $\psi_0 > 0$, our predictive methods and sideband measurements suggest that this 'oscillatory-like' instability is a controller instability. The means by which this threshold is reduced in the real machine is currently unknown, and represents an avenue for a future study.

In a previous work, we noted that the oscillatory instability thresholds decreased as we increased the amplitude ADRC controller bandwidth. It is predicted that for linear controllers, the instability threshold can be pushed arbitrarily further with increasing gain. Our predictive methods also capture this trends, and using both we were able to identify the means by which this occurs. When using ADRC for both amplitude and phase control, a peak with frequency f_{pk} is created in the process variable crosstalk magnitude (Eq. (3.22)) that varies with detuning. When f_{pk} approaches a harmonic of one of the mechanical modes, ponderomotive oscillations of the strongly coupled mode and their harmonics are excited, leading to earlier instabilities. This effect is not purely related to the ADRC controllers: it requires strongly coupled mechanical modes with frequencies on the order of f_{pk}. The expected trend in the oscillatory instability threshold reappeared in our predictive methods when the strongly coupled mechanical modes were dropped to below 100 Hz.

Comparing instability thresholds under A/ϕ and I/Q control, we reaffirm that I/Q provides much larger instability thresholds when compared to A/ϕ control. We attribute this to increased crosstalk between deviations in phase to deviations in the amplitude, which can also lead to controller-induced instability if the system is pushed sufficiently far from resonance. We also compared the behavior of the process variable crosstalk of ADRC and PI-controlled cavities. We find that PI control can be beneficial for cavities with wider bandwidths, where the detuning impacts

the cavity phase much less than in the narrow-band cases. ADRC can then provide a good control alternative for narrow-band cavities where disturbances to the phase are more significant.

This work provides the first identification of a difference in ponderomotive instability thresholds for SRF cavities at various temperatures. We report that cavities operating at 4.3 K have statistically higher instability thresholds than those at 2 K. We use our Simulink and analytical models to rule out the increased microphonic background at 4.3 K as a means of preventing the oscillatory instability. Our predictive methods suggest that a 53% drop in the mechanical mode quality factor is sufficient to produce the instability thresholds we see. One possible explanation is the increased bath pressure at 4.3 K (880 Torr v. 40 Torr) providing additional stiffness to the cavity and reducing Q_μ.

We measured the quality factors of mechanical resonances in FRIB $\beta = 0.53$ HWRs at 4.3 K. We find that modes near the instability-driving mode do see a drop in quality factor: the mode correlated with the 259.3 Hz resonance sees a 27.5% percent drop and the mode correlated with 260.12 Hz is correlated sees a 67.9% drop. While one mode falls below the 53% drop needed for higher instability thresholds, using our measured values with our prediction tools shows deviations from the measured thresholds. Thus this story is not yet complete, as there are likely other factors at play.

Finally, we showed the first measurement of the Lorentz transfer function for medium velocity, 5-cell elliptical cavities. These cavities are key components for upcoming machines, and possess strong LFD effects. We show the first predictions of ponderomotive instability thresholds for this cavity type. We find that we must move to higher controller or observer gains in order to push the instability threshold beyond the half-bandwidth.

In Chapter 5, we discuss a key factor in preventing ponderomotive instability: resonance control. We used real piezo transfer function data from a room temperature HB650 cavity to create a Simulink model of the tuner in the presence various feedback controllers. In particular, we show the first application of ADRC to the double lever-arm, LCLS-II style tuner control. Our simulation shows that ADRC outperforms traditional PI control in terms of microphonics reduction. Additionally, the LMS algorithm can be used to help remove troublesome components from the

microphonics.

We experimentally demonstrate our ADRC implementation on a room temperature cavity, and compare its performance to a PI controller. We find that ADRC gives more consistent control behavior despite initial overshoot when compared to PI control. There is still room for improvement in this area; active efforts are underway to deploy this algorithm to an FPGA for testing on cold cavities. This will allow for us to better gauge the performance of the algorithm in accurate operational conditions.

6.1 Outlook

This work has presented an exhaustive look at ponderomotive effects in a variety of cavity geometries. From coaxial resonators to elliptical cavities, these instabilities remain present and pose a possible roadblock in the quest for higher gradients and lower power costs. There has been an uptick in work regarding this topic this decade, and the number of tools for predicting instability thresholds has increased.

One area for expansion on the topic of ponderomotive instabilities is establishing more concrete relationships between the geometry and the thresholds. That is, it would be beneficial to be able to reliably predict mechanical parameters from CAD models of cavities. From simulated values, early predictions for instability thresholds can be made before the cavity is even produced. This will also allow us to better understand which mechanical parameters are key determinants for moving the instability thresholds.

6.2 Funding Acknowledgments

This material is based upon work supported by the U.S. Department of Energy, Office of Science, Office of Workforce Development for Teachers and Scientists, Office of Science Graduate Student Research (SCGSR) program. The SCGSR program is administered by the Oak Ridge Institute for Science and Education for the DOE under contract number DE-SC0014664

In addition to the above source, this material is based upon work supported by the U.S. Department of Energy, Office of Science, Office of Nuclear Physics and used the resources of the Facility for Rare Isotope Beams (FRIB) operations, which is a DOE Office of Science User Facility

under award number DE-SC0023633. This material is based upon work supported by the U.S. Department of Energy, Office of Science, Office of High Energy Physics, under Award Number DE-SC0018362

Additionally, this work was produced by Fermi Forward Discovery Group, LLC under Contract No. 89243024CSC000002 with the U.S. Department of Energy, Office of Science, Office of High Energy Physics. Publisher acknowledges the U.S. Government license to provide public access under the DOE Public Access Plan https://www.energy.gov/downloads/doe-public-access-plan.

BIBLIOGRAPHY

[1] E. D. Courant et al. *Reviews of Accelerator Science and Technology*. Ed. by A. Chao and W. Chou. World Scientific Connect, 2008. ISBN: 978-981-4469-78-4. DOI: https://doi.org/10.1142/7037.

[2] J. A. Martin. "Accelerators for Heavy Ions". In: *Proc. of 7th International Conference on Cyclotrons and their Applications*. 1975, pp. 574–583.

[3] K. Hubner. "Accelerators for high-energy physics". In: *2004 European School for High Energy Physics*. 2004, pp. 361–394. DOI: http://dx.doi.org/10.5170/CERN-2006-003.361.

[4] R. W. Schoenlein et al. *LCLS-II High Energy (LCLS-II-HE): A transformative X-ray laser for science*. Tech. rep. SLAC National Accelerator Laboratory (SLAC), Menlo Park, CA (United States), Aug. 2016. DOI: 10.2172/1634206. URL: https://www.osti.gov/biblio/1634206.

[5] S. Sheehy. "Applications of Particle Accelerators". In: *Proceedings of the General Introductory CAS Course "Introduction to Accelerator Physics", 2019 and Beyond*. 2019.

[6] K. Londhe et al. "Application of electron beam technology to decompose per- and polyfluoroalkyl substances in water". In: *Environmental Pollution* 348 (2024), p. 123770. ISSN: 0269-7491. DOI: https://doi.org/10.1016/j.envpol.2024.123770. URL: https://www.sciencedirect.com/science/article/pii/S0269749124004846.

[7] J. D. Jackson. *Classical Electrodynamics*. 3rd. Wiley, 1999. ISBN: 9780471309321.

[8] H. E. Wegner. "Tandem Accelerators". In: *IEEE* (1969).

[9] Burkhard J. "Vacuum breakdown". In: *Nuclear Instruments and Methods in Physics Research Section A: Accelerators, Spectrometers, Detectors and Associated Equipment* 268.2 (1988), pp. 390–396. ISSN: 0168-9002. DOI: https://doi.org/10.1016/0168-9002(88)90541-4. URL: https://www.sciencedirect.com/science/article/pii/0168900288905414.

[10] P. Thieberger et al. "Novel high-energy ion implantation facility using a 15 MV Tandem Van de Graaff accelerator". In: *Nuclear Instruments and Methods in Physics Research Section B: Beam Interactions with Materials and Atoms* 442 (2019), pp. 36–40. ISSN: 0168-583X. DOI: 10.1016/j.nimb.2019.01.016. URL: https://www.sciencedirect.com/science/article/pii/S0168583X1930014X (visited on 01/10/2026).

[11] G. Ising. "Prinzip einer Methode zur Herstellung von Kanalstrahlen hoher Voltzahl". In: *Ark. Mat. Astron. Fys.* 18.30 (1924), pp. 1–4. URL: https://cds.cern.ch/record/433984 (visited on 01/05/2026).

[12] R. Wideröe. "Über ein neues Prinzip zur Herstellung hoher Spannungen". In: *Archiv für Elektrotechnik* 21.4 (July 1, 1928), pp. 387–406. ISSN: 1432-0487. DOI: 10.1007/BF01656341. URL: https://doi.org/10.1007/BF01656341 (visited on 01/05/2026).

[13] P. Tracz and Graduate. "RF LINAC DESIGN MODELLING FOR OPTIMIZATION OF BEAM PARAMETERS FOR ICS γ-RAY SOURCE SYSTEM". PhD thesis. University Politehnica of Bucharest, 2022. DOI: 10.13140/RG.2.2.27250.99525.

[14] R. B. Neal. "The Stanford Two-Mile Linear Electron Accelerator". In: *Journal of Vacuum Science and Technology* 2.3 (May 1965), pp. 149–159. ISSN: 0022-5355. DOI: 10.1116/1.1492417. eprint: https://pubs.aip.org/avs/jvst/article-pdf/2/3/149/11885499/149_1_online.pdf. URL: https://doi.org/10.1116/1.1492417.

[15] T. Wangler. *Microwave Topics for Linacs*. John Wiley & Sons, Ltd, 2008. Chap. 5, pp. 135–174. ISBN: 9783527623426. DOI: 10.1002/9783527623426.ch5. eprint: https://onlinelibrary.wiley.com/doi/pdf/10.1002/9783527623426.ch5. URL: https://onlinelibrary.wiley.com/doi/abs/10.1002/9783527623426.ch5.

[16] Ulrich B. "CST's commercial beam-physics codes". presented at ICAP 2006: 9th Int. Computational Accelerator Physics Conference, Chamonix Mont-Blanc, France, Talk THM2IS03. 2006. URL: https://jacow.org/icap06/TALKS/THM2IS03_TALK.PDF.

[17] T. Pozar. *Microwave Engineering*. 4th. John Wiley and Sons, Inc, 2012.

[18] H. K. Onnes. "Further experiments with liquid helium. C. On the change of electric resistance of pure metals at very low temperatures etc. IV. The resistance of pure mercury at helium temperatures". In: Heike Kamerlingh Onnes. *Through Measurement to Knowledge*. Ed. by K. Gavroglu and Y. Goudaroulis. Red. by Robert S. Cohen. Vol. 124. Series Title: Boston Studies in the Philosophy of Science. Dordrecht: Springer Netherlands, 1991, pp. 261–263. ISBN: 978-94-010-7433-9. DOI: 10.1007/978-94-009-2079-8_15. URL: http://link.springer.com/10.1007/978-94-009-2079-8_15 (visited on 05/23/2026).

[19] W. Meissner and R. Ochsenfeld. "Ein neuer Effekt bei Eintritt der Supraleitfähigkeit". In: *Naturwissenschaften* 21.44 (Nov. 1, 1933), pp. 787–788. ISSN: 1432-1904. DOI: 10.1007/BF01504252. URL: https://doi.org/10.1007/BF01504252 (visited on 05/23/2026).

[20] F. London, H. London, and F. A. Lindeman. "The Electromagnetic Equations of the Supraconductor". In: *Proceedings of the Royal Society of London. Series A - Mathematical and Physical Sciences*. Royal Society, 1935, pp. 71–88. DOI: 10.1098/rspa.1935.0048.

[21] V. Ginzburg and L. Landau. "ON THE THEORY OF SUPERCONDUCTIVITY". in: *Collected Papers of L.D. Landau*. Pergamon, Jan. 1, 1965, pp. 546–568. DOI: 10.1016/B978-0-08-010586-4.50078-X. URL: https://www.sciencedirect.com/

science/chapter/edited-volume/pii/B978008010586450078X (visited on 05/23/2026).

[22] L. Landau. "On the Theory of Phase Transition". In: *Zh. Eksp. Teor. Fiz* 7 (1937), pp. 19–32.

[23] U. Köbler. "On the Difference Between Type I and Type II Superconductors". In: *Journal of Low Temperature Physics* 213.1 (Oct. 1, 2023), pp. 51–69. ISSN: 1573-7357. DOI: 10.1007/s10909-023-02991-1. URL: https://doi.org/10.1007/s10909-023-02991-1 (visited on 05/23/2026).

[24] J. Bardeen, L. N. Cooper, and J. R. Schrieffer. "Microscopic Theory of Superconductivity". In: *Physical Review* 106.1 (Apr. 1, 1957), pp. 162–164. DOI: 10.1103/PhysRev.106.162. URL: https://link.aps.org/doi/10.1103/PhysRev.106.162 (visited on 05/23/2026).

[25] H. Padamsee, J. Knoblach, and T. Hays. *RF Superconductivity for Accelerators*. 2nd. Wiley-VCH Verlag GmbH, 2008. ISBN: 978-3-527-40842-9.

[26] H. Padamsee. *RF Superconductivity: Science, Technology, and Applications*. Wiley-VCH Verlag GmbH, 2009. ISBN: 978-3-527-40572-5.

[27] A. Gurevich. "Superconducting Radio-Frequency Fundamentals for Particle Accelerators". In: *Reviews of Accelerator Science and Technology* 05 (2012), pp. 119–146. DOI: 10.1142/S1793626812300058. eprint: https://doi.org/10.1142/S1793626812300058. URL: https://doi.org/10.1142/S1793626812300058.

[28] B. Aune et al. "Superconducting TESLA cavities". In: *Physical Review Special Topics - Accelerators and Beams* 3.9 (Sept. 22, 2000), p. 092001. DOI: 10.1103/PhysRevSTAB.3.092001. URL: https://link.aps.org/doi/10.1103/PhysRevSTAB.3.092001 (visited on 05/30/2026).

[29] H. Padamsee. "50 years of success for SRF accelerators -a review". In: *Superconductor Science and Technology* 30.5 (2017). DOI: 10.1088/1361-6668/aa6376.

[30] G. Fortuna et al. "The ALPI project at the Laboratori Nazionali di Legnaro". In: *Nuclear Instruments and Methods in Physics Research Section A: Accelerators, Spectrometers, Detectors and Associated Equipment* 287.1 (1990), pp. 253–256. ISSN: 0168-9002. DOI: https://doi.org/10.1016/0168-9002(90)91803-J.

[31] Argonne National Lab. *ATLAS: a proposal for a precision heavy ion accelerator at Argonne National Laboratory*. Tech. rep. Argonne National Lab., IL (USA), Feb. 1978. DOI: 10.2172/5991052. URL: https://www.osti.gov/biblio/5991052.

[32] M. Lewitowicz. "The SPIRAL 2 Project". In: *Nuclear Physics A* 805.1 (2008). INPC 2007, pp. 519c–525c. ISSN: 0375-9474. DOI: https://doi.org/10.1016/j.nuclphysa.

2008.02.290.

[33] O. Kester et al. "The MSU/NSCL Re-Accelerator ReA3". In: *Proc. of SRF2009: The 14th International Conference on RF Superconductivity*. 2009.

[34] J. Wei et al. "Accelerator commissioning and rare isotope identification at the Facility for Rare Isotope Beams". In: *Modern Physics Letters A* 37.09 (2022), p. 2230006. DOI: 10.1142/S0217732322300063. eprint: https://doi.org/10.1142/S0217732322300063. URL: https://doi.org/10.1142/S0217732322300063.

[35] J. Wei et al. "FRIB Transition to User Operations, Power Ramp Up, and Upgrade Perspectives". In: *Proc. SRF 2023: 21st Int. Conf. RF Superconductivity, Grand Rapids, MI, USA* (Grand Rapids, MI, USA). JACoW, 2023, pp. 1–8. DOI: 10.18429/JACoW-SRF2023-MOIAA01.

[36] T. Xu et al. "Progress of FRIB SRF production". In: *Proc. of 18'th International Conference on RF Superconductivity (SRF'17), Lanzhou, China, July 17-21* (Lanzhou, China). International Conference on RF Superconductivity 18. 2017, pp. 345–352. DOI: https://doi.org/10.18429/JACoW-SRF2017-TUXAA03.

[37] C. Zhang et al. "Certification testing of production superconducting quarter-wave and half-wave resonators for FRIB". in: *Nucl. Instrum. Methods Phys. Res. A* 1014 (2021), p. 165675. DOI: 10.1016/j.nima.2021.165675.

[38] H. Ren et al. "Development and status of the FRIB 28 GHz SC ECRIS". in: *Journal of Physics: Conference Series* 2244.1 (Apr. 2022), p. 012008. ISSN: 1742-6596. DOI: 10.1088/1742-6596/2244/1/012008. URL: https://doi.org/10.1088/1742-6596/2244/1/012008 (visited on 06/10/2026).

[39] P.N. Ostroumov et al. "Elliptical superconducting RF cavities for FRIB energy upgrade". In: *Nuclear Instruments and Methods in Physics Research Section A: Accelerators, Spectrometers, Detectors and Associated Equipment* 888 (2018), pp. 53–63. ISSN: 0168-9002. DOI: https://doi.org/10.1016/j.nima.2018.01.001. URL: https://www.sciencedirect.com/science/article/pii/S0168900218300019.

[40] K. McGee et al. "Medium-velocity superconducting cavity for high accelerating gradient continuous-wave hadron linear accelerators". In: *Phys. Rev. Accel. Beams* 24 (11 Nov. 2021), p. 112003. DOI: 10.1103/PhysRevAccelBeams.24.112003. URL: https://link.aps.org/doi/10.1103/PhysRevAccelBeams.24.112003.

[41] FRIB Science Community, A. Gade, and B. Sherrill. *The Scientific Case for the 400 MeV/u Energy Upgrade of FRIB*. tech. rep. The Facility for Rare Isotope Beams, 2019.

[42] V. S. Morozov, C.C. Peters, and A.P. Shishlo. "Oak Ridge Spallation Neutron Source superconducting rf linac availability performance and demonstration of operation restoration with

superconducting rf cavity off". In: *Physical Review Accelerators and Beams* 25.2 (Feb. 17, 2022), p. 020101. ISSN: 2469-9888. DOI: 10.1103/PhysRevAccelBeams.25.020101. URL: https://link.aps.org/doi/10.1103/PhysRevAccelBeams.25.020101 (visited on 06/02/2026).

[43] P. Dhakal et al. "Performance of Oak Ridge National Laboratory spallation neutron source proton power upgrade cavities and cryomodule production". In: *Physical Review Accelerators and Beams* 27.10 (Oct. 10, 2024), p. 102001. DOI: 10.1103/PhysRevAccelBeams.27.102001. URL: https://link.aps.org/doi/10.1103/PhysRevAccelBeams.27.102001 (visited on 06/11/2026).

[44] V. Lebedev. *The PIP-II Reference Design Report*. Tech. rep. Fermi National Accelerator Laboratory (FNAL), Batavia, IL (United States), June 2015. DOI: 10.2172/1365571. URL: https://www.osti.gov/biblio/1365571.

[45] P. A. Adderley et al. "The Continuous Electron Beam Accelerator Facility at 12 GeV". in: *Physical Review Accelerators and Beams* 27.8 (Aug. 15, 2024), p. 084802. ISSN: 2469-9888. DOI: 10.1103/PhysRevAccelBeams.27.084802. URL: https://link.aps.org/doi/10.1103/PhysRevAccelBeams.27.084802 (visited on 06/09/2026).

[46] T. Behnke et al. *The International Linear Collider Technical Design Report - Volume 1: Executive Summary*. Tech. rep. _eprint: 1306.6327. The ILC Design Committee, June 2013.

[47] M. Benedikt et al. *Future Circular Collider Feasibility Study Report Volume 2: Accelerators, technical infrastructure and safety*. 2025. DOI: 10.17181/CERN.EBAY.7W4X. URL: http://cds.cern.ch/record/2928793.

[48] J. Galayda. "The Linac Coherent Light Source-II Project". In: *Proceedings of the 5th Int. Particle Accelerator Conf.* IPAC2014 (2014). Ed. by Petit-Jean-Genaz Christine (Ed.) et al. Artwork Size: 3 pages, 0.475 MB ISBN: 9783954501328 Medium: PDF, 3 pages, 0.475 MB. DOI: 10.18429/JACOW-IPAC2014-TUOCA01. URL: http://jacow.org/IPAC2014/doi/JACoW-IPAC2014-TUOCA01.html (visited on 06/09/2026).

[49] D. Gonnella. "Status of the LCLS-II Superconducting Linac". Presentation. Presentation. Workshop on Future Light Sources. Lucerne, Sweeden, Aug. 28, 2023. URL: https://fls2023.vrws.de/talks/mo3a3_talk.pdf.

[50] M. King et al. *Controls Abstraction Towards Accelerator Physics: A Middle Layer Python Package for Particle Accelerator Control*. Sept. 2025. DOI: 10.48550/arXiv.2509.19794.

[51] H. Padamsee. "The science and technology of superconducting cavities for accelerators". In: *Supercond. Sci. Technol.* 14.4 (Apr. 2001), R28. DOI: 10.1088/0953-2048/14/4/202.

[52] John Byrd. "RF Cavities and Linacs". USPAS Lecture. USPAS Lecture. United States Particle Accelerator School (USPAS). Albuquerque, NM, 2014. URL: https://uspas.fnal.gov/materials/14UNM/RF_Structures.pdf.

[53] P. Owen and T. Powers. "An overview of microphonics in CEBAF and current moderation techniques". English. In: *Proc. LINAC2024* (Chicago, IL, USA). International Linear Accelerator Conference 32. JACoW Publishing, Geneva, Switzerland, Aug. 2024, pp. 59–62. ISBN: 978-3-95450-219-6. DOI: 10.18429/JACoW-LINAC2024-MOPB007. URL: https://indico.jacow.org/event/71/contributions/5719.

[54] T. Powers, K. Davis, and N. Brock. "MICROPHONICS TESTING OF LCLS II CRYOMODULES AT JLAB". in: *Proc. of 19th International Conference on RF Superconductivity*. Thomas Jefferson National Accelerator Facility, Newport News, VA (United States). Aug. 2019. DOI: 10.18429/JACoW-SRF2019-TUP034. URL: https://www.osti.gov/biblio/1975495.

[55] K. Villafania et al. "Control of microphonics for a superconducting radio-frequency photoinjector cryomodule". English. In: *Proc. HIAT2025* (East Lansing, MI, USA). HIAT 16. JACoW Publishing, Geneva, Switzerland, June 2025, pp. 42–45. ISBN: 978-3-95450-260-8. DOI: 10.18429/JACoW-HIAT2025-MOP07. URL: https://indico.jacow.org/event/82/contributions/8966.

[56] P. Gupta and R. Rabehl. "Design guidelines for avoiding thermo-acoustic oscillations in helium piping systems". In: *Applied Thermal Engineering* 84 (2015), pp. 104–109. ISSN: 1359-4311. DOI: https://doi.org/10.1016/j.applthermaleng.2015.03.051. URL: https://www.sciencedirect.com/science/article/pii/S1359431115002756.

[57] T. Powers. "Analysis and Management of Microphonics in Operational SRF Cavities with Bandwidths of Approximately 10 Hz" (Lanzhou, China). presented at SRF2017 in Lanzhou, China, unpublished. Geneva, Switzerland, Jan. 2018.

[58] Zheng Gao et al. "A new microphonics measurement method for superconducting RF cavities". In: *Nuclear Instruments and Methods in Physics Research Section A: Accelerators, Spectrometers, Detectors and Associated Equipment* 767 (2014), pp. 212–217. ISSN: 0168-9002. DOI: https://doi.org/10.1016/j.nima.2014.08.030. URL: https://www.sciencedirect.com/science/article/pii/S0168900214009590.

[59] M. Ge et al. "Measurements and Analysis of Cavity Microphonics and Frequency Control in the Cornell ERL Main Linac Prototype Cryomodule". In: *Proc. of Linear Accelerator Conference (LINAC'16), East Lansing, MI, USA, 25-30 September 2016* (East Lansing, MI, USA). Linear Accelerator Conference 28. https://doi.org/10.18429/JACoW-LINAC2016-TUPLR010. Geneva, Switzerland: JACoW, May 2017, pp. 488–491. ISBN: 978-3-95450-169-4. DOI: https://doi.org/10.18429/JACoW-LINAC2016-TUPLR010. URL: http://jacow.org/linac2016/papers/tuplr010.pdf.

[60] M. Karliner, V. Shapiro, and I. Shekhtman. "Instability in the Walls of a Cavity Due to Ponderomotive Forces of the Electromagnetic Field". In: *Soviet Physics-Technical Physics* 11.11 (May 1967), pp. 1501–1507.

[61] M. Karliner, V. Petrov, and I. Shekhtman. "Vibration of the Walls of a Cavity Resonator Under Ponderomotive Forces in the Presence of Feedback". In: *Soviet Physics-Technical Physics* 14.8 (Feb. 1970), pp. 1041–1043.

[62] D. Schulze and Kernforschungszentrum Karlsruhe (F R. Germany) Inst fuer Experimentelle Kernphysik. *Ponderomotive stability of rf resonators and resonator control systems*. en. Tech. rep. ANL-Trans–944. Kernforschungszentrum Karlsruhe (F.R. Germany). Inst. fuer Experimentelle Kernphysik, 1971. URL: https://inis.iaea.org/records/z9f8a-szy02 (visited on 08/01/2025).

[63] K. Jordan et al. "Damping microphonics in SRF cavities using boron nitride nanotubes". English (Tokyo, Japan, Sept. 18–26, 2025). presented at SRF2025, Tokyo, Japan, 2025, paper TUP75, unpublished. Sept. 2025. URL: https://jacow.org/srf2025/pdf/TUP75.pdf.

[64] A. Facco. "Mechanical mode damping in superconducting low- β resonators". In: *Part. Accel.* 61 (1998), pp. 1–14.

[65] L. Yang et al. "Damping of vibrations in superconducting quarter wave resonators". In: *Phys. Rev. Accel. Beams* 22 (3 Mar. 2019), p. 030103. DOI: 10.1103/PhysRevAccelBeams.22.030103. URL: https://link.aps.org/doi/10.1103/PhysRevAccelBeams.22.030103.

[66] M. Balestri et al. "Adjustable vibration damper design for superconducting quarter wave resonators". In: *Journal of Vibrations and Control* 32 (2025). URL: https://doi.org/10.1177/10775463241312818.

[67] J. Brown et al. "Experimental Study of Mechanical Dampers for the FRIB beta=0.041 Quarter-Wave Resonators". In: *Proc. 21th Int. Conf. RF Supercond. (SRF'23)* (Grand Rapids, MI, USA). International Conference on RF Superconductivity 21. JACoW Publishing, Geneva, Switzerland, Sept. 2023, WEPWB128, pp. 898–901. ISBN: 978-3-95450-234-9. DOI: 10.18429/JACoW-SRF2023-WEPWB128. URL: https://jacow.org/srf2023/papers/wepwb128.pdf.

[68] S. Ghosh et al. "Method to reduce microphonics in superconducting resonators". In: *Phys. Rev. ST Accel. Beams* 10 (4 Apr. 2007), p. 042002. DOI: 10.1103/PhysRevSTAB.10.042002. URL: https://link.aps.org/doi/10.1103/PhysRevSTAB.10.042002.

[69] J. R. Delayen. "Ponderomotive instabilities and microphonics—a tutorial". In: *Physica C: Superconductivity*. Proceedings of the 12th International Workshop on RF Superconductivity 441.1 (July 2006), pp. 1–6. ISSN: 0921-4534. DOI: 10.1016/j.physc.

2006.03.050. URL: https://www.sciencedirect.com/science/article/pii/S0921453406001432 (visited on 08/02/2025).

[70] J. Brown et al. *The Ponderomotive Effects of Narrow-band, Superconducting Resonators in Open and Closed Loop*. 2026. arXiv: 2607.28806 [physics.acc-ph]. URL: https://arxiv.org/abs/2607.28806.

[71] L. D. Landau and E. M. Lifshitz. *Mechanics*. Elsevier Ltd, 2005, pp. 87–93.

[72] M.J. Brennan et al. "On the jump-up and jump-down frequencies of the Duffing oscillator". In: *Journal of Sound and Vibration* 318.4 (2008), pp. 1250–1261. ISSN: 0022-460X. DOI: https://doi.org/10.1016/j.jsv.2008.04.032. URL: https://www.sciencedirect.com/science/article/pii/S0022460X08003805.

[73] F. Qiu et al. "Analytical modeling and experimental verification of oscillatory ponderomotive instabilities in closed-loop superconducting rf cavities". In: *Phys. Rev. Accel. Beams* 28 (11 Nov. 2025), p. 112001. DOI: 10.1103/hs5q-q5xc. URL: https://link.aps.org/doi/10.1103/hs5q-q5xc.

[74] J. R. Delayen. "Phase and Amplitude Stabilization of Superconducting Resonators". en. phd. California Institute of Technology, 1978. DOI: 10.7907/ZS1J-1E35. URL: https://resolver.caltech.edu/CaltechETD:etd-03042008-083340 (visited on 08/01/2025).

[75] K. Davis, T. Powers, and Newport News Thomas Jefferson National Accelerator Facility. *Transient ponderomotive effects in superconducting cavities*. English. Tech. rep. JLAB-ACE–05-439. Thomas Jefferson National Accelerator Facility, Newport News, VA (United States), July 2005. URL: https://inis.iaea.org/records/sr1yx-etg05 (visited on 08/04/2025).

[76] A. Bellandi et al. "Integral Resonance Control In Continuous Wave Superconducting Particle Accelerators". In: *IFAC-PapersOnLine* 53.2 (2020). 21st IFAC World Congress, pp. 361–367. ISSN: 2405-8963. DOI: https://doi.org/10.1016/j.ifacol.2020.12.186. URL: https://www.sciencedirect.com/science/article/pii/S2405896320304511.

[77] A. Bellandi. "LLRF Control Techniques for the European XFEL Continuous Wave Upgrade". PhD thesis. Universitat Hamburg, 2021.

[78] S.R. Koscielniak. "Ponderomotive Instability of Generator-Driven Cavity". In: *Proc. 10th International Particle Accelerator Conference (IPAC'19), Melbourne, Australia, 19-24 May 2019* (Melbourne, Australia). International Particle Accelerator Conference 10. https://doi.org/10.18429/JACoW-IPAC2019-THPRB010. Geneva, Switzerland: JACoW Publishing, June 2019, pp. 3820–3823. ISBN: 978-3-95450-208-0. DOI: doi:10.18429/JACoW-IPAC2019-THPRB010. URL: http://jacow.org/ipac2019/papers/thprb010.pdf.

[79] S.R. Koscielniak. "Ponderomotive Instability of Self-Excited Cavity". In: *Proc. 10th International Particle Accelerator Conference (IPAC'19), Melbourne, Australia, 19-24 May 2019* (Melbourne, Australia). International Particle Accelerator Conference 10. https://doi.org/10.18429/JACoW-IPAC2019-THPRB007. Geneva, Switzerland: JACoW Publishing, June 2019, pp. 3808–3811. ISBN: 978-3-95450-208-0. DOI: doi:10.18429/JACoW-IPAC2019-THPRB007. URL: http://jacow.org/ipac2019/papers/thprb007.pdf.

[80] S.R. Koscielniak. "Ponderomotive Instability of Two Self-Excited Cavities". In: *Proc. 10th International Particle Accelerator Conference (IPAC'19), Melbourne, Australia, 19-24 May 2019* (Melbourne, Australia). International Particle Accelerator Conference 10. https://doi.org/10.18429/JACoW-IPAC2019-THPRB008. Geneva, Switzerland: JACoW Publishing, June 2019, pp. 3812–3815. ISBN: 978-3-95450-208-0. DOI: doi:10.18429/JACoW-IPAC2019-THPRB008. URL: http://jacow.org/ipac2019/papers/thprb008.pdf.

[81] S.R. Koscielniak. "Vector Sum & Diffference Control of SRF Cavities". In: *Proc. 10th International Particle Accelerator Conference (IPAC'19), Melbourne, Australia, 19-24 May 2019* (Melbourne, Australia). International Particle Accelerator Conference 10. https://doi.org/10.18429/JACoW-IPAC2019-THPRB009. Geneva, Switzerland: JACoW Publishing, June 2019, pp. 3816–3819. ISBN: 978-3-95450-208-0. DOI: doi:10.18429/JACoW-IPAC2019-THPRB009. URL: http://jacow.org/ipac2019/papers/thprb009.pdf.

[82] S. Koscielniak. *Ponderomotive Instability of RF Cavities with Vector Sum Control, and Cure By Difference Control*. 2019. arXiv: 1910.07106 [physics.acc-ph]. URL: https://arxiv.org/abs/1910.07106.

[83] K. Fong and R. Leewe. "Parametric Pumped Oscillation by Lorentz Force in Superconducting Rf Cavity". In: *Proc. 10th International Particle Accelerator Conference (IPAC'19), Melbourne, Australia, 19-24 May 2019* (Melbourne, Australia). International Particle Accelerator Conference 10. https://doi.org/10.18429/JACoW-IPAC2019-WEPRB003. Geneva, Switzerland: JACoW Publishing, June 2019, pp. 2798–2800. ISBN: 978-3-95450-208-0. DOI: doi:10.18429/JACoW-IPAC2019-WEPRB003. URL: http://jacow.org/ipac2019/papers/weprb003.pdf.

[84] J. Brown et al. "Study of ponderomotive Instability in the FRIB beta=0.53 half-wave resonator". English. In: *HIAT2025 - Proceedings*. HIAT. Michigan State University, East Lansing, MI, USA: JACoW Publishing, June 2025, pp. 242–245. ISBN: 978-3-95450-260-8. DOI: 10.18429/JACoW-HIAT2025-WEP19.

[85] S. Simrock and Z. Geng. *Low-level Radio Frequency Systems*. Ed. by A. Chao et al. Springer Nature, 2022.

[86] S. Stark et al. "FRIB HWR Tuner Development". In: *Proc. of Linear Accelerator*

Conference (LINAC'16), East Lansing, MI, USA, 25-30 September 2016 (East Lansing, MI, USA). Linear Accelerator Conference 28. https://doi.org/10.18429/JACoW-LINAC2016-TUPLR029. Geneva, Switzerland: JACoW, May 2017, pp. 535–537. ISBN: 978-3-95450-169-4. DOI: https://doi.org/10.18429/JACoW-LINAC2016-TUPLR029. URL: http://jacow.org/linac2016/papers/tuplr029.pdf.

[87] W. Chang et al. "Enhanced Pneumatic Tuner Control for FRIB Half-Wave Resonators". In: *Proc. SRF'21* (East Lansing, MI, USA). International Conference on RF Superconductivity 20. JACoW Publishing, Geneva, Switzerland, Oct. 2022, THPTEV002, pp. 829–831. ISBN: 978-3-95450-233-2. DOI: 10.18429/JACoW-SRF2021-THPTEV002. URL: https://jacow.org/srf2021/papers/thptev002.pdf.

[88] M. Ge et al. "Frequency Tuner Development at Cornell for the RAON Half Wave Resonators". In: *Proc. IPAC'18* (Vancouver, Canada, Apr.-May 2018). JACoW Publishing, Geneva, Switzerland, 2018, pp. 2461–2464. DOI: 10.18429/JACoW-IPAC2018-WEPMF043. URL: http://accelconf.web.cern.ch/ipac2018/papers/WEPMF043.pdf.

[89] P. Varghese et al. "Resonance Control System for the PIP-II IT HWR Cryomodule". In: *Proc. IPAC'21* (Campinas, SP, Brazil). International Particle Accelerator Conference 12. https://doi.org/10.18429/JACoW-IPAC2021-THPAB337. JACoW Publishing, Geneva, Switzerland, Aug. 2021, THPAB337, pp. 4446–4449. ISBN: 978-3-95450-214-1. DOI: 10.18429/JACoW-IPAC2021-THPAB337. URL: https://jacow.org/ipac2021/papers/thpab337.pdf.

[90] Y.M. Pischalnikov et al. "Design and Test of the Compact Tuner for Narrow Bandwidth SRF Cavities". In: *Proc. 6th International Particle Accelerator Conference (IPAC'15), Richmond, VA, USA, May 3-8, 2015* (Richmond, VA, USA). International Particle Accelerator Conference 6. https://doi.org/10.18429/JACoW-IPAC2015-WEPTY035. Geneva, Switzerland: JACoW, June 2015, pp. 3352–3354. ISBN: 978-3-95450-168-7. DOI: https://doi.org/10.18429/JACoW-IPAC2015-WEPTY035. URL: http://jacow.org/ipac2015/papers/wepty035.pdf.

[91] Yuriy Pischalnikov, Sergey Cheban, and Jae-Chul Yun. "Design of 650 MHz Tuner for PIP-II Project". In: *9th International Particle Accelerator Conference*. June 2018. DOI: 10.18429/JACoW-IPAC2018-WEPML002.

[92] C. Contreras-Martinez et al. "Testing of the SSR2 SRF cavity tuner for PIP-II at 2 K". English. In: *Proc. LINAC2024* (Chicago, IL, USA). International Linear Accelerator Conference 32. JACoW Publishing, Geneva, Switzerland, Aug. 2024, pp. 174–176. ISBN: 978-3-95450-219-6. DOI: 10.18429/JACoW-LINAC2024-MOPB058. URL: https://indico.jacow.org/event/71/contributions/5695.

[93] J.P. Holzbauer, D. Passarelli, and Y.M. Pischalnikov. "Testing of SSR1 Production Tuner for PIP-II". in: *Proc. 9th International Particle Accelerator Conference (IPAC'18), Vancouver, BC, Canada, April 29-May 4, 2018* (Vancouver, BC, Canada). Interna-

tional Particle Accelerator Conference 9. https://doi.org/10.18429/JACoW-IPAC2018-WEPML005. Geneva, Switzerland: JACoW Publishing, June 2018, pp. 2681–2683. ISBN: 978-3-95450-184-7. DOI: doi:10.18429/JACoW-IPAC2018-WEPML005. URL: http://jacow.org/ipac2018/papers/wepml005.pdf.

[94] G. Devanz et al. "Compensation of Lorentz Force Detuning of a TTF 9-Cell Cavity with a New Integrated Piezo Tuner". In: *Proceedings of EPAC 2006*. 2006.

[95] D. Barni et al. "A New Tuner for TESLA". in: *Proceedings of EPAC 2002*. 2002.

[96] S. Yu Kazakov et al. "Fast ferroelectric phase shifters for energy recovery linacs". In: *Physical Review Special Topics - Accelerators and Beams* 13.11 (Nov. 24, 2010), p. 113501. DOI: 10.1103/PhysRevSTAB.13.113501. URL: https://link.aps.org/doi/10.1103/PhysRevSTAB.13.113501 (visited on 05/18/2026).

[97] Y. Pischalnikov and W. Schappert. *Adaptive compensation of Lorentz force detuning in superconducting RF cavities*. Tech. rep. FERMILAB-TM–2476-TD. Fermi National Accelerator Laboratory (FNAL), Batavia, IL (United States), Nov. 1, 2011. DOI: 10.2172/1433326. URL: https://www.osti.gov/biblio/1433326 (visited on 08/04/2025).

[98] S. Pfeiffer, A. Eichler, and H. Schlarb. "Model-based feed-forward control for time-varying systems with an example for SRF cavities". In: *IFAC-PapersOnLine* 53.2 (2020). 21st IFAC World Congress, pp. 1331–1336. ISSN: 2405-8963. DOI: https://doi.org/10.1016/j.ifacol.2020.12.1868. URL: https://www.sciencedirect.com/science/article/pii/S2405896320324824.

[99] J. C. Maxwell. "I. On governors". In: *Proceedings of the Royal Society of London* 16 (Dec. 1868), pp. 270–283. ISSN: 0370-1662. DOI: 10.1098/rspl.1867.0055. eprint: https://royalsocietypublishing.org/rspl/article-pdf/doi/10.1098/rspl.1867.0055/1270802/rspl.1867.0055.pdf. URL: https://doi.org/10.1098/rspl.1867.0055.

[100] C. G. Kang. "Origin of Stability Analysis: Ön Governorsb"y J.C. Maxwell [Historical Perspectives]". In: *IEEE Control Systems* 36.5 (2016), pp. 77–88. DOI: 10.1109/MCS.2016.2584358.

[101] Paul A. Lynn. "The Laplace Transform and the z-transform". In: *Electronic Signals and Systems*. Ed. by Paul A. Lynn. London: Macmillan Education UK, 1986, pp. 225–272. ISBN: 978-1-349-18461-3. DOI: 10.1007/978-1-349-18461-3_6. URL: https://doi.org/10.1007/978-1-349-18461-3_6 (visited on 05/18/2026).

[102] R. Miklosovic, A. Radke, and Z. Gao. "Discrete implementation and generalization of the extended state observer". In: *2006 American Control Conference*. 2006, pp. 6–. DOI: 10.1109/ACC.2006.1656547.

[103] Z. Li. "Review of PID control design and tuning methods". In: *Journal of Physics Conference Series*. Vol. 2649. ADS Bibcode: 2023JPhCS2649a2009L. IOP, Nov. 1, 2023, p. 012009. DOI: 10.1088/1742-6596/2649/1/012009. URL: https://ui.adsabs.harvard.edu/abs/2023JPhCS2649a2009L (visited on 04/26/2026).

[104] S. I. Kwon, Y. M. Wang, and A. Regan. "SNS LLRF control system model design". In: *Proceedings of the 1999 Particle Accelerator Conference (Cat. No.99CH36366)*. the 1999 Particle Accelerator Conference (Cat. No.99CH36366). Vol. 2. Mar. 1999, 1067–1069 vol.2. DOI: 10.1109/PAC.1999.795450. URL: https://ieeexplore.ieee.org/document/795450 (visited on 08/13/2025).

[105] C. Serrano et al. "Design and Implementation of the LLRF System for LCLS-II". in: *No journal information* (Jan. 1, 2018). Institution: Thomas Jefferson National Accelerator Facility (TJNAF), Newport News, VA (United States); LBNL, Berkeley; Fermi National Accelerator Laboratory (FNAL), Batavia, IL (United States); SLAC National Accelerator Laboratory (SLAC), Menlo Park, CA (United States) Number: FERMILAB-CONF-18-787-AD-PIP2. DOI: 10.18429/JACoW-ICALEPCS2017-THSH202. URL: https://www.osti.gov/biblio/3012627 (visited on 04/26/2026).

[106] S. N. Simrock. "Low level radio frequency control system for the european XFEL". in: *Proceedings of the International Conference Mixed Design of Integrated Circuits and System, 2006. MIXDES 2006.* the International Conference Mixed Design of Integrated Circuits and System, 2006. MIXDES 2006. June 2006, pp. 79–84. DOI: 10.1109/MIXDES.2006.1706542. URL: https://ieeexplore.ieee.org/document/1706542 (visited on 04/26/2026).

[107] P. Varghese et al. *LLRF System for the Fermilab PIP-II Superconducting LINAC*. Nov. 10, 2023. DOI: 10.48550/arXiv.2311.00900. arXiv: 2311.00900[physics]. URL: http://arxiv.org/abs/2311.00900 (visited on 04/26/2026).

[108] J. Han. "From PID to Active Disturbance Rejection Control". In: *IEEE Transactions on Industrial Electronics* 56.3 (Mar. 2009), pp. 900–906. ISSN: 1557-9948. DOI: 10.1109/TIE.2008.2011621. URL: https://ieeexplore.ieee.org/document/4796887 (visited on 08/04/2025).

[109] Zhiqiang G. "Active disturbance rejection control: a paradigm shift in feedback control system design". In: *2006 American Control Conference*. 2006. DOI: 10.1109/ACC.2006.1656579.

[110] John Vincent et al. "On active disturbance rejection based control design for superconducting RF cavities". In: *Nuclear Instruments and Methods in Physics Research Section A: Accelerators, Spectrometers, Detectors and Associated Equipment* 643.1 (July 1, 2011), pp. 11–16. ISSN: 0168-9002. DOI: 10.1016/j.nima.2011.04.033. URL: https://www.sciencedirect.com/science/article/pii/S0168900211007716 (visited on 08/02/2025).

[111] Shen Zhao et al. “Fixed-point implementation of active disturbance rejection control for superconducting radio frequency cavities”. In: *2013 American Control Conference*. 2013, pp. 2693–2698. DOI: 10.1109/ACC.2013.6580241.

[112] S. Zhao and Z. Gao. “Active disturbance rejection control for non-minimum phase systems”. In: *Proceedings of the 29th Chinese Control Conference*. 2010, pp. 6066–6070.

[113] Gang Tian and Zhiqiang Gao. “Frequency Response Analysis of Active Disturbance Rejection Based Control System”. In: *2007 IEEE International Conference on Control Applications*. Oct. 2007, pp. 1595–1599. DOI: 10.1109/CCA.2007.4389465. URL: https://ieeexplore.ieee.org/document/4389465 (visited on 08/02/2025).

[114] A. Bellandi et al. “Narrow Bandwidth Active Noise Control for Microphonics Rejection in Superconducting Cavities at LCLS-II”. in: *JACoW* LINAC2022 (2022), THPOPA21. DOI: 10.18429/JACoW-LINAC2022-THPOPA21. arXiv: 2209.13896 [physics.acc-ph].

[115] R. Rybaniec et al. “FPGA-Based RF and Piezocontrollers for SRF Cavities in CW Mode”. In: *IEEE Transactions on Nuclear Science* 64.6 (2017), pp. 1382–1388. DOI: 10.1109/TNS.2017.2687981.

[116] N. Banerjee et al. “Active suppression of microphonics detuning in high ${Q}_{L}$ cavities”. In: *Physical Review Accelerators and Beams* 22.5 (May 9, 2019), p. 052002. DOI: 10.1103/PhysRevAccelBeams.22.052002. URL: https://link.aps.org/doi/10.1103/PhysRevAccelBeams.22.052002 (visited on 05/04/2026).

[117] Q. Feng et al. “An approach to characterize Lorentz force transfer function for superconducting cavities”. In: *Nuclear Instruments and Methods in Physics Research Section A: Accelerators, Spectrometers, Detectors and Associated Equipment* 1012 (2021), p. 165633. ISSN: 0168-9002. DOI: https://doi.org/10.1016/j.nima.2021.165633. URL: https://www.sciencedirect.com/science/article/pii/S0168900221006185.

[118] S. D. Murthy, L. Doolittle, and A. Benwell. *Analog Cavity Emulators to Support LLRF Development*. Oct. 15, 2022. DOI: 10.48550/arXiv.2210.05430. arXiv: 2210.05430[physics]. URL: http://arxiv.org/abs/2210.05430 (visited on 05/06/2026).

[119] C. Serrano, L. Doolittle, and V. Vytla. “Cryomodule-on-Chip Simulation Engine”. In: *Proceedings of the 16th Int. Conf. on Accelerator and Large Experimental Control Systems* ICALEPCS2017 (2018). Ed. by Schaa RW (Ed.) Volker et al. Artwork Size: 8 pages, 0.763 MB ISBN: 9783954501939 Medium: PDF, p. 8. DOI: 10.18429/JACOW-ICALEPCS2017-TUAPL06. URL: http://jacow.org/icalepcs2017/doi/JACoW-ICALEPCS2html (visited on 05/06/2026).

[120] F. Stocklin. *Relative sideband amplitudes versus modulation index for common functions using frequency and phase modulation*. Tech. rep. X-863-73-112. NASA Goddard Space Flight Center, 1973.

[121] C. Contreras-Martinez. “Electromagnetic and Mechanical Properties of Medium beta SRF Elliptical Cavities”. PhD thesis. Michigan State University, 2021.

[122] A. Elejaga et al. “Experimental testing of a modified active disturbance rejection control for microphonics reduction in a 9-cell TESLA superconducting cavity”. In: *Phys. Rev. Accel. Beams* 27 (11 Nov. 2024), p. 113501. DOI: 10.1103/PhysRevAccelBeams.27.113501. URL: https://link.aps.org/doi/10.1103/PhysRevAccelBeams.27.113501.

[123] S. Zhao and Z. Gao. “Modified active disturbance rejection control for time-delay systems”. In: *ISA Transactions* 53.4 (2014). Disturbance Estimation and Mitigation, pp. 882–888. ISSN: 0019-0578. DOI: https://doi.org/10.1016/j.isatra.2013.09.013. URL: https://www.sciencedirect.com/science/article/pii/S0019057813001560.

[124] *Analog Devices AD8302 Data Sheet Rev. B*. Analog Devices.